Surface Characterization by Electrokinetics: Interfaces, Adsorption, and Microplastics

Dissertation

zur Erlangung des akademischen Grades
eines Doktors der Naturwissenschaften (Dr. rer. nat.) der Fakultät für Biologie, Chemie und Geowissenschaften der Universität Bayreuth.

UNIVERSITÄT
BAYREUTH

vorgelegt von

Matthias Bruno Engelhardt

geboren in Roth, Deutschland

Bayreuth, 2025

Surface Characterization by Electrokinetics: Interfaces, Adsorption, and Microplastics

Dissertation

zur Erlangung des akademischen Grades
eines Doktors der Naturwissenschaften (Dr. rer. nat.) der Fakultät für Biologie, Chemie und Geowissenschaften der Universität Bayreuth.

UNIVERSITÄT
BAYREUTH

vorgelegt von

Matthias Bruno Engelhardt

geboren in Roth, Deutschland

Bayreuth, 2025

Die vorliegende Arbeit wurde in der Zeit von Oktober 2021 bis August 2025 am Lehrstuhl Physikalische Chemie II unter Betreuung von Herrn Professor Dr. Georg Papastavrou angefertigt.

Vollständiger Abdruck der von der Fakultät für Biologie, Chemie und Geowissenschaften der Universität Bayreuth genehmigten Dissertation zur Erlangung des akademischen Grades eines Doktors der Naturwissenschaften (Dr. rer. Nat.).

Form der Dissertation:	Kumulative Dissertation
Dissertation eingereicht am:	06.08.2025
Zulassung durch die Promotionskommission:	13.08.2025
Wissenschaftliches Kolloquium:	23.03.2026

Amtierender Dekan:

Prof. Dr. Janosch Hennig

Prüfungsausschuss:

Prof. Dr. Georg Papastavrou	(Gutachter)
Prof. Dr. Markus Retsch	(Gutachter)
Prof. Dr. Andre Gröschel	(Vorsitz)
Prof. Dr. Jürgen Senker	

„Von Arbeit stirbet kein Mensch. Aber von Ledig- und Müßiggehen kommen die Leute um Leib und Leben; denn der Mensch ist zur Arbeit geboren wie der Vogel zum Fliegen."

Dr. Martin Luther (1483 – 1546)

Contents

Contents i

Zusammenfassung ii

Summary v

1. Introduction 1

2. Theoretical Background 8

3. Synopsis 31

Manuscripts and Publications 70

4. Effective charge of high-generation PAMAM dendrimers in the adsorbed state 71

5. Preparation of geometrically highly controlled Ga particle arrays on quasi-planar nanostructured surfaces as a SCALMS model system 103

6. Preparation and Surface Functionalization of a Tunable Porous System Featuring Stacked Spheres in Cylindrical Pores 116

7. Following Changes at the Solid/Liquid Interface for Large Microplastic Particles by Streaming Potential 131

8. Electrophoretic mobility of nanoparticle aggregates: Independence from aggregate size 169

List of Publications 182

Danksagung 186

(Eidesstattliche) Versicherung und Erklärung 189

Zusammenfassung

Diese Dissertation untersucht die vielfältigen Anwendungen elektrokinetischer Phänomene und beleuchtet deren Nutzen in verschiedenen wissenschaftlichen Bereichen. Durch fünf verschiedene Forschungsprojekte werden diverse Aspekte der Elektrokinetik untersucht, darunter die Ladung adsorbierter Makromoleküle, die Azidität von Katalysatorträgern, die durch Oberflächenladung beeinflusste Partikelstapelung in Poren, Veränderungen der Mikroplastik-Oberflächenchemie durch künstliche Verwitterung und die Anwendbarkeit der elektrophoretischen Mobilität für Nanopartikelaggregate. Das übergeordnete Ziel ist es, verschiedene Grenzflächenphänomene zu untersuchen, indem verschiedene elektrokinetischen Methoden genutzt werden.

Der erste Teil dieser Dissertation untersuchte, wie sich die Oberflächenbedeckung und der pH-Wert auf die effektive Ladung adsorbierter Makromoleküle auf verschiedenen Substraten auswirken. Muskovit-Glimmer und Quarzglas wurden mit einem speziell angefertigten Strömungspotenzial-Messgerät charakterisiert, wobei sich ein unterschiedliches elektrokinetisches Verhalten über den pH-Bereich zeigte. Poly(amidoamin) (PAMAM) Dendrimere der Generation 10 wurden auf diesen Oberflächen adsorbiert, wobei eine substratabhängige maximale Bedeckung beobachtet wurde. Strömungspotenzialmessungen zeigten signifikante Unterschiede in der effektiven Ladung von PAMAM auf den Substraten. Die effektive Ladung für Substrate, deren Oberflächenladung mit dem pH-Wert variiert, variiert nicht nur durch die Titration der ionisierbaren Gruppen der Polyelektrolyte, sondern auch aufgrund der elektrostatischen Wechselwirkung mit dem Substrat. Dadurch stellte sich das Zeta-Potenzial als guter Indikator für die Polyelektrolyt-Belegung von Oberflächen heraus. Diese Ergebnisse unterstrichen den signifikanten Einfluss der Substrateigenschaften auf die makromolekularen Ladungen im Rahmen des elektrostatischen RSA-Modells.

Im Rahmen einer Kollaboration wurden Strömungspotenzialmessungen im zweiten Teil dieser Dissertation verwendet, um ein neuartiges Modellsystem für unterstützte katalytisch aktive flüssige Metalllösungen (SCALMS) zu charakterisieren. Hierbei wurden Dünnschichten verschiedener Metalloxide durch das Strömungspotenzial im Hinblick auf deren Azidität untersucht, um dessen Zusammenhang mit der Größenverteilung von katalytisch aktiven Gallium (Ga)-Tröpfchen zu verstehen. Strömungspotenzialmessungen, die den isoelektrischen Punkt (IEP) der Metalloxidbeschichtungen (SiO_2, TiO_2, Al_2O_3 und MgO) bestimmten, zeigten eine klare Korrelation: die sauren Oxide SiO_2 und TiO_2 führten zu den kleinsten Ga-Partikeldurchmessern und engsten Größenverteilungen, was eine gute Prozesskontrolle und katalytische Leistung implizierten. Diese Forschung validierte die Strömungspotenzialtechnik als ein leistungsstarkes Werkzeug zur Charakterisierung der Oberflächenazidität und zeigte, dass die Oberflächenazidität ein kritischer Faktor bei der Kontrolle der Ga-Partikelbildung ist.

Der dritte Abschnitt erweiterte die Anwendung des Strömungsstroms, um die Entwicklung von Katalysatorträgern in einer weiteren Kollaboration zu optimieren. Der Fokus lag auf der Partikelbeladung innerhalb eines porösen anodischen Aluminiumoxid (AAO)-Gerüsts. Dieses Gerüst wurde mit verschiedenen Funktionalisierungen beschichtet. Ziel war es, die Packungsdichte von Polystyrol (PS)-Kugeltemplaten innerhalb dieser Poren zu maximieren, um die Porosität zu erhöhen. Die höchsten PS-Beladungen wurden für unbeschichtetes Al_2O_3- und HfO_2-Beschichtungen im Gegensatz zu ZnO gefunden. Strömungsstrommessungen mit unserer speziellen asymmetrischen Zelle analysierten HfO_2- und ZnO-beschichtete Substrate, die Porenwandbeschichtungen repräsentieren. Der IEP von HfO_2- und ZnO-Beschichtungen wurde über den Strömungsstrom bestimmt, was zeigte,

dass die saure Oberfläche von HfO_2 eine effektive Kugelstapelung durch elektrostatische Abstoßung ermöglichte. Im Gegensatz dazu führte die basische Oberfläche von ZnO aufgrund von Anziehung zu einer ungeordneten Packung. Dieses Projekt fertigte erfolgreich kontrollierte poröse Systeme mit hohen Oberflächen durch die Kombination von elektrokinetischer Charakterisierung mit Materialdesign.

Der vierte Teil erweiterte die Anwendung von Strömungspotenzialmessungen auf granulare Proben, wobei der Schwerpunkt insbesondere auf der Charakterisierung von Mikroplastikpartikeln (MPPs) lag. In der Vergangenheit konzentrierte sich die Forschung auf Partikel, die kleiner als 5 µm und größer als 50 µm waren. Mittels Strömungspotenzialmessungen lieferte diese Studie Einblicke in die Oberflächenladungseigenschaften von künstlichen MPPs in einem Größenbereich von 15 µm bis 250 µm und schloss damit eine wichtige analytische Lücke. Zeta-Potenzial-Experimente zeigten vergleichbar saure Oberflächen in allen PS-Partikelgrößenfraktionen, die durch einen Mahlprozess hergestellt wurden. Die Oberflächenladung von künstlich verwitterten MPPs wurde ebenfalls untersucht, wobei ein zunehmend saures Verhalten bei längerer Verwitterung festgestellt wurde, was auf die Bildung von sauerstoffbasierten funktionellen Gruppen zurückgeführt wurde. Die Verwitterung führte zu kleineren, unregelmäßig geformten Partikeln mit erhöhter Oberfläche und Reaktivität. Diese Studie demonstrierte das breite Spektrum der Anwendungen des Strömungspotenzials und zeigt die Auswirkungen der Verwitterung auf die Oberflächenchemie, die die Wechselwirkungen mit organischen Substanzen in der Umwelt beeinflussen.

Während der vorherige Abschnitt die Oberflächenladung von Mikropartikeln mittels Strömungspotenzial untersuchte, befasste sich der letzte Abschnitt dieser Arbeit mit der elektrophoretischen Mobilität (EPM) von Nanopartikeln und ging dabei auf eine zentrale Einschränkung der EPM-Messungen ein: die Verwendung von EPM bei Aggregaten. Pyrogene Kieselsäure, eine fraktalartige Struktur aus sphärischen Nanopartikeln, wurde in zwei Varianten mit unterschiedlichen Primärpartikeldurchmessern untersucht. EPM-Messungen zeigten Unterschiede im elektrokinetischen Verhalten der beiden Typen, insbesondere in alkalischen Medien. Die O'Brien-White-Theorie erklärte diese Trends und zeigte, dass die EPM von Aggregaten hauptsächlich durch die EPM ihrer Primärpartikel bestimmt wird. Aggregate, die aus verschiedenen Primärpartikeln gebildet wurden, zeigten konstante EPM-Werte, unabhängig von der Aggregatgröße. Diese Studie demonstrierte, dass die minimale Überlappung der Doppelschichten innerhalb der fraktalartigen Struktur die Verwendung von EPM in der Nähe kritischer Koagulationskonzentrationen (CCC) unterstützt und bietet eine Grundlage für die Vorhersage des Aggregatverhaltens in kolloidalen Systemen.

Zusammenfassend demonstriert diese Dissertation die außerordentliche Bandbreite elektrokinetischer Methoden zur Aufklärung von Wechselwirkungen an Grenzflächen vielseitiger Systeme. Die zielgerichtete Anwendung elektrokinetischer Techniken ermöglichte es, signifikante Einblicke in grundlegende Fragestellungen der Material- und Umweltwissenschaften zu gewinnen.

Summary

This thesis explores the broad applications of electrokinetic phenomena, showcasing their utility across various scientific disciplines. Through five distinct research projects, this work examines diverse aspects of electrokinetics, including the charge of adsorbed macromolecules, the acidity of catalyst carrier interfaces, particle stacking in pores influenced by surface charge, changes in microplastic surface chemistry due to artificial weathering, and the applicability of electrophoretic mobility for nanoparticle aggregates. The overarching aim is to understand and manipulate various interfacial phenomena by exploiting the electrokinetic properties.

The first part of this thesis investigated how surface coverage and pH affect the effective charge of adsorbed macromolecules on different substrates. Muscovite mica and fused silica were characterized using a custom-built streaming potential apparatus, demonstrating distinct electrokinetic behavior across pH ranges. Generation 10 poly(amidoamine) (PAMAM) dendrimers were adsorbed onto these surfaces, showing substrate-dependent maximum coverage. Streaming potential measurements revealed significant differences in the effective charge of PAMAM on each substrate. The effective charge for substrates whose surface charge varies with pH varies not only by the titration of the ionizable groups of the polyelectrolytes but also due to the electrostatic interaction with the substrate. These findings emphasized the significant impact of substrate properties on macromolecular charge within the electrostatic RSA framework.

In the context of a collaboration, streaming potential measurements were employed in the second part of this dissertation to characterize a novel model system for supported catalytically active liquid metal solutions (SCALMS). In this study, thin films of metal oxides (SiO_2, TiO_2, Al_2O_3, and MgO) were investigated via streaming potential measurements to understand the relationship between their acidity and the size distribution of catalytically active gallium (Ga) droplets. Streaming potential measurements that determined the isoelectric point (IEP) of the metal oxide coatings revealed a clear correlation: the acidic oxides SiO_2 and TiO_2 led to the smallest Ga particle diameters and narrowest size distributions, implying good process control and catalytic performance. This research validated the streaming potential technique as a powerful tool for characterizing surface acidity and demonstrated that surface acidity is a critical factor in controlling Ga particle formation.

Section three expanded the application of electrokinetic measurements, specifically the streaming current, to optimize catalyst carrier development by focusing on particle loading within a porous anodic aluminum oxide (AAO) framework. This framework was coated with different functionalizations. The objective was to maximize the packing density of sacrificial polystyrene (PS) spheres within these pores to enhance porosity. The highest PS loadings were found for bare Al_2O_3 and HfO_2 coatings, in contrast to ZnO. Streaming current measurements with our custom asymmetric cell analyzed HfO_2 and ZnO coated substrates, representing pore wall coatings. The IEP of HfO_2 and ZnO coatings was determined via the streaming current, revealing that HfO_2's acidic surface facilitated effective sphere stacking by electrostatic repulsion. In contrast, due to attraction, ZnO's basic surface led to disordered packing. This project successfully fabricated tunable porous systems with enhanced surface areas by combining electrokinetic characterization with materials design.

The fourth part advanced the application of streaming potential measurements to granular samples, specifically focusing on the characterization of microplastic particles (MPPs). Previously, research focused on particles smaller than 5 µm and larger than 50 µm. Using streaming potential measurements, this study provided insights into the surface charge properties of artificial MPs within

a size range of 15 µm to 250 µm, addressing a key analytical gap. Zeta-potential experiments revealed similarly acidic surfaces across all PS particle size fractions produced by milling. The surface charge of artificially weathered MPPs was also investigated, showing increasingly acidic behavior with prolonged weathering, attributed to the incorporation of oxygen-based functional groups. Weathering produced smaller, irregularly shaped particles with increased surface area. This study demonstrated the wide range of streaming potential applications and shows weathering effects on surface chemistry, affecting interactions with natural organic matter and soil.

While the previous section explored the surface charge of microparticles using streaming potential, this final section delves into the electrophoretic mobility (EPM) of nanoparticles. Fumed silica, a fractal-like structure of spherical primary nanoparticles, was investigated in two variants with different primary particle diameters. EPM measurements revealed significant differences in the electrokinetic behavior of the two types, especially in alkaline media. The O'Brien-White theory accurately explained these trends, showing that the EPM of aggregates is primarily determined by the EPM of their primary particles. Aggregates formed from distinct primary particles showed constant EPM values, independent of aggregate size. This study demonstrated the dominant impact of primary particle diameters on EPM by precisely engineering fumed silica aggregates with varying diameters.

In summary, this dissertation demonstrates the wide scope of electrokinetic methods in studying interfacial interactions within diverse systems. The targeted application of electrokinetic techniques enabled the acquisition of significant insights into fundamental questions in materials science and environmental science.

1. Introduction

1. Introduction

Interfaces are fundamental to countless natural and engineered systems, representing the boundary regions between two distinct phases[1, 2]. These regions govern critical processes such as energy transfer[1, 3], chemical reactions[1, 4, 5], and material interactions[6, 7], making them crucial to advancements in science and technology. The properties of interfaces – ranging from surface charge[1, 2, 8, 9] and roughness[1, 7] to adhesion[1, 6, 7] and wettability[1, 2] – play pivotal roles in applications as diverse as material design[10-13], catalysis[14-18], and environmental restoration[9, 19-25].

Given the wide-ranging significance of interfaces, accurately characterizing their properties is essential. Over the years, various analytical techniques have been developed to study solid/liquid- and solid/gaseous interfaces, each offering unique insights into their structure and chemistry. Microscopy techniques such as Atomic Force Microscopy (AFM)[26, 27] and Scanning Electron Microscopy (SEM)[28] provide nanoscale resolution of surface topography and morphology, while spectroscopic methods like X-ray Photoelectron Spectroscopy (XPS)[29] and Fourier Transform Infrared Spectroscopy (FTIR)[30] enable chemical analysis on a molecular level. Light scattering methods, including Dynamic Light Scattering (DLS)[31, 32] and Static Light Scattering (SLS)[33], are invaluable for characterizing colloidal systems and molecular interactions in solution. Electrochemical techniques, such as Electrochemical Impedance Spectroscopy (EIS)[3], probe interfacial charge transfer, while surface-specific tools like Quartz Crystal Microbalance (QCM)[34] and ellipsometry[35] provide insights into mass changes and thin film properties, respectively.

Due to the abundance of analytical techniques to characterize solid/liquid interfaces, some remain underutilized, particularly those focusing on the diffuse layer properties. For more than 200 years, the field of electrokinetics steadily evolved, starting from simple observations – from a modern perspective – of electro-osmosis and electrophoresis in U-tubes[36], discovering the streaming potential by pumping water through a channel[37], and measuring the sedimentation potential by settling sand grains in a vertical glass cylinder[38]. These techniques are referred to as classical electrokinetic phenomena. Despite the development of modern electrokinetic techniques like electroacoustics[39], dielectric dispersion[40], and dielectrophoresis[41, 42], the classical techniques never lost their potential. These classical electrokinetic techniques, such as the streaming potential and electrophoresis, offer unique advantages for studying the surface charge properties of solid/liquid interfaces. These methods relate the movement of ions and particles in response to external forces, directly quantifying electrostatic interactions at surfaces[8, 9, 43-45].

The basis of electrokinetic phenomena is the so-called electrical double layer at the solid/liquid interface[8, 9, 44]. According to the Stern model, this double layer consists of a charged surface, a rigid layer of adsorbed co- and/or counterions, and a diffuse layer of excess counterions extending into the solution[46]. The boundary between the rigid and diffuse layer is the so-called shear plane, from where ions in the double layer can be sheared off by tangential fluid motion. Here, the zeta-potential ζ is defined. ζ reflects the surface charge and is a versatile measure for colloidal interactions[8, 9, 44]. Electrokinetic techniques exploit the interaction between the double layer and an applied electric field or pressure gradient to provide insights into interfacial charge properties[8, 9, 44].

Historically, electrokinetic techniques have been predominantly applied to colloidal systems, where zeta-potential measurements are used to evaluate particle stability and aggregation[8, 9, 43, 45, 47-50]. However, their broader potential remains largely untapped. The ability of electrokinetic methods to indirectly characterize surface charge makes them particularly promising for emerging challenges in interface science. For example, studying the charge properties of macromolecules can yield critical insights into their stability and behavior in aquatic systems[51-57]. In catalysis, the surface charge of catalyst carriers is closely tied to their efficiency, as electrostatic interactions control the binding of reactants to active sites[58-60]. Additionally, as environmental concerns grow, the aging processes of microplastics – driven by chemical degradation[23, 61-63] and biofilm formation[64-67] – require advanced tools for characterization. Researchers can address important interdisciplinary questions by extending the scope of electrokinetic techniques to such complex systems.

To demonstrate the versatility of electrokinetic techniques in different scientific fields, this thesis focuses on developing and applying an in-house built streaming potential analyzer with purposely constructed measurement cells, complemented by commercial streaming potential and light scattering devices. This approach aims to enable the precise characterization of interfacial charge properties across a diverse range of systems, including macromolecules, catalyst carriers, and aged microplastics.

This dissertation aims to deepen our understanding of interfacial phenomena and broaden the utility of electrokinetic techniques. The insights gained are expected to contribute to the fields of material science and environmental research, promoting innovative solutions to current and future challenges in interface characterization.

References

[1] Butt, H.-J.; Graf, K. and Kappl, M., Physics and chemistry of interfaces, 1st ed., Wiley-VCH, Weinheim, **2003**

[2] Myers, D., Surfaces, interfaces, and colloids, 2nd ed., John Wiley & Sons, New York, **1999**

[3] Barsoukov, E. and Macdonald, J. R., Impedance spectroscopy. Theory, experiment, and applications, 2nd ed., Wiley-Interscience, Hoboken, **2005**

[4] Tro, N. J., Chemistry: A molecular approach, 4th ed., Pearson, Harlow, **2017**

[5] Wedler, G., Lehrbuch der Physikalischen Chemie, 4th ed., Wiley-VCH, Weinheim, **1997**

[6] Israelachvili, J. N., Intermolecular and surface forces, 3rd ed., Elsevier, Oxford, **2011**

[7] Rabinowicz, E., Friction and wear of materials, 2nd ed., John Wiley & Sons, New York, **1995**

[8] Hunter, R. J., Zeta potential in colloid science: Principles and applications, 1st ed., Academic Press, London, **1981**

[9] Ohshima, H., Electrical phenomena at interfaces and biointerfaces: Fundamentals and applications in nano-, bio-, and environmental sciences, 1st ed., John Wiley & Sons, Hoboken, **2012**

[10] Berger, A.; Theis, M.; von Wedel, H.; Rößler, T.; Papastavrou, G.; Senker, J. and Retsch, M., A versatile method for facile and reliable synthesis of colloidal particles with a size and composition gradient, Colloid Polym. Sci., **2024**

[11] Berger, A.; Schöttle, M.; Lebeda, F.; Schmalz, H.; Bösecke, P.; Rosenfeldt, S.; Greiner, A. and Retsch, M., Carbon materials with conductivity gradients allow dynamic screening of steep temperature differences along thin films, Adv. Funct. Mater., 34(45), 2400740, **2024**

[12] Klein, I.; Tran, T.; Reiser, R.; Theis, M.; Rosenfeldt, S.; Schöttle, M.; Schirmeister, C.; Bösecke, P.; Rettinger, S.; Mülhaupt, R. and Retsch, M., High and tuneable anisotropic thermal conductivity controls the temperature distribution of 3D printed all-polyethylene objects, J. Mater. Chem. A, 11(41), 22492, **2023**

[13] Schöttle, M.; Lauster, T.; Roemling, L. J.; Vogel, N. and Retsch, M., A continuous gradient colloidal glass, Adv. Mater., 35(7), 2208745, **2023**

[14] Rothenberg, G., Catalysis. Concepts and green applications, 1st ed., Wiley-VCH, Weinheim, **2008**

[15] Hofer, A.; Taccardi, N.; Moritz, M.; Wichmann, C.; Hübner, S.; Drobek, D.; Engelhardt, M.; Papastavrou, G.; Spiecker, E. and Papp, C., Preparation of geometrically highly controlled Ga particle arrays on quasi-planar nanostructured surfaces as a SCALMS model system, RSC Adv., 13(6), 4011, **2023**

[16] Ruiz M, C. V.; Terlinden, M.; Engelhardt, M.; Magnabosco, G.; Papastavrou, G.; Vogel, N.; Thommes, M. and Bachmann, J., Preparation and surface functionalization of a tunable porous system featuring stacked spheres in cylindrical pores, Adv. Mater. Interfaces, 10(33), 2300436, **2023**

[17] Fu, Q. and Wagner, T., Interaction of nanostructured metal overlayers with oxide surfaces, Surf. Sci. Rep., 62(11), 431, **2007**

[18] Lyaskovskyy, V. and de Bruin, B., Redox non-innocent ligands: Versatile new tools to control catalytic reactions, ACS Catalysis, 2(2), 270, **2012**

[19] Amobonye, A.; Bhagwat, P.; Raveendran, S.; Singh, S. and Pillai, S., Environmental impacts of microplastics and nanoplastics: A current overview, Front. Microbiol., 12, 768297, **2021**

[20] Childress, A. E. and Elimelech, M., Effect of solution chemistry on the surface charge of polymeric reverse osmosis and nanofiltration membranes, J. Membr. Sci., 119(2), 253, **1996**

[21] Elimelech, M.; Chen, W. H. and Waypa, J. J., Measuring the zeta (electrokinetic) potential of reverse osmosis membranes by a streaming potential analyzer, Desalination, 95(3), 269, **1994**

[22] Löder, M. G. J. and Gerdts, G., Methodology used for the detection and identification of microplastics - A critical appraisal, 1st ed., Springer International Publishing, Cham, **2015**

[23] Meides, N.; Menzel, T.; Poetzschner, B.; Löder, M. G. J.; Mansfeld, U.; Strohriegl, P.; Altstaedt, V. and Senker, J., Reconstructing the environmental degradation of polystyrene by accelerated weathering, Environ. Sci. Technol., 55(12), 7930, **2021**

[24] Ramsperger, A. F. R. M.; Jasinski, J.; Völkl, M.; Witzmann, T.; Meinhart, M.; Jérôme, V.; Kretschmer, W. P.; Freitag, R.; Senker, J.; Fery, A.; Kress, H.; Scheibel, T. and Laforsch, C., Supposedly identical microplastic particles substantially differ in their material properties influencing particle-cell interactions and cellular responses, J. Hazard. Mater., 425, 127961, **2022**

[25] Ramsperger, A. F. R. M.; Bergamaschi, E.; Panizzolo, M.; Fenoglio, I.; Barbero, F.; Peters, R.; Undas, A.; Purker, S.; Giese, B.; Lalyer, C. R.; Tamargo, A.; Moreno-Arribas, M. V.; Grossart, H.-P.; Kühnel, D.; Dietrich, J.; Paulsen, F.; Afanou, A. K.; Zienolddiny-Narui, S.; Eriksen Hammer, S.; Kringlen Ervik, T.; Graff, P.; Brinchmann, B. C.; Nordby, K.-C.; Wallin, H.; Nassi, M.; Benetti, F.; Zanella, M.; Brehm, J.; Kress, H.; Löder, M. G. J. and Laforsch, C., Nano- and microplastics: A comprehensive review on their exposure routes, translocation, and fate in humans, NanoImpact, 29, 100441, **2023**

[26] Binnig, G.; Quate, C. F. and Gerber, C., Atomic force microscope, Phys. Rev. Lett., 56(9), 930, **1986**

[27] Butt, H.-J.; Cappella, B. and Kappl, M., Force measurements with the atomic force microscope: Technique, interpretation and applications, Surf. Sci. Rep., 59(1-6), 1, **2005**

[28] Goldstein, J. I.; Newbury, D. E.; Michael, J. R.; Ritchie, N. W. M.; Scott, J. H. J. and Joy, D. C., Scanning electron microscopy and X-ray microanalysis, 4th ed., Springer, New York, **2018**

[29] Krishna, D. N. G. and Philip, J., Review on surface-characterization applications of X-ray photoelectron spectroscopy (XPS): Recent developments and challenges, Appl. Surf. Sci. Adv., 12, 100332, **2022**

[30] Berthomieu, C. and Hienerwadel, R., Fourier transform infrared (FTIR) spectroscopy, Photosynth. Res., 101(2-3), 157, **2009**

[31] Bellmann, C.; Caspari, A.; Moitzi, C. and Babick, F., Dynamische und elektrophoretische Lichtstreuung, 2nd ed., Anton Paar GmbH, Graz, **2020**

[32] Stetefeld, J.; McKenna, S. A. and Patel, T. R., Dynamic light scattering: A practical guide and applications in biomedical sciences., Biophys. Rev., 8(4), 409, **2016**

[33] Brar, S. K. and Verma, M., Measurement of nanoparticles by light-scattering techniques, Trends Anal. Chem., 30(1), 4, **2011**

[34] Reviakine, I.; Johannsmann, D. and Richter, R. P., Hearing what you cannot see and visualizing what you hear: Interpreting quartz crystal microbalance data from solvated interfaces, Anal. Chem., 83(23), 8838, **2011**

[35] Losurdo, M. and Hingerl, K., Ellipsometry at the nanoscale, 1st ed., Springer, Berlin, Heidelberg, **2013**

[36] Reuß, F. F., Sur un nouvel effet de l'électricité galvanique, Mem. Soc. Imp. Natur. Moscou, 2, 327, **1809**

[37] Quincke, G., Ueber die Fortführung materieller Theilchen durch strömende Elektricität, Ann. Phys., 189(8), 513, **1861**

[38] Dorn, E., Ueber die Fortführung der Electricität durch strömendes Wasser in Röhren und verwandte Erscheinungen, Ann. Phys. Chem., 10, 46, **1880**

[39] Debye, P., A Method for the determination of the mass of electrolytic ions, J. Chem. Phys., 1(1), 13, **1933**

[40] Schwan, H. P.; Schwarz, G.; Maczuk, J. and Pauly, H., On the low-frequency dielectric dispersion of colloidal particles in electrolyte solution, J. Phys. Chem., 66(12), 2626, **1962**

[41] Chen, C.-S.; Pohl, H. A.; Huebner, J. S. and Bruner, L. J., Dielectrophoretic precipitation of silver bromide suspensions, J. Colloid Interface Sci., 37(2), 354, **1971**

[42] Elul, R., Applications of non-uniform electric fields. Part 1. - Electrophoretic evaluation of adsorption, Trans. Faraday Soc., 62(0), 3484, **1966**

[43] Delgado, Á. V. and Arroyo, F. J., Electrokinetic phenomena and their experimental determination: An overview, 1st ed., CRC Press, New York, **2001**

[44] Delgado, Á. V.; González-Caballero, F.; Hunter, R. J.; Koopal, L. K. and Lyklema, J., Measurement and interpretation of electrokinetic phenomena, J. Colloid Interface Sci., 309(2), 194, **2007**

[45] Ohshima, H., Theory of colloid and interfacial electric phenomena, 1st ed., Academic Press, **2006**

[46] Stern, O., Zur Theorie der elektrolytischen Doppelschicht, Z. Elektrochem. Angew. Phys. Chem., 30(21-22), 508, **1924**

[47] Kobayashi, M.; Juillerat, F.; Galletto, P.; Bowen, P. and Borkovec, M., Aggregation and charging of colloidal silica particles: Effect of particle size, Langmuir, 21(13), 5761, **2005**

[48] Kobayashi, M.; Skarba, M.; Galletto, P.; Cakara, D. and Borkovec, M., Effects of heat treatment on the aggregation and charging of Stöber-type silica, J. Colloid Interface Sci., 292(1), 139, **2005**

[49] Kobayashi, M., An analysis on electrophoretic mobility of hydrophobic polystyrene particles with low surface charge density: Effect of hydrodynamic slip, Colloid Polym. Sci., 298(10), 1313, **2020**

[50] Wall, S., The history of electrokinetic phenomena, Curr. Opin. Colloid Interface Sci., 15(3), 119, **2010**

[51] Adachi, Y., Dynamic aspects of coagulation and flocculation, Adv. Colloid Interface Sci., 56, 1, **1995**

[52] Adachi, Y.; Kobayashi, A. and Kobayashi, M., Structure of colloidal flocs in relation to the dynamic properties of unstable suspension, Int. J. Polym. Sci., 2012, 1, **2012**

[53] Adachi, Y., Sedimentation and electrophoresis of a porous floc and a colloidal particle coated with polyelectrolytes, Curr. Opin. Colloid Interface Sci., 24, 72, **2016**

[54] Geonzon, L. C.; Kobayashi, M.; Sugimoto, T. and Adachi, Y., Study on the kinetics of adsorption of poly(ethylene oxide) onto a silica particle using optical tweezers and microfluidics, Colloids Surf. A, 642, 128691, **2022**

[55] Hakim, A.; Suzuki, T. and Kobayashi, M., Strength of humic acid aggregates: Effects of divalent cations and solution pH, ACS Omega, 4(5), 8559, **2019**

[56] Michna, A., Macroion adsorption - Electrokinetic and optical methods, Adv. Colloid Interface Sci., 250, 95, **2017**

[57] Saha, S. and Adachi, Y., Shielding behavior of electrokinetic properties of polystyrene latex particle by the adsorption of neutral poly(ethylene oxide), J. Colloid Interface Sci., 626, 930, **2022**

[58] Bai, Y.; Huang, H.; Wang, C.; Long, R. and Xiong, Y., Engineering the surface charge states of nanostructures for enhanced catalytic performance, Mater. Chem. Front., 1(10), 1951, **2017**

[59] Park, S.; Nam, G.; Lee, J.-S.; Cho, J. and Jung, J.-I., Influence of surface charges/chemistry on the catalysis of perovskite complexes, ACS Appl. Mater. Interfaces, 10(34), 28502, **2018**

[60] Huang, H.; Jin, Y.; Chai, Z.; Gu, X.; Liang, Y.; Li, Q.; Liu, H.; Jiang, H. and Xu, D., Surface charge-induced activation of Ni-loaded CdS for efficient and robust photocatalytic dehydrogenation of methanol, Appl. Catal. B: Environ., 257, 117869, **2019**

[61] Meides, N.; Mauel, A.; Menzel, T.; Altstädt, V.; Ruckdäschel, H.; Senker, J. and Strohriegl, P., Quantifying the fragmentation of polypropylene upon exposure to accelerated weathering, Microplast. Nanoplast., 2(1), 22, **2022**

[62] Mauel, A.; Pötzschner, B.; Meides, N.; Siegel, R.; Strohriegl, P. and Senker, J., Quantification of photooxidative defects in weathered microplastics using ^{13}C multiCP NMR spectroscopy, RSC Adv., 12(18), 10875, **2022**

[63] Menzel, T.; Meides, N.; Mauel, A.; Mansfeld, U.; Kretschmer, W.; Kuhn, M.; Herzig, E. M.; Altstädt, V.; Strohriegl, P.; Senker, J. and Ruckdäschel, H., Degradation of low-density polyethylene to nanoplastic particles by accelerated weathering, Sci. Total Environ., 826, 154035, **2022**

[64] Witzmann, T.; Ramsperger, A. F. R. M.; Wieland, S.; Laforsch, C.; Kress, H.; Fery, A. and Auernhammer, G. K., Repulsive interactions of eco-corona-covered microplastic particles quantitatively follow modeling of polymer brushes, Langmuir, 38(29), 8748, **2022**

[65] Schefer, R. B.; Armanious, A. and Mitrano, D. M., Eco-corona formation on plastics: Adsorption of dissolved organic matter to pristine and photochemically weathered polymer surfaces, Environ. Sci. Technol., 57(39), 14707, **2023**

[66] Ramsperger, A. F. R. M.; Narayana, V. K. B.; Gross, W.; Mohanraj, J.; Thelakkat, M.; Greiner, A.; Schmalz, H.; Kress, H. and Laforsch, C., Environmental exposure enhances the internalization of microplastic particles into cells, Sci. Adv., 6(50), eabd1211, **2020**

[67] Wieland, S.; Ramsperger, A. F. R. M.; Gross, W.; Lehmann, M.; Witzmann, T.; Caspari, A.; Obst, M.; Gekle, S.; Auernhammer, G. K.; Fery, A.; Laforsch, C. and Kress, H., Nominally identical microplastic models differ greatly in their particle-cell interactions, Nat. Commun., 15(1), 922, **2024**

2. Theoretical Background

2. Theoretical Background

The study of electrokinetic phenomena dates to the early 19th century with the work of F. F. Reuß, who first observed electro-osmosis and electrophoresis[1]. In the following decades, Reuß' findings laid the groundwork for the development of fundamental concepts in colloid science, including the electrical double layer (EDL)[2-5]. Hence, this chapter explores the formation of interfacial charges at solid-liquid interfaces, examines commonly used EDL models, and reviews selected electrokinetic techniques.

2.1 Charge Formation at Solid/Water Interfaces

This chapter focuses on charged solid surfaces in liquids. Here, water is emphasized due to its high dielectric constant, making it an effective solvent for ions. When a solid is in contact with an aqueous solution, an electric charge can develop at the interface between the two phases. This charging can occur through various processes[6-10]:

The pH value of a solution affects the charge of surface groups. For example, hydroxyl groups on metal oxides can be (de-)protonated, becoming positively or negatively charged. Polymers can also have charged groups like hydroxy-, sulfonate-, carboxyl-, and amine groups. The type and density of these groups, along with the pH value and ion concentration in the electrolyte, determine the overall surface charge properties[11-13].

Even without chargeable functional groups, a solid surface can become charged when placed in an electrolyte solution. This phenomenon arises from the preferential adsorption of certain ions to the surface. The type of ions present in the solution significantly influences the resulting surface charge[14-20]. For instance, studies have shown that hydroxide ions (OH^-) readily adsorb to perfluorinated polymers, leading to a negative surface charge[20, 21]. However, also hydrophilic charged interfaces experience specific ion adsorption[21]. The driving force behind this specific ion adsorption lies in the interplay between ion hydration and the interfacial properties. Ions in bulk solution are surrounded by structured hydration shells due to strong ion-dipole interactions with water molecules. However, at the interface, the hydrogen-bonding network of water is disrupted, leading to an anisotropic hydration structure. Large ions with low charge density, such as halides (e.g., Br^-, I^-), have less structured hydration shells. These ions are more likely to be attracted to the interface, where the disordered water structure is less constraining. In contrast, small ions with high charge density, like sodium (Na^+), possess strong hydration shells and prefer the ordered bulk environment[22].

Furthermore, solid surfaces can acquire an electrical charge through the preferential dissolution of ions from the surface of a sparingly soluble crystalline material. For example, silver iodide (AgI) crystals in water will release ions until the product of the concentrations of the two ions equals the solubility product. However, the preferential dissolution of silver ions (Ag^+) over iodide ions (I^-) can lead to a negative surface charge due to the accumulation of excess I^- on the crystal surface[9].

Many clays, oxides, and minerals undergo isomorphous substitution, where ions within their structure are replaced by less charged ones. This exchange creates a net negative charge on the surface. For

example, in clay minerals, Al^{3+} might replace Si^{4+}. In muscovite mica, K^+ can be exchanged with H^+ in acidic solutions, creating a less negative surface charge[23, 24]. This K^+ substitution only happens when the H^+ concentration outweighs the K^+ concentration. The reason is likely because H^+ ions can integrate into the sheet openings far more effectively than other cations[23].

Also, anisotropic crystals, such as those found in kaolinite clay, exhibit distinctive surface charge properties. It possesses two primary surface types, a tetrahedral siloxane and an octahedral hydroxyl face [25, 26]. Minor isomorphic substitution in the tetrahedral sheet results in a slight permanent negative charge. Two categories of inorganic surface hydroxyl groups are present in kaolinite: i) charge-neutral ones bound to fully coordinated metal atoms and ii) reactive silanol and aluminol groups found on broken edges and octahedral planes bound to undercoordinated metal atoms. These amphoteric edges and octahedral sites exhibit pH-dependent charges, developing positive or negative charges *via* direct H^+ and OH^- transfer from the aqueous phase[25, 26]. Consequently, kaolinite demonstrates the appearance of multiple points of zero charge (PZC), where the net surface charge is zero, and a substantial volume expansion upon hydration. These behaviors are directly attributable to the inherent properties of its anisotropic crystal structure[9]. Figure 2.1 provides an overview of the previously described sources of surface charges.

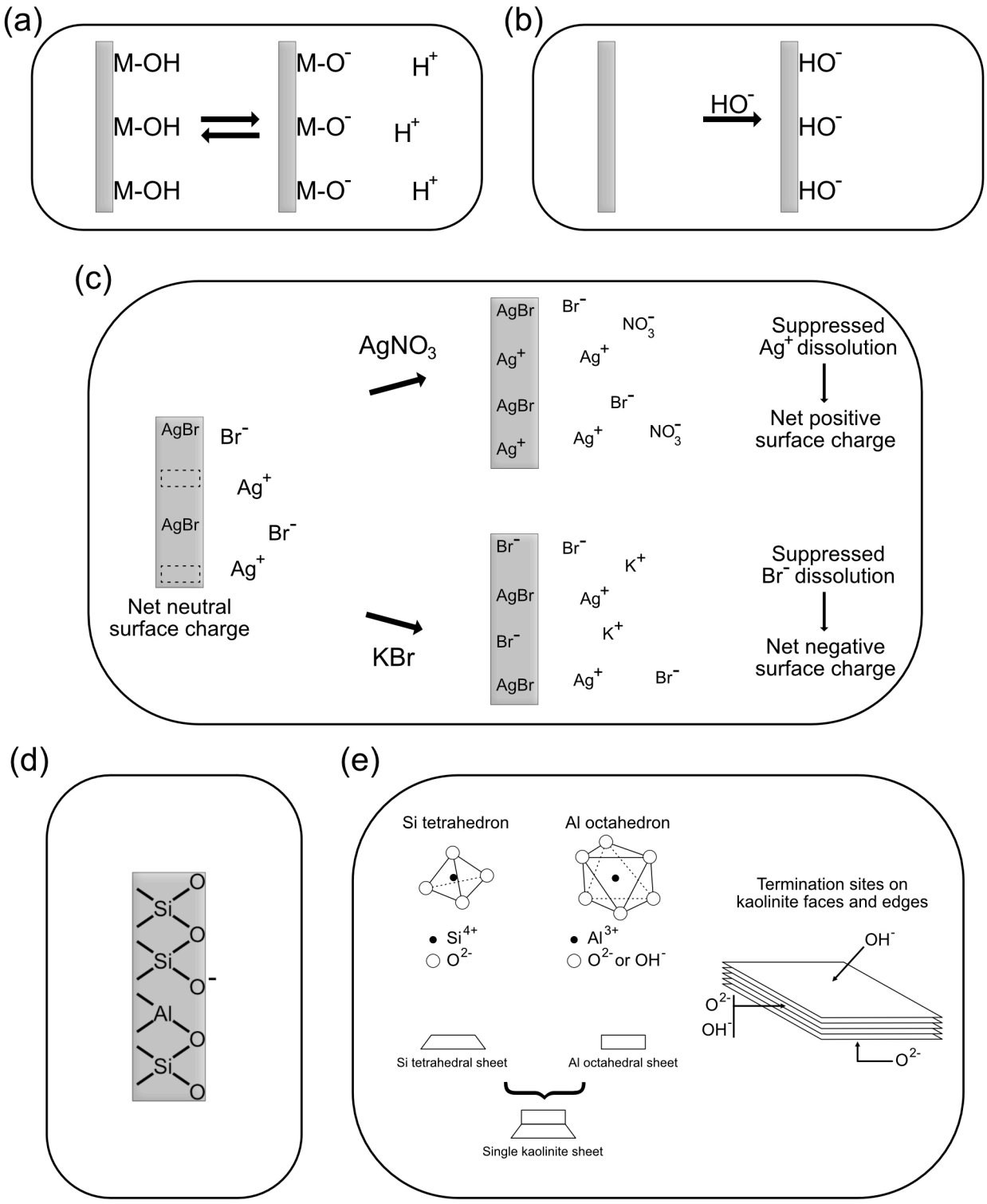

Figure 2.1: Mechanisms contributing to surface charge development on solid materials, illustrated by (a) ionization of surface functional groups[9], (b) adsorption of specific ions from solution[9], (c) selective dissolution of ionic species[9], (d) isomorphous substitution[9], and (e) anisotropic crystal structures[27].

Furthermore, the surface charge of an electrically conductive material can be controlled by applying a voltage between the substrate and the counter electrode in an electrochemical cell. The applied voltage creates an electric field that drives the redistribution of ions in the electrolyte, affecting the surface charge density. The properties of the electrolyte, such as the ionic concentration and the dielectric permittivity, also play a role in determining the surface charge density. The relationship

between the applied voltage and the surface charge density is complex and nonlinear. At low voltages, the surface charge density is proportional to the applied voltage. However, at higher voltages, the surface charge density saturates and becomes independent of the applied voltage. This saturation effect is due to the formation of a Stern layer, which is a compact layer of ions that specifically adsorb to the electrode surface[28, 29]. The Stern layer will be introduced in detail in Chapter 2.2.

As a result, most surfaces carry charges in an aqueous environment. It should be noted that these charging processes do not always occur separately. They contribute to the net interfacial charge cumulatively. The interfacial charges attract counterions from the bulk solution. Consequently, the next chapter introduces different models of the resulting so-called electrical double layer.

2.2 The Electrical Double Layer

This chapter explores the formation of the electrical double layer (EDL) within an aqueous environment, which is the basis for exploring electrokinetic phenomena. The electrical double layer forms at the interface between a charged surface and an electrolyte solution. Surface charges on the solid create an electric field that attracts ions of opposite charge (i.e., counter ions) from the solution[7, 30]. Electrokinetic phenomena hinge on precisely understanding the distribution of co- and counterions near a substrate's surface.

Von Helmholtz developed the most straightforward description of the EDL in 1879[4]. This model assumes an ordered plane of immobile counter ions closely attached to the charged solid surface, forming the analog of a parallel-plate capacitor. Consequently, the electric field would be limited to this thin monolayer of counter ions. However, the charge carriers in the solution obey thermal motion and are disordered. In turn, von Helmholtz´s model fails to describe experimentally obtained double layer capacitances[7, 31].

Gouy[32] and Chapman[33] enhanced the understanding of colloid science by incorporating the thermal motion of ions into their analysis. They recognized that thermal fluctuations cause counterions to be displaced from the surface, resulting in a diffuse layer that extends further into the electrolyte solution compared to the von Helmholtz model. Their theoretical framework specifically addressed the electric double layer on flat surfaces, focusing on the straightforward scenario of a negatively charged planar surface. Subsequently, Debye and Hückel[34] expanded on this work by calculating the electric potential and ion distribution surrounding spherical surfaces. Both the Gouy-Chapman and Debye-Hückel theories are classified as continuum theories. They conceptualize the solvent as a continuous medium characterized by a specific dielectric constant while neglecting the molecular characteristics of the liquid. Additionally, ions are not represented with a discrete size but as a continuous charge distribution[7, 35]. This description of the electrical double layer is often sufficient to describe experimental results in contrast to the von Helmholtz model[7]. The Gouy-Chapman theory serves as a basis to determine the electric potential in the EDL by the Poisson-Boltzmann theory.

This approach merges the Poisson equation (Eq. 2.1), governing the potential distribution ψ near a charged surface, with Boltzmann statistics (Eq. 2.2), which describe the charge density ρ_e relative to the thermal energy $k_B T$[7, 35].

$$\nabla^2 \psi = -\frac{\rho_e}{\varepsilon_r \varepsilon_0} \tag{2.1}$$

$$\rho_e = \sum_{i=1}^{N} z_i e c_i \, exp\left(-\frac{z_i e \psi(x,y,z)}{k_B T}\right) \tag{2.2}$$

where ∇ is the Nabla operator, ε_r is the dielectric constant of the medium, and ε_0 is the permittivity of the free space. The electrolyte is composed of N ions with the valency z_i and bulk concentration c_i $(i = 1, 2, \dots N)$. e is the elementary charge, k_B is the Boltzmann constant, and T is the temperature. Substitution of eq. 2.2 into eq. 2.1 yields the Poisson-Boltzmann equation. To simplify the model, we consider a planar surface for which only electric work is required to bring an ion from the bulk solution to, neglecting the displacement of other molecules, and assuming a symmetric monovalent electrolyte and get[7]

$$\nabla^2 \psi = \frac{c_o e}{\varepsilon_r \varepsilon_0}\left(e^{-\frac{e\psi(x,y,z)}{k_B T}} - e^{\frac{e\psi(x,y,z)}{k_B T}}\right) \tag{2.3}$$

While the Poisson-Boltzmann equation (cf. eq. 2.3) requires numerical solutions due to its complexity as a second-order partial differential equation, simplification is possible. When dealing with low potentials, say $|\psi| \leq 25$ mV at room temperature, linearization becomes a viable approach. Under consideration of the boundary conditions that the potential at the surface equals the surface potential ψ_0 and that the potential decays to zero at infinite separation, we get[7, 35]

$$\psi = \psi_0 e^{-\kappa x} \tag{2.4}$$

where ψ_0 is the surface potential and κ is called Debye-Hückel parameter or inverse Debye length λ_D^{-1}[36]

$$\kappa = \lambda_D^{-1} = \sqrt{\frac{2000 \cdot e^2 N_A I}{\varepsilon_r \varepsilon_0 k_B T}} \tag{2.5}$$

Here, N_A is Avogadro´s number and $I = 0.5 \sum c_i z_i^2$ is the ionic strength in units of mol L^{-1}[30]. The Debye length decreases for higher salt concentrations. A higher concentration of ions in solution enhances the screening effect on the surface charge. For a 1:1 electrolyte in water at 25 °C, the Debye length can be approximated by $\lambda_D = 3.04\ \text{Å}\sqrt{c_0^{-1}\ L\ mol^{-1}}$ where c_0 is the salt concentration. In 1947, Grahame[31] derived an expression directly relating the surface charge density σ_0 to ψ_0 based on the Gouy-Chapman theory:

$$\sigma_0 = \sqrt{8 c_0 \varepsilon_r \varepsilon_0 k_B T}\sinh\left(\frac{e\psi_0}{2k_B T}\right) \tag{2.6}$$

In 1924, Stern[37] combined the concepts of the von Helmholtz- and the Gouy-Chapman model into a cohesive theory. Stern considered the finite size of the ions, reduced permittivity of the solvent near the surface, and specific ion adsorption in his model. This extension accounts for most experimental results. Stern's framework divides the electric double layer into two distinct components: the inner Stern layer and the outer diffuse layer. A distance δ separates the layers and describes the distance between the surface and the electrical center of immobile adsorbed ions, i.e., the Stern layer. A linear decay of ψ_0 as a function of the distance from the surface is described until the Stern layer is reached. To estimate the capacitance of the Stern layer C_{St}^A, we can use the simple equation for a parallel plate

capacitor, where the two plates are formed by the surface and the adsorbed ions and are separated by the distance δ[37]. In contrast, the diffuse layer comprises mobile ions that follow Poisson-Boltzmann statistics. The Stern potential ψ_δ at the distance δ from the surface, where the diffuse layer starts, will be later treated as the diffuse layer potential ψ_d. From the Stern layer outward, an exponential potential decay is described by the Poisson-Boltzmann statistics. The potential at the plane that separates the stationary layer(s) from the mobile layers is the electrokinetic- or zeta-potential ζ[37, 38]. This plane is called shear plane[5, 38, 39]. Since at least the first molecular layer of ions adjacent to the interface adheres firmly to the surface, ζ is equal to ψ_δ or smaller[37]. Thus, the distance between the surface and the shear plane is δ or greater. Figure 2.2 shows a simplified version of the EDL after Stern.

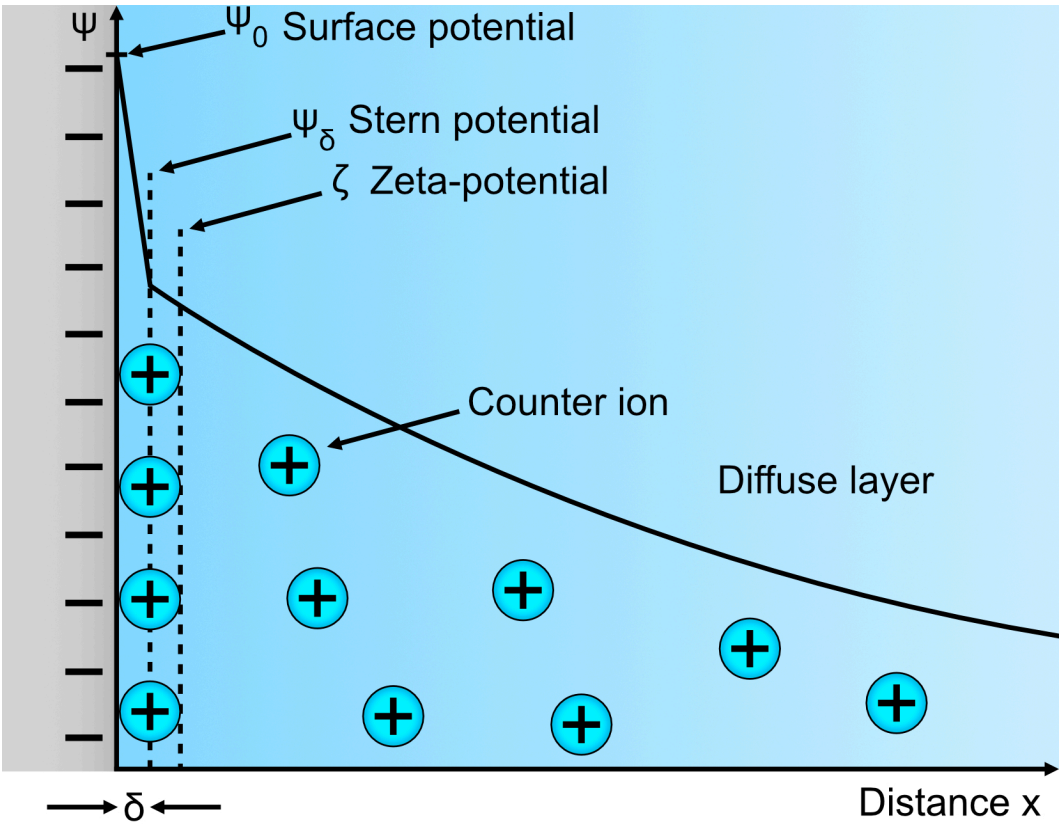

Figure 2.2: A simplified representation of the Stern layer and the diffuse layer at a solid-liquid interface. The surface has the potential ψ_0. The distance δ denotes the electrical center of adsorbed ions and acts as a boundary between the Stern layer and the diffuse layer[37]. The solid black line illustrates the potential profile as a function of the separation distance from the charged interface. (Adsorbed) coions are not depicted due to simplicity reasons.

The basic Stern model[40] is often used to numerically derive σ_0, ψ_0, and ψ_d from the total site density of charged groups Γ at the interface, the acid dissociation constant (pK), C_{St}^A, the pH value, and the ionic strength[41, 42]. The surface charge is controlled by the equilibrium between protonated and deprotonated surface groups as shown in Chapter 2.1. If this equilibrium is described by a single protonation step, this approach is called 1-pK basic Stern model. The equilibrium can be exemplarily represented by the reaction (M-OH $\leftrightarrows$ M-O$^-$ + H$^+$) of a metal oxide. The relative concentrations of these surface species are governed by the mass action law:

$$\frac{\Gamma_{\mathrm{M-O^-}}\, a_{\mathrm{H}}}{\Gamma_{\mathrm{M-OH}}} = K \exp\left(\frac{e\,\psi_0}{k_B T}\right) \tag{2.7}$$

Here, a_H is the activity of protons (related to the pH value as pH = -$\log_{10}$ a_H) and K is the intrinsic equilibrium constant (with pK = -$\log_{10}$ K). The term $\Gamma_{\mathrm{M-O^-}}\, a_{\mathrm{H}}$ represents the concentration of deprotonated and $\Gamma_{\mathrm{M-OH}}$ of protonated surface groups. At equilibrium, this ratio is equal to the product of the intrinsic equilibrium constant K and the Boltzmann factor. This means that the relative concentrations of deprotonated and protonated surface groups are determined not only by the intrinsic affinity of the surface group for protons but also by the electrostatic interactions between the surface and the solution. The total concentration of these surface sites is

$$\Gamma_0 = \Gamma_{\mathrm{M-OH}} + \Gamma_{\mathrm{M-O^-}} \tag{2.8}$$

The surface charge density is defined as

$$\sigma_0 = -e\Gamma_{\mathrm{M-O^-}} \tag{2.9}$$

This surface charge is associated with the potential drop across the Stern layer, given by

$$\sigma_0 = C_{St}^{A}\left(\psi_0 - \psi_d\right) \tag{2.10}$$

The obtained ψ_d, for instance, can then be used in a suitable variation of the Poisson-Boltzmann equation to calculate ζ[36].

An essential parameter for experimental validation is the differential capacitance of the total electric double layer. Within the Stern model, this capacitance is represented as two capacitors in series: the Stern layer C_{St}^{A} and the diffuse Gouy-Chapman layer C_{GC}^{A} capacitance. The total capacitance per unit area can be expressed as[7]:

$$\frac{1}{C^A} = \frac{1}{C_{St}^{A}} + \frac{1}{C_{GC}^{A}} \tag{2.11}$$

The foundational work by Gouy[32] and Chapman[33], Stern[37] and Grahame[31] has led to the development of a comprehensive model of the EDL, called the Gouy-Chapman-Stern-Grahame-model (GCSG-model)[30]. A schematic of the GCSG model is shown in Figure 2.3.

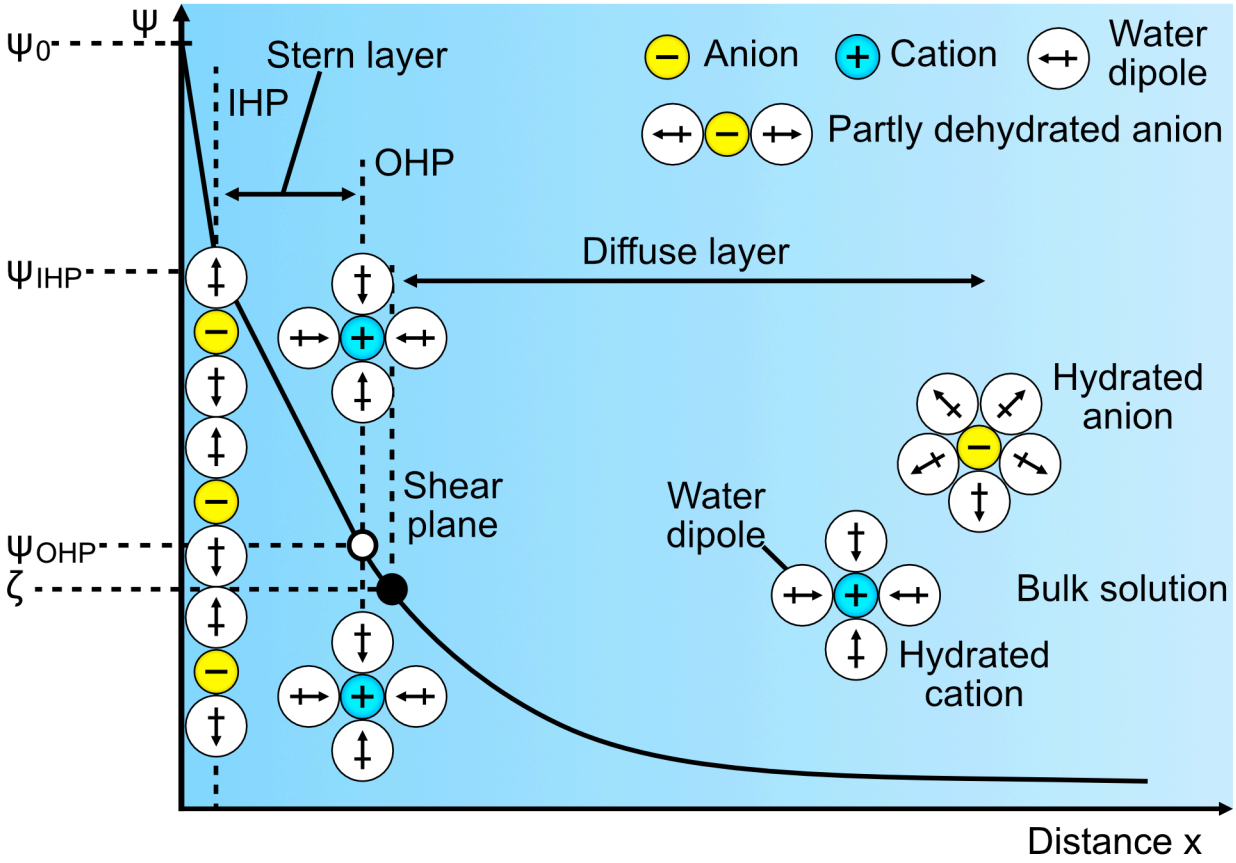

Figure 2.3: Schematic representation of the Gouy-Chapman-Stern-Grahame model of the electrical double layer. This model consists of a surface with the potential ψ_0 and two distinct layers of adsorbed ions: an inner layer of partially dehydrated anions (inner Helmholtz plane, IHP) and an outer layer of hydrated cations (outer Helmholtz plane, OHP). A linear potential drop is assumed between the IHP and OHP. Beyond the OHP, a diffuse layer of mobile counterions and coions balances the net surface charge, with an ion concentration decreasing with distance from the surface. The potential distribution in the diffuse layer follows the Boltzmann distribution. The zeta-potential ζ is located at the shear plane, where a sufficiently strong shear force can remove the diffuse layer outwards.

Here, the EDL is categorized into a rigid (hydrodynamically immobile) layer and a diffuse (hydrodynamically mobile) layer of ions. According to Grahame[31], the rigid layer is further divided into two components. The inner Helmholtz plane (IHP) corresponds to the charge centers of the adsorbed and partially dehydrated ions. The outer Helmholtz plane (OHP) is formed by the charge centers of the predominantly electrostatically bound hydrated counterions. The region between the IHP and the OHP is called Stern layer. Within the Stern layer, the potential gradient is assumed to be linear. The ion distribution within the diffuse portion of the double layer is governed by the interplay between the electrostatic energy of the ions and their thermal energy as described by the Poisson-Boltzmann theory[31]. Ohshima[35] modified equation (2.6) to link the electrokinetic charge density σ^{ek} at the shear plane to ζ:

$$\sigma^{ek} = \sqrt{8c_0\varepsilon_r\varepsilon_0 k_B T}\sinh\left(\frac{e\zeta}{2k_B T}\right) \tag{2.12}$$

The presented theoretical frameworks are the foundation for electrokinetic techniques to deduct ζ experimentally.

2.3 Electrokinetic phenomena

Electrokinetic phenomena (EKP) occur when a fluid streams alongside a charged surface. These phenomena provide unique insights into the interfacial charging behavior. Electrokinetics are based on the electrical double layer and electrostatic surface forces[6]. Figure 2.4 shows an overview of the classical EKPs.

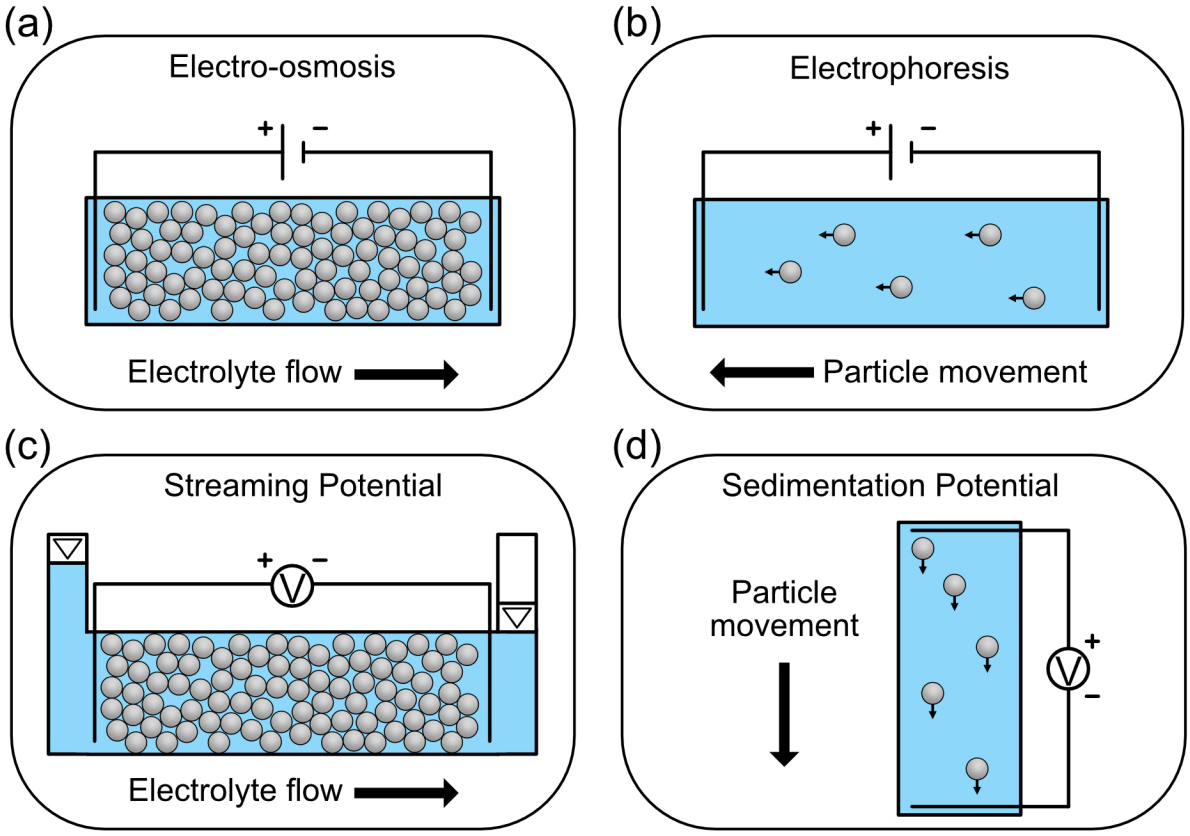

Figure 2.4: Overview of the classical electrokinetic phenomena: (a) electro-osmosis, (b) electrophoresis, (c) streaming potential, and (d) sedimentation potential. The particles carry negative surface charges.

Examples for electrokinetic phenomena are electro-osmosis (cf. Fig. 2.4a) and electrophoresis (cf. Fig. 2.4b), where an electric field induces mechanical motion. Electro-osmosis is the movement of a liquid through a stationary charged porous material (e.g., particles, capillaries, membrane) under the influence of an applied electric field. The electric field acts on the excess counterions in the liquid within the charged pores, causing them to move and drag the surrounding liquid along with them. Electrophoresis is the motion of charged colloidal particles or polyelectrolytes driven by an electric field when they are dispersed in a liquid. In contrast, when a pressure gradient forces a liquid through a charged porous material like a capillary or membrane, counterions within the pores move. The resulting charge accumulation on the other side of the porous material causes a potential difference known as the streaming potential (cf. Fig. 2.4c). Under open-circuit conditions, the streaming potential is measured, whereas the streaming current is measured under short-circuit conditions. Charged particles create an electric field when they settle through an electrolyte solution, termed the sedimentation field. This field generates a voltage difference between the electrodes, the sedimentation potential (cf. Fig. 2.4d). Analysis of these phenomena provides a comprehensive understanding of the electrostatic properties of a surface in a liquid environment[6]. In the following,

the electrophoretic mobility and the streaming potential are explained in detail. Furthermore, the influence of surface conductivity, which refers to the enhanced electrical conduction along a charged surface, will be discussed.

2.3.1 Electrophoretic Mobility

Electrophoresis is the movement of charged particles and molecules suspended in a liquid caused by an external electric field[43]. This technique is widely used in colloid and biologic science[36, 43]. The electric field generates a force on the charged colloid, causing the colloid to move towards the electrode of the opposite charge while the liquid counteracts the movement by an opposing viscous force[35]. This movement reaches a terminal velocity when the force exerted by the electric field is balanced by the opposing viscous drag from the liquid medium. The electrophoretic mobility μ is a measure of how fast a particle moves in an electric field and is calculated by:

$$\mu = \frac{v}{E} = \frac{q}{6\pi\eta a} \tag{2.13}$$

Here, v is the particle velocity, E is the electric field, q is the charge of the particle, η is the dynamic viscosity of the liquid, and a is the particle radius. The electrophoretic mobility μ can be related to the zeta-potential ζ. However, choosing the right framework for this calculation depends on the particle radius, the inverse Debye length and, thus, the ionic strength[6]. The extreme cases for very thin and thick EDLs relative to the particle radius are presented in equations 2.14 and 2.15, respectively. The Smoluchowski equation[44]

$$\mu = \frac{\varepsilon_r \varepsilon_0 \zeta}{\eta} \tag{2.14}$$

is valid when the particle radius is significantly larger than the thickness of the EDL, expressed as $\kappa a \gg 1$. In contrast, the Hückel equation is valid for very thick double layers relative to the particle radius, $\kappa a < 1$[45]:

$$\mu = \frac{2\varepsilon_r \varepsilon_0 \zeta}{3\eta} \tag{2.15}$$

The Smoluchowski and Hückel limits are visualized in Figure 2.5a and 2.5b, respectively. The discrepancy between von Smoluchowski's equation and Hückel's equation arises from the distortion of the electric field near the particle surface. Since the electrophoretic mobility is primarily influenced by counterions within the electrical double layer, the degree of field distortion experienced by these ions plays a crucial role. The electric field becomes distorted around a nanoparticle due to polarization of the counterions near the interface[46]. The local electric field strength in proximity to the surface of a charged particle is amplified relative to the undisturbed field by a factor of 3/2. Figure 2.5a illustrates that in thin double layers $\kappa a \gg 1$, most ions experience a distorted electric field. Conversely, in thick electrical double layers $\kappa a < 1$ (cf. Fig. 2.5b), most ions within the double layer are exposed to the original, undistorted electric field. This difference in field distortion explains why the electrophoretic mobility predicted by the Smoluchowski equation is 3/2 times larger than that predicted by the Hückel equation[35].

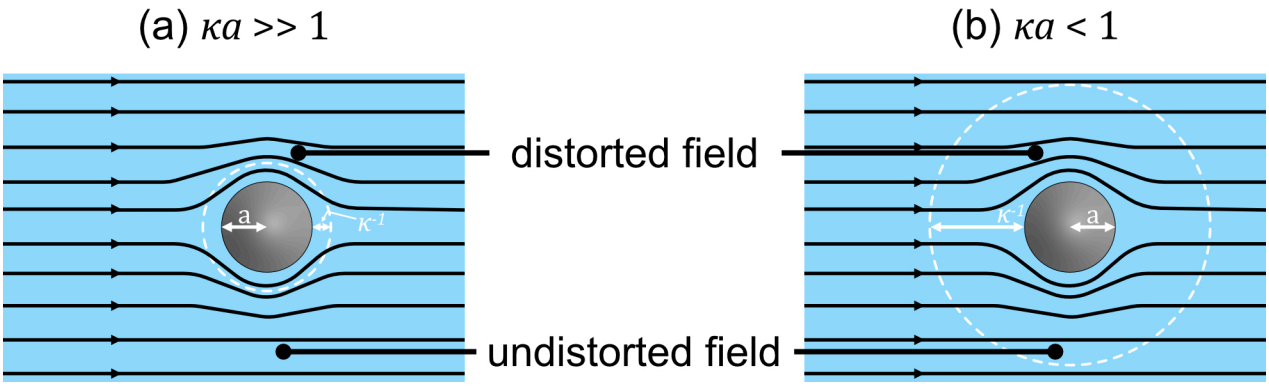

Figure 2.5: Distortion of the electric field near the surface of moving particles in an electrolyte. The dashed circles represent the EDL. When (a) the double layer is thin $\kappa a \gg 1$, electrolyte ions experience a strongly distorted electric field compared to when (b) the double layer is thick, $\kappa a < 1$.

Henry developed a more comprehensive expression that bridges the gap between the Smoluchowski and Hückel equations at low potentials, say $|\zeta| < 50$ mV, and arbitrary κa[47]:

$$\mu = \frac{2\varepsilon_r \varepsilon_0 \zeta}{3\eta} f(\kappa a) \tag{2.16}$$

where the function $f(\kappa a)$ varies smoothly between 1.5 for $(\kappa a \to \infty)$ and 1.0 for $(\kappa a \to 0)$. These boundary conditions reflect the Smoluchowski and Hückel expressions, respectively. However, equations 2.14 to 2.16 are only valid for small ζ, when relaxation effects of the EDL are negligible[6]. For scenarios with substantial zeta-potentials, say $|\zeta| > 75$ mV and double layer polarization, accurate analysis necessitates numerical calculations such as the established electrokinetic model developed by O'Brien and White[48].

A popular method to determine the electrophoretic mobility is the electrophoretic light scattering (ELS) technique. ELS works by applying an electric field to a suspension of charged particles, causing them to move towards the electrode with the opposite charge. A laser beam illuminates these moving particles, and the scattered light experiences a Doppler shift, indicating a change in its frequency. By analyzing this frequency change, the electrophoretic mobility of the particles can be determined[49, 50]. ELS offers several advantages over traditional electrophoresis techniques, including the ability to measure the mobility of many particles simultaneously, eliminating the need for particle selection. ELS can be easily combined with dynamic light scattering (DLS), allowing for parallel determination of particle size and the electrophoretic mobility, which is crucial for monitoring dispersion stability[49]. In contrast to electrophoresis, the next sub-chapter introduces the streaming potential technique where the solid is stationary, but the electrolyte is the mobile phase.

2.3.2 Streaming Potential

In the previous section, we explored electrophoretic light scattering, a technique that analyzes the movement of charged colloids within a liquid under the influence of an electric field[6, 35]. Now, we shift our attention to another electrokinetic technique known as streaming potential. In contrast to ELS, where the particles move while the solid phase remains stationary, streaming potential focuses on the movement of the electrolyte solution while the solid phase is held immobile[6]. This shift in

perspective allows us to investigate the surface charge properties of micro- and macroscopic materials by examining the electric potential generated by the flow of electrolyte solution.

When a liquid is forced through a microchannel under an applied pressure Δp, the resulting tangential shear flow disrupts the equilibrium distribution of mobile ions within the diffuse layer, specifically those located beyond the shear plane. This tangential shear flow drags these ions along with the liquid, generating an ionic flow - the streaming current I_{str} - which can be measured under closed-circuit conditions by an electrometer connected to electrodes positioned outside the capillary ends[6, 30]. The working principle of streaming current measurements in rectangular micro slit channels is shown in Figure 2.6. These micro slit cells, also known as parallel-plate or symmetric cells, are a common configuration used in streaming current/potential measurements, particularly for studying planar interfaces. In this type of cell, two flat plates of the substrate material are positioned parallel-facing to each other, creating a microchannel through which an electrolyte solution is forced to flow[51].

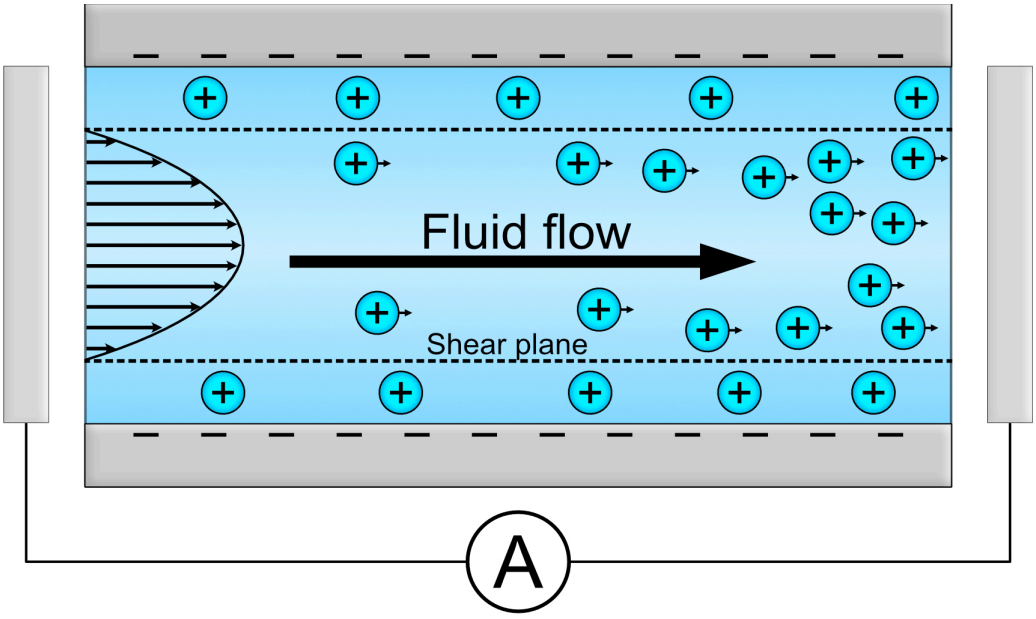

Figure 2.6: Simplified schematic of a rectangular microchannel for streaming current measurements. The substrates at the top and bottom of the channel carry negative charges. Pressure is applied to the left-hand side of the channel. The pressure-induced fluid flow drags hydrodynamically mobile ions beyond the shear plane toward the opposing end of the capillary, where the ions accumulate. Black arrows illustrate the laminar flow profile and the moving direction of ions beyond the shear plane. Ions closer to the substrates remain stationary.

As described, the application of pressure Δp forces liquid through the microchannel, disrupting the diffuse layer and dragging mobile ions towards the opposite capillary end. This process, illustrated in Figure 2.6, leads to a measurable streaming current I_{str}:

$$\frac{I_{str}}{\Delta p} = -\frac{\varepsilon_r \varepsilon_0 bh}{\eta L}\zeta \tag{2.17}$$

where L is the length, b the width, and h the height of a rectangular micro slit channel. For cylindrical capillaries, the term bh is substituted with πR^2 to describe the cross-sectional area of the capillary[6, 30, 51]. R is the capillary radius. Open-circuit conditions lead to an accumulation of charges of opposite sign between the ends of the microchannel. This charge separation gives rise to a potential

difference, the streaming potential U_{str}. The streaming potential causes a conduction current I_c in the opposite direction of the streaming current[6, 30]:

$$I_c = K_L bh \frac{U_{str}}{L} \tag{2.18}$$

where K_L is the bulk conductivity of the electrolyte solution. The streaming potential is defined by the point of zero net current, where I_c and I_{str} are equal:

$$\frac{U_{str}}{\Delta p} = \frac{\varepsilon_r \varepsilon_0 \zeta}{\eta K_L} \tag{2.19}$$

This equation is known as the Helmholtz-Smoluchowski equation and relates U_{str} to the zeta-potential ζ [6, 30, 44]. While parallel-plate cells are frequently used in streaming current/potential measurements, there is another type of cell called an asymmetric or clamping cell. In this cell type, the channel is integrated into the measurement cell body itself, which is constructed from a well-characterized material. This cell body is then placed onto the flat substrate material to carry out the measurements[52]. Figure 2.7 schematically shows the measurement cells for streaming current/potential measurements in symmetric (cf. Fig. 2.7a) and asymmetric (cf. Fig. 2.7b) configurations.

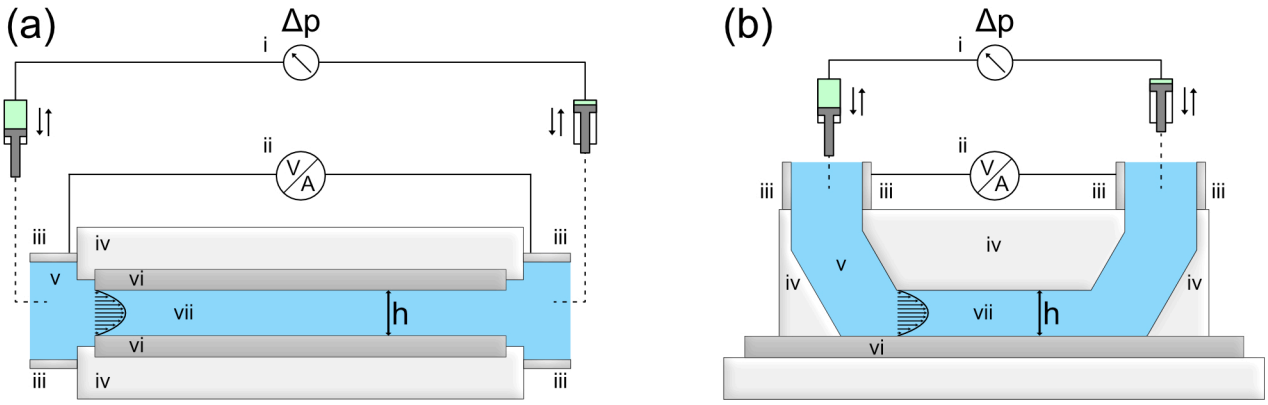

Figure 2.7: Schematic illustration of (a) a parallel plate and (b) an asymmetric streaming current/potential measurement cell setup. These setups typically consist of (i) a differential pressure sensor, (ii) an electrometer, (iii) cylindrical Ag/AgCl electrodes, (iv) a cell body, (v) a bulk electrolyte, (vi) samples, and (vii) the micro slit channel/capillary. Components outside the cell like a nitrogen gas supply for applying pressure to liquid reservoirs to induce liquid flow, valves, conductivity-, temperature-, and pH-sensors, and flow sensors are not shown for simplicity reasons.

Symmetric and asymmetric measurement cells, which are parts of the custom-built streaming potential setup for planar substrates used in this thesis, are thoroughly described in Chapter 4. There are two major benefits of asymmetric over parallel plate cells: the reduced number of samples needed, i.e., half, and the ability to measure flexible and arbitrarily shaped, yet flat, samples[52]. However, the determination of ζ is not as straight-forward as in symmetric cells. Walker et al.[52] established a relationship between the zeta-potential of the substrate being analyzed ζ_{Test}, the measured asymmetric zeta-potential ζ_{Avg}, and the zeta-potential of the reference material ζ_{Ref}, i.e., the cell body (cf. Fig. 2.7b):

$$\zeta_{Test} = 2\zeta_{Avg} - \zeta_{Ref} \tag{2.20}$$

To apply equation (2.20), the zeta-potential ζ_{Ref} must first be determined using the Helmholtz-Smoluchowski equation in a symmetric configuration (cf. Fig. 2.6 and 2.7a).

Equations (2.19) and (2.20) hold for sufficiently high ion concentrations and large $\kappa a_c \gg 1$[6, 36], where a_c is the characteristic dimension. Here, a_c is the capillary radius R[6, 36], or the height h of a rectangular microchannel[51, 53, 54], respectively. However, if the bulk ion concentration is low, the conductivity within the double layer cannot be neglected. The contribution of the so-called surface conductivity K^σ may no longer be negligible[6, 30, 55]. The influence of K^σ also plays a crucial role for non-planar substrates. Geometries such as particle plugs, diaphragms, and membranes can be studied with the streaming potential technique[6]. The Helmholtz-Smoluchowski equation (Eq. 2.19) conveniently applies to porous particle plugs, provided that double layer relaxation effects and K^σ are insignificant[6]. This is the case for $\kappa a_c \gg 1$, say $\kappa a_c > 100$, where a_c is the pore radius r[56]. Under these conditions, the zeta-potential remains unaffected by the plug's geometry or particle shape[56, 57]. However, for scenarios where $\kappa a_c < 100$, more intricate models, such as the capillary model by Levine et al.[58] or the approach by Anderson and Koh[59], become necessary. As the conduction within the EDL dictates the methodical approach to electrokinetic experiments and the calculation of ζ, the following sub-chapter explores this additional conduction phenomenon.

2.3.3 Surface Conductivity

The presence of electric double layers in dispersed systems gives rise to a unique phenomenon: surface conduction. Ions within the EDL, when subjected to tangential electric fields, contribute to the electrical conductivity beyond the conductivity of the bulk solution. This excess conductivity, termed surface conductivity K^σ, is the surface-specific analogy to the bulk conductivity K_L and serves as a fundamental metric for understanding interfacial charge transport[6, 55]. Building on the GCSG double layer model, it is appropriate to decompose the surface conductivity K^σ into contributions from the ions in the rigid or hydrodynamically immobile layer $\left(K^{\sigma,i}\right)$ and from the ions in the diffuse or hydrodynamically mobile layer $\left(K^{\sigma,d}\right)$[6, 36, 55]:

$$K^\sigma = K^{\sigma,i} + K^{\sigma,d} \tag{2.21}$$

Figure 2.8 schematically shows the conductivity contribution of the stagnant Stern layer and the diffuse layer.

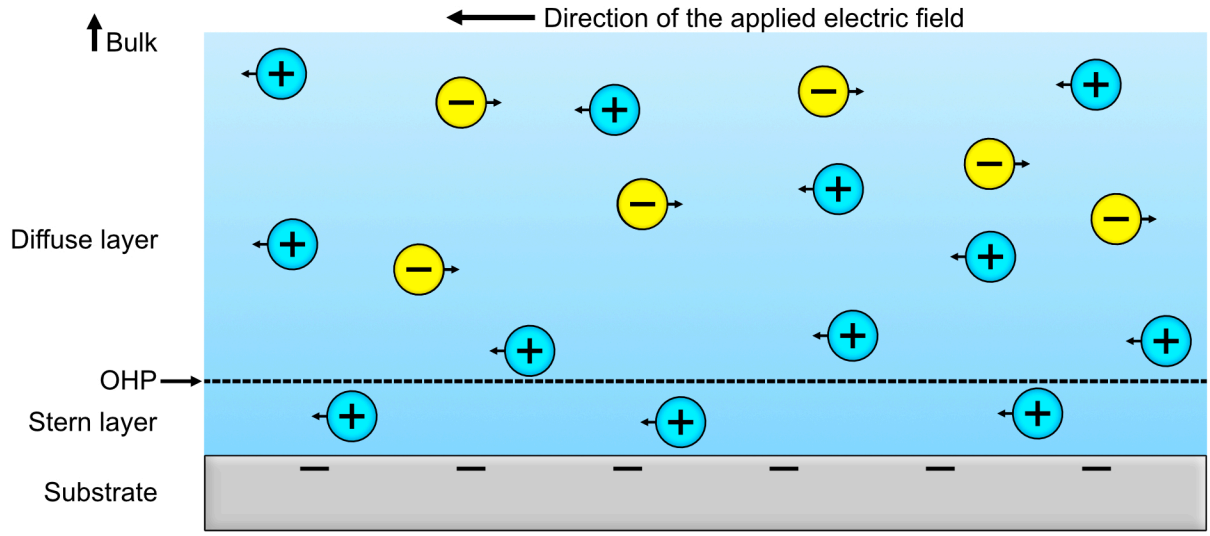

Figure 2.8: Schematic illustration of the surface conductivity on a flat interface. An applied tangential electric field forces the ions in the bulk solution, diffuse part of the EDL, and even within the Stern layer to move. The movement of ions in the Stern- and diffuse layer contributes to the overall conductivity and is called surface conductivity.

It is theoretically possible for K^σ to take on negative values. A reduction in the mobility of ions along solid surfaces may occur due to the depletion of charge carriers in the stagnant layer[55]. Furthermore, the presence of adsorbed or covalently attached polymers increases the path length that ions must traverse within the polymer network[36, 55].

An experimental method to calculate K^σ is presented by Werner et al.[51]. K^σ can be determined through analysis of streaming current and streaming potential data from measurements at various channel heights h in a well-defined micro slit channel geometry:

$$K^\sigma = \frac{1}{2}\left(\frac{I_{str}L}{U_{str}b} - K_L h\right) \tag{2.22}$$

Here, constant L and b are crucial when varying h. Equation (2.22) is valid when K^σ significantly contributes to the total microchannel conductivity[51]. Various other experimental methods to determine K^σ are summarized by Lyklema[55].

The surface conductivity influences transport processes occurring in electrokinetic phenomena. Thus, K^σ must be considered at low ionic strengths[6]. The Dukhin number Du relates K^σ to the characteristic dimension a_c of the system and K_L[6, 55]:

$$Du = \frac{K^\sigma}{a_c K_L} \tag{2.23}$$

In the case of rectangular flow channels, which were used in this work to investigate charge formation processes, a_c corresponds to the channel height h[51, 53, 54]. If K^σ is known, for example from equation (2.22), the streaming potential U_{str} can be used to reliably calculate ζ even at low ionic strength. Under consideration of Du, equation (2.19) is then written as[6, 55]:

$$\zeta = \frac{\eta K_L (1 + 2Du)}{\varepsilon_r \varepsilon_0} \frac{U_{str}}{\Delta p} \tag{2.24}$$

So far, streaming potential measurements have proven to provide a detailed understanding of surface charging and electrokinetic properties. Hence, this technique allows for insightful studies on the adsorption behavior of polyelectrolytes and their effective charge in the adsorbed state. Thus, the next sub-chapter introduces adsorption phenomena.

2.4 Adsorption

Adsorption is the process of (ir)reversible immobilization of molecules and particles (adsorbates) at interfaces (substrate or adsorbent). Molecules in solution adhere to surfaces due to attractive forces like van der Waals interactions. This adsorption process is influenced by various factors, most importantly the concentration of the adsorbate and the adsorption time. Upon adsorption, these molecules typically experience reduced rotational and vibrational freedom, and even their electrical properties may be altered. Some molecules exhibit lateral diffusion or undergo chemical reactions on the surface[7]. Experimental observations reveal a wide range of adsorption isotherms, while one widely known is the Langmuir isotherm. The Langmuir isotherm is schematically shown in Figure 2.9.

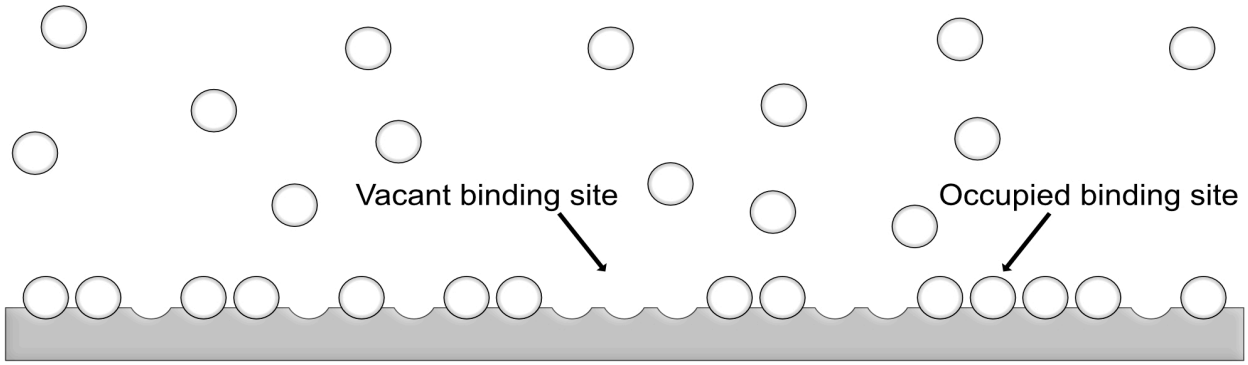

Figure 2.9: Schematic representation of the Langmuir isotherm. Gas molecules may only adsorb to vacant binding sites. As adsorption proceeds, these sites become occupied, and the model assumes that no further adsorption can occur on top of already adsorbed molecules, resulting in monolayer adsorption.

The Langmuir isotherm describes monolayer adsorption and is derived from a kinetic perspective, considering the rates of adsorption and desorption. The surface is modelled as possessing a fixed concentration of adsorption sites, S (mol m^{-2}), which can be categorized as occupied S_1 or vacant $S_0 = S - S_1$. The adsorption process, where gas molecules attach to the surface, proceeds at a rate proportional to the product of the adsorbate partial pressure P and the concentration of vacant sites S_0, formalized as $k_{ad}PS_0$, where k_{ad} is the adsorption rate constant. Simultaneously, adsorbed molecules desorb at a rate proportional to the concentration of occupied sites S_1, expressed as $k_{de}S_0$, where k_{de} is the desorption rate constant. Equilibrium is reached when the adsorption and desorption rates become equal, resulting in a steady-state surface coverage, described by the Langmuir equation[7, 60]:

$$\frac{S_1}{S} = \frac{K_{eq}P}{1 + K_{eq}P} \tag{2.25}$$

where $K_{eq} = k_{ad}\, k_{de}^{-1}$. This model assumes monolayer adsorption which imposes a fundamental limitation: it predicts saturation at high pressures, which demonstrably fails to represent the behavior

of numerous real-world adsorption systems[7]. To address the limitations of monolayer adsorption, Brunauer, Emmett, and Teller developed the BET isotherm, extending the Langmuir theory by fundamentally postulating that each adsorbed layer adheres to Langmuir's principles[61]. Although these isotherms are foundational for understanding general adsorption phenomena, the adsorption of macromolecules from solution is better described by the random sequential adsorption (RSA) model that accounts for the interplay between molecular size, surface coverage, and steric effects[62, 63].

2.4.1 Random Sequential Adsorption

Random sequential adsorption is a powerful theoretical model used extensively in colloid and interface science to study the adsorption of particles and macromolecules[63-65]. The RSA model was first used by Feder to simulate irreversible adsorption processes of proteins[65]. This model provides valuable insights into key aspects of adsorption, including monolayer density, kinetics, and microstructural properties like pair-correlation functions and roughness[63].

In the RSA model, adsorbates are considered as hard objects, where overlapping of these objects is not allowed. During the RSA process, adsorbates are sequentially and randomly placed on the substrate. Adsorbates are not allowed to desorb or move laterally on the substrate[63, 65, 66]. The maximum surface coverage in the RSA model is less than 100% because of the excluded area around each adsorbed particle. The excluded area is the region around an adsorbed objects where the center of another particle cannot be placed without overlapping the first particle. The shape of the excluded area depends on the shape of the adsorbed particle and the orientation of the trial particle. For example, if the adsorbed particle is a disk of radius a, then the excluded area is a circle of radius $2a$. This means that no other disk can be placed within a distance of $2a$ from the center of the first disk [63, 65]. As more and more particles randomly adsorb, the excluded areas start to overlap, and it becomes increasingly difficult for further objects to adsorb. Eventually, the surface becomes so crowded that it is impossible to add any more objects without overlapping existing ones. This is called the jamming limit θ_{jam}[63, 65, 66]. Figure 2.10 illustrates a saturated RSA packing of disks based on the two-dimensional RSA model.

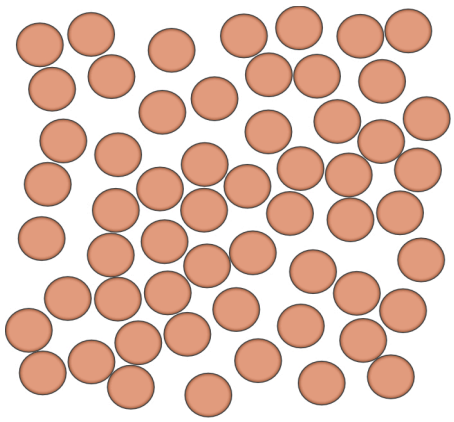

Figure 2.10: Exemplary 2D schematic of a saturated RSA packing from adsorbed disks. The maximum surface coverage for adsorbed hard disks is $\theta_{jam} \cong 0.547$.

In the two-dimensional RSA model, as shown in Fig. 2.10 for hard discs, the adsorption leads to a jamming limit at a fractional surface coverage of $\theta_{jam} \cong 0.547$[65]. Feder's model proposes a linear dependence between surface coverage $\theta$and the square root of time $\sqrt{t}$ until the jamming limit θ_{jam} is achieved. The RSA model can accurately predict packing fractions, comparable to those observed in real adsorption monolayers[63]. However, this simplicity relies on several key assumptions like a homogeneous adsorbent, a dilute suspension, monodisperse adsorbates, stationary flux, irreversible adsorption, no adsorbate-adsorbate interactions, negligible influence of external forces like gravity, no consideration of hydrodynamics and diffusion, and monolayer adsorption[63].

In practice, significantly lower saturation limits $\theta_{plat} < \theta_{jam}$ are found. For a better understanding of adsorption kinetics of highly charged macromolecules like dendrimers, an extended (or electrostatic) RSA model incorporating electrostatic interactions has been developed[67-69]. This model considers the charge of the adsorbates in electrolyte solutions, governed by the ionic strength and the pH value. The resulting electrostatic repulsion between two adsorbates plays a crucial role for the saturation limit θ_{plat}[62, 64, 66, 70-73]. To account for the electrostatic repulsion, an effective hard sphere radius a_{eff} for the adsorbates is introduced[66]:

$$a_{eff} = (2\kappa)^{-1} ln(A/ln\, A) \tag{2.26}$$

with $A = \lambda Z^2 \kappa L_B \exp[2\kappa a(1+\kappa a)^{-2}]$, where $\lambda = 2.8$, Z is the adsorbate charge, and $L_B = e^2(4\pi\varepsilon_r\varepsilon_0 k_B T)^{-1}$ is the Bjerrum length[66]. a_{eff} considers the electrostatic interactions between two adsorbates. One must also consider that the adsorbates may carry an effective charge Z_{eff} which is less than the theoretical charge. Charged colloids will be surrounded by a cloud of ions, which will screen the bare charge. The effective charge of the colloid is the charge that is experienced by other colloids in the solution, after the screening effect of the ions has been taken into account. The effective charge is a function of the geometry of the colloid, the temperature, and the presence of added salt[74-76]. The effective charge is defined as[74]:

$$Z_{eff} = (a/L_B)(4\kappa a + 6) \tag{2.27}$$

Equation 2.27 is valid for high salt concentrations, i.e., $\kappa a \geq 5$[66, 74]. Assuming a jamming limit $\theta_{jam} \cong 0.547$, the resulting maximum surface coverage θ_{plat}, following the extended RSA model, is calculated by[66]:

$$\theta_{plat} = \theta_{jam}\left(a/a_{eff}\right)^2 \tag{2.28}$$

So far in this sub-chapter, the substrate was treated as an ideal collector interface. However, the surface charge of the substrate strongly influences the adsorption of charged macromolecules. This influence is due to the attractive three-body interactions between a pair of dendrimers and the surface. The so-called three-body RSA model is a model that describes the adsorption of charged macromolecules, like dendrimers, to a charged substrate[62, 72]. This model is an extension of the electrostatic RSA model, which only considers the interaction between two adsorbing dendrimers[64, 70, 71]. The three-body RSA model also considers the interaction between the adsorbing dendrimers and the charged substrate. This interaction is described by a three-body potential, which is less repulsive than the potential in solution. The reduced repulsion can be interpreted as an attractive three-body contribution, which acts in addition to the usual screened Coulomb two-body potential[62, 72]. The three-body RSA model has been shown to be in good agreement with experimental data for the adsorption of PAMAM dendrimers to silica substrates[62].

References

[1] Reuß, F. F., Sur un nouvel effet de l'électricité galvanique, Mem. Soc. Imp. Natur. Moscou, 2, 327, **1809**

[2] Wiedemann, G., Ueber die Bewegung von Flüssigkeiten im Kreise der geschlossenen galvanischen Säule, Ann. Phys., 163(11), 321, **1852**

[3] Quincke, G., Ueber die Fortführung materieller Theilchen durch strömende Elektricität, Ann. Phys., 189(8), 513, **1861**

[4] von Helmholtz, H., Studien über electrische Grenzschichten, Ann. Phys., 243(7), 337, **1879**

[5] Wall, S., The history of electrokinetic phenomena, Curr. Opin. Colloid Interface Sci., 15(3), 119, **2010**

[6] Delgado, Á. V.; González-Caballero, F.; Hunter, R. J.; Koopal, L. K. and Lyklema, J., Measurement and interpretation of electrokinetic phenomena, J. Colloid Interface Sci., 309(2), 194, **2007**

[7] Butt, H.-J.; Graf, K. and Kappl, M., Physics and chemistry of interfaces, 1st ed., Wiley-VCH, Weinheim, **2003**

[8] Delgado, Á. V. and Arroyo, F. J., Electrokinetic phenomena and their experimental determination: An overview, 1st ed., CRC Press, New York, **2001**

[9] Myers, D., Surfaces, interfaces, and colloids, 2nd ed., John Wiley & Sons, New York, **1999**

[10] Wedler, G., Lehrbuch der Physikalischen Chemie, 4th ed., Wiley-VCH, Weinheim, **1997**

[11] Chechik, V.; Crooks, R. M. and Stirling, C. J. M., Reactions and reactivity in self-assembled monolayers, Adv. Mater., 12, 1161, **2000**

[12] Kakiuchi, T.; Sato, K.; Iida, M.; Hobara, D.; Imabayashi, S.-i. and Niki, K., Phase separation of alkanethiol self-assembled monolayers during the replacement of adsorbed thiolates on Au(111) with thiols in solution, Langmuir, 16(18), 7238, **2000**

[13] Vezenov, D. V.; Noy, A.; Rozsnyai, L. F. and Lieber, C. M., Force titrations and ionization state sensitive imaging of functional groups in aqueous solutions by chemical force microscopy, J. Am. Chem. Soc., 119(8), 2006, **1997**

[14] Beneš, P. and Paulenová, M., Surface charge and adsorption properties of polyethylene in aqueous solutions of inorganic electrolytes. I. Streaming potential measurement, Kolloid Z. Z. Polym., 251(10), 766, **1973**

[15] Elimelech, M. and O'Melia, C. R., Effect of electrolyte type on the electrophoretic mobility of polystyrene latex colloids, Colloids Surf., 44, 165, **1990**

[16] Elimelech, M.; Chen, W. H. and Waypa, J. J., Measuring the zeta (electrokinetic) potential of reverse osmosis membranes by a streaming potential analyzer, Desalination, 95(3), 269, **1994**

[17] Jacobasch, H.-J. and Schurz, J., Characterization of polymer surfaces by means of electrokinetic measurements, Progr. Colloid Polym. Sci., 77, 40, **1988**

[18] Ottewill, R. H. and Shaw, J. N., Studies on the preparation and characterisation of monodisperse polystyrene latices. Part 2: Electrophoretic characterisation of surface groupings, Kolloid Z. Z. Polym., 218(1), 34, **1967**

[19] Voegtli, L. P. and Zukoski, C. F., Adsorption of ionic species to the surface of polystyrene latexes, J. Colloid Interface Sci., 141(1), 92, **1991**

[20] Zimmermann, R.; Dukhin, S. and Werner, C., Electrokinetic measurements reveal interfacial charge at polymer films caused by simple electrolyte ions, J. Phys. Chem. B, 105(36), 8544, **2001**

[21] Zimmermann, R.; Freudenberg, U.; Schweiß, R.; Küttner, D. and Werner, C., Hydroxide and hydronium ion adsorption - A survey, Curr. Opin. Colloid Interface Sci., 15(3), 196, **2010**

[22] Horinek, D. and Netz, R. R., Specific ion adsorption at hydrophobic solid surfaces, Phys. Rev. Lett., 99(22), 226104, **2007**

[23] Lyons, J. S.; Furlong, D. N. and Healy, T. W., The electrical double-layer properties of the mica (muscovite)-aqueous electrolyte interface, Aust. J. Chem., 34(6), 1177, **1981**

[24] Maslova, M. V.; Gerasimova, L. G. and Forsling, W., Surface properties of cleaved mica, Colloid J., 66(3), 322, **2004**

[25] Oyegbile, B.; Ay, P. and Narra, S., Optimization of physicochemical process for pre-treatment of fine suspension by flocculation prior to dewatering, Desalin. Water Treat., 57(6), 2726, **2016**

[26] Tombácz, E. and Szekeres, M., Surface charge heterogeneity of kaolinite in aqueous suspension in comparison with montmorillonite, Appl. Clay Sci., 34(1-4), 105, **2006**

[27] Palomino, A. M. and Santamarina, J. C., Fabric map for kaolinite: Effects of pH and ionic concentration on behavior, Clays Clay Miner., 53(3), 211, **2005**

[28] Bazant, M. Z.; Chu, K. T. and Bayly, B. J., Current-voltage relations for electrochemical thin films, SIAM J. Appl. Math., 65(5), 1463, **2005**

[29] Karg, A.; Rößler, T.; Mark, A.; Markus, P.; Lauster, T.; Helfricht, N. and Papastavrou, G., A versatile and simple approach to electrochemical colloidal probes for direct force measurements, Langmuir, 37(46), 13537, **2021**

[30] Hunter, R. J., Zeta potential in colloid science: Principles and applications, 1st ed., Academic Press, London, **1981**

[31] Grahame, D. C., The electrical double layer and the theory of electrocapillarity, Chem. Rev., 41(3), 441, **1947**

[32] Gouy, M., Sur la constitution de la charge électrique à la surface d'un électrolyte, J. Phys. Theor. Appl., 9, 457, **1910**

[33] Chapman, D. L., A contribution to the theory of electrocapillarity, Lond. Edinb. Dubl. Phil. Mag., 25(148), 475, **1913**

[34] Debye, P. and Hückel, E., De la theorie des electrolytes. I. Abaissement du point de congelation et phenomenes associes, Phys. Z., 24(9), 185, **1923**

[35] Ohshima, H., Theory of colloid and interfacial electric phenomena, 1st ed., Academic Press, **2006**

[36] Ohshima, H., Electrical phenomena at interfaces and biointerfaces: Fundamentals and applications in nano-, bio-, and environmental sciences, 1st ed., John Wiley & Sons, Hoboken, **2012**

[37] Stern, O., Zur Theorie der elektrolytischen Doppelschicht, Z. Elektrochem. Angew. Phys. Chem., 30(21-22), 508, **1924**

[38] Freundlich, H., Kapillarchemie, 1st ed., Akademische Verlagsgesellschaft, Leipzig, **1922**

[39] Lamb, H., VIII. On the theory of electric endosmose and other allied phenomean, and on the existence of a sliding coefficient for a fluid in contact with a solid, Lond. Edinb. Phil. Mag. J. Sci., 25(152), 52, **1888**

[40] Westall, J. and Hohl, H., A comparison of electrostatic models for the oxide/solution interface, Adv. Colloid Interface Sci., 12(4), 265, **1980**

[41] Hiemstra, T.; Van Riemsdijk, W. H. and Bolt, G. H., Multisite proton adsorption modeling at the solid/solution interface of (hydr)oxides: A new approach, J. Colloid Interface Sci., 133(1), 91, **1989**

[42] Hiemstra, T.; De Wit, J. C. M. and Van Riemsdijk, W. H., Multisite proton adsorption modeling at the solid/solution interface of (hydr)oxides: A new approach, J. Colloid Interface Sci., 133(1), 105, **1989**

[43] Viovy, J.-L., Electrophoresis of DNA and other polyelectrolytes: Physical mechanisms, Rev. Mod. Phys., 72(3), 813, **2000**

[44] von Smoluchowski, M., Handbuch der Elektrizität und des Magnetismus, 1st ed., J. A. Barth, Leipzig, **1921**

[45] Hückel, E., Die Kataphorese der Kugel, Phys. Z., 25, 204, **1924**

[46] Zhao, K. and He, K., Dielectric relaxation of suspensions of nanoscale particles surrounded by a thick electric double layer, Phys. Rev. B, 74(20), 33, **2006**

[47] Henry, D. C., The cataphoresis of suspended particles. Part I. - The equation of cataphoresis, Proc. R. Soc. Lond. A, 133(821), 106, **1931**

[48] O'Brien, R. W. and White, L. R., Electrophoretic mobility of a spherical colloidal particle, J. Chem. Soc., Faraday Trans. 2, 74, 1607, **1978**

[49] Bellmann, C.; Caspari, A.; Moitzi, C. and Babick, F., Dynamische und elektrophoretische Lichtstreuung, 2nd ed., Anton Paar GmbH, Graz, **2020**

[50] Uzgiris, E. E., Laser Doppler methods in electrophoresis, Prog. Surf. Sci., 10(1), 53, **1981**

[51] Werner, C.; Körber, H.; Zimmermann, R.; Dukhin, S. and Jacobasch, H. J., Extended electrokinetic characterization of flat solid surfaces, J. Colloid Interface Sci., 208(1), 329, **1998**

[52] Walker, S. L.; Bhattacharjee, S.; Hoek, E. M. V. and Elimelech, M., A novel asymmetric clamping cell for measuring streaming potential of flat surfaces, Langmuir, 18(6), 2193, **2002**

[53] Werner, C.; Zimmermann, R. and Kratzmüller, T., Streaming potential and streaming current measurements at planar solid/liquid interfaces for simultaneous determination of zeta potential and surface conductivity, Colloids Surf. A., 192(1-3), 205, **2001**

[54] Zimmermann, R., Charakterisierung von Ladungsbildungsprozessen an Polymeren in wässrigen Lösungen, Dissertation, Technische Universität Dresden, Dresden, **2004**

[55] Lyklema, J., Surface conduction, J. Phys. Condens. Matter, 13(21), 5027, **2001**

[56] Hidalgo-Alvarez, R.; de las Nieves, F. J. and Pardo, G., Comparative sedimentation and streaming potential studies for ζ potential determination, J. Colloid Interface Sci., 107(2), 295, **1985**

[57] Li, H. C. and De Bruyn, P. L., Electrokinetic and adsorption studies on quartz, Surf. Sci., 5(2), 203, **1966**

[58] Levine, S.; Marriott, J. R.; Neale, G. and Epstein, N., Theory of electrokinetic flow in fine cylindrical capillaries at high zeta-potentials, J. Colloid Interface Sci., 52(1), 136, **1975**

[59] Anderson, J. L. and Koh, W.-H., Electrokinetic parameters for capillaries of different geometries, J. Colloid Interface Sci., 59(1), 149, **1977**

[60] Langmuir, I., The adsorption of gases on plane surfaces of glass, mica and platinum., J. Am. Chem. Soc., 40(9), 1361, **1918**

[61] Brunauer, S.; Emmett, P. H. and Teller, E., Adsorption of gases in multimolecular layers, J. Am. Chem. Soc., 60(2), 309, **1938**

[62] Cahill, B. P.; Papastavrou, G.; Koper, G. J. and Borkovec, M., Adsorption of poly(amido amine) (PAMAM) dendrimers on silica: Importance of electrostatic three-body attraction, Langmuir, 24(2), 465, **2008**

[63] Kubala, P.; Batys, P.; Barbasz, J.; Weroński, P. and Cieśla, M., Random sequential adsorption: An efficient tool for investigating the deposition of macromolecules and colloidal particles, Adv. Colloid Interface Sci., 306, 102692, **2022**

[64] Adamczyk, Z. and Warszyński, P., Role of electrostatic interactions in particle adsorption, Adv. Colloid Interface Sci., 63, 41, **1996**

[65] Feder, J., Random sequential adsorption, J. Theor. Biol., 87(2), 237, **1980**

[66] Pericet-Camara, R.; Papastavrou, G. and Borkovec, M., Atomic force microscopy study of the adsorption and electrostatic self-organization of poly(amidoamine) dendrimers on mica, Langmuir, 20(8), 3264, **2004**

[67] Adamczyk, Z.; Zembala, M.; Siwek, B. and Warszyński, P., Structure and ordering in localized adsorption of particles, J. Colloid Interface Sci., 140(1), 123, **1990**

[68] Oberholzer, M. R.; Wagner, N. J. and Lenhoff, A. M., Grand canonical Brownian dynamics simulation of colloidal adsorption, J. Chem. Phys., 107(21), 9157, **1997**

[69] Weroński, P., Effect of electrostatic interaction on deposition of colloid on partially covered surfaces, Colloids Surf. A., 294(1-3), 254, **2007**

[70] Adamczyk, Z., Modeling adsorption of colloids and proteins, Curr. Opin. Colloid Interface Sci., 17(3), 173, **2012**

[71] Borkovec, M.; Szilagyi, I.; Popa, I.; Finessi, M.; Sinha, P.; Maroni, P. and Papastavrou, G., Investigating forces between charged particles in the presence of oppositely charged polyelectrolytes with the multi-particle colloidal probe technique, Adv. Colloid Interface Sci., 179-182, 85, **2012**

[72] Pericet-Camara, R.; Cahill, B. P.; Papastavrou, G. and Borkovec, M., Nano-patterning of solid substrates by adsorbed dendrimers, Chem. Commun., (3), 266, **2007**

[73] Pericet-Camara, R.; Papastavrou, G. and Borkovec, M., Effective charge of adsorbed poly(amidoamine) dendrimers from direct force measurements, Macromolecules, 42(5), 1749, **2009**

[74] Bocquet, L.; Trizac, E. and Aubouy, M., Effective charge saturation in colloidal suspensions, J. Chem. Phys., 117(17), 8138, **2002**

[75] Chew, W. C. and Sen, P. N., Potential of a sphere in an ionic solution in thin double layer approximations, J. Chem. Phys., 77(4), 2042, **1982**

[76] Semmler, M.; Mann, E. K.; Rička, J. and Borkovec, M., Diffusional deposition of charged latex particles on water−solid interfaces at low ionic strength, Langmuir, 14(18), 5127, **1998**

3. Synopsis

3. Synopsis

3.1 Outline

This thesis investigates the multifaceted nature of electrokinetic phenomena, focusing on their diverse applications. Through five research projects, this work explores the determination of the effective charge of individual adsorbed macromolecules, the acidity of catalyst-carrying interfaces, the surface-charge-related particle stacking in pores, changes in microplastic surface chemistry by weathering, and the applicability of electrophoretic mobility for nanoparticle aggregates. Ultimately, these research projects converge on a common goal: understanding and analyzing interfacial phenomena by applying electrokinetic techniques. The following chapter summarizes the content of all joint publications of the presented thesis. The individual contributions of each co-author are detailed at the end of the chapter.

3.2 Content of Joint Publications

All electrokinetic phenomena arise from the interaction between charged surfaces and electrolytes. This thesis comprises two general thematic areas for electrokinetic applications: Planar and granular samples of various size ranges. For planar surfaces, (A) the streaming potential and -current technique was employed to study the adsorption of macromolecules, (B) the acidity of catalyst-carrying interfaces, and (C) the surface charge controlling the particle loading into pores. In the intermediate size range, particle plugs of µm-sized particles were studied using streaming potential measurements to assess the impact of weathering on microplastic surface chemistry (D). For aggregates comprised of nanoparticles, however, electrophoretic light scattering was utilized to investigate the electrokinetic behavior and the role of the primary particle diameter (E). Figure 3.1 offers a comprehensive view of the different samples investigated in this thesis using electrokinetic techniques.

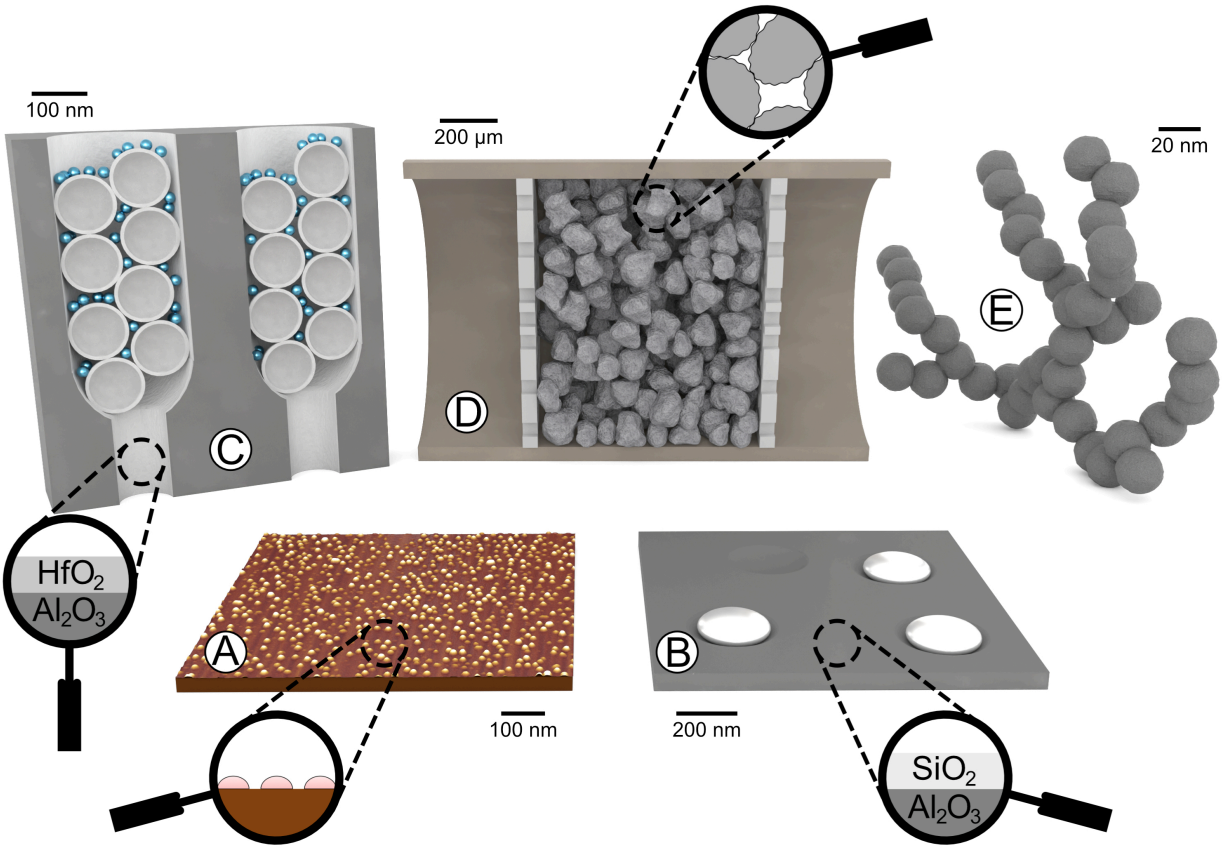

Figure 3.1: Collection of the specimens under investigation in the framework of this thesis. The magnifying glass icons highlight the interfaces studied *via* streaming potential or -current. (A) poly(amidoamine) dendrimers adsorbed to an inorganic collector surface (cf. Chapter 4). (B) Nanostructured oxide-coated surface carrying liquid drops of gallium as a catalyst substrate (cf. Chapter 5). (C) Metal oxide-coated porous structure of hollow spheres loaded with noble metal catalyst particles (cf. Chapter 6). (D) Particle plug filled with arbitrarily shaped microplastic particles (cf. Chapter 7). (E) Fumed silica nanoparticle aggregate (cf. Chapter 8).

The first project (cf. Chapter 4) utilized the streaming potential technique to investigate the effective charge of globular poly(amidoamine) (PAMAM) dendrimers adsorbed onto planar interfaces of silica and muscovite mica. This work highlights the substrate's significant and previously underappreciated influence on the effective charge of macromolecules adsorbed at planar interfaces, particularly within the context of the random sequential adsorption (RSA) model. Furthermore, it demonstrates the capability of the streaming potential technique to characterize the charges of these adsorbed macromolecules at the nanoscale.

The second part of this thesis (cf. Chapter 5) made use of the streaming potential technique to characterize the surface acidity of thin films of oxide catalyst carrier materials. Streaming potential measurements directly assessed the acidity of these substrates, revealing a critical correlation: the support's acidity directly influences gallium (Ga) droplet size, size distribution, and the effective surface area of the catalyst-carrying liquid metal. More acidic interfaces resulted in smaller Ga droplets with narrower distributions, leading to optimized catalysis systems with enhanced performance. Streaming potential measurements provided a direct access to the charge at the interface.

The third study (cf. Chapter 6) investigated the surface charge of HfO_2 and ZnO thin planar films by the streaming current technique. In particular, the position of the isoelectric point has been determined. The metal oxide films coat the pore walls of an anodized aluminum oxide (AAO) framework. The goal was to understand and optimize the loading of negatively charged sacrificial polystyrene nanospheres used as templates within these pores. Streaming current measurements revealed how the surface chemistry of the metal oxide layers influenced the adsorption and packing density of the polystyrene particles. Specifically, the acidic nature of the HfO_2 coating prevented strong adhesion of the negatively charged polystyrene particles, ultimately leading to a higher particle loading within the AAO pores than the ZnO coating. Therefore, the streaming current technique was critical for characterizing the interfacial properties that govern particle loading in this porous structure.

The fourth project (cf. Chapter 7) applied the streaming potential technique differently: to study microplastic particles ranging from 15 µm to 250 µm in diameter. Unlike the previous publications, where flat interfaces were investigated, we studied the surface charge properties of three categories of microplastic particles in a packed arrangement: commercial spherical, fragmented, and artificially weathered fragmented microplastic particles. We showed the applicability of the streaming potential technique for the different size fractions of particles and the increasing acidity arising from weathering. Additionally, this publication demonstrated a previously overlooked application of the streaming potential technique: its use as an analytical tool in environmental science for studying particle systems too large for analysis by light scattering methods.

In contrast to the previous projects, the fifth part of this thesis (cf. Chapter 8) explored the electrokinetic properties of nanoparticle aggregates. Since this paper studied dispersed colloidal objects, the streaming potential technique is no longer a viable tool. We employed electrophoretic light scattering (ELS) to investigate how the size of primary fumed silica particles and the size of the aggregates they form influenced electrophoretic mobility. Fumed silica aggregates of different sizes were grown from smaller aggregates and single primary particles. This study found that the primary particle size rather than the aggregate size predominantly determines the electrophoretic mobility. Analytical and numerical calculations of electrokinetic models supported the results. This finding has wide implications, for example, for analyzing degraded microplastic particles in the nanometer range.

Streaming Potential Technique

Since its first description in 1861[1], the streaming potential technique has been widely utilized and continuously refined for characterizing the interfacial properties of various materials[2-5]. In general, streaming potential measurements involve forcing an electrolyte solution through a defined channel or packed bed, allowing for the calculation of the zeta-potential ζ. This approach facilitates the quantitative, yet indirect, surface charge analysis for both planar and granular samples, providing critical insights into diverse applications, including surface modification[6], adsorption[7], and water treatment[8].

Building upon the fundamentals of the streaming potential, our first project applied this technique to determine the effective charge of macromolecules at solid-liquid interfaces. Specifically, we investigated the adsorption of globular PAMAM dendrimers onto planar silica and muscovite mica substrates, utilizing streaming potential measurements to quantify the influence of the substrate on the overall interfacial charge.

3.2.1 Effective charge of high-generation PAMAM dendrimers in the adsorbed state

The adsorption of charged macromolecules on solid substrates is a common phenomenon in colloid and interface science[9-11], occurring in aqueous solutions in natural (e.g., humic acid on microplastics[12-14]) and industrial contexts (e.g., polyelectrolyte-based colloid stabilization or surface modification[7, 15, 16]). Solid/electrolyte interfaces gain charges *via* (de-)protonation or ion adsorption. The charged nature of macromolecules and substrates makes electrostatic interactions critical to adsorption kinetics and determining the adsorbed mass plateau. We investigated how the effective charge of adsorbed PAMAM dendrimers of generation 10 (G10) evolves with the surface coverage on distinct substrates. Therefore, we performed streaming potential measurements with a custom-built device to characterize bare collector substrates, systematically varied the dendrimer surface coverage, and correlated electrokinetic results to coverage for both substrate types. The streaming potential measurements were performed using a custom-made setup developed in Prof. Dr. Georg Papastavrou's laboratory, shown in Figure 3.2.

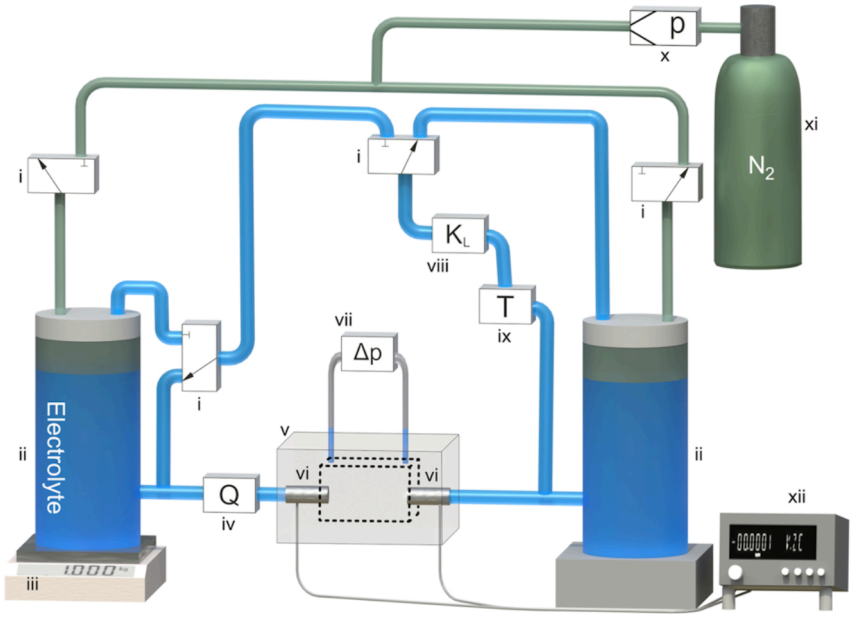

Figure 3.2: Schematic illustration of the streaming potential apparatus. This custom-built system includes several key components for precise control and measurement: (i) 3/2 way valves, (ii) electrolyte reservoirs, (iii) a mass flow balance, and (iv) a flow meter for flow rate control. The core measurement components are (v) modular streaming potential cells, (vi) Ag/AgCl electrodes, and (vii) a differential pressure sensor. Additional components include (viii) a conductivity cell, (ix) a PT100 temperature sensor, (x) a proportional valve, (xi) a nitrogen reservoir, and (xii) an electrometer for data acquisition. Adapted with permission from Engelhardt et al., *Journal of Colloid and Interface Science*, **2025**, 686, 852-863, © 2025 Elsevier B.V.

This device comprised a flow control system, exchangeable streaming potential cells made from poly(tetrafluoroethylene) (PTFE), custom-made Ag/AgCl electrodes, a differential pressure sensor, and a data acquisition system. Nitrogen pressure and precision valves controlled the electrolyte flow through the cell, while the flow rate was monitored by a mass flow balance and a flow meter. The streaming potential, generated across the sample within the cell, is measured by the Ag/AgCl electrodes and an electrometer. A differential pressure sensor measures the pressure drop, and additional sensors monitor conductivity and temperature. A custom script controlled all components and recorded the data. The pH is measured externally. The streaming potential cells used in this study were custom-designed in two distinct configurations: a classical parallel-plate cell and an asymmetric cell. Experiments with the parallel-plate cell, using two identical substrates in a parallel-facing arrangement, allowed for straightforward data evaluation, as the measured streaming potential could be directly converted to the zeta-potential. In contrast, the asymmetric cell required initial characterization of the PTFE body at each ionic strength and pH of interest. Only after this pre-characterization could the zeta-potential be determined from asymmetric measurements, where the streaming channel was formed by the PTFE body and the substrate under investigation. Despite this added complexity, the asymmetric cell offered two key advantages: the shape of the flat substrate was not critical if the channel was fully covered and tightly sealed, and only one sample substrate needed to be prepared. Both cell types were employed in this study. However, we focused on the asymmetric cell due to its versatility. The asymmetric cell could accommodate both silica and mica substrates, whereas the symmetric cell required individual fabrication for each specific sample size and thickness.

Two distinct substrates, muscovite mica and fused silica, were used to investigate the adsorption of dendrimers. The zeta-potentials ζ of both substrates are presented in Figure 3.2.

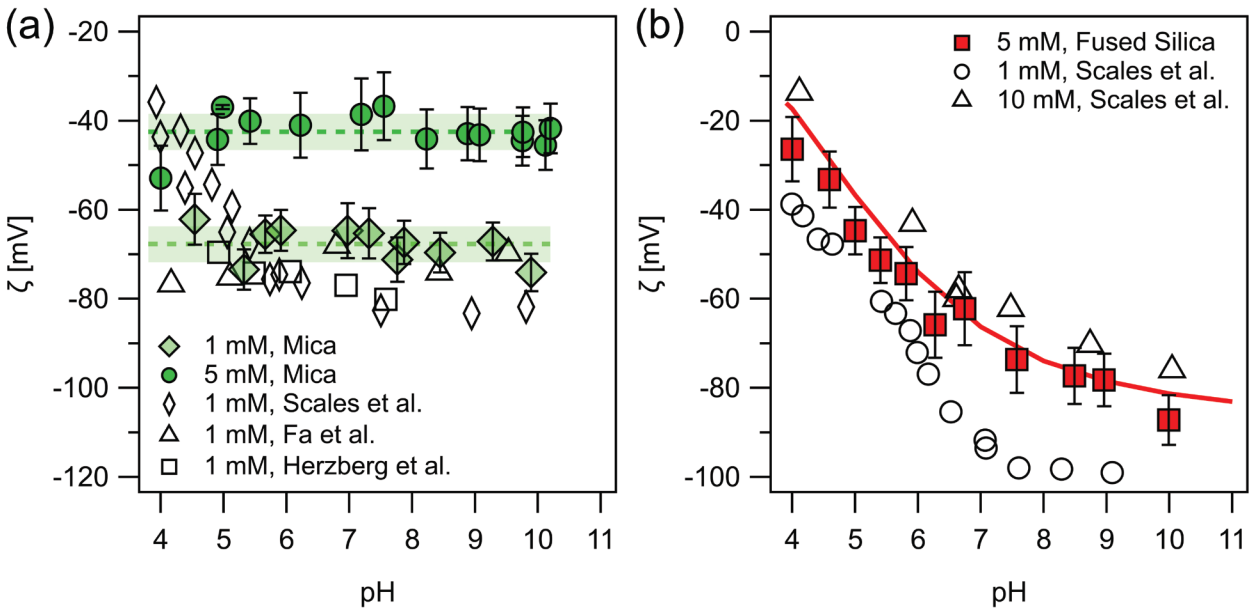

Figure 3.3: Zeta-potential ζ of (a) muscovite mica and (b) fused silica as a function of pH (filled markers). Mica was analyzed at ionic strengths of 1 mM and 5 mM, while silica was exclusively studied at 5 mM. For reference, literature data are included (open markers)[17-20]. Adapted with permission from Engelhardt et al., *Journal of Colloid and Interface Science*, **2025**, 686, 852-863, © 2025 Elsevier B.V.

The ζ values of mica (cf. Figure 3.3a) determined in this study align with previously reported data[17-19]. ζ showed no notable pH dependence for both ionic strengths (I) which is consistent with earlier findings[17, 21]. A clear pH dependence of ζ was observed for silica surfaces in Figure 3.3b. The data obtained at an ionic strength of 5 mM lay within the range reported for I = 1 mM and 10 mM[20]. Furthermore, the key features of the 1-pK model (red line) proposed for silica were successfully replicated[22-25]. The substrates were then used for adsorption studies. Figure 3.4 presents AFM images of PAMAM G10 dendrimers adsorbed on mica and silica substrates as a function of the adsorption time. As anticipated, the fractional surface coverage varied with the adsorption time, ultimately reaching a plateau beyond 15 minutes for both surface types.

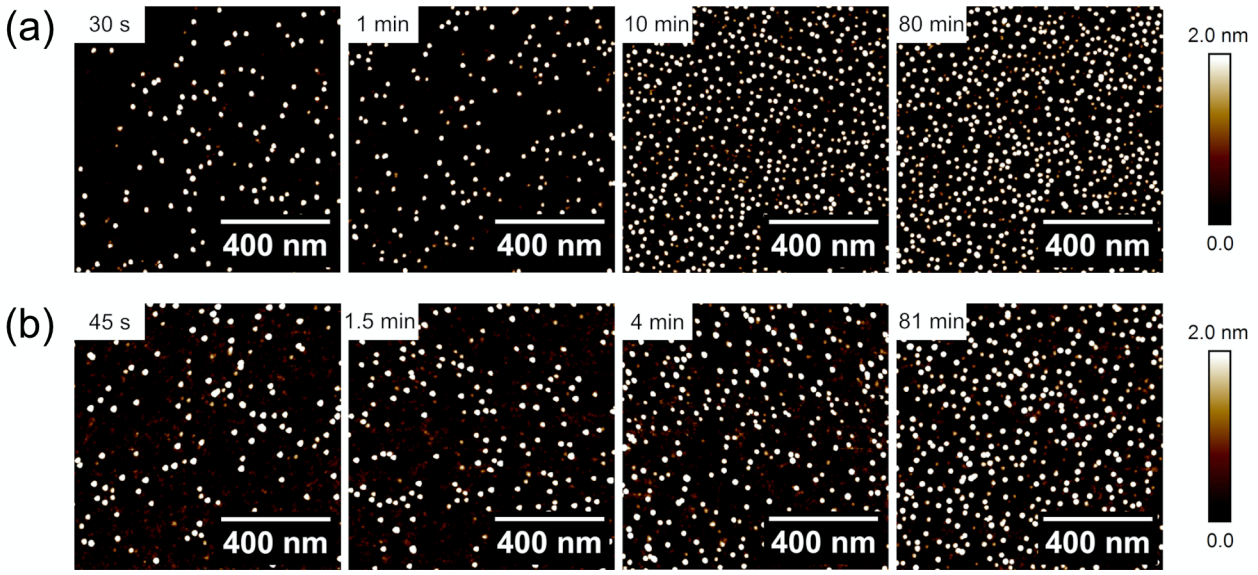

Figure 3.4: AFM images showing PAMAM G10 dendrimers adsorbed on (a) mica and (b) silica surfaces at various adsorption times. All images were captured in air using PeakForce Tapping® mode with a scan size of 1 µm × 1 µm. Adapted with permission from Engelhardt et al., *Journal of Colloid and Interface Science*, **2025**, 686, 852-863, © 2025 Elsevier B.V.

However, the maximum coverage of PAMAM on both interfaces strongly varied as determined from at least five AFM images. The coverage θ was calculated using reported PAMAM G10 dimensions of a_{ads} = 9.15 nm[26]. Maximum coverages were (9.2 ± 0.2) % on silica and (13.5 ± 0.3) % on mica.

The streaming potential technique was used to analyze ζ as a function of surface coverage and pH (Figure 3.5a,b). Both dendrimer-covered substrates showed notable ζ variations with pH. For mica, the sigmoidal ζ(pH) trend is easier to interpret since its bare surface remains unchanged with pH, allowing the electrokinetic charge density σ to be considered constant (cf. Figure 3.5a; black markers). Thus, ζ variations stem solely from dendrimer ionization at constant coverage. In contrast, bare silica strongly depends on pH (cf. Figure 3.5b; black markers), yet PAMAM-covered silica exhibits a similar sigmoidal trend as mica. The modified Grahame equation[27] was used to convert ζ (Figure 3.5a,b) into σ and, in turn, into the effective charge Z_{eff} of adsorbed PAMAM dendrimers for mica and silica (Figure 3.5c,d)[28-31].

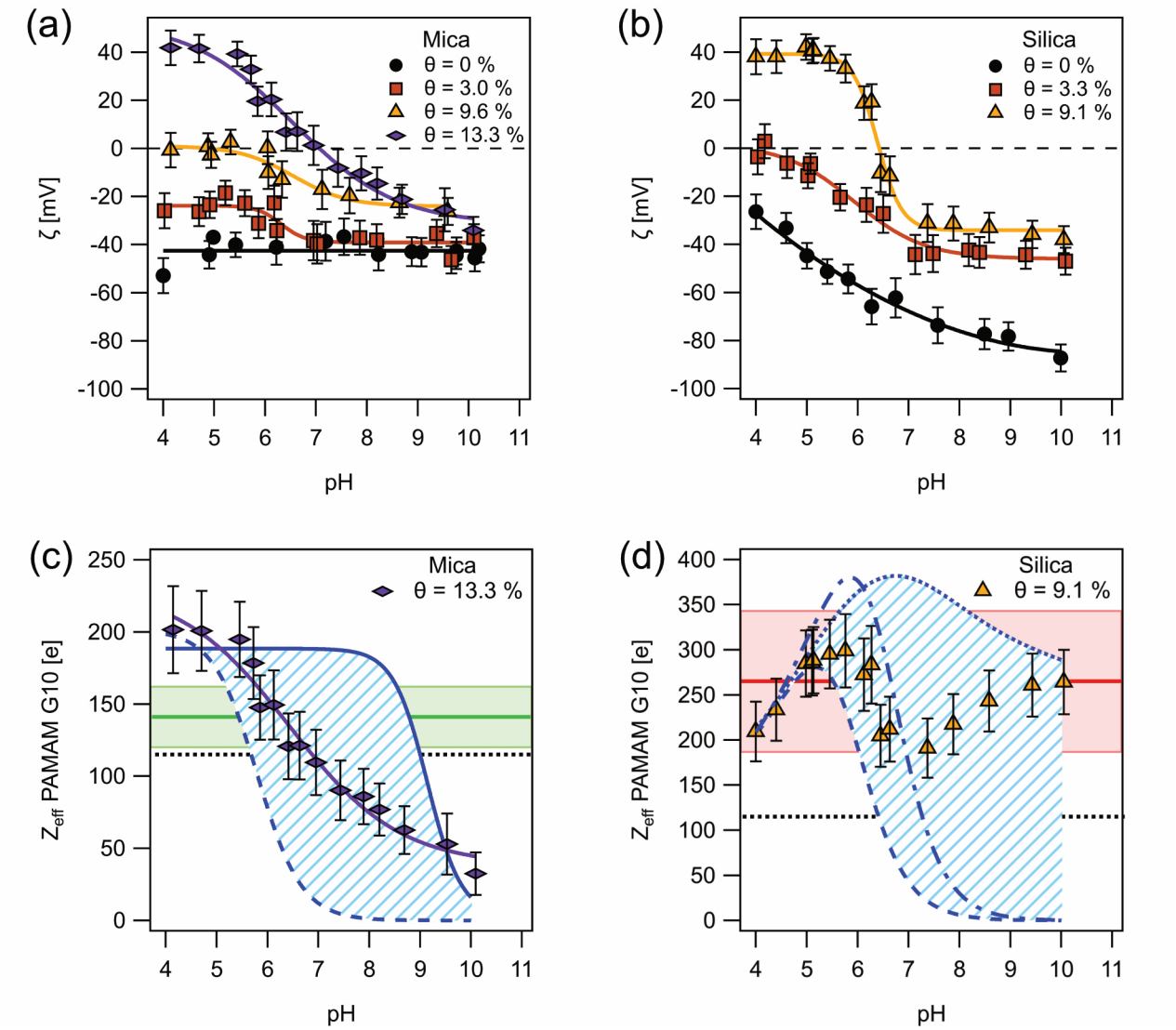

Figure 3.5: Zeta-potential ζ versus pH for bare and PAMAM-covered (a) mica and (b) fused silica. (c) Calculated effective charge Z_{eff} of single PAMAM G10 dendrimers on mica as a function of pH. Blue lines represent different theoretical calculations to describe the experimental trends lying in between a protonation equilibrium (dashed line) and normalized effective charges of PAMAM in solution[28] (solid line) (d) Calculated effective charge Z_{eff} of single PAMAM G10 dendrimers on silica as a function of pH. Dashed and broken blue lines represent two different protonation equilibria combined with the purple sigmoidal fit in (c). The dotted curve was calculated from the purple sigmoidal fit in (c) combined with Z_{eff} from the mean-field approach[32]. Black dotted lines represent the mean-field Z_{eff} in solution. Colored shaded areas represent mean Z_{eff} from various θ with standard deviations. Experimental Z_{eff} were calculated only for the highest surface coverages. Adapted with permission from Engelhardt et al., *Journal of Colloid and Interface Science*, **2025**, 686, 852-863, © 2025 Elsevier B.V.

On mica (Figure 3.5c), Z_{eff} follows a sigmoidal trend, falling between the Henderson-Hasselbalch model (pK = 5.8, dashed blue line) and the normalized electrophoretic mobility-based charge from Michna et al.[28] (solid blue line). Their data confirm the mean-field approach's limitations[32] and, in turn, indicate the substrate's influence on Z_{eff} in our data. On silica (Figure 3.5d), Z_{eff}(pH) behaves more complexly, showing slight oscillations in the basic pH range rather than a sharp drop, likely due to silica's charging properties increasing counterion concentration at higher pH. We incorporate the substrate's effect *via* an effective inverse Debye length κ_{eff} to approximate this. By combining κ_{eff} with

either the Henderson-Hasselbalch model (blue dashed pK = 5.8, blue broken pK = 6.5) or a mean-field approach using mica's sigmoidal fit (dotted blue line, Figure 3.5c), the overall Z_{eff} trend on silica is roughly described.

This study demonstrated that the often-assumed superposition of charge from the substrate and adsorbed polyelectrolytes is surprisingly accurate. The streaming potential technique proved highly versatile in capturing these interactions, providing a sensitive and reliable determination of the zeta-potential ζ across different conditions. Furthermore, the streaming potential allowed the calculation of the effective charge of the adsorbed PAMAM dendrimers from the zeta-potential of bare and polyelectrolyte-covered surfaces and the polyelectrolyte coverage. Since the effective charge influences intermolecular interaction forces, it plays a critical role in the electrostatic RSA model.

This project introduced our custom-built streaming potential analyzer and the different measurement cells to examine macromolecule adsorption. The herein utilized setup was used in the following project to extend this technique to characterize the surface acidity of catalyst support materials and their impact on catalytic performance. Specifically, we investigated thin films of oxide catalyst carriers. We used streaming potential measurements to link the surface acidity to the size distribution of Ga droplets in a liquid metal catalyst system.

3.2.2 Preparation of geometrically highly controlled Ga particle arrays on quasi-planar nanostructured surfaces as a SCALMS model system

This project utilized the streaming potential technique and the custom-built analyzer presented in the previous study, using our parallel plate cell. Here, we collaborated to extend its application to characterize the surface acidity of catalyst support materials and their impact on catalytic performance. In this collaborative project, the group of Prof. Dr. Julien Bachmann established a new preparative route toward a model system for SCALMS on nanostructured substrates. Specifically, we focused on thin films of oxide catalyst carriers. We employed streaming potential measurements to establish a link between surface acidity and the size distribution of Ga droplets in a liquid metal catalyst system.

In the realm of catalysis, liquid metals (LM) have gathered significant attention due to their unique properties, including their existence in the liquid phase over a wide temperature range, high electric and thermal conductivity, exceptional alloy ability, and no coking deactivation. These properties make LMs appealing for catalytic applications[33]. A specific application of LMs in catalysis involves using supported catalytically active liquid metal solutions (SCALMS). SCALMS typically consist of a catalytically active element dissolved in a liquid metal placed on a porous solid substrate for easy handling. The dynamic nature of the catalyst element in the liquid matrix offers protection against deactivation and allows for simple catalyst modifications.

The presented SCALMS model system provided uniquely precise geometrical control of the Ga particle size distribution with minimized oxide layer formation of the Ga LM particles. Electrochemical anodization was used to nanostructure aluminum (Al)-based substrates[34-36]. The highly ordered substrates were then functionalized with distinct metal oxide coatings (SiO_2, TiO_2, Al_2O_3, or MgO) using atomic layer deposition (ALD) and spin-coating of a Ga precursor. Heating caused the thermal decomposition of the Ga complex, resulting in the formation of Ga particles on the nanostructured surface. Since SiO_2 treatments are well established in SCALMS systems[37], we focused on these interfaces first. Figure 3.6 shows SEM images of Ga droplets on SiO_2-coated substrates.

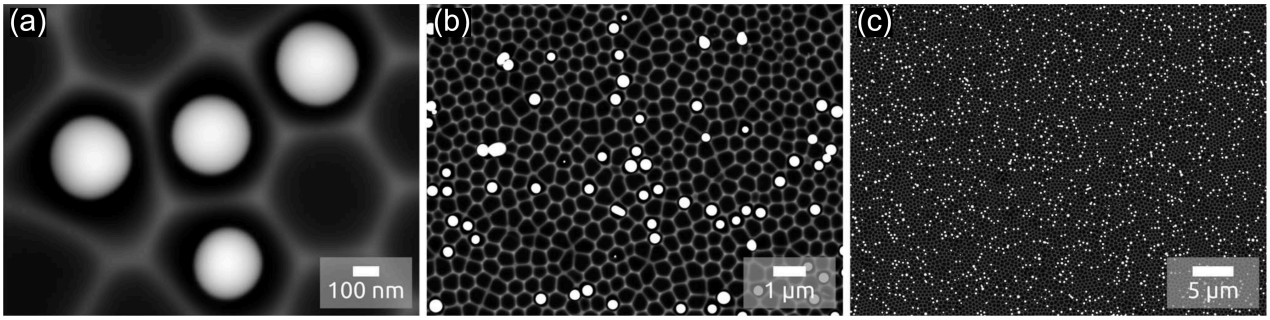

Figure 3.6: SEM micrographs (a-c) with decreasing magnifications, captured using a backscattered electron detector to enhance material contrast. The micrographs revealed the formation of Ga spheres (bright spots) on a highly ordered nanostructured substrate. This substrate, composed of hexagons with a center-to-center distance of ~450 nm and an indentation depth of ~130 nm, was pre-coated with a ~10 nm silica film via ALD. Adapted with permission from Hofer et al., *RSC Advances*, **2023**, 13, 4011-4018, © 2023 The Royal Society of Chemistry.

The high-magnification SEM micrograph (Fig. 3.6a) revealed the distinct separation of Ga spheres formed within the individual indentations of the nanostructured substrate. This separation, driven by dewetting forces, prevented the coalescence of the Ga spheres in a liquid state above their melting point. The lower magnification images (Fig. 3.6b,c) provided a broader view, demonstrating the homogeneous distribution of these Ga spheres across the substrate. Figure 3.6 proved strong control over Ga particle sizes and distribution with SiO_2-coated substrates. Shifting the focus from SiO_2 to a broader range of surface coatings, Figure 3.7 shows SEM micrographs of Ga particles on different metal oxide-coated surfaces.

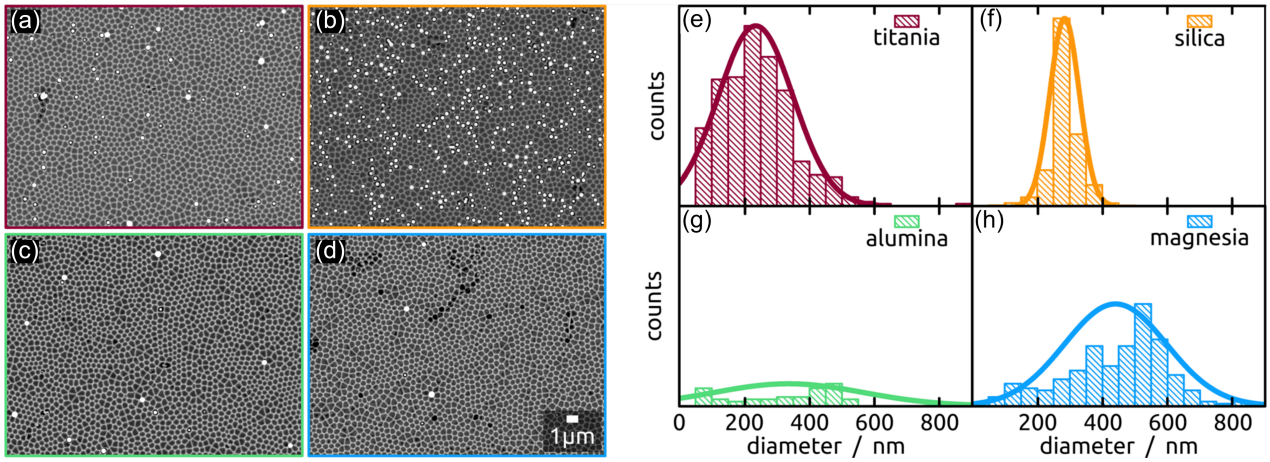

Figure 3.7: (a-d) SEM micrographs reveal the morphology of Ga particles formed on nanostructured substrates coated with different metal oxide thin films by ALD. The brighter Ga particles are clearly visible against the darker substrates. (e-h) Corresponding histograms display the diameter distributions of the Ga particles, with normal distribution fits, highlighting the impact of the different metal oxide coatings on particle size and homogeneity. Each substrate was coated with a distinct metal oxide thin film using ALD: (a,e) TiO_2, (b,e) SiO_2, (c,g) Al_2O_3, and (d,h) MgO. Adapted with permission from Hofer et al., *RSC Advances*, **2023**, 13, 4011-4018, © 2023 The Royal Society of Chemistry.

Analysis of the SEM micrographs (Fig. 3.7) revealed a correlation between the average Ga particle diameter and the underlying metal oxide coating. Substrates coated with TiO_2 (Fig. 3.7a,e) and SiO_2 (Fig. 3.7b,f) exhibited the smallest average Ga particle diameters while showing narrow size distributions. In contrast, substrates coated with Al_2O_3 and MgO (Fig. 3.7c,g and 3.7d,h) yield larger Ga particles and broad distributions. This observation suggested that surface acidity plays a significant role in controlling the size and distribution of Ga particles. Furthermore, an increasing number of catalysis literature highlighted that even in redox catalysis, relevance is attributed to the redox-active noble metal and the acid–base interaction with the underlying oxide substrate[38, 39]. To investigate the influence of the oxide support on the Ga particle formation, we employed streaming potential measurements to determine the isoelectric point (IEP) of various metal oxides. The IEP, where the zeta-potential ζ is zero, provides insight into the surface acidity of the material[40]. Thin layers of the water-insoluble TiO_2, SiO_2, and Al_2O_3 were deployed on muscovite mica substrates, respectively. These substrates were investigated with our custom-made streaming potential analyzer and the parallel plate cell (cf. Chapter 3.2.1). Figure 3.8 shows the zeta-potential ζ as a function of the pH for three different metal oxides stable in acidic aqueous solutions.

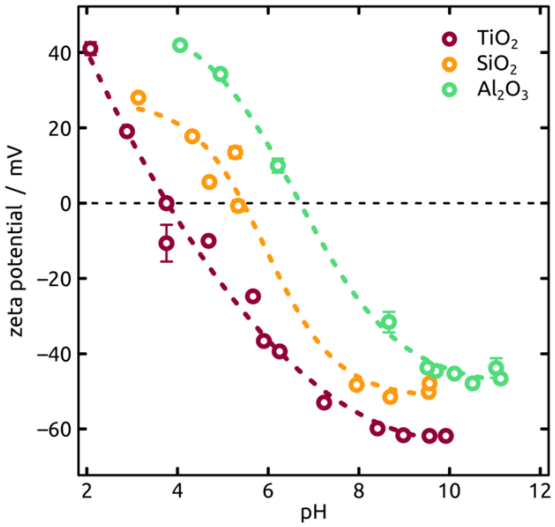

Figure 3.8: Determination of the IEP (intersection of colored dashed lines with the dashed black line) from streaming potential measurements of various metal oxides. The metal oxides were deposited on mica sheets. The streaming potential measurements were conducted at an ionic strength of 10 mM KCl as a function of the pH. Adapted with permission from Hofer et al., *RSC Advances*, **2023**, 13, 4011-4018, © 2023 The Royal Society of Chemistry.

The streaming potential measurements revealed TiO_2 as the most acidic coating with an IEP at < pH 4, followed by SiO_2 with an IEP < pH 6, and Al_2O_3 at an IEP < pH 7. Typically, SiO_2 interfaces are considered more acidic than TiO_2[40]. However, the zeta-potential is very sensitive to surface impurities[40]. The SiO_2 layer generated by ALD may contain residues of the basic (3-aminopropyl)triethoxysilane precursor[41, 42], counteracting the strongly acidic nature of SiO_2 interfaces. The IEPs of the oxides were correlated with the gallium particle diameters, diameter distribution, and particle densities in Figure 3.9. The corresponding data was gained from scanning electron microscopy (SEM) images.

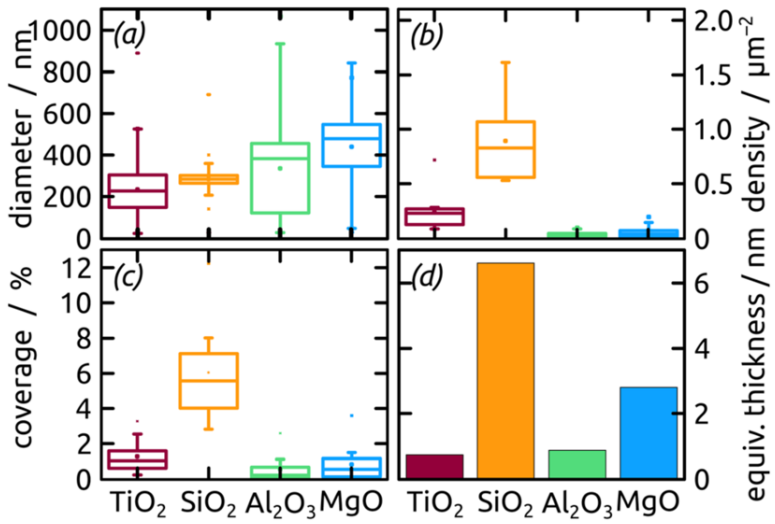

Figure 3.9: Box–whisker plots illustrating the (a) particle diameter, (b) particle density, (c) coverage distribution, and (d) equivalent thickness of Ga droplets on various metal oxides with distinct surface chemistries. Adapted with permission from Hofer et al., *RSC Advances*, **2023**, 13, 4011-4018, © 2023 The Royal Society of Chemistry.

The results in Figures 3.8 and 3.9 indicated that the most acidic oxides, TiO_2 and SiO_2, yielded the smallest average diameters, followed by the amphoteric Al_2O_3 and the basic MgO. Notably, SiO_2 exhibited the narrowest size distribution and highest particle density. SiO_2 appeared to be the most suitable surface for achieving highly controlled geometries of Ga particles. The preparative methods of this flexible model system can be further optimized, allowing the system to be tailored to specific applications with different noble metal catalysts employed.

In summary, this study demonstrates the significant influence of surface acidity on the size and distribution of Ga particles in a SCALMS model system. By employing our custom streaming potential setup, we established a clear correlation between the isoelectric point of the metal oxide coating and the resulting Ga particle characteristics. This knowledge can be leveraged to design and optimize catalysts with enhanced performance by tailoring the surface acidity of the support material. Building on this understanding of how surface properties influence the formation of liquid metal particles, we next investigated the role of the surface charge in optimizing particle loading within a porous aluminum oxide framework for catalyst carrier development.

3.2.3 Preparation and Surface Functionalization of a Tunable Porous System Featuring Stacked Spheres in Cylindrical Pores

This project further extended the application of electrokinetic measurements, specifically streaming current measurements, to optimize catalyst carrier development. Building upon the insights gained from previous projects, we focused on optimizing particle loading within a porous AAO framework. This framework is crucial for creating high-surface-area catalyst carriers, as the design of geometry and morphology in nanostructured surfaces plays a critical role in various applications, including catalysis, drug delivery, and environmental technologies[43, 44]. Tailored engineering of geometrical parameters in porous systems with precisely controlled sizes and shapes allows for optimizing functional performance[45-47]. This geometric precision is particularly significant in catalysis and electrocatalysis, where the available surface area directly influences chemical and electrochemical turnover rates. To understand the parameters of optimal loading, i.e. maximum stacking of sacrificial particles, within this framework, we used streaming current measurements of planar samples of HfO_2 and ZnO thin films, representing the intended pore wall coatings. We conducted these experiments with our custom-built streaming potential setup and the asymmetric cell (cf. Chapter 3.2.1). The measurements helped us understand how the surface charge influences the stacking of sacrificial polystyrene nanospheres in the pores, ultimately aiming to improve particle stacking and enhance catalytic performance by increasing the surface area.

The manufacturing process started with parallel AAO tubes generated by anodization techniques[34-36]. These tubes are characterized by their high structural uniformity and abrupt pore diameter transitions, which were confirmed by SEM imaging (cf. Fig. 3.10).

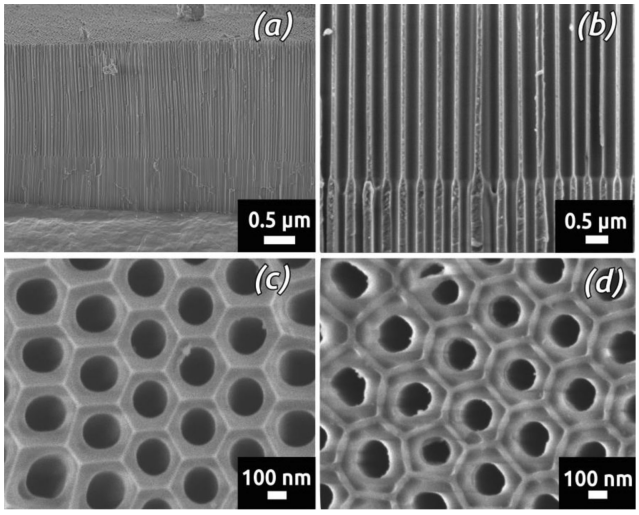

Figure 3.10: SEM micrographs (a-d) reveal the highly ordered, tunable porous system with segmented pores fabricated through anodization. Cross-sectional views (a, b) highlight the sharp transition between pore segments with distinct diameters. Face views (c, d) showcase the well-defined pore openings, demonstrating the precision and control achieved in the fabrication process. Adapted with permission from Ruiz M et al., *Advanced Materials Interfaces*, **2023**, 10, 2300436, © 2023 WILEY-VCH Verlag GmbH & Co. KGaA.

The porous AAO framework was filled with sacrificial polystyrene (PS) spheres. The assembly process focused on maximizing the packing density of PS spheres to achieve the highest porosity in the final

product. A systematic optimization involving flow rates, suspension concentrations, and flow durations revealed that high flow rates yielded denser assemblies, while excessively high sphere concentrations led to clogging. To further improve the stacking density, surface functionalizations of the AAO pores with ZnO, HfO_2, (3-aminopropyl)triethoxysilane (APTES), and hexamethyldisilazane (HMDS) were tested. Particle-loaded pores were covered with a thin film of electrically conductive ZnO to retain the arrangement and reduce charging effects during SEM studies. SEM imaging and energy-dispersive X-ray spectroscopy (EDX) analysis were performed on cross-sections of metal oxide-covered filled pores to evaluate the particle loading, as shown in Figure 3.11.

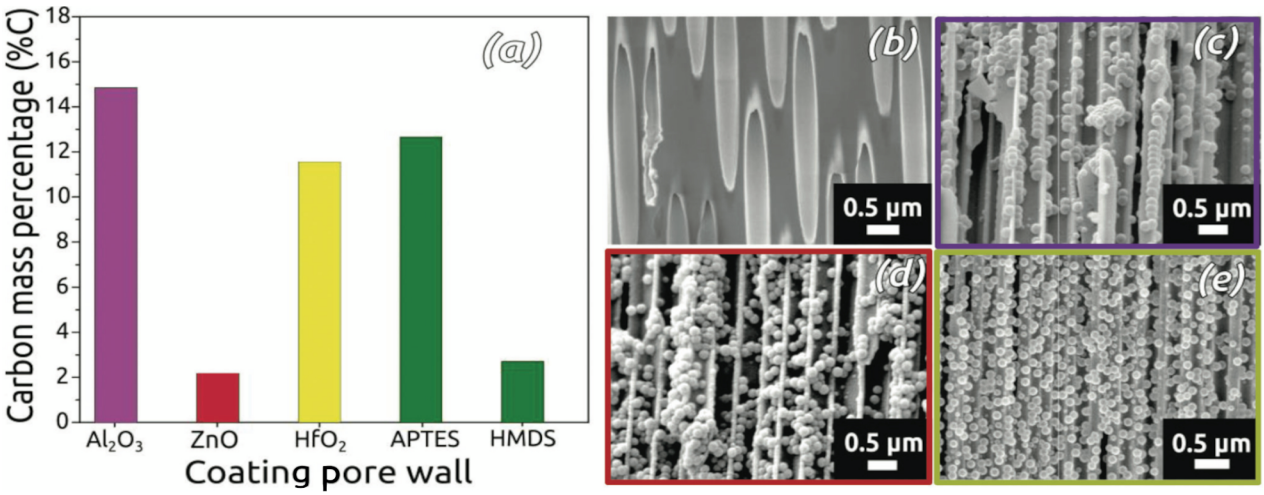

Figure 3.11: (a) Quantification of carbon mass percentage (%C) across different surface-functionalized porous systems using EDX to rate the particle loading. SEM provided detailed visualization of surface-functionalized porous structures: (b) pores coated with a layer of HfO_2 and (c-e) the arrangement of polystyrene (PS) sphere templates following deposition of a ZnO layer *via* atomic layer deposition (ALD) and subsequent thermal treatment at 450 °C. The configurations observed included PS spheres directly assembled within pores with (c) no coating and modified with coatings of (d) ZnO and (e) HfO_2. Adapted with permission from Ruiz M et al., *Advanced Materials Interfaces*, **2023**, 10, 2300436, © 2023 WILEY-VCH Verlag GmbH & Co. KGaA.

EDX results (cf. Fig. 3.11a) show the carbon content and, thus, the particle loading within the pores. For comparison, (b) shows HfO_2-coated pores before treatment with PS spheres. EDX studies revealed high PS loadings for (c) bare Al_2O_3 pore walls, (e) HfO_2, and APTES coatings. In contrast, (d) ZnO and HMDS modifications lead to low stacking densities. Rendering the pore walls hydrophobic with HMDS was clearly detrimental to the stacking density. However, the influence of hydrophilicity alone does not explain the low particle concentration within ZnO-coated pores. To address this question, we adapted our custom-built streaming potential analyzer to fit silicon wafer pieces, using the asymmetric cell. The silicon pieces were coated with HfO_2 and ZnO, respectively, to study the surface charge at various pH values and determine the acidity of the interfaces. Here, we used the streaming current technique because of the electrically conductive nature of the employed ALD coatings. Calculating the zeta-potential ζ from the streaming current does not demand information about the electrical conductivity of the sample[48]. The zeta-potential was then presented as a function of the pH value to determine the IEP in Figure 3.12.

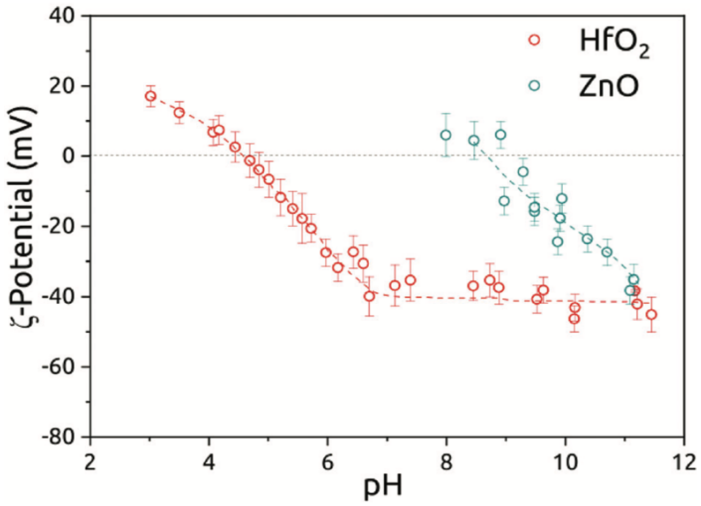

Figure 3.12: Zeta-potential ζ as a function of the pH for HfO2 and ZnO coated silicon wafer pieces. The overall ionic strength was 10 mM in KCl. No zeta-potentials of ZnO are shown below pH 8 due to dissolving ZnO layers. Adapted with permission from Ruiz M et al., *Advanced Materials Interfaces*, **2023**, 10, 2300436, © 2023 WILEY-VCH Verlag GmbH & Co. KGaA.

The IEP is a useful indicator in understanding the surface acidity of materials. It represents the pH at which the zeta-potential is zero, providing insights into the material's electrostatic behavior and its interaction with charged species in solution[40]. Electrokinetic measurements (cf. Fig. 3.12) showed a negative ζ for HfO_2 at neutral pH, which facilitated the effective stacking of spheres due to repulsion between HfO_2 and the PS spheres. In contrast, ZnO's positive zeta-potential at close-to-neutral pH induced electrostatic attraction with the PS spheres, resulting in disordered packing by adsorption to the pore walls. ZnO dissolved from the silicon wafer at pH < 8. The results highlighted that HfO_2 coatings provided optimal sphere packing, attributable to reduced adhesion and improved suspension flow through the pores.

To analyze the impact of optimized particle loading on the catalytic performance of the fabricated systems, krypton adsorption experiments and electrochemical impedance spectroscopy (EIS) were used. Krypton adsorption revealed a significant increase in specific surface area for systems with PS spheres compared to those with smooth pores, highlighting the contribution of the stacked spheres to increased surface area. After decorating the porous systems with platinum (Pt), EIS measurements further demonstrated the functional consequences of this enhanced surface area with lower charge transfer resistance for densely packed systems, indicating improved catalytic efficiency. These findings underscore the importance of optimizing particle loading in porous systems to enhance catalytic performance.

This project showed the fabrication of tunable porous systems with enhanced surface areas. We successfully created high-performance electrocatalytic substrates by assembling polystyrene spheres within a porous AAO framework and optimizing parameters like flow rate and sphere concentration. This achievement was guided by streaming current measurements, which allowed us to understand and control the surface charge's influence on particle loading. The resulting systems demonstrated improved catalytic efficiency, highlighting the effectiveness of the presented approach. This study

underscores the power of combining electrokinetic characterization with materials design to develop nanostructured materials with tailored properties and enhanced performance.

While this work and the preceding projects primarily focused on materials science applications of electrokinetic techniques, the fourth project broadened the scope to environmental science. This subsequent study utilized the streaming potential to investigate the surface charge of various microplastic particles, demonstrating the technique's versatility in characterizing granular samples.

3.2.4 Following Changes at the Solid/Liquid Interface for Large Microplastic Particles by Streaming Potential

Microplastic particles (MPP) have been identified as significant environmental contaminants due to their widespread distribution across diverse ecosystems[49-55]. Their heterogeneity in composition and size necessitates advanced analytical methods for characterization[56-58]. In this project, we shifted our focus from planar surfaces to explore the versatility of the streaming potential technique in characterizing the surface chemistry of large microplastic particles. This study addressed an analytical gap in the characterization of microplastics, since conventional methods are best suited for either nanoparticles or macroscopic objects. This study demonstrated the applicability of streaming potential measurements to assess the interfacial properties of larger microplastic fractions, typically those larger than 15 µm in diameter. This approach enabled examining large, immobile particles, including those derived from fragmentation processes, which generated size fractions comparable to environmental samples. By characterizing the surface charge and acidity of these microplastic particles, we gained valuable insights into their behavior and interactions within environmental matrices.

In general, most microplastics research has focused on particles ranging from 50 µm to 1 mm in diameter, as these sizes are easy to isolate from environmental samples[56-60]. Smaller particles, particularly those below 5 µm, are often studied for colloidal properties using spherical model particles[57, 61-64]. Classical techniques such as Fourier transform infrared (FTIR) spectroscopy[56, 57], Raman spectroscopy[56, 57, 65], scanning electron microscopy (SEM) with energy-dispersive X-ray spectroscopy (EDX)[56, 57, 66], and nuclear magnetic resonance (NMR) spectroscopy[65-67] have been widely employed to investigate MPPs at the molecular level. However, the diffuse layer influencing MPP interactions within environmental matrices remain less comprehensively explored[51, 68-71].

Streaming potential measurements were utilized to assess the interfacial properties of larger MPP fractions. The methodology enables the examination of large, immobile particles. This permits the study of MPPs derived from milling processes, which generate size fractions comparable to environmental samples [67, 72-76]. The reliability of this approach has been validated by evaluating milled polystyrene particles across a size range of 15 µm to 250 µm. The size distribution, shape, and topography of these milled, i.e., fragmented, MPPs are presented in Figure 3.13.

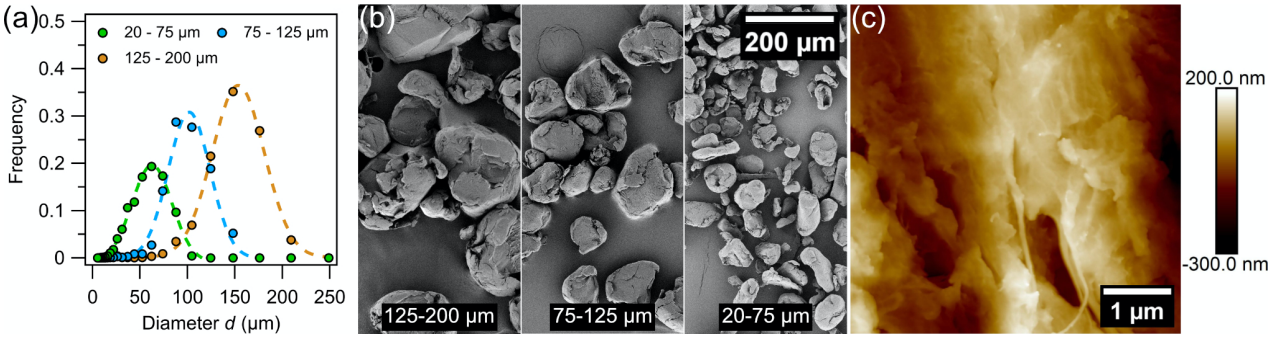

Figure 3.13: Morphological and dimensional analysis of fragmented polystyrene microplastic particles. (a) Particle size distributions of distinct size fractions *via* laser diffraction. (b) Representative SEM images of particles illustrating three different size fractions. (c) High-resolution (5 x 5) µm² AFM scan of a particle within the 125 - 200 µm fraction. Adapted with permission from Engelhardt et al., *Chemistry-Methods*, **2025**, 5(12), e202500102, © 2025 Wiley-VCH.

The size fractions (cf. Fig. 3.13a) showed broad, partially overlapping size distributions, corroborated by SEM imaging (Fig. 3.13b). The smallest fraction contained more elongated fragments, and milling introduced considerable nanoscale roughness (Fig. 3.13c). Building on particle morphology and size distribution, we investigated the surface charge properties of these large microplastic fractions using streaming potential measurements to assess their interfacial properties. A schematic and photograph of the particle plug streaming potential cell are shown in Figure 3.14.

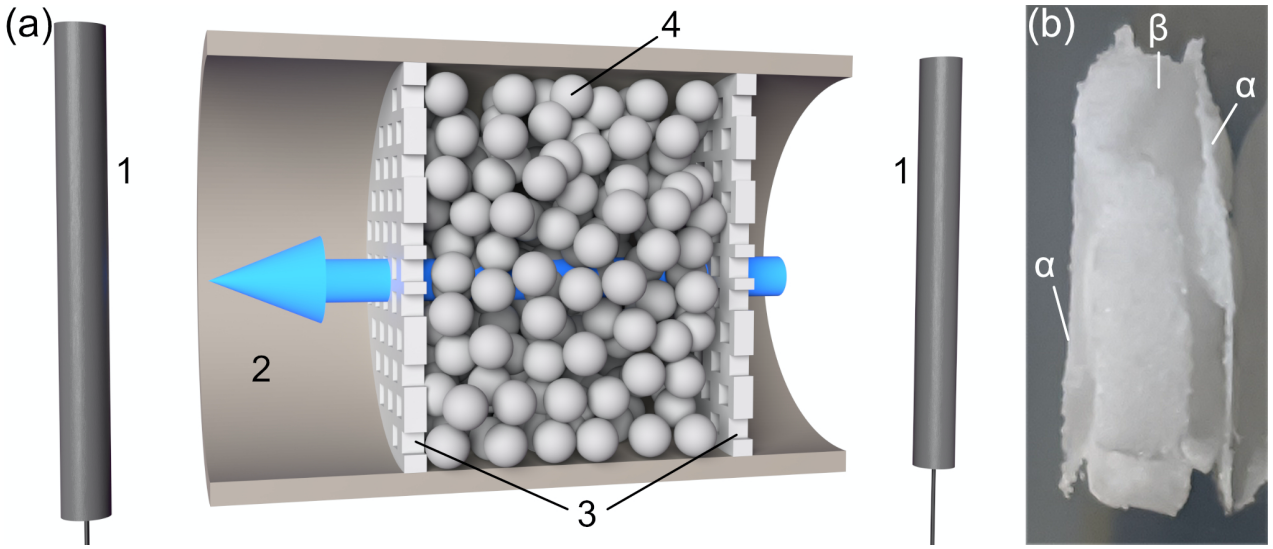

Figure 3.14: Illustration of the particle plug cell utilized for streaming potential measurements (a). The cell consists of two Ag/AgCl electrodes (1) to measure the streaming potential, a cylindrical body (2) fabricated from polyether ether ketone (PEEK), which encapsulates a particle bed (4) comprising randomly packed microplastic particles. The particle bed is retained by two PA-6,6 filter mats (3). A photograph of a representative particle plug, following streaming potential measurements, is also shown (b). The PA-6,6 filter mats (α) surrounding the plug and the microplastic particles (β) forming the particle bed are clearly visible, demonstrating the integrity of the particle plug after measurement. The particle plug was 1 cm wide and approximately 3 mm tall. Adapted with permission from Engelhardt et al., *Chemistry-Methods*, **2025**, 5(12), e202500102, © 2025 Wiley-VCH.

The setup illustrated in Figure 3.14 was used to study the effects of mechanochemical processing on the surface properties of fragmented polystyrene microparticles. Thus, Figure 3.15 shows ζ of the three different size fractions (cf. Fig. 3.13) as a function of the pH.

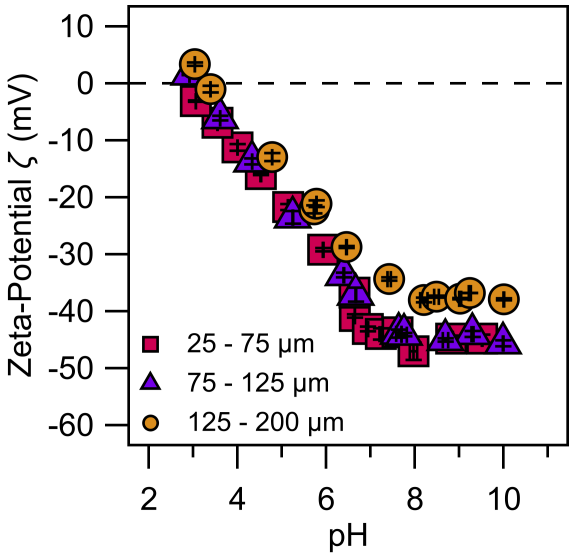

Figure 3.15: Zeta-potential ζ measurements as a function of the pH for fragmented polystyrene microparticles with varying size ranges. All measurements were conducted at a constant ionic strength of 10 mM KCl. The isoelectric point, where the net surface charge is zero, is indicated by a dashed line. Adapted with permission from Engelhardt et al., *Chemistry-Methods*, **2025**, 5(12), e202500102, © 2025 Wiley-VCH.

Measurements of ζ revealed an isoelectric point (IEP) between pH 3 and 4 across all size fractions. Smaller fractions exhibited marginally more acidic behavior, probably due to an increased number of functional groups produced by milling. Furthermore, we investigated the influence of artificial weathering on the surface charges of these types of MPPs. The artificial weathering of an aqueous suspension of fragmented PS particles, with a size fraction of 125 to 200 µm, was conducted through a combination of stirring and intense UV irradiation. This investigation utilized samples that had been previously characterized by Meides et al. [66] using a range of analytical techniques, including SEM-EDX, laser diffraction, and NMR spectroscopy. They reported the generation of oxygen-based functional groups due to aging by NMR and SEM-EDX analyses. Functional groups such as carboxylic acids were identified at the interface of these particles. To complement these existing analyses, we incorporated streaming potential measurements into the experimental protocol, thereby enabling the assessment of the diffuse layer properties and providing a more comprehensive understanding of the surface chemistry of the weathered microplastic particles. Figure 3.16 shows the effects of artificial weathering on ζ and the size distribution of fragmented MPPs.

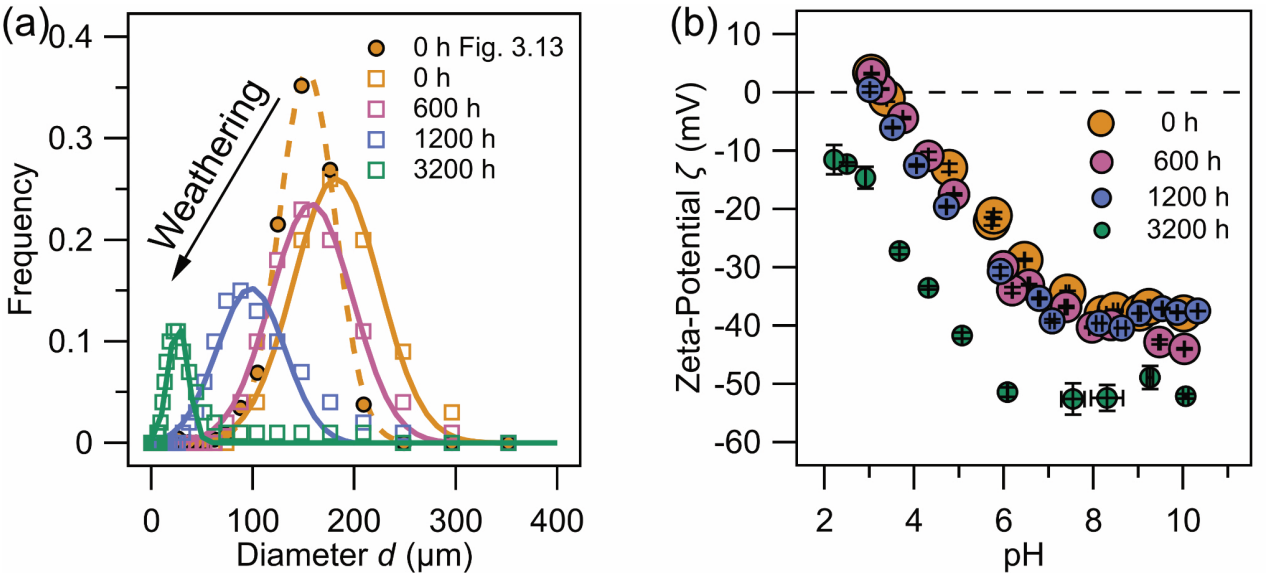

Figure 3.16: (a) Comparison of particle size distributions determined by laser diffraction, contrasting weathered microparticles (solid lines, open data points; data from Meides et al. [66]) with their unweathered (0 h) counterparts shown in Figure 3.13 (dashed line, solid data points). (b) The effect of the pH on the zeta-potential ζ of weathered fragmented microplastics, measured at a constant ionic strength of 10 mM in KCl. Adapted with permission from Engelhardt et al., *Chemistry-Methods*, **2025**, 5(12), e202500102, © 2025 Wiley-VCH.

Prolonged weathering resulted in smaller and more irregularly shaped particles, thereby increasing the surface area (cf. Fig. 3.16a) and, in turn, enhancing reactivity. Extended exposure to simulated sunlight and aqueous conditions resulted in significant changes in the zeta-potential vs pH profiles, with more acidic behavior observed after prolonged weathering (cf. Fig. 3.16b). Comparisons between pristine and weathered MPPs highlighted the progression of surface changes. The interplay between size reduction, increasing numbers of functional groups, and surface roughness was emphasized as a likely critical factor influencing MPP interactions with natural organic matter and soil components. The insights gained from streaming potential measurements complement molecular-level analyses, providing a holistic understanding of MPP behavior under environmental conditions.

This study demonstrated the applicability of streaming potential measurements for characterizing large MPPs, addressing a significant gap in currently used analytical capabilities. The technique's ability to evaluate surface charge properties and their development during aging processes established its utility in environmental research. However, it is recognized that particle systems in the environment were often of colloidal length scales, necessitating the study of smaller particles.

In contrast to the prior focus on planar interfaces and larger particles using streaming potential, research project 5 extended the investigation of electrokinetic phenomena to the nanoscale, specifically nanoparticle aggregates, which are also environmentally relevant. Due to the limitations of the streaming potential for these systems, we employed electrophoretic light scattering to determine how the size of primary fumed silica particles and the aggregates they form influence their electrokinetic behavior. This approach provides valuable insights into the fate and transport of nanoparticles in the environment, contributing to a more comprehensive understanding of environmental pollution and its impact on ecosystems.

Electrophoretic Light Scattering

Since the discovery of electrophoresis over 200 years ago[77], various technical developments have led to the emergence of electrophoretic light scattering (ELS) as a cornerstone technique for characterizing the electrokinetic properties of colloidal dispersions[78, 79]. Generally, ELS measurements involve applying an electric field to a dispersion, causing charged particles to migrate. The velocity of these particles, which is directly related to their electrophoretic mobility, is then determined by analyzing the Doppler shift of scattered laser light. This approach facilitates the quantitative determination of the zeta-potential ζ and the electrophoretic mobility, providing critical insights into diverse applications, including nanoparticle stability[80] and biopharmaceutical characterization[79].

To explore the electrokinetic behavior of nanoparticle aggregates, a system not accessible by streaming potential measurements, we utilized the ELS described above. This technique allowed us to systematically investigate the influence of primary particle and aggregate size on the electrophoretic mobility.

3.2.5 Electrophoretic Mobility of Nanoparticle Aggregates: Independence from Aggregate Size

Current methods for calculating ζ from the electrophoretic mobility often oversimplify the behavior of aggregates found in real-world systems. The influence of aggregate size on the mobility remains largely unexplored. While various approximations allow for a direct connection between mobility and the zeta-potential ζ for single particles[79, 81-86], this correlation becomes more complex for aggregates. We approached this challenge using two types of fumed silica, each with a unique primary particle diameter, to engineer additive-free aggregates of controlled sizes for mobility measurements.

Firstly, the aggregate morphology and the differences in primary particle size were studied with scanning transmission electron microscopy (TEM). Figure 3.17 presents representative TEM images of Aerosil 50 (cf. Fig. 3.17a) and Aerosil 200 (cf. Fig. 3.17b) aggregates, revealing distinct structural characteristics. Fumed silica aggregates comprise smaller primary particles (PP) that form an irregular fractal-like structure. These PPs are generally spherical in shape, although some may have indistinct boundaries with neighboring particles. The observations from TEM images suggested that Aerosil 50 primary particles have larger diameters than those of Aerosil 200. Moreover, the diameters of the Aerosil 50 aggregates were larger than those of Aerosil 200.

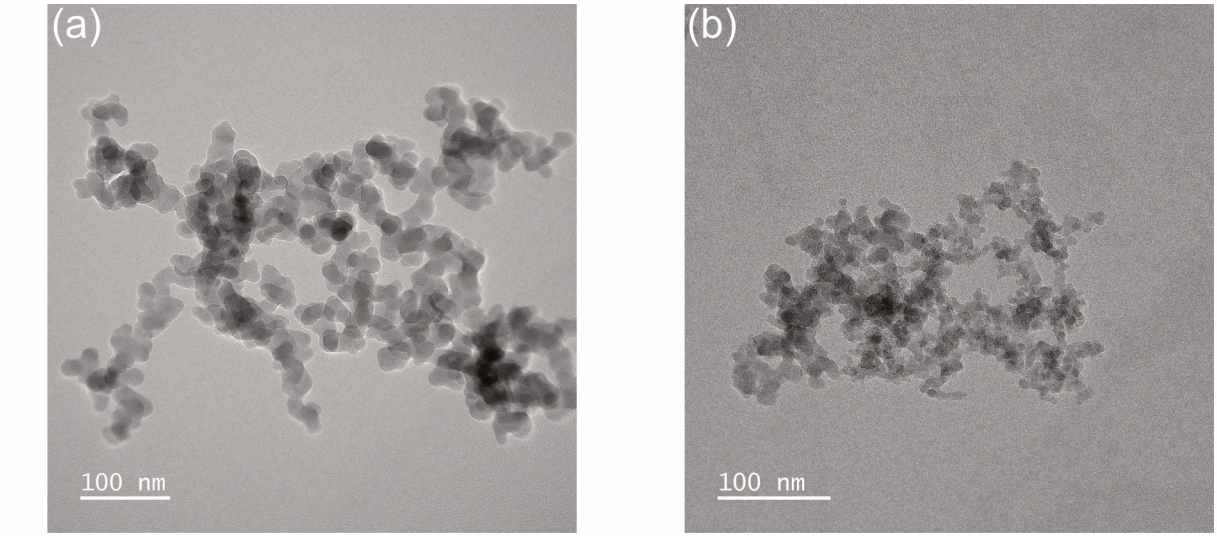

Figure 3.17: Transmission electron microscopy images of (a) Aerosil 50 and (b) Aerosil 200 aggregates, respectively. Adapted with permission from Engelhardt et al., *Colloids and Surfaces A: Physicochemical and Engineering Aspects*, **2024**, 703, Part 1, 135244, © 2024 Elsevier B.V.

Primary particle diameter d_{pp} evaluations from TEM images with the software ImageJ[87] resulted in diameters of (24.9 ± 0.5) nm for Aerosil 50 and (10.8 ± 0.2) nm for Aerosil 200, respectively. In contrast, dynamic light scattering experiments with aggregate concentrations of 0.1 wt% yielded hydrodynamic diameters d_H of (328.2 ± 4.6) nm and (184.3 ± 1.0) nm, respectively. Electrophoretic mobility measurements were also conducted at an aggregate concentration of 0.1 wt% to study the electrokinetic behavior at salt concentrations between 1 mM and 10 mM of both Aerosil types. Figure 3.18 shows the electrophoretic mobility as a function of the KCl concentration at acidic and alkaline pH values.

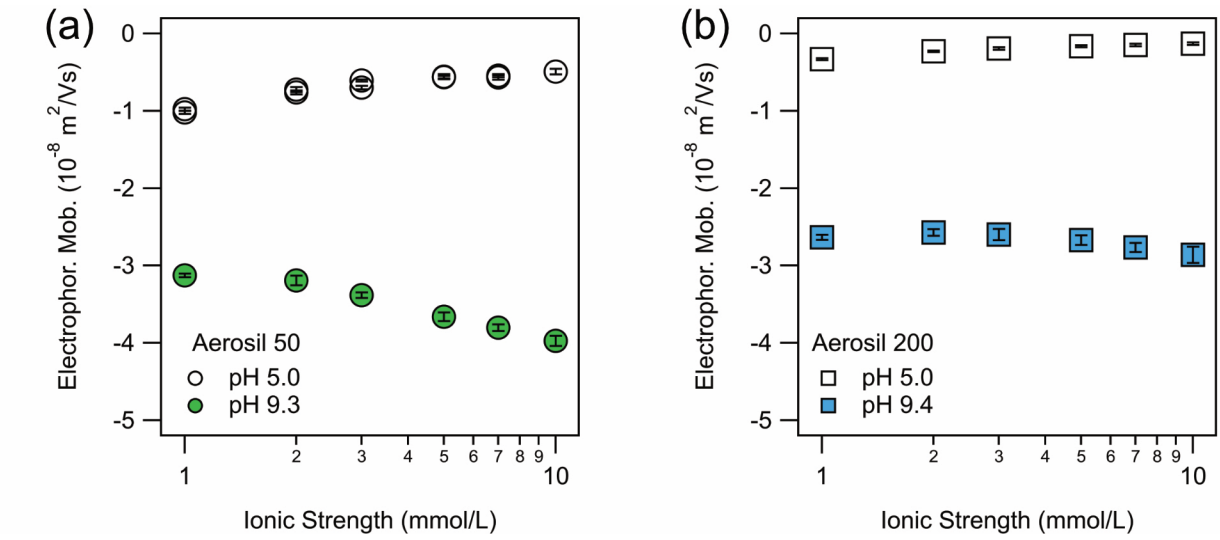

Figure 3.18: Electrophoretic mobilities as functions of the ionic strength of (a) Aerosil 50 and (b) Aerosil 200 in KCl. The particle concentration was 0.1 wt%. Adapted with permission from Engelhardt et al., *Colloids and Surfaces A: Physicochemical and Engineering Aspects*, **2024**, 703, Part 1, 135244, © 2024 Elsevier B.V.

A comparison of the electrophoretic mobility of aggregates of Aerosil 50 and Aerosil 200 fumed silica (cf. Fig. 3.18) revealed similar trends but distinct magnitudes. In acidic environments, increasing ionic strengths reduced the mobility, with Aerosil 50 exhibiting greater magnitudes. Alkaline conditions increased the mobility for both materials, while Aerosil 50 showed a more pronounced increase in mobility with rising ionic strength. This size-dependent behavior is consistent with the standard electrokinetic theory by O'Brien and White[88], reflecting the influence of particle size on the retardation of the electrical double layer with distinct mobility maxima[89, 90]. Based on the significant differences shown in Figure 3.18, understanding the impact of a wide pH range on electrokinetic behavior at a constant ionic strength is essential. Mobility measurements revealed differences in the electrokinetic behavior of the fumed silica types as a function of the pH (cf. Figure 3.19).

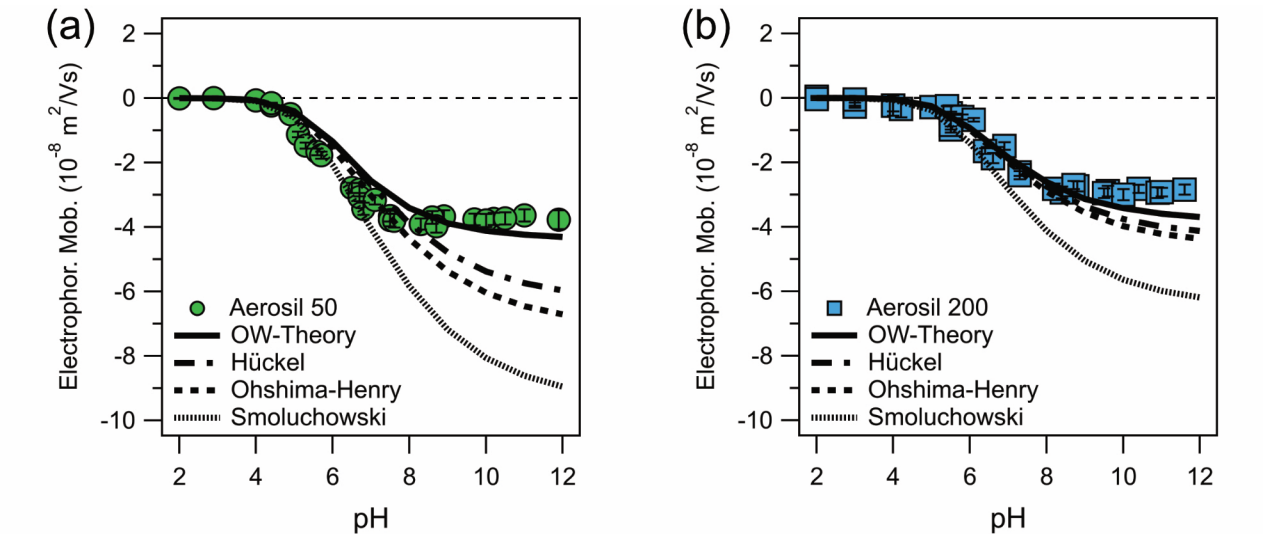

Figure 3.19: Electrophoretic mobilities as a function of the pH of (a) Aerosil 50 and (b) Aerosil 200 aggregates. The mobility was measured at an ionic strength of 10 mM in KCl. The particle concentration was 0.1 wt%. The O'Brien-White (OW) theory is depicted by a solid line, the Hückel equation by a dash-dot line, the Ohshima-Henry equation by a dashed line, and the Smoluchowski equation by a broken line. Adapted with permission from Engelhardt et al., *Colloids and Surfaces A: Physicochemical and Engineering Aspects*, **2024**, 703, Part 1, 135244, © 2024 Elsevier B.V.

Under acidic conditions (pH < 5), both Aerosil 50 (cf. Fig. 3.19a) and Aerosil 200 (cf. Fig. 3.19b) exhibited negligible mobility. However, a distinct difference in mobility emerged between the two silica types as the pH transitioned from neutral to alkaline, and the silanol groups at the interface became deprotonated. Notably, the magnitude of the mobility for Aerosil 50 displayed a steeper increase towards basic pH than Aerosil 200. This resulted in higher mobility for Aerosil 50 in the alkaline plateau than Aerosil 200.

The 1-pK basic Stern model[23, 24], which calculates the surface charge density and the diffuse layer potential as a function of the pH, ionic strength, and the site density of functional groups, and various electrokinetic theories were employed to analyze the results presented in Fig. 3.19[88, 91-93]. The O'Brien-White theory[88] effectively described the overall trend for both Aerosil types, suggesting that the mobility of fumed silica aggregates was determined by the mobility of the primary particles, influenced by double layer polarization. This observation is consistent with previous studies that have

shown the mobility of a swarm of particles to be the same as that of a single particle at low volume fractions[94-96]. The observation of distinct mobility plateaus for Aerosil 50 and Aerosil 200 in alkaline environments prompted further investigation into the relationship between the electrophoretic mobility and the aggregate size.

Various aggregate sizes were generated using chemically identical Aerosil 50 and Aerosil 200 powders. We carefully controlled the aggregation process by combining centrifugation and high ionic strengths without using surfactants or additives to preserve the inherent surface chemistry of the materials. Figure 3.20 shows the relationship between the mobility of distinct Aerosil types over a wide range of hydrodynamic diameters.

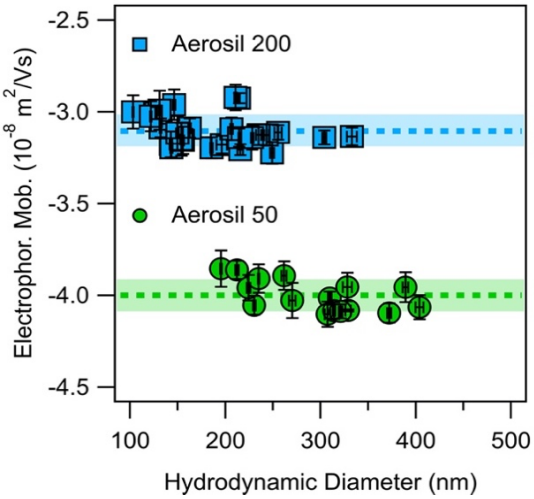

Figure 3.20: Electrophoretic mobilities of Aerosil 50 and Aerosil 200 aggregates of various hydrodynamic diameters. The ionic strength was set to 10 mM in KCl and the measurements were conducted in the alkaline mobility plateau. Mean mobility values are indicated by dashed lines, with the shaded regions representing the corresponding standard deviations. Adapted with permission from Engelhardt et al., *Colloids and Surfaces A: Physicochemical and Engineering Aspects*, **2024**, 703, Part 1, 135244, © 2024 Elsevier B.V.

Figure 3.20 clearly showed that the mobility is independent of the hydrodynamic diameter of the respective aggregates. This observation lead to the conclusion that the primary particle diameter was the key differentiating factor between the two Aerosil types. The dominating influence of the PP diameter was likely attributed to the weak overlap of double layers within the fractal-like structure of fumed silica. Given that colloidal aggregates generally exhibit a fractal-like structure[97], this finding can be extended to many aggregates from nanoparticles.

Controlling the aggregate size of two fumed silica types with the identical surface chemistry, Aerosil 50 and Aerosil 200, allowed the influence of both primary particle diameter and aggregate size on the electrophoretic mobility to be systematically assessed. A key finding was discovered through comprehensive electrophoretic and dynamic light scattering measurements: the primary particle diameter is the defining factor for the electrophoretic mobility of the aggregates. This discovery has significant implications, validating the application of mobility measurements near the critical coagulation concentration (CCC) even when aggregates are present and underscoring the dominant role of primary particle characteristics in colloidal systems. These findings are relevant to a broad

range of environmental systems, including organic matter-associated samples such as those arising from microplastic degradation.

3.3 Individual Contributions to Joint Publications

This thesis presents the results of five scientific publications, primarily developed through collaborative research projects. As such, numerous co-authors were involved in the research and writing processes. The specific contributions of each co-author for the joint publications are outlined below, with asterisks indicating the corresponding authors.

Chapter 4: Effective charge of high-generation PAMAM dendrimers in the adsorbed state

Matthias B. Engelhardt, Paul Markus, Nicolas Helfricht, and Georg Papastavrou*

Published in *Journal of Colloid and Interface Science*, **2025**, *686*, *852-863*

I contributed to developing the herein-presented streaming potential analyzer and designed the asymmetric streaming potential cell. I performed the sample preparation, including the adsorption experiments, and acquired and evaluated all streaming potential and AFM data presented. I partly wrote the original manuscript. Paul Markus also contributed to developing the streaming potential analyzer, designed the parallel plate streaming potential cell, and performed preliminary adsorption and streaming potential studies on muscovite mica substrates. Dr. Nicolas Helfricht supervised the development process by Paul Markus and me, assisted in the experimental design, and validated the collected data. Prof. Dr. Georg Papastavrou invented the herein presented in-house built streaming potential analyzer. He developed the presented theoretical approaches to model the effective charge of the dendrimers under consideration of the influence of the substrates. He also contributed to curating and validating the experimental results, supervised the project, and wrote, reviewed, and edited the manuscript. All authors contributed to scientific discussions and the experimental methodology.

Chapter 5: Preparation of geometrically highly controlled Ga particle arrays on quasi-planar nanostructured surfaces as a SCALMS model system

André Hofer, Nicola Taccardi, Michael Moritz, Christoph Wichmann, Sabine Hübner, Dominik Drobek, Matthias Engelhardt, Georg Papastavrou, Erdmann Spiecker, Christian Papp, Peter Wasserscheid, and Julien Bachmann*

published in *RSC Advances*, **2023**, *13*, *4011-4018*

Dr. André Hofer and Prof. Dr. Julien Bachmann conceptualized the experimental methodology. Dr. Andre Hofer developed the preparative approach. This route included nanostructuration, ALD coating, and Ga particle deposition. Specifically, this involved the anodization of aluminum, ALD of metal oxides, and spin coating. Dr. André Hofer also designed and performed the thermal decomposition route. He wrote the original manuscript. Dr. Nicola Taccardi did the Trihydridogallium(quinuclidine) synthesis. Michael Moritz performed XPS measurements. Sabine Hübner created cross-sections of the samples *via* FIB. Dominik Drobek recorded STEM micrographs and EDX maps. I performed streaming potential measurements and evaluations to study the IEP of the metal oxides. Prof. Dr. Georg Papastavrou, Prof. Dr. Erdmann Spiecker, Prof. Dr. Christian Papp, Prof. Dr. Peter Wasserscheid, and Prof. Dr. Julien Bachmann validated experimental results, supervised the project, and reviewed and edited the manuscript. All authors contributed to scientific discussions and writing the manuscript.

Chapter 6: Preparation and Surface Functionalization of a Tunable Porous System Featuring Stacked Spheres in Cylindrical Pores

Christhy V. Ruiz M., Markus Terlinden, Matthias Engelhardt, Giulia Magnabosco, Georg Papastavrou, Nicolas Vogel, Matthias Thommes, and Julien Bachmann*

published in *Advanced Materials Interfaces*, **2023**, *33(10)*, *2300436*

Dr. Christhy V. Ruiz M. and Prof. Dr. Julien Bachmann conceptualized the experimental methodology. Dr. Christhy V. Ruiz M. prepared the modified porous system and assembled polystyrene spheres within it. She functionalized the pore walls using ALD. She led the characterization of the samples, which included SEM imaging and EDX measurements. Furthermore, she conducted electrochemical impedance spectroscopy and the associated data evaluation. Markus Terlinden led the adsorption experiments and the surface area calculation for all samples using the BET method with Krypton. I contributed to this publication by measuring the streaming current of metal oxide films to determine the IEP and, thus, the acidity of the metal oxides. Dr. Giulia Magnabosco synthesized the narrowly dispersed polystyrene spheres. Prof. Dr. Georg Papastavrou, Prof. Dr. Nicolas Vogel, Prof. Dr. Matthias Thommes, and Prof. Dr. Julien Bachmann supervised the project, validated and helped interpret the data, and reviewed and edited the manuscript. All authors contributed to scientific discussions and the writing of the manuscript.

Chapter 7: Following Changes at the Solid/Liquid Interface for Large Microplastic Particles by Streaming Potential

Matthias B. Engelhardt, Daniel Wagner, Mohsen Zarebanadkouki, Nora Meides, Christian Schulbert, Martin G. J. Löder, Nicolas Helfricht, Seema Agarwal, Andrea Carminati, Peter Strohriegl, Jürgen Senker, Christian Laforsch, and Georg Papastavrou*

Published in *Chemistry-Methods,* **2025**, *5(12), e202500102*

I performed all the presented streaming potential measurements and in part the AFM measurements. I also contributed to the diameter evaluations of the particles. Furthermore, I handled the corresponding data evaluation and wrote the original manuscript. Dr. Daniel Wagner provided the fragmented particles and measured their diameters by laser diffraction. Prof. Dr. Mohsen Zarebanadkouki reconstructed and evaluated the µCT data. Dr. Nora Meides took care of the weathering experiments of the milled particles. Christian Schulbert and Dr. Martin G. J. Löder performed the µCT measurements. Dr. Nicolas Helfricht supervised the streaming potential, AFM, and SEM experiments and helped interpret the data. Prof. Dr. Georg Papastavrou developed the concept and the methodology of this project. Prof. Dr. Seema Agarwal, Prof. Dr. Andrea Carminati, Prof. Dr. Peter Strohriegl, Prof. Dr. Jürgen Senker, Prof. Dr. Christian Laforsch, and Prof. Dr. Georg Papastavrou supervised the project, contributed to data validation and interpretation, and reviewed and edited the manuscript. All authors were involved in writing and revising the manuscript as well as scientific discussions. Furthermore, Nina Volk performed most of the SEM imaging and Markus Hund contributed by AFM measurements.

Chapter 8: Electrophoretic mobility of nanoparticle aggregates: Independence from aggregate size

Matthias B. Engelhardt, Takuya Sugimoto, Georg Papastavrou, and Motoyoshi Kobayashi*

published in *Colloids and Surfaces A: Physicochemical and Engineering Aspects*, **2024**, *703*, *Part 1*, *135244*

I performed all electrophoretic mobility and dynamic light scattering experiments, evaluated all data, and wrote the original manuscript. Prof. Dr. Takuya Sugimoto, Prof. Dr. Motoyoshi Kobayashi, and I developed the experimental methodology. They also provided the software for the O'Brien-White calculations and Python code for the other electrokinetic models and helped interpret the results. Prof. Takuya Sugimoto, Prof. Dr. Georg Papastavrou, and Prof. Dr. Motoyoshi Kobayashi supervised the project and validated the data. All authors were involved in scientific discussions and writing and revising the manuscript.

References

[1] Quincke, G., Ueber die Fortführung materieller Theilchen durch strömende Elektricität, Ann. Phys., 189(8), 513, **1861**

[2] Adamczyk, Z.; Zembala, M. and Michna, A., Polyelectrolyte adsorption layers studied by streaming potential and particle deposition, J. Colloid Interface Sci., 303(2), 353, **2006**

[3] Childress, A. E. and Elimelech, M., Relating nanofiltration membrane performance to membrane charge (electrokinetic) characteristics, Environ. Sci. Technol., 34(17), 3710, **2000**

[4] Minor, M.; van der Linde, A. J.; van Leeuwen, H. P. and Lyklema, J., Streaming potentials and conductivities of porous silica plugs, Colloids Surf. A, 142(2-3), 165, **1998**

[5] Werner, C.; Zimmermann, R. and Kratzmüller, T., Streaming potential and streaming current measurements at planar solid/liquid interfaces for simultaneous determination of zeta potential and surface conductivity, Colloids Surf. A., 192(1-3), 205, **2001**

[6] Bellmann, C.; Klinger, C.; Opfermann, A.; Böhme, F. and Adler, H.-J. P., Evaluation of surface modification by electrokinetic measurements, Prog. Org. Coat., 44(2), 93, **2002**

[7] Szilagyi, I.; Trefalt, G.; Tiraferri, A.; Maroni, P. and Borkovec, M., Polyelectrolyte adsorption, interparticle forces, and colloidal aggregation, Soft Matter, 10(15), 2479, **2014**

[8] Elimelech, M.; Chen, W. H. and Waypa, J. J., Measuring the zeta (electrokinetic) potential of reverse osmosis membranes by a streaming potential analyzer, Desalination, 95(3), 269, **1994**

[9] Adamczyk, Z., Modeling adsorption of colloids and proteins, Curr. Opin. Colloid Interface Sci., 17(3), 173, **2012**

[10] Netz, R. R. and Andelman, D., Neutral and charged polymers at interfaces, Phys. Rep., 380(1-2), 1, **2003**

[11] Van de Steeg, H. G. M.; Cohen Stuart, M. A.; De Keizer, A. and Bijsterbosch, B. H., Polyelectrolyte adsorption: A subtle balance of forces, Langmuir, 8(10), 2538, **1992**

[12] Abdurahman, A.; Cui, K.; Wu, J.; Li, S.; Gao, R.; Dai, J.; Liang, W. and Zeng, F., Adsorption of dissolved organic matter (DOM) on polystyrene microplastics in aquatic environments: Kinetic, isotherm and site energy distribution analysis., Ecotox. Environ. Safe., 198, 110658, **2020**

[13] Hüffer, T.; Praetorius, A.; Wagner, S.; von der Kammer, F. and Hofmann, T., Microplastic exposure assessment in aquatic environments: Learning from similarities and differences to engineered nanoparticles, Environ. Sci. Technol., 51(5), 2499, **2017**

[14] Schefer, R. B.; Armanious, A. and Mitrano, D. M., Eco-corona formation on plastics: Adsorption of dissolved organic matter to pristine and photochemically weathered polymer surfaces, Environ. Sci. Technol., 57(39), 14707, **2023**

[15] Gregory, J., Rates of flocculation of latex particles by cationic polymers, J. Colloid Interface Sci., 42(2), 448, **1973**

[16] Schönhoff, M., Layered polyelectrolyte complexes: Physics of formation and molecular properties, J. Phys. Condens. Matter, 15(49), R1781, **2003**

[17] Fa, K.; Paruchuri, V. K.; Brown, S. C.; Moudgil, B. M. and Miller, J. D., The significance of electrokinetic characterization for interpreting interfacial phenomena at planar, macroscopic interfaces, Phys. Chem. Chem. Phys., 7(4), 678, **2005**

[18] Herzberg, M.; Dobberschütz, S.; Okhrimenko, D.; Bovet, N. E.; Andersson, M. P.; Stipp, S. L. S. and Hassenkam, T., Comparison of atomic force microscopy and zeta potential derived surface charge density, EPL, 130(3), 36001, **2020**

[19] Scales, P. J.; Grieser, F. and Healy, T. W., Electrokinetics of the muscovite mica-aqueous solution interface, Langmuir, 6(3), 582, **1990**

[20] Scales, P. J.; Grieser, F.; Healy, T. W.; White, L. R. and Chan, D. Y. C., Electrokinetics of the silica-solution interface: A flat plate streaming potential study, Langmuir, 8(3), 965, **1992**

[21] Lyons, J. S.; Furlong, D. N. and Healy, T. W., The electrical double-layer properties of the mica (muscovite)-aqueous electrolyte interface, Aust. J. Chem., 34(6), 1177, **1981**

[22] Behrens, S. H.; Christl, D. I.; Emmerzael, R.; Schurtenberger, P. and Borkovec, M., Charging and aggregation properties of carboxyl latex particles: Experiments versus DLVO theory, Langmuir, 16(6), 2566, **2000**

[23] Hiemstra, T.; Van Riemsdijk, W. H. and Bolt, G. H., Multisite proton adsorption modeling at the solid/solution interface of (hydr)oxides: A new approach, J. Colloid Interface Sci., 133(1), 91, **1989**

[24] Hiemstra, T.; De Wit, J. C. M. and Van Riemsdijk, W. H., Multisite proton adsorption modeling at the solid/solution interface of (hydr)oxides: A new approach, J. Colloid Interface Sci., 133(1), 105, **1989**

[25] Kobayashi, M.; Juillerat, F.; Galletto, P.; Bowen, P. and Borkovec, M., Aggregation and charging of colloidal silica particles: Effect of particle size, Langmuir, 21(13), 5761, **2005**

[26] Pericet-Camara, R.; Papastavrou, G. and Borkovec, M., Atomic force microscopy study of the adsorption and electrostatic self-organization of poly(amidoamine) dendrimers on mica, Langmuir, 20(8), 3264, **2004**

[27] Ohshima, H., Theory of colloid and interfacial electric phenomena, 1st ed., Academic Press, **2006**

[28] Michna, A.; Adamczyk, Z.; Sofińska, K. and Matusik, K., Monolayers of poly(amido amine) dendrimers on mica - In situ streaming potential measurements, J. Colloid Interface Sci., 485, 232, **2017**

[29] Morga, M. and Adamczyk, Z., Monolayers of cationic polyelectrolytes on mica - Electrokinetic studies, J. Colloid Interface Sci., 407, 196, **2013**

[30] Morga, M.; Adamczyk, Z.; Gödrich, S.; Oćwieja, M. and Papastavrou, G., Monolayers of poly-L-lysine on mica - Electrokinetic characteristics, J. Colloid Interface Sci., 456, 116, **2015**

[31] Pericet-Camara, R.; Papastavrou, G. and Borkovec, M., Effective charge of adsorbed poly(amidoamine) dendrimers from direct force measurements, Macromolecules, 42(5), 1749, **2009**

[32] Bocquet, L.; Trizac, E. and Aubouy, M., Effective charge saturation in colloidal suspensions, J. Chem. Phys., 117(17), 8138, **2002**

[33] Zuraiqi, K.; Zavabeti, A.; Allioux, F.-M.; Tang, J.; Nguyen, C. K.; Tafazolymotie, P.; Mayyas, M.; Ramarao, A. V.; Spencer, M.; Shah, K.; McConville, C. F.; Kalantar-Zadeh, K.; Chiang, K. and Daeneke, T., Liquid metals in catalysis for energy applications, Joule, 4(11), 2290, **2020**

[34] Grünzel, T.; Lee, Y. J.; Kuepper, K. and Bachmann, J., Preparation of electrochemically active silicon nanotubes in highly ordered arrays, Beilstein J. Nanotechnol., 4, 655, **2013**

[35] Nielsch, K.; Choi, J.; Schwirn, K.; Wehrspohn, R. B. and Gösele, U., Self-ordering regimes of porous alumina: The 10 porosity rule, Nano Lett., 2(7), 677, **2002**

[36] Schlicht, S.; Haschke, S.; Mikhailovskii, V.; Manshina, A. and Bachmann, J., Highly reversible water oxidation at ordered nanoporous iridium electrodes based on an original atomic layer deposition, ChemElectroChem, 5(9), 1259, **2018**

[37] Taccardi, N.; Grabau, M.; Debuschewitz, J.; Distaso, M.; Brandl, M.; Hock, R.; Maier, F.; Papp, C.; Erhard, J.; Neiss, C.; Peukert, W.; Görling, A.; Steinrück, H.-P. and Wasserscheid, P., Gallium-rich Pd-Ga phases as supported liquid metal catalysts, Nat. Chem., 9(9), 862, **2017**

[38] Fu, Q. and Wagner, T., Interaction of nanostructured metal overlayers with oxide surfaces, Surf. Sci. Rep., 62(11), 431, **2007**

[39] Lyaskovskyy, V. and de Bruin, B., Redox non-innocent ligands: Versatile new tools to control catalytic reactions, ACS Catalysis, 2(2), 270, **2012**

[40] Kosmulski, M., The pH dependent surface charging and points of zero charge. X. Update, Adv. Colloid Interface Sci., 319, 102973, **2023**

[41] Etienne, M. and Walcarius, A., Analytical investigation of the chemical reactivity and stability of aminopropyl-grafted silica in aqueous medium, Talanta, 59(6), 1173, **2003**

[42] Liu, C.; Han, Y.; Wang, Z.; Zhang, L. and Yang, W., Preparation of (3-aminopropyl)triethoxysilane-modified silica particles with tunable isoelectric point, Langmuir, 40(24), 12565, **2024**

[43] Xiao, Y.; Lv, Q.; Zhu, J.; Yao, S.; Liu, C. and Xing, W., Preparation of Pt hollow nanotubes with adjustable diameters for methanol electrooxidation, RSC Adv., 4(41), 21176, **2014**

[44] Zhu, H.; Tolmachev, Y. V. and Scherson, D. A., Electrocatalysis at microelectrodes: Geometrical considerations, J. Phys. Chem. C, 114(32), 13650, **2010**

[45] Indira, K.; Mudali, U. K.; Nishimura, T. and Rajendran, N., A review on TiO_2 nanotubes: Influence of anodization parameters, formation mechanism, properties, corrosion behavior, and biomedical applications, J. Bio. Tribo. Corros., 1(4), 196, **2015**

[46] Liu, L.; Pippel, E.; Scholz, R. and Gösele, U., Nanoporous Pt-Co alloy nanowires: Fabrication, characterization, and electrocatalytic properties, Nano Lett., 9(12), 4352, **2009**

[47] Xu, R.; Du, L.; Adekoya, D.; Zhang, G.; Zhang, S.; Sun, S. and Lei, Y., Well-defined nanostructures for electrochemical energy conversion and storage, Adv. Energy Mater., 11(15), 126, **2021**

[48] Hurd, R. M. and Hackerman, N., Electrokinetic potentials of bulk metals by streaming current measurements, J. Electrochem. Soc., 102(10), 594, **1955**

[49] Chae, Y. and An, Y.-J., Current research trends on plastic pollution and ecological impacts on the soil ecosystem: A review, Environ. Pollut., 240, 387, **2018**

[50] de Souza Machado, A. A.; Kloas, W.; Zarfl, C.; Hempel, S. and Rillig, M. C., Microplastics as an emerging threat to terrestrial ecosystems, Glob. Change Biol., 24(4), 1405, **2018**

[51] Galloway, T. S.; Cole, M. and Lewis, C., Interactions of microplastic debris throughout the marine ecosystem, Nat. Ecol. Evol., 1(5), 116, **2017**

[52] Geyer, R.; Jambeck, J. R. and Law, K. L., Production, use, and fate of all plastics ever made, Sci. Adv., 3(7), e1700782, **2017**

[53] Lambert, S. and Wagner, M., Microplastics are contaminants of emerging concern in freshwater environments: An overview, 1st ed., Springer International Publishing, Cham, **2018**

[54] Ramsperger, A. F. R. M.; Bergamaschi, E.; Panizzolo, M.; Fenoglio, I.; Barbero, F.; Peters, R.; Undas, A.; Purker, S.; Giese, B.; Lalyer, C. R.; Tamargo, A.; Moreno-Arribas, M. V.; Grossart, H.-P.; Kühnel, D.; Dietrich, J.; Paulsen, F.; Afanou, A. K.; Zienolddiny-Narui, S.; Eriksen Hammer, S.; Kringlen Ervik, T.; Graff, P.; Brinchmann, B. C.; Nordby, K.-C.; Wallin, H.; Nassi, M.; Benetti, F.; Zanella, M.; Brehm, J.; Kress, H.; Löder, M. G. J. and Laforsch, C., Nano- and microplastics: A comprehensive review on their exposure routes, translocation, and fate in humans, NanoImpact, 29, 100441, **2023**

[55] Wang, Y.; Xiang, L.; Amelung, W.; Elsner, M.; Gan, J.; Kueppers, S.; Christian, L.; Jiang, X.; Adu-Gyamfi, J.; Heng, L.; Ok, Y. S.; Ivleva, N. P.; Luo, Y.; Barceló, D.; Schäffer, A. and Wang, F., Micro- and nanoplastics in soil ecosystems: Analytical methods, fate, and effects, Trends Anal. Chem., 169, 117309, **2023**

[56] Huang, Z.; Hu, B. and Wang, H., Analytical methods for microplastics in the environment: A review, Environ. Chem. Lett., 21(1), 383, **2023**

[57] Löder, M. G. J. and Gerdts, G., Methodology used for the detection and identification of microplastics - A critical appraisal, 1st ed., Springer International Publishing, Cham, **2015**

[58] Möller, J. N.; Löder, M. G. J. and Laforsch, C., Finding microplastics in soils: A review of analytical methods, Environ. Sci. Technol., 54(4), 2078, **2020**

[59] Conkle, J. L.; Báez Del Valle, C. D. and Turner, J. W., Are we underestimating microplastic contamination in aquatic environments?, Environ. Manag., 61(1), 1, **2018**

[60] Shamskhany, A.; Li, Z.; Patel, P. and Karimpour, S., Evidence of microplastic size impact on mobility and transport in the marine environment: A review and synthesis of recent research, Front. Mar. Sci., 8, 63, **2021**

[61] Al Harraq, A. and Bharti, B., Microplastics through the lens of colloid science, ACS Environ. Au, 2(1), 3, **2022**

[62] Amobonye, A.; Bhagwat, P.; Raveendran, S.; Singh, S. and Pillai, S., Environmental impacts of microplastics and nanoplastics: A current overview, Front. Microbiol., 12, 768297, **2021**

[63] Nguyen, B.; Claveau-Mallet, D.; Hernandez, L. M.; Xu, E. G.; Farner, J. M. and Tufenkji, N., Separation and analysis of microplastics and nanoplastics in complex environmental samples, Acc. Chem. Res., 52(4), 858, **2019**

[64] Sobhani, Z.; Zhang, X.; Gibson, C.; Naidu, R.; Megharaj, M. and Fang, C., Identification and visualisation of microplastics/nanoplastics by Raman imaging (i): Down to 100 nm, Water Res., 174, 115658, **2020**

[65] Brehm, J.; Wilde, M. V.; Reiche, L.; Leitner, L.-C.; Petran, B.; Meinhart, M.; Wieland, S.; Ritschar, S.; Schott, M.; Boos, J.-P.; Frei, S.; Kress, H.; Senker, J.; Greiner, A.; Fröhlich, T. and Laforsch, C., In-depth characterization revealed polymer type and chemical content specific effects of microplastic on Dreissena bugensis, J. Hazard. Mater., 437, 129351, **2022**

[66] Meides, N.; Menzel, T.; Poetzschner, B.; Löder, M. G. J.; Mansfeld, U.; Strohriegl, P.; Altstaedt, V. and Senker, J., Reconstructing the environmental degradation of polystyrene by accelerated weathering, Environ. Sci. Technol., 55(12), 7930, **2021**

[67] Mauel, A.; Pötzschner, B.; Meides, N.; Siegel, R.; Strohriegl, P. and Senker, J., Quantification of photooxidative defects in weathered microplastics using ^{13}C multiCP NMR spectroscopy, RSC Adv., 12(18), 10875, **2022**

[68] Adachi, Y.; Feng, L. and Kobayashi, M., Kinetics of flocculation of polystyrene latex particles in the mixing flow induced with high charge density polycation near the isoelectric point, Colloids Surf. A, 471, 38, **2015**

[69] Cramer, A.; Schmidtmann, J.; Benard, P.; Kaestner, A.; Engelhardt, M.; Peiffer, S. and Carminati, A., Ferrihydrite coating reduces microplastic induced soil water repellency, Environ. Sci.: Process. Impacts, 25(6), 1094, **2023**

[70] Kobayashi, M.; Ookawa, M. and Yamada, S., The effects of surface charging properties on colloid transport in porous media, J. Jpn. Soc. Civ. Eng., Ser. A2, 70(2), I_743, **2014**

[71] Ramsperger, A. F. R. M.; Jasinski, J.; Völkl, M.; Witzmann, T.; Meinhart, M.; Jérôme, V.; Kretschmer, W. P.; Freitag, R.; Senker, J.; Fery, A.; Kress, H.; Scheibel, T. and Laforsch, C., Supposedly identical microplastic particles substantially differ in their material properties influencing particle-cell interactions and cellular responses, J. Hazard. Mater., 425, 127961, **2022**

[72] Meides, N.; Mauel, A.; Menzel, T.; Altstädt, V.; Ruckdäschel, H.; Senker, J. and Strohriegl, P., Quantifying the fragmentation of polypropylene upon exposure to accelerated weathering, Microplast. Nanoplast., 2(1), 30, **2022**

[73] Möller, J. N.; Heisel, I.; Satzger, A.; Vizsolyi, E. C.; Oster, S. D. J.; Agarwal, S.; Laforsch, C. and Löder, M. G. J., Tackling the challenge of extracting microplastics from soils: A protocol to purify soil samples for spectroscopic analysis, Environ. Toxicol. Chem., 41(4), 844, **2022**

[74] Ramsperger, A. F. R. M.; Stellwag, A. C.; Caspari, A.; Fery, A.; Lueders, T.; Kress, H.; Löder, M. G. J. and Laforsch, C., Structural diversity in early-stage biofilm formation on microplastics depends on environmental medium and polymer properties, Water, 12(11), 3216, **2020**

[75] Trotter, B.; Wilde, M. V.; Brehm, J.; Dafni, E.; Aliu, A.; Arnold, G. J.; Fröhlich, T. and Laforsch, C., Long-term exposure of Daphnia magna to polystyrene microplastic (PS-MP) leads to alterations of the proteome, morphology and life-history., Sci. Total Environ., 795, 148822, **2021**

[76] Völkl, M.; Jérôme, V.; Weig, A.; Jasinski, J.; Meides, N.; Strohriegl, P.; Scheibel, T. and Freitag, R., Pristine and artificially-aged polystyrene microplastic particles differ in regard to cellular response., J. Hazard. Mater., 435, 128955, **2022**

[77] Reuß, F. F., Sur un Nouvel Effet de l'Électricité Galvanique Mémoires de la Société Impériale des Naturalistes de Moskou, 2, 327, **1809**

[78] Delgado, A. V.; González-Caballero, F.; Hunter, R. J.; Koopal, L. K.; Lyklema, J. and International Union of Pure and Applied Chemistry, Physical and Biophysical Chemistry Division IUPAC Technical Report, Measurement and interpretation of electrokinetic phenomena, J. Colloid Interface Sci., 309(2), 194, **2007**

[79] Ohshima, H., Electrical phenomena at interfaces and biointerfaces. Fundamentals and applications in nano-, bio-, and environmental sciences, 1st ed., John Wiley & Sons, Hoboken, **2012**

[80] Adachi, Y., Dynamic aspects of coagulation and flocculation, Adv. Colloid Interface Sci., 56, 1, **1995**

[81] Gopmandal, P. P.; Bhattacharyya, S. and Ohshima, H., On the similarity between the electrophoresis of a liquid drop and a spherical hydrophobic particle, Colloid Polym. Sci., 295(10), 2077, **2017**

[82] Helfricht, N.; Doblhofer, E.; Duval, J. F. L.; Scheibel, T. and Papastavrou, G., Colloidal properties of recombinant spider silk protein particles, J. Phys. Chem. C, 120(32), 18015, **2016**

[83] Kobayashi, M., An analysis on electrophoretic mobility of hydrophobic polystyrene particles with low surface charge density: Effect of hydrodynamic slip, Colloid Polym. Sci., 298(10), 1313, **2020**

[84] Maurya, S. K.; Gopmandal, P. P.; Ohshima, H. and Duval, J. F. L., Electrophoresis of composite soft particles with differentiated core and shell permeabilities to ions and fluid flow, J. Colloid Interface Sci., 558, 280, **2020**

[85] Ohshima, H., Electrokinetic phenomena in a dilute suspension of spherical solid colloidal particles with a hydrodynamically slipping surface in an aqueous electrolyte solution., Adv. Colloid Interface Sci., 272, 101996, **2019**

[86] Sato, Y.; Kusaka, Y. and Kobayashi, M., Charging and aggregation behavior of cellulose nanofibers in aqueous solution, Langmuir, 33(44), 12660, **2017**

[87] Schindelin, J.; Arganda-Carreras, I.; Frise, E.; Kaynig, V.; Longair, M.; Pietzsch, T.; Preibisch, S.; Rueden, C.; Saalfeld, S.; Schmid, B.; Tinevez, J.-Y.; White, D. J.; Hartenstein, V.; Eliceiri, K.; Tomancak, P. and Cardona, A., Fiji: an open-source platform for biological-image analysis, Nat. Methods, 9(7), 676, **2012**

[88] O'Brien, R. W. and White, L. R., Electrophoretic mobility of a spherical colloidal particle, J. Chem. Soc., Faraday Trans. 2, 74, 1607, **1978**

[89] Antonietti, M. and Vorwerg, L., Examination of the atypical electrophoretic mobility behavior of charged colloids in the low salt region using the O'Brian-White theory, Colloid Polym. Sci., 275(9), 883, **1997**

[90] Borkovec, M.; Behrens, S. H. and Semmler, M., Observation of the mobility maximum predicted by the standard electrokinetic model for highly charged amidine latex particles, Langmuir, 16(11), 5209, **2000**

[91] Hückel, E., Die Katophorese der Kugel, Phys. Z., 25, 204, **1924**

[92] Ohshima, H., A simple expression for Henry's function for the retardation effect in electrophoresis of spherical colloidal particles, J. Colloid Interface Sci., 168(1), 269, **1994**

[93] von Smoluchowski, M., Handbuch der Elektrizität und des Magnetismus, 1st ed., J.A. Barth, Leipzig, **1921**

[94] Coelho, D.; Thovert, J.-F.; Thouy, R. and Adler, P. M., Hydrodynamic drag and electrophoresis of suspensions of fractal aggregates, Fractals, 05(03), 507, **1997**

[95] Levine, S. and Neale, G. H., The prediction of electrokinetic phenomena within multiparticle systems. I. Electrophoresis and electroosmosis, J. Colloid Interface Sci., 47(2), 520, **1974**

[96] Miller, N. P.; Berg, J. C. and O'Brien, R. W., The electrophoretic mobility of a porous aggregate, J. Colloid Interface Sci., 153(1), 237, **1992**

[97] Lin, M. Y.; Lindsay, H. M.; Weitz, D. A.; Ball, R. C.; Klein, R. and Meakin, P., Universality in colloid aggregation, Nature, 339(6223), 360, **1989**

Manuscripts and Publications

4. Effective charge of high-generation PAMAM dendrimers in the adsorbed state

Matthias B. Engelhardt, Paul Markus, Nicolas Helfricht, and Georg Papastavrou*

"Effective charge of high-generation PAMAM dendrimers in the adsorbed state"

Journal of Colloid and Interface Science, **2025**, *686, 852-863*.

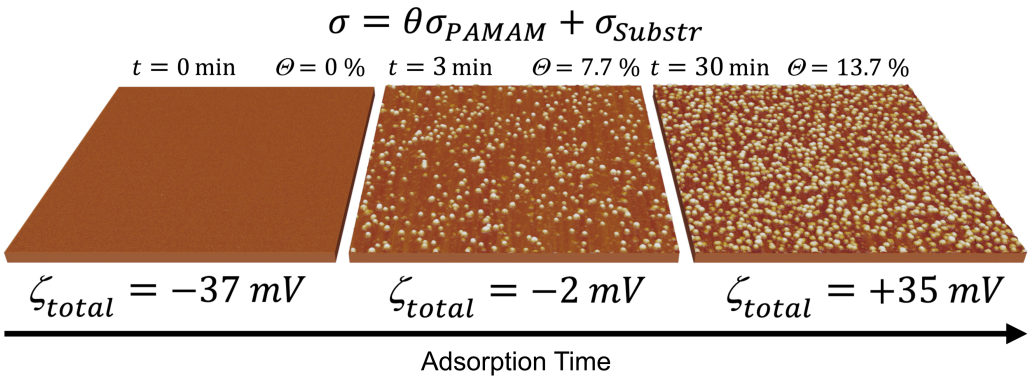

Reprinted with permission from:

"Effective charge of high-generation PAMAM dendrimers in the adsorbed state", M. B. Engelhardt, P. Markus, N. Helfricht, G. Papastavrou, *Journal of Colloid and Interface Science,* **2025**, *686, 852-863*.

DOI: 10.1016/j.jcis.2025.02.008

Under terms of the CC BY license

Journal of Colloid and Interface Science 686 (2025) 852–863

Contents lists available at ScienceDirect

Journal of Colloid And Interface Science

journal homepage: www.elsevier.com/locate/jcis

Effective charge of high-generation PAMAM dendrimers in the adsorbed state

Matthias B. Engelhardt, Paul Markus, Nicolas Helfricht, Georg Papastavrou *

Physical Chemistry II, University of Bayreuth, Universitaetsstrasse 30 95447 Bayreuth, Germany

HIGHLIGHTS

- Followed dendrimer adsorption and characterized charge on different substrates by streaming potential measurement and AFM.
- Effective charge for single poly(amidoamine) dendrimers on different substrates and as a function of pH by correlation of AFM and electrokinetics.
- The diffuse layer of the collector substrates modulated not only the interdendrimers interactions but also determined the effective charge of the dendrimers.

GRAPHICAL ABSTRACT

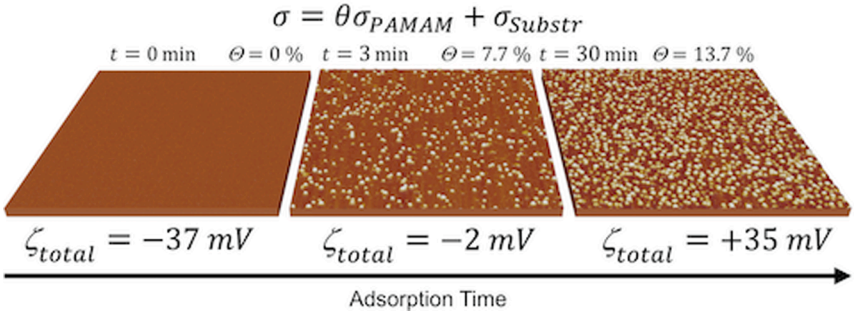

ABSTRACT

The adsorption of macromolecules onto charged surfaces is an ubiquitous process in nature and industrial processes; it has, for example, important implications for surface modification and sensors in analytics. In the case of proteins and some polyelectrolytes, such as dendritic ones, the adsorption process and the resulting final coverage can be described within the framework of the random sequential adsorption (RSA) model. To provide a quantitative description of the intermolecular interaction potential, the effective charge of the molecules is of great importance. The incorporation of charge effects results in the so-called extended or electrostatic RSA model. Here, it is demonstrated for poly(amidoamine) (PAMAM) dendrimers of generation 10 that the influence of the substrate on the effective charge must be considered. Streaming potential measurements of PAMAM G10 adsorbed onto mica and silica showed that the effective charge differed significantly for both substrates. Moreover, for substrates whose surface charge varies with pH, the effective charge varies not only by the titration of the ionizable groups of the polyelectrolytes but also due to the electrostatic interaction with the substrate. A first estimation to account for these effects is provided.

1. Introduction

The adsorption of charged macromolecules to solid substrates is ubiquitous in colloid and interface science [1–5]. Many adsorption processes take place in aqueous solutions, either in natural environment, e.g., the adsorption of humic acid on microplastics [6–8], or for industrial applications, such as the polyelectrolyte-based stabilization of colloidal suspensions or surface modification [5,9–12]. Moreover, many analytical techniques, such as surface plasmon spectroscopy (SPR) or quartz crystal microbalance (QCM), rely on the adsorption of macromolecules, such as proteins, to the sensor [13–16]. Electrolyte/solid interfaces acquire charges, either by protonation/deprotonation of surface functional groups or by ion adsorption [17]. All aforementioned processes have in common that not only the adsorbent, i.e., the macromolecules, but also the collector substrate are charged. Due to the long-range nature of electrostatic forces, the resulting electrostatic interactions play an important role in the adsorption kinetics, as well as in

* Corresponding author.
E-mail address: georg.papastavrou@uni-bayreuth.de (G. Papastavrou).

https://doi.org/10.1016/j.jcis.2025.02.008
Received 12 December 2024; Received in revised form 24 January 2025; Accepted 1 February 2025
Available online 2 February 2025
0021-9797/© 2025 The Authors. Published by Elsevier Inc. This is an open access article under the CC BY license (http://creativecommons.org/licenses/by/4.0/).

Nomenclature

List of symbols

a	particle radius for mean-field theory
a_{sol}	radius of a PAMAM dendrimer in solution
a_{ads}	radius of a PAMAM dendrimer in the adsorbed state
a_{eff}	effective radius of a PAMAM dendrimer including interaction potential
A_{PAMAM}	area occupied by one PAMAM dendrimer
C_s	Stern layer capacitance
I	ionic strength
K_L	bulk conductivity of the liquid
k_B	Boltzmann constant
L_B	Bjerrum length
N_A	Avogadrós number
t	adsorption time
T	temperature
U_{str}	streaming potential
Z_{eff}	effective charge in elementary charges
$\tilde{Z}_{eff}$	normalized effective charge
Z_{ref}	effective charge in reference to published data
Δp	pressure difference
Δx	shift of the shear plane
ε_0	permittivity of free space
ε_r	relative permittivity of the continuum phase
η	dynamic viscosity
κ	inverse Debye length
κ_{eff}	inverse effective Debye length
θ	fractional surface coverage
θ_{jam}	surface coverage in the jamming limit
θ_{plat}	maximum surface coverage in adsorption plateau
ζ	zeta-potential
ζ_{Avg}	zeta-potential measured in an asymmetric cell
ζ_{Ref}	zeta-potential of the reference material
ζ_{Test}	zeta-potential for the substrate under evaluation
σ	total electrokinetic surface charge density
σ_0^{PAMAM}	electrokinetic surface charge density of adsorbed PAMAM dendrimers
σ_0^{sub}	electrokinetic surface charge density of substrate
ψ_d	diffuse layer potential at substrate

reaching a plateau for the maximum adsorbed mass.

The adsorption of polyelectrolytes has been studied extensively in recent decades, including the influence of various parameters such as the polymer topology (e.g. branched versus linear), the charge density, and the molecular weight [2,5,12,18,19]. Dendritic polyelectrolytes play a special role due to their highly-defined shape and low polydispersity index [20–22]. In general, dendrimers can be regarded as nearly comparable to proteins in terms of their adsorption behavior, which can be described within the framework of the random sequential adsorption (RSA) model [23–26]. In particular, poly(amidoamine) (PAMAM) dendrimers have been utilized as model systems for macromolecule adsorption [27,28]. The classical RSA model assumes an ideal collector surface and only hard sphere repulsion between the adsorbing colloids or macromolecules, in particular proteins [25,29,30]. Adamczyk and coworkers have extended this classical RSA model to include the electrostatic repulsion between the adsorbates [23,31]. More recently, also the influence of the substrate has been studied, allowing for a more accurate description of highly charged macromolecular systems [32,33]. We will refer to this approach as the 3-body RSA model.

Electrokinetic methods are often used to characterize charged particles and interfaces in electrolyte solutions [34,35]. Electrophoretic mobility provides information about the charging state of dispersed colloidal objects, including macromolecules, by measuring their mobility in an externally applied electric field [36,37]. Also, PAMAM dendrimers of higher generations have been studied by electrophoretic mobility [38]. For extended flat substrates, the streaming potential technique provides analogous information [34,35]. In this case, the charged macroscopic object, e.g., a silica wafer or a piece of mica, remains stationary and the electrolyte solution is streamed over it, which leads to a displacement of ions in the diffuse layer. The thereby resulting potential difference between two electrodes placed in the channel can be measured and is directly related to the diffuse layer potential of the substrate at the shear plane, the so-called zeta-potential ζ [35]. The streaming potential technique has been applied to bare surfaces and those modified by adsorbed colloids, polymers, and proteins, respectively [27,38–43]. However, the description of determined ζ for heterogeneous charge distributions is often based on a number of assumptions, such as that the charge density of the polyelectrolytes does not depend on the coverage and that it is independent of the state of the collector surface [38,44–46]. Recent studies, including PAMAM dendrimers, indicate that these assumptions are not necessarily fulfilled under all conditions [38,47–50]. Moreover, theoretical studies indicate that the interaction of PAMAM dendrimers with solid substrates is rather complex and includes also conformational changes [51–53].

Here, we study the development of the effective charge of adsorbed PAMAM G10 dendrimers as a function of the surface coverage on different types of substrates *via* streaming potential measurements. The measurements were performed using a custom-made setup developed in our laboratory. By using PAMAM dendrimers of generation 10, we were able to determine the surface coverage by atomic force microscopy (AFM) imaging. The measured streaming potential correlated with the surface coverage, thereby allowing for an unambiguous determination of the effective charge for single dendrimers. This effective charge depended on the substrate, which was unexpected. Moreover, the determined effective charges were different from those calculated on the basis of the mean-field approach [54], which has been previously used to calculate the effective radii in the extended RSA models and the three-body RSA model [28,32,33,55]. This finding has been corroborated by streaming potential measurements as a function of the solution pH on samples with different surface coverage of G10 PAMAM dendrimers. Both the dendrimers and the substrate showed dissociation of functional groups, which led to complex charge regulation of the dendrimers with the substrate. Our experimental results indicate that the effective charge of dendrimers critically depends on the state of the underlying substrate. This finding has important consequences for modeling the 3-body RSA adsorption model and macromolecule adsorption in general.

2. Materials and methods

2.1. Materials

Water of Millipore-quality (MilliQ® IQ 7000, Merck KGaA, Darmstadt, Germany) was used for all preparations and cleaning processes. The specific resistivity of water was 18.2 MΩ cm and the total organic content was always < 6 ppb. Analytic grade potassium chloride (Bio-Ultra, Merck KGaA, Darmstadt, Germany), potassium hydroxide, and hydrochloric acid Titrisol® ampoules (Merck KGaA, Darmstadt, Germany) were used to prepare electrolyte solutions. PAMAM dendrimers of generation 10 were purchased from Dendritech Inc. (Midland, MI, USA). For the collector substrates, muscovite mica (V1-grade, Ted Pella Inc., Redding, CA, USA) and diced fused silica wafer pieces (JGS1-grade, MicroChemicals GmbH, Ulm, Germany) were used.

2.2. Methods

Streaming Potential Setup. Fig. 1 schematically shows the in-house built streaming potential setup. All materials in contact with electrolyte solutions during the measurements were made of glass or fluorinated polymers. A proportional valve (PRA00-A500, AirCom Pneumatic GmbH, Ratingen, Germany) and a 3/2-way valve (Christian Bürkert GmbH & Co. KG, Ingelfingen, Germany) controlled the nitrogen gas stream toward the glass bottles, which were acting as electrolyte reservoirs. Consequently, the electrolyte flow and its direction were controlled by the nitrogen pressure difference between the reservoirs. The electrolyte was driven through the measurement cell. A differential pressure sensor (PX26-005DV, Omega Engineering Inc., Connecticut, USA) was connected to the measurement cell to measure the differential pressure. Cylindrical in-house-built Ag/AgCl electrodes (99.99 % Ag tubes, Advent Research Materials, Oxford, England) were located on both sides of the measurement cell. The electrodes had an inner diameter of 0.8 cm and a length of 5.0 cm. Chlorination of the electrodes was carried out with an electrochemical workstation (Zennium, Zahner-Elektrik GmbH, Kronach, Germany) at a current density of 1 mA cm^{-2} in a 1 M KCl solution for 1 min. The potential difference between the electrodes was determined using an electrometer (Keithley 6514, Tektronix Inc., Oregon, USA). A balance (AND EK-2000i, A&D Company Ltd., Tokyo, Japan) was used to quantify the volume flow rate through the measurement cell. The resulting flow rate was validated using a commercial flow meter (DFM-ECTFE, B.I.O.-TECH e. K., Vilshofen, Germany), which is located between one reservoir and the measurement cell. Furthermore, the measurement setup was equipped with a conductometry cell (3446 conductometry cell, YSI Inc., Ohio, USA) and a Fisherbrand™ pH electrode (Bioblock, Fisher Scientific GmbH, Schwerte, Germany) with an integrated PT100 temperature sensor, which allowed for determining the conductance and temperature in-line between the reservoirs. Therefore, a LCR bridge (HM8118, Rohde & Schwarz GmbH & Co. KG, Munich, Germany) was used to measure the solution conductance in a conductometry cell. All electrical components (proportional valves, pressure sensors, balance, LCR bridge, pH electrode, temperature sensor, flow sensor, and electrometer) were connected to a multifunction I/O device 6008 (National Instruments Corp., Austin, Texas, United States), which allowed interfacing with the software. All components were controlled, and measurement data were collected using a home-written script in IgorPro (version 6.37, Wavemetrics, Portland, OR, USA). The solution pH value was measured using a pH station (827 pH lab, Deutsche Metrohm GmbH & Co. KG, Filderstadt, Germany) and a pH electrode (Aquatrode plus, Deutsche Metrohm GmbH & Co. KG, Filderstadt, Germany) externally before the streaming potential measurements. The asymmetric streaming potential cell was manufactured from non-reinforced poly(tetrafluoroethylene) (PTFE) (Auer Kunststofftechnik GmbH, Olching, Germany). Details of the construction of this cell can be found in the supporting information (SI) (cf. Fig. S1, Table TS1, and Fig. S2). Glass-fiber-reinforced PTFE (ENFLON®, Enflo Canada Ltd., Grand Falls, NB, Canada) was used to build the symmetric streaming potential cell. Further details are given in the SI (cf. Fig. S3, Table TS2, and Figs. S4, S5).

Cleaning of substrates. Adhesive tape was used to cleave the top layer of mica sheets to create molecularly flat pristine interfaces [56]. A modified cleaning procedure from RCA laboratories was used to clean the fused silica wafers [57]. Hellmanex® III surfactant (Hellma Analytics, Müllheim, Germany) solution with a volume fraction of 2 % in water was used to immerse the wafers. The wafers were sonicated for 20 min at 40 °C and then rinsed with water. Next, the samples were immersed in a solution of analytic-grade isopropyl alcohol with a volume fraction of 75 % (VWR Chemical, Darmstadt, Germany) in water and subjected to sonication treatment for 20 min, followed by rinsing with water. Finally, oxidative surface cleaning was performed using a volumetric mixture of laboratory-grade hydrogen peroxide (Fisher Scientific GmbH, Schwerte, Germany), ammonia (25 % in water, AnalaR NORMAPUR®, VWR Chemical), and water at a ratio of 1:1:5. The samples were rinsed with water and dried under a nitrogen stream. The modified RCA treatment was also applied to clean all fluorinated parts of the streaming potential measurement setup in contact with the electrolyte solution.

Dendrimer adsorption. Freshly cleaned substrates were immersed for 0.5–81 min to achieve different fractional surface coverages in a suspension of 5 ppm PAMAM G10 dendrimers at pH = 5 and an overall ionic strength of 5 mM in KCl. Afterward, the substrates were rinsed with approx. 10 mL of water on each side and dried under a nitrogen stream.

Streaming potential measurements. Prior to the measurements, the mounted dry substrates were subjected to 5 min of liquid flow in alternating directions to wet the interface and remove air bubbles from the channel. The electric conductivity of the solution and temperature were recorded for 10 and 100 data points, respectively, and averaged before each streaming potential experiment. In general, a pH titration

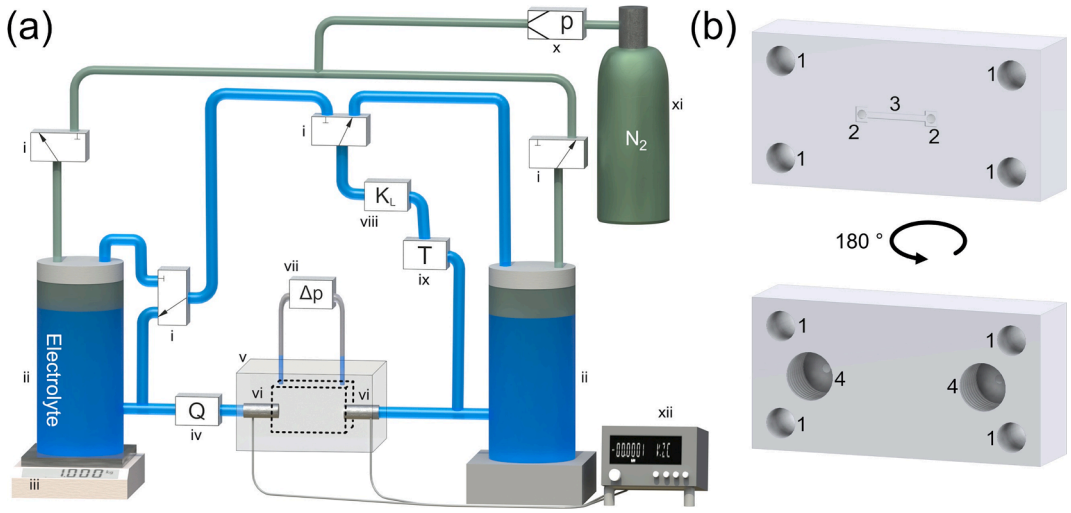

Fig. 1. (a) Schematic illustration of the purposely constructed streaming potential setup with (i) 3/2 way valves, (ii) electrolyte solution reservoirs, (iii) mass flow balance, (iv) flow meter, (v) modular streaming potential cells, (vi) cylindrical Ag/AgCl electrodes, (vii) differential pressure sensor, (viii) conductivity cell, (ix) PT100 temperature sensor, (x) proportional valve, (xi) nitrogen reservoir, and (xii) electrometer. (b) Bottom and top side view of the asymmetric streaming potential cell with (1) mounting holes to connect the cell with the substrate and carrier plate, (2) ends of the tubes that connect the microchannel (3) with the electrodes and electrolyte reservoirs, and (4) threads to connect the cell to the rest of the setup.

was conducted from neutral to either alkaline or acidic pH. For measurements at pH 5, distinct solutions were prepared externally. The experiments recorded the streaming potential and the pressure 10 times at a given applied pressure between ± 200 mbar for 10 different pressures in two directions. The streaming potential coupling coefficient was determined by linear regression of the streaming potential as a function of the applied pressure. The zeta-potential ζ was then calculated using the Helmholtz-Smoluchowski equation for data recorded in the symmetric or asymmetric cell with a PTFE piece as reference substrate. Streaming potential measurements with the asymmetric cell required reference data to evaluate the actual ζ for the test substrates: The procedure outlined by Walker and coworkers was used [58]. The reference data were measured at the pH and ionic strength of interest using the same material as the cell body. The resulting reference curves are shown in the SI (cf. Fig. S6). All streaming potential experiments were conducted at constant ionic strength of 5 mM in KCl between pH 4 and pH 10, or at varying ionic strengths and at a fixed pH of 5.

Atomic Force Microscopy. A Dimension Icon (Bruker Corp., Billerica, MA, USA) equipped with a NanoScope V controller (Bruker Corp., Billerica, MA, USA) was employed in PeakForce Tapping® mode. ScanAsyst Air cantilevers (Bruker Corp., Billerica, MA, USA) were used under ambient conditions to determine the surface topography of pristine and dendrimer-covered substrates. The cantilevers have a nominal resonance frequency of 70 kHz, a nominal spring constant of 0.4 N/m, and a typical tip radius of less than 5 nm. AFM images with scan sizes of (1 × 1) μm^2 were acquired at a scan rate of 0.5 Hz to determine the number density of adsorbed PAMAM dendrimers. The AFM images were evaluated using the NanoScope Analysis software (Version 1.8, Bruker Corp., Billerica, MA, USA). Plane fits of 1st order were applied before counting the number of adsorbed dendrimers.

AFM image evaluation. The number density of PAMAM dendrimers on the inorganic surface was evaluated from at least five flattened AFM images per adsorption state using the Fiji software version 1.54f [59]. We used the "Analyze Particle" function and restricted the particle area to (140 – 1050) nm^2 and circularity between 0.7 and 1. The surface coverage was calculated from the number of adsorbed dendrimers in a 1 μm x 1 μm area and a nominal adsorbed dendrimer radius of 9.15 nm [28]. This procedure was validated with the "Cell Counter" plugin and manual number density determinations (cf. Table S3, Fig. S7, and Table S4, respectively, in the SI).

3. Results and Discussion

3.1. Streaming potential measurements

For this study, we used a purpose-constructed streaming potential setup based on a micro-slit channel configuration with a parallel-plate streaming cell. Our setup was inspired by similar setups from Van Wagenen [60], Werner et al.[61], and Zembala et al.[62,63]. Fig. 1a shows a schematic representation of this streaming potential setup. An external pneumatic pressure was applied to two reservoirs containing electrolyte solution in order to pump the liquid through the measurement cell (cf. Fig. 1b). The pneumatic pressure control was based on a semi-closed system (cf. green lines in Fig. 1a), controlled by a pressure controller for the gas supply lines, and connected to the gas phase of the two liquid reservoirs. The parallel-plate cell (cf. Fig. 1b) was attached in a flow-through configuration to both reservoirs. The hydrostatic pressure difference between the inlet and outlet of the measurement cell was directly measured by a bridging sensor and controlled via a proportional gas valve. The liquid flow through the cell was determined by the mass change in the reservoir using a balance. Determining the liquid volume passing through the cell is essential to verify that a laminar flow regime has been established. Two hollow cylindrical electrodes through which the electrolyte passed were connected to an electrometer to determine the resulting streaming potential U_{str} as a function of the pressure difference Δp.

An electrical double layer of ions is formed at the solid–liquid interface of charged surfaces. The mobile ions in the diffuse layer, i.e., those beyond the plane of the shear, are forced to delocalize from their equilibrium distance when an external pressure is applied and liquid streams along the solid surface [34,35]. The resulting ion delocalization leads to a shift of charges compared to equilibrium without external liquid flow. Consequently, ion movement occurs. This ion movement by the liquid flow accumulates charges at the end of the channel under open-circuit conditions. Thus, a potential builds up for a given pressure difference Δp, which is the streaming potential U_{str}. The current and potential due to the liquid streaming through the channel can be directly measured if two electrodes are placed at both ends of the measurement cell. The relation between ζ and U_{str} is given by the Helmholtz-Smoluchowski approximation [34]:

$$\zeta = \frac{\eta K_L}{\varepsilon_r \varepsilon_0} \frac{U_{str}}{\Delta p} \tag{1}$$

where η is the dynamic viscosity, K_L is the bulk conductivity of the liquid, ε_r is the relative permittivity of the continuum phase, and ε_0 is the permittivity of free space. Equation (1) is based on a two-dimensional flow and a fully developed laminar flow regime in a rectangular channel with a corresponding aspect ratio. In addition, the channel is composed of two chemically identical surfaces. To account for asymmetric electrode potentials, the flow was also reversed for each pressure [64], and discrete pressure ramps were applied to perform a linear regression for eq. (1) [65].

ζ can be also derived for planar-flow cells with two chemically different surfaces [58]. Walker et al. proposed a relation between the measured asymmetric zeta-potential ζ_{Avg}, the zeta-potential of the reference material ζ_{Ref}, and the zeta-potential for the substrate under evaluation ζ_{Test}, respectively:

$$\zeta_{Test} = 2\zeta_{Avg} - \zeta_{Ref} \tag{2}$$

In order to apply eq. (2), ζ_{Ref} has to be determined beforehand in a symmetric cell configuration according to eq. (1). Here, we used PTFE as a reference material for the asymmetric planar-flow cell, which is shown in Fig. 1b.

The electrokinetic charge density σ in the diffuse layer can be calculated from ζ by the modified Grahame equation according to Ohshima [66]:

$$\sigma = \frac{2\varepsilon_r \varepsilon_0 k_B T}{e} \kappa sinh\left(\frac{e\zeta}{2k_B T}\right) \tag{3}$$

κ^{-1} is the so-called Debye length, which is given for a 1:1 electrolyte as [17]:

$$\kappa^{-1} = \sqrt{\frac{\varepsilon_r \varepsilon_0 k_B T}{2N_A I e^2}} \tag{4}$$

Here, k_B is the Boltzmann constant, T is the temperature, N_A is Avogadrós number, I is the ionic strength in mol m^{-3}, and e is the elementary charge.

3.2. Characterization of the substrates

In this study, we concentrated on two different collector surfaces for the adsorption of PAMAM dendrimers: fused silica and muscovite mica. Both substrates have been previously studied by streaming potential measurements, albeit under slightly different electrolyte conditions [67–69]. Moreover, there is a significant scattering in the literature for the streaming potentials of these two surfaces. Muscovite mica is a natural material [70], hence its properties vary with origin. In addition, the time between preparation and measurement plays an important role [71,72]. Moreover, the release of potassium ions and adsorption of

electrolyte ions to mica account for variations in the reported ζ [72]. Also, in the case of silica, the preparation history is of crucial importance for the electrokinetic properties [73]. All data presented in the following have been acquired with an asymmetric measurement cell. In the case of mica, we also performed a comparison for a symmetric planar-flow cell. The corresponding data are provided in the supporting information (cf. Fig. S8).

Fig. 2a shows ζ of mica as a function of pH for two ionic strengths (1 mM and 5 mM, respectively). The ionic strength of 1 mM is shown only for comparison with the literature values. The here-determined ζ match the values reported previously [67–69]. No significant dependence of ζ on pH has been observed for both ionic strengths, which is in-line with literature [68,74].

Fig. 2b shows ζ as function of pH for fused silica substrates under analogous conditions to mica substrates. The silica wafers have always been freshly oxidized by a modified RCA-procedure [57]. As expected for silica surfaces, a clear dependence of ζ on the pH has been observed [76,77]. The here acquired data at $I = 5$ mM fall between the data reported for $I = 1$ mM and 10 mM [75]. Moreover, the main characteristics of the 1-pK model proposed for silica have been reproduced [73,76–78]. The solid red line in Fig. 2b is based on a total site density of silanol groups $\Gamma = 5{\cdot}10^{8}$ m^{-2} and a pK$_a$ of 5.8, similar to values reported previously [75]. ζ(pH) has been calculated from ψ_d(pH) by

$$\zeta = \frac{4}{k_B T e} arctanh\left[\exp(-\kappa\Delta x) tanh\left(\frac{k_B T e \psi_d}{4}\right)\right] \quad (5)$$

for large κh analogously to Kobayashi et al.[79] where h corresponds to the channel height. For the calculation, we assume a Stern layer capacitance $C_s = 1.4$ F m^{-2} (cf. ref. [75]) and a shift of the shear plane by $\Delta x = 1.5$ nm due to the surface roughness (cf. Fig. S9) of the fused silica substrate [78].

The surface charge densities σ of the substrates are important for the following data analysis and can be calculated using the modified Grahame equation (cf. Eq. (3)) from the here-obtained ζ. In order to verify the validity of Eq. (3) for our purposes, we additionally determined ζ as a function of the ionic strength I for constant pH = 5. Fig. 3 shows the corresponding data for muscovite mica (cf. Fig. 3a) and fused silica (cf. Fig. 3b). Data for mica acquired in a symmetric streaming potential cell are compiled in the SI (cf. Fig. S10) and fall in the same range of values as those obtained with the asymmetric cell. The solid lines indicate the fits to Eq. (3) and provide an estimate of the electrokinetic charge density σ of both substrates. We find σ = -6.9 ± 0.2 mC m^{-2} for muscovite mica and -8.4 ± 0.4 mC m^{-2} for fused silica. The latter value for the silica substrate is in good agreement with values calculated from the literature under nearly comparable conditions with -8.3 ± 1.9 mC m^{-2} by Scales et al. and -8.1 ± 1.1 mC m^{-2} by Kosior et al., respectively [67,80]. The lower charge density of the mica substrate can be rationalized in terms of ion adsorption [81]. Nevertheless, the charge density for mica was lower than reported elsewhere, albeit measured at higher pH [67,82]. However, also smaller values have been reported from Israelachvili and Adams [83]. Lyons and coworkers [74] found no dependence for mica of ζ on pH with low ζ-values, using the mica as the aforementioned study. Hence, there might be a relationship between low charge densities and no obvious pH dependence.

3.3. Adsorption of PAMAM dendrimers

PAMAM dendrimers are monodisperse macromolecules, which have an onion-like structure and a spherical shape in solution (cf. Fig. 4a) [20,84]. For PAMAM G10 a radius $a_{sol} = 6.75$ nm in solution has been reported [28]. However, upon adsorption onto a solid substrate, the dendrimers deform (cf. schematic representation in Fig. 4b) as demonstrated by simulations [51–53], and corroborated by AFM imaging [22,22,28,85–88]. When adsorbed to mica, their radius increases while flattening leads to a reduced height. Here, we assume $a_{ads} = 9.15$ nm and a height of 4.28 nm [28]. Recent studies indicate that the dimensions in the adsorbed state depend on the electrolyte, pH, ionic strength, and type of substrate [49,50]. A PAMAM G10 dendrimer has 4096 ionizable groups, which are practically all charged at pH 4–5 [89]. However, the condensation of counter ions does lead to a strongly reduced effective charge Z_{eff} compared to the bare charge. For Z_{eff}, Bocquet et al. approximated the limit of low ionic strength and large particle radii a [54]:

$$Z_{eff} = \frac{a}{L_B}(4\kappa a + 6) \quad (6)$$

where L_B is the Bjerrum length and a is the radius. This Z_{eff} is responsible for the interdendrimer or interparticle repulsion in the extended (or electrostatic) RSA model and leads in the framework of the RSA model to an increased, effective radius that critically depends on the total ionic strength [4,31].

The adsorption kinetics and the resulting saturated layer of adsorbed PAMAM dendrimers has been studied previously [28,32,33,38,47,48,90]. PAMAM adsorption can be followed by atomic force microscopy (AFM) [28,32], quartz crystal microbalance (QCM) [47], streaming potential [38], and reflectometry [33,90]. The

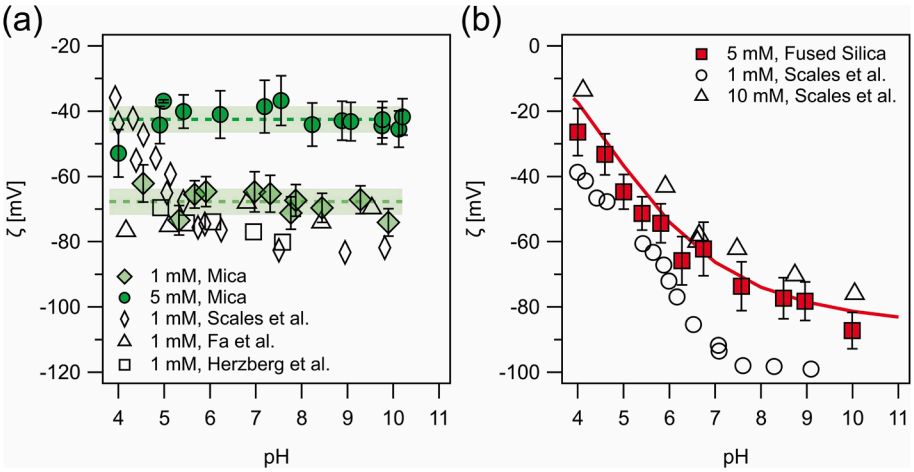

Fig. 2. Zeta-potential ζ of (a) muscovite mica and (b) fused silica as functions of pH (filled data points) in KCl. The pH titrations of mica were carried out at ionic strengths of 1 mM and 5 mM, whereas silica was studied only at 5 mM. All data presented have been acquired using an asymmetric cell. For comparison, data reported in the literature are shown (open data points) [67–69,75]. The dashed lines are the mean constant ζ with the corresponding standard deviations for ζ for mica at 1 mM and 5 mM ionic strength, respectively, in (a), while the solid line represents the 1-pK model used to describe the pH dependence of silica (b).

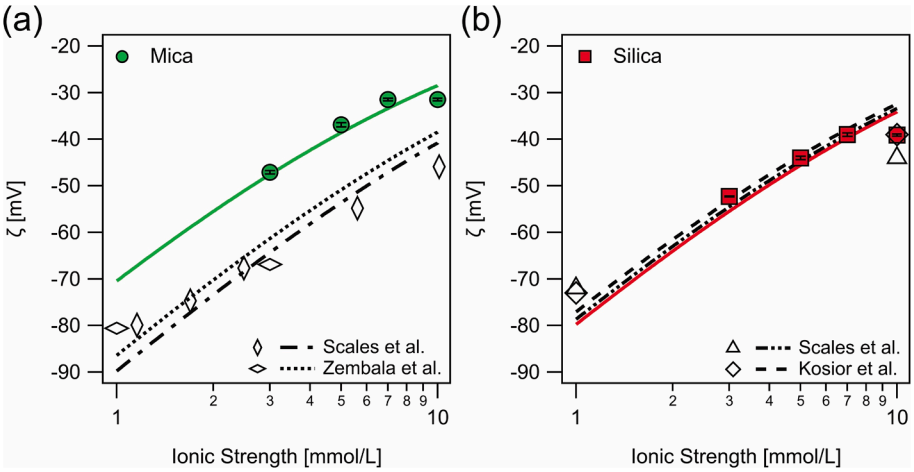

Fig. 3. Zeta-potential ζ of muscovite mica (a) and fused silica (b) as function of the ionic strength at pH = 5. Open symbols show literature data acquired at pH 5.8 [67,75,80,82]. Fits to the modified Grahame equation of the presented data are shown as solid lines. The broken and dashed lines originate from fits to the literature data.

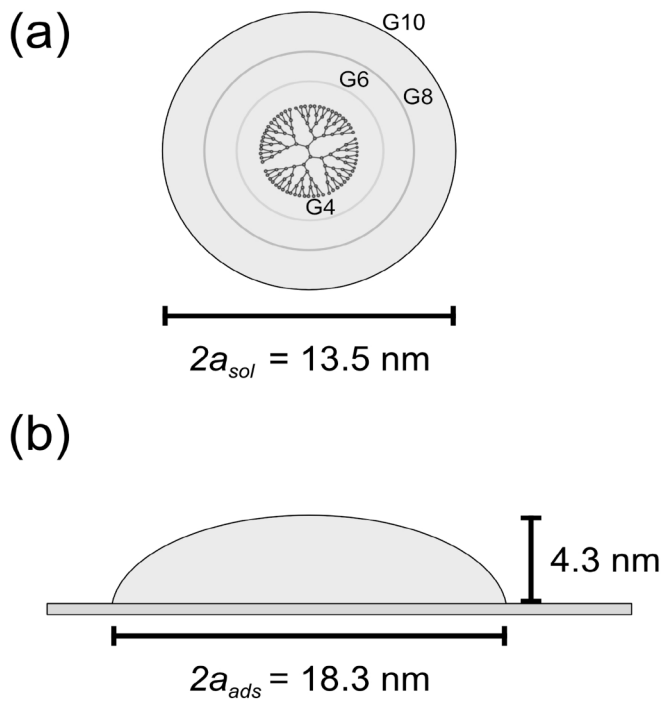

Fig. 4. (a) Schematic representation of poly(amidoamine) (PAMAM) dendrimers of generation 10 in solution. The different generations grow in an onion-like structure during polymerization. PAMAM G10 has a solution radius a_{sol}. Modified from Pericet-Camara et al. [32] (b) Upon adsorption, the dendrimers flatten with a larger radius a_{ads} [28]. The geometrical dimensions used in this study are shown.

adsorption of PAMAM G10 dendrimers can be qualitatively described within the framework of the electrostatic random sequential (RSA) model [28]. Due to the repulsion between the dendrimers based on the overlap of their electrical double layers, the surface coverage depends on the electrostatic screening and thus the electrolyte's ionic strength. However, the charge of the collector surface creates a double layer. This affects the screening length and changes the interdendrimer interaction potential as described by the 3-body RSA model [32,33].

Fig. 5 shows AFM images of substrates with PAMAM G10 adsorbed on mica and silica substrates. The images were acquired in air using PeakForce Tapping® mode. As expected, different fractional surface coverages were obtained depending on the adsorption time. For adsorption times greater than 15 min, an adsorption plateau was reached for both types of surfaces. Due to the repulsive interaction between the like-charged dendrimers, there remains a minimal distance between the adsorbed dendrimers, as predicted by the extended RSA model. Moreover, the substrate has an influence according to the 3-body RSA model [32,33]. The previously reported lower coverage on silica than for mica has also been observed here [32]. However, it should be noted that the effect was less pronounced as the adsorption was carried out at a higher ionic strength compared to the aforementioned study. The number of adsorbed dendrimers was determined by automatic image analysis from at least five AFM images acquired at different spots on the substrates. To convert dendrimer number densities to fractional surface coverage θ, we used previously reported dimensions of adsorbed PAMAM G10 dendrimers of a_{ads} = 9.15 nm [28]. It should be stressed that a quantitative description of the adsorption kinetics is not necessary for the here-conducted experiments, as the surface coverage can be determined independently by AFM imaging for each adsorption time.

3.4. Fractional surface coverage and zeta-potential ζ

Fig. 6 plots the surface coverage θ as function of adsorption time t. A linear dependence $\theta(t) \propto \sqrt{t}$ has been observed as long as the so-called jamming limit has not been reached, which is in-line with a diffusion limited transport [24,28,33]. This dependence $\propto \sqrt{t}$ has been observed for the initial adsorption onto both substrates (cf. Fig. 6a,b). The similar slopes for mica (cf. Fig. 6a) and silica (cf. Fig. 6b) indicate that the sticking coefficients for both surfaces were approximately comparable. For both materials, the surface coverage reached a plateau for $t \gtrsim 15$ min. These findings were also verified for mica in a symmetric streaming potential cell (cf. Fig. S12 and the corresponding data in Fig. S11). The existence of plateaus with $\theta < 1$ in coverage was expected within the framework of the RSA model and corresponded to the jamming limit θ_{jam} based on the effective radius of the PAMAM G10 dendrimers due to their electrostatic interaction. However, the plateaus differed significantly for these two substrates, which has already been observed previously [32]. On fused silica, a surface coverage of about $\theta_{plat} = 0.092 \pm 0.002$ has been determined. By contrast, we found about $\theta_{plat} = 0.135 \pm 0.003$ for mica. We compared the experimental values to the theoretical values for θ_{plat} calculated on the basis of the extended RSA model, considering Z_{eff} based on the mean-field approach according to Eq. (6). We found a clear deviation from the experimental values. We return to this point at a later stage when Z_{eff} will be determined independently by the streaming potential measurements presented in the following.

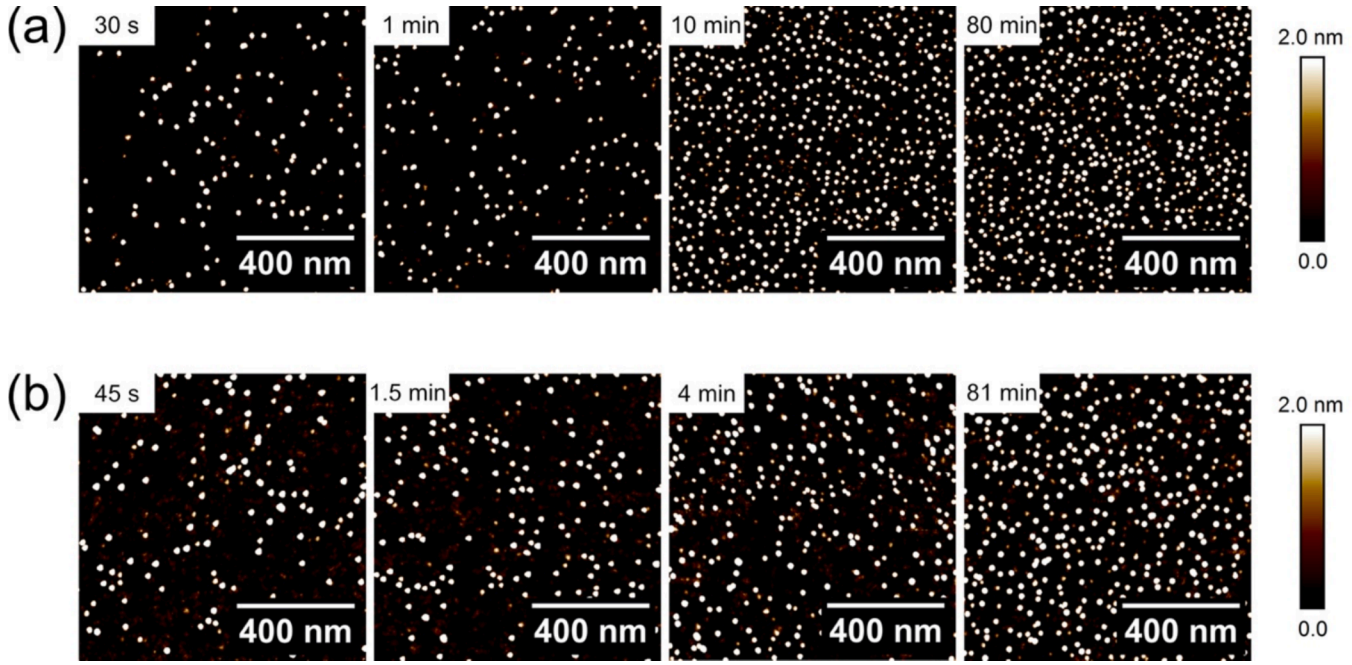

Fig. 5. AFM images of PAMAM G10 dendrimers adsorbed on (a) mica and (b) silica surfaces for different adsorption times. The scan size was always 1 μm x 1 μm and the images were acquired in air using PeakForce Tapping® mode. Slight variations in the dimensions of the dendrimers were attributed to the different AFM tips used.

Fig. 6c,d show ζ as function of the adsorption time t determined according to equations (1) and (2). The fractional surface coverage was characterized by AFM for a simultaneously prepared sample. For both surfaces, the values of $\zeta(t)$ correlate strongly with coverage $\theta(t)$. This correlation is elucidated in the following paragraph in more detail as it allows to estimate Z_{eff}.

3.5. Determination of effective charge in the adsorbed state

Fig. 7a shows ζ as a function of the fractional surface coverage θ. For both substrates ζ was increasing quasi-linearly with surface coverage. However, the slope of this increase is significantly different and is related to a different Z_{eff} on both substrates: Assuming that each PAMAM G10 dendrimer carries an effective charge Z_{eff} and occupies an area $A_{PAMAM} = \pi a_{ads}^2$, we can attribute an electrokinetic charge density σ_0^{PAMAM} to the places where dendrimers are adsorbed

$$\sigma_0^{PAMAM} = \frac{eZ_{eff}}{\pi a_{ads}^2} \tag{7}$$

Thus, we obtain the total electrokinetic charge density σ for a substrate with σ_0^{sub} with a given fractional surface coverage θ of PAMAM G10 dendrimers as follows:

$$\sigma = \sigma_0^{sub} + \theta\sigma_0^{PAMAM} \tag{8}$$

This equation considers the complete charge of the bare substrate rather than only the area that is not covered by dendrimers, which would correspond to 1-θ. Thereby, the charge compensation in between dendrimers and substrate in the adsorption sites is accounted for. A similar expression for linear superposition of charges has been postulated previously by Miklavic [91], Adamczyk and coworkers for streaming potential measurements of adsorbed linear as well as branched polyelectrolytes [38,45,46,92], and by Pericet-Camara et al. for direct force measurements with the colloidal probe technique [55]. Based on equations (7) and (8), we determined the effective charge for each fractional surface coverage on both substrates. The modified Grahame equation (3) was used to convert the measured ζ to σ while θ has been independently determined from the AFM images. Fig. 7b shows the thereby determined values for Z_{eff} as a function of the fractional surface coverage θ. The corresponding results obtained with the symmetric streaming potential cell are presented in the SI (cf. Fig. S13).

For both substrates, the dendrimeŕs effective charge was independent of the surface coverage. Hence, no inter-dendrimer charge regulation was present for the separation distances studied here. However, we found two very different effective charges for the two substrates. In the case of mica $Z_{eff}|_{\text{mica}} = 141 \pm 21$, which differs significantly from $Z_{eff}|_{\text{silica}} = 265 \pm 78$ on fused silica. The former value is much closer to the mean field approximation in a bulk solution of $Z_{eff} = 115$ under the conditions studied here, i.e., $I = 5$ mM. It should also be noted that all measurements were performed at pH 5. At this pH, the dendrimers should be nearly fully charged according to titration data [89]. However, it should be pointed out that this approximation is valid for low ionic strength [54]. This condition might not be strictly fulfilled for the ionic strength utilized here.

3.6. Effective charge as function of pH

To further elucidate the role of the substrate for the effective charge of the dendrimers, we varied the pH as a further parameter. The pH was varied only post-adsorption: The dendrimers were adsorbed first at pH 5, and then the pH of the solution was varied, while streaming potential data were acquired. The pH titrations were carried out in this way to ensure constant surface coverage. We assume that no dendrimers were removed during these measurements because it is known that dendrimers of higher generations, i.e., PAMAM > G6, adhere strongly to the substrate at all pH [90]. The corresponding ζ-values as function of the solution pH for the bare substrates have been presented previously in Fig. 3 for pH 4–10 and constant ionic strength $I = 5$ mM. For comparison, these data ($\theta = 0$) are also included in Fig. 8a and 8b, which show ζ for surface coverages of $\theta \approx 0.03$ (3 %) and $\theta \approx 0.09$ (9 %), respectively. Additionally, a higher surface coverage of $\theta \approx 0.13$ (13 %) was studied in the case of mica (cf. Fig. 8a).

For both dendrimer-covered substrates, a significant change of ζ as function of pH has been observed. A striking feature of both graphs is the

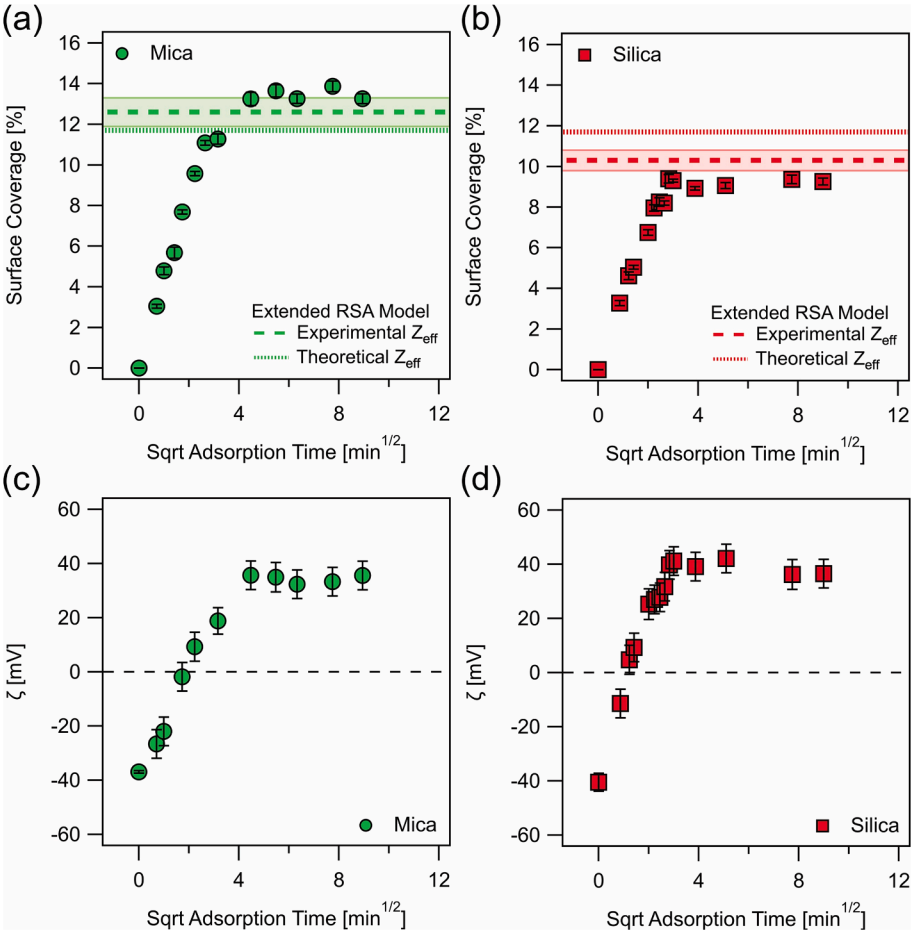

Fig. 6. Fractional surface coverage (a, b) and zeta-potential ζ (c, d) as functions of adsorption time $t^{1/2}$ at a constant pH 5 and ionic strength of 5 mM. The data for muscovite mica are shown in green (a, c), whereas the data for fused silica are shown in red (b, d). The dashed colored lines show the jamming limit calculated by experimental Z_{eff} from streaming potential (cf. Fig. 7b), while the dotted lines represent the jamming limit calculated by theoretical Z_{eff} (cf. Eq. (6)). The jamming limit was calculated as reported previously for PAMAM G10 [28]. (For interpretation of the references to colour in this figure legend, the reader is referred to the web version of this article.)

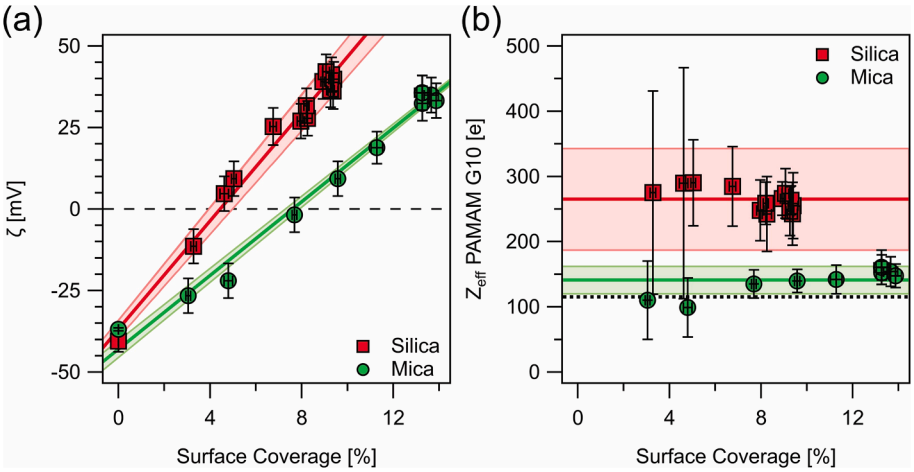

Fig. 7. (a) Zeta-potential ζ as a function of surface coverage for silica (red) and mica (green) at pH 5 and ionic strength $I = 5$ mM. The solid lines are fits assuming a linear dependence of ζ on the fractional surface coverage, including the fit errors as colored regions around the fit line. (b) Effective charge Z_{eff} in units of the elementary charge as a function of the surface coverage. The solid lines represent the mean of these Z_{eff} and the corresponding standard deviation (shaded area). The dotted line represents the mean field approximation for a PAMAM G10 dendrimer in solution according to equation (6). (For interpretation of the references to colour in this figure legend, the reader is referred to the web version of this article.)

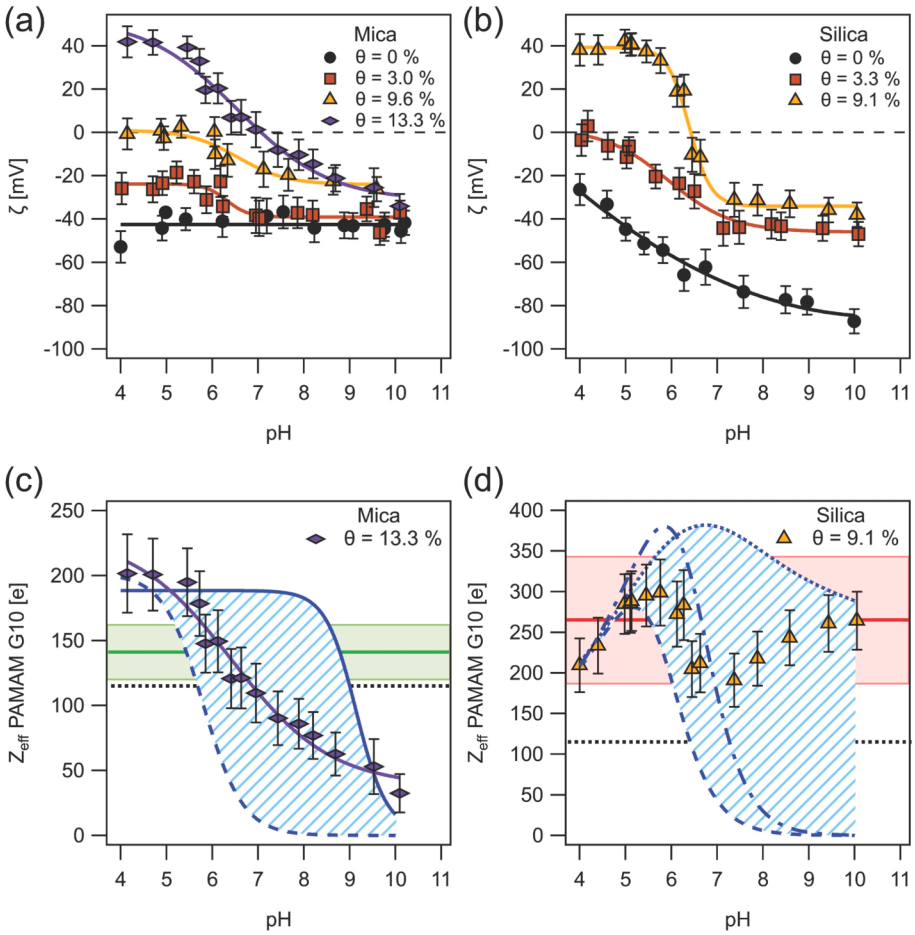

Fig. 8. (a) Zeta-potential ζ versus pH for bare mica (black) and three different surface coverages of PAMAM G10 dendrimers. (b) Zeta-potential ζ versus pH for fused silica (black) and two different surface coverages of PAMAM G10 dendrimers. (c) Calculated effective charge Z_{eff} of single PAMAM G10 dendrimers on mica as a function of pH. Z_{eff} was calculated only for the highest surface coverage. The dashed blue line represents ionization according to the Henderson-Hasselbalch equation with the pK = 5.8 [89] while the purple line represents a fit to a sigmoidal function, resulting in pK = 6.5 ± 0.1. The solid blue line represents the renormalized data from Michna et al. originating from the electrophoretic mobility of PAMAM G8 dendrimers [38]. The solid green line represents the mean experimental Z_{eff} on mica from Fig. 7b at pH 5 for comparison. (d) Calculated effective charge Z_{eff} of single PAMAM G10 dendrimers on silica as a function of pH. The dashed and broken blue lines represent the data for Z_{eff} calculated by Henderson-Hasselbalch with either the theoretical pK [89] or the pK obtained from the fit to the sigmoidal function in Fig. 8c (cf. purple line in Fig. 8c). The dotted blue line represents the sigmoidal fit to the experimental data for mica (cf. purple line in Fig. 8c) combined with Z_{eff} calculated by Eq. (6) for PAMAM at silica. In all cases, theoretical Z_{eff} were normalized following Eq. (9) and the variation in the effective inverse Debye-length κ_{eff} due to the pH dependence of the silica substrate was considered. For mica, a constant value (cf. black line Fig. 7a) was assumed. The solid red line represents the mean experimental Z_{eff} on silica (Fig. 7b) at pH 5. (For interpretation of the references to colour in this figure legend, the reader is referred to the web version of this article.)

presence of an isoelectric point where ζ and thus, the overall electrokinetic charge completely vanished and then changed sign with increasing pH. This charge-inversion effect only occurred at the highest surface coverages of $\theta = 0.13$ for mica and $\theta = 0.09$ for silica, respectively. Only for such high coverages a sufficient number of dendrimers adsorb and their positive charges allowed to compensate for the intrinsic charge of the collector substrates. A comparison of ζ as function of pH at the respective maximum coverage points is shown in Fig. S14. The overall pK for the PAMAM-covered substrates can be derived based on Ottewill's and Shaw's procedure [93]. However, for all coverages θ, a quasi-sigmoidal dependence of ζ on pH was observed for both substrates. The calculated pKs are roughly in line with the inflection points in Fig. 8a and 8b and are summarized in the supporting information (cf. Table S5).

The interpretation of the sigmoidal shape of ζ(pH) is more straightforward for mica than for silica, as former does not vary with pH. For mica, ζ of the bare surface remained constant for all the pH values studied here (cf. black data points in Fig. 8a). Hence, a constant σ can be assumed and any change in ζ(pH) must be attributed to the ionization of the adsorbed dendrimers as their coverage θ remained constant. Qualitatively, one expects that the tertiary amine groups are deprotonated in the acidic regime and thus the positive charge contributions diminish at higher pH, which has also been observed experimentally by bulk titrations [89]. Based on equations (7) and (8), we can calculate Z_{eff}(pH) from the ζ(pH)-measurements. The resulting data for Z_{eff}(pH) on mica and silica are shown in Fig. 8c and 8d for $\theta = 0.13$ and $\theta = 0.09$, respectively. The data for the lower surface coverages are shown in the SI (Fig. S15a and S15b) and show a similar pH dependence for mica. A fit according to a sigmoidal function gives a pK = 6.5 ± 0.1 for PAMAM G10 dendrimers on mica, which is in good correspondence with the extrapolation of pK = 5.8 by Cakara et al. for higher dendrimer generations G6-G10 in bulk solution [89]. The resulting dependence is shown as a dashed line according to the Henderson-Hasselbalch equation with $Z_{ref} \approx 200$ at pH = 4 and:

$$Z_{eff}(pH) = Z_{ref} \bullet \widetilde{Z}_{eff}(pH) = Z_{ref} \bullet e^{-(pK-pH)} \quad (9)$$

These data can also be compared to the electrophoretic mobility of single PAMAM G8 dendrimers in suspension as reported by Michna et al.

(cf. solid blue line in Fig. 8c) [38]. Please, notice that we normalized the experimental fit to the electrophoretic mobility data for PAMAM G8 dendrimers (cf. Fig. 2 in ref. [38]) to obtain $0 \leq \widetilde{Z}_{eff}(\mathrm{pH}) \leq 1$ and $\widetilde{Z}_{eff}(\mathrm{pH}=4)=1$ from the experimental data rather than the theoretical values according to Henderson-Hasselbalch. The experimental data for the PAMAM G8 dendrimers corroborate the limitations of Eq. (6), indicating the influence of the substrate on Z_{eff}.

For the PAMAM G10 dendrimers adsorbed on silica, Z_{eff}(pH) exhibited a more complex behavior. Silica varies its charge with pH as described within the framework of the 1-pK model with pK = 5.8 (cf. Fig. 2b) [75]. While the overall ζ(pH)-curves of the silica with adsorbed PAMAM G10 dendrimers showed a pronounced sigmoidal behavior (cf. Fig. 8b), the derived effective charge Z_{eff}(pH) of the single PAMAM dendrimers did not follow the same trend as on mica (cf. Fig. 8c). The effective charge for the PAMAM G10 dendrimers shows instead a slightly oscillatory behavior around a much higher effective charge of $Z_{eff} \sim 270$ and does not decline steeply in the basic regime as for PAMAM G10 dendrimers on mica or in bulk solution. This change is most likely attributed to the charging behavior of silica, which leads to an increased counterion concentration at the interface with increasing pH. Desorption of PAMAM G10 would be unlikely as origin for the oscillatory behavior of Z_{eff} and would occur only at very high pH if at all [38,90]. As a first approximation, we consider the influence of the substrate on the local ion concentration around the dendrimers *via* an effective inverse Debye length κ_{eff} [33]:

$$\kappa_{eff} = \kappa \cosh\left(\frac{e\psi_d}{k_B T}\right) \tag{10}$$

Here, κ is the inverse bulk Debye length of the electrolyte solution and ψ_d the diffuse layer potential at the solid substrate, which can be approximated by $\psi_d \simeq \zeta(\mathrm{pH})$. Please note that an expression analogous to Eq. (10) is used in the 3-body RSA model to account for the reduced interaction between dendrimers on a highly charged substrate [32,33]. By utilizing κ_{eff} at the interface rather than κ in Eq. (6) to calculate Z_{eff}, the influence of varying charge with pH on silica can be modeled. Here, we assume that the titration of the dendrimers and substrate are independent of each other and that the latter provides only modulation of the former by its diffuse layer. Hence, the results of Eq. (6) and Eq. (10) resulting in a $Z_{eff}(\mathrm{pH})$ due to counter-ion condensation are multiplied with $\widetilde{Z}_{eff}(\mathrm{pH})$ due to the deprotonation of the charged groups. Again, $\widetilde{Z}_{eff}(\mathrm{pH})$ results from the Henderson-Hasselbalch equation for dendrimer ionization (dashed blue line in Fig. 8c,d) or bulk electrophoretic mobility (solid blue line, Fig. 8c). The renormalized data from Michna et al. originating from the electrophoretic mobility of PAMAM G8 dendrimers was calculated analogously to the dotted blue line in Fig. 8d (cf. Fig. S16 in the SI). Interestingly, our data for the PAMAM G10 dendrimer Z_{eff} on silica corresponded rather well to the simple boundary conditions enforced in Fig. 8d. Noticeably, the decrease in Z_{eff} for $5.5 < \mathrm{pH} < 8$ is matched rather well. However, at higher pH values, when the dendrimer charge diminishes significantly, other processes, such as the direct charge regulation between the dendrimer and substrate [50,53], are playing an increasingly important role compared to counter ion condensation.

4. Conclusions

In this study, we found that the common assumption of the superposition of charge from the substrate and adsorbed polyelectrolytes (cf. Eq. (8)) holds with surprisingly good accuracy. We could also reproduce for mica the dependence of the streaming potential from PAMAM G10 dendrimer coverage as reported by Michna et al. for PAMAM G8 [38]. Hence, the ζ-potential indeed provides a good indicator for polyelectrolyte coverage as utilized in various studies, including for linear polyelectrolytes [44–46]. Moreover, the adsorption of charged biomacromolecules, such as humic acids, to membranes can be followed by streaming potential with high accuracy [94]. We did not find any indication of inter-dendrimer charge regulation. However, for fractional coverages of less than 20 %, the spacing between the dendrimers was larger than the Debye length, which is a typical length scale in which charge regulation plays a crucial role.

This study highlights the somehow neglected importance of substrates for the effective charge of macromolecules. As the effective charge governs the intermolecular interaction forces, they are crucial in the framework of the electrostatic RSA model. Our measurements clearly show that the commonly used approximation by Bocquet et al. [54] underestimates the effective charge in many cases, especially for highly charged substrates. In this case, the effective Debye length due to counterions from the substrates provides a much better approximation than the bulk Debye length. While this effect is not of importance for colloidal particles with diameters > 20 nm, it should be considered when describing the adsorption of macromolecules. The effective Debye length has been considered previously to model inter-molecular interaction potentials in the framework of the 3-body RSA model [33]. However, it is more consistent to include the effect of κ_{eff} also on the effective charge. Finally, there could also be an influence on direct force measurements. Previously, it has been assumed that Z_{eff} remains constant for heterogeneously charged surfaces [55]. However, for separation distances D between the two surfaces that are below the bulk Debye length, the counter ion concentration increases and might have an influence by a distance-dependent effect on κ_{eff} and thereby on Z_{eff}. For $D < \kappa^{-1}$ charge regulation also plays an important role, which is primarily of chemical origin [95,96]. Varying the electrolyte composition might help in the future to separate the mean-field approach to the effective charge by counter ion condensation from the influence of charge regulation, either between the adsorbed macromolecules themselves or between macromolecule and substrate.

CRediT authorship contribution statement

Matthias B. Engelhardt: Writing – review & editing, Writing – original draft, Visualization, Methodology, Investigation, Formal analysis, Conceptualization. **Paul Markus:** Writing – review & editing, Software, Methodology, Investigation, Formal analysis, Conceptualization. **Nicolas Helfricht:** Writing – review & editing, Methodology, Formal analysis. **Georg Papastavrou:** Writing – review & editing, Writing – original draft, Supervision, Resources, Project administration, Funding acquisition, Formal analysis, Conceptualization.

Declaration of competing interest

The authors declare that they have no known competing financial interests or personal relationships that could have appeared to influence the work reported in this paper.

Acknowledgments

G.P. thanks Dr. Brian Cahill (now Hochschule Bielefeld) for his help with early versions of the streaming potential setup. We thank Dr. Motoyoshi Kobayashi (University of Tsukuba, Japan) for access to the program for calculating the theoretical zeta-potential ζ. This study was funded by the Deutsche Forschungsgemeinschaft (DFG, German Research Foundation): 391977956-SFB 1357/B01, 491183248. M.B.E. thanks the Elite Network of Bavaria through the study program "Macromolecular Science".

Appendix A. Supplementary data

Supplementary data to this article can be found online at https://doi.org/10.1016/j.jcis.2025.02.008.

Data availability

Data will be made available on request.

References

[1] H. G. M. Van de Steeg, M. A. Cohen Stuart, A. De Keizer and B. H. Bijsterbosch, Langmuir, 8(10), 1992, 2538-2546. https://doi.org/10.1021/la00046a030.
[2] R.R. Netz, D. Andelman, Phys. Rep. 380 (1–2) (2003) 1–95, https://doi.org/10.1016/s0370-1573(03)00118-2.
[3] A.V. Dobrynin, M. Rubinstein, Prog. Polym. Sci. 30 (11) (2005) 1049–1118, https://doi.org/10.1016/j.progpolymsci.2005.07.006.
[4] Z. Adamczyk, Curr. Opin. Colloid Interface Sci. 17 (3) (2012) 173–186, https://doi.org/10.1016/j.cocis.2011.12.002.
[5] I. Szilagyi, G. Trefalt, A. Tiraferri, P. Maroni, M. Borkovec, Soft Matter 10 (15) (2014) 2479–2502, https://doi.org/10.1039/c3sm52132j.
[6] A. Abdurahman, K. Cui, J. Wu, S. Li, R. Gao, J. Dai, W. Liang, F. Zeng, Ecotox. Environ. Safe. 198 (2020) 110658, https://doi.org/10.1016/j.ecoenv.2020.110658.
[7] T. Hüffer, A. Praetorius, S. Wagner, F. Von der Kammer, T. Hofmann, Environ. Sci. Technol. 51 (5) (2017) 2499–2507, https://doi.org/10.1021/acs.est.6b04054.
[8] R.B. Schefer, A. Armanious, D.M. Mitrano, Environ. Sci. Technol. 57 (39) (2023) 14707–14716, https://doi.org/10.1021/acs.est.3c04180.
[9] J. Gregory, J. Colloid Interface Sci. 42 (2) (1973) 448–456, https://doi.org/10.1016/0021-9797(73)90311-1.
[10] P.M. Claesson, A. Dedinaite, O.J. Rojas, Adv. Colloid Interface Sci. 104 (1–3) (2003) 53–74, https://doi.org/10.1016/S0001-8686(03)00036-8.
[11] M. Schönhoff, J. Phys. Condens. Matter 15 (49) (2003) R1781, https://doi.org/10.1088/0953-8984/15/49/R01.
[12] M. Borkovec, I. Szilagyi, I. Popa, M. Finessi, P. Sinha, P. Maroni, G. Papastavrou, Adv. Colloid Interface Sci. 179 (2012) 85–98, https://doi.org/10.1016/j.cis.2012.06.005.
[13] J.N. Anker, W.P. Hall, O. Lyandres, N.C. Shah, J. Zhao, R.P. Van Duyne, Nat. Mater. 7 (2008) 442–453, https://doi.org/10.1038/nmat2162.
[14] J. Homola, Chem. Rev. 108 (2) (2008) 462–493, https://doi.org/10.1021/cr068107d.
[15] A. Michna, Adv. Colloid Interface Sci. 250 (2017) 95–131, https://doi.org/10.1016/j.cis.2017.09.004.
[16] D. Johannsmann, I. Reviakine, Nat. Rev. Methods Primers 4 (2024) 63, https://doi.org/10.1038/s43586-024-00340-4.
[17] H. Butt, K. Graf, M. Kappl, Physics and chemistry of interfaces, WILEY-VCH, Weinheim, 2003.
[18] R.R. Netz, J.-F. Joanny, Macromolecules 32 (26) (1999) 9013–9025, https://doi.org/10.1021/ma990263h.
[19] A.V. Dobrynin, A. Deshkovski, M. Rubinstein, PhysRevLett. 84 (14) (2000) 3101, https://doi.org/10.1103/PhysRevLett.84.3101.
[20] D.A. Tomalia, H. Baker, J. Dewald, M. Hall, G. Kallos, S. Martin, J. Roeck, J. Ryder, P. Smith, Macromolecules 19 (9) (1986) 2466–2468, https://doi.org/10.1021/ma00163a029.
[21] V.A. Kabanov, A.B. Zezin, V.B. Rogacheva, Z.G. Gulyaeva, M.F. Zansochova, J.G. H. Joosten, J. Brackman, Macromolecules 31 (15) (1998) 5142–5144, https://doi.org/10.1021/ma971643a.
[22] V.V. Tsukruk, Adv. Mater. 10 (3) (1998) 253–257, https://doi.org/10.1002/(SICI)1521-4095(199802)10:3<253::AID-ADMA253>3.0.CO;2-E.
[23] Z. Adamczyk, B. Siwek, M. Zembala, P. Belouschek, Adv. Colloid Interface Sci. 48 (1994) 151–280, https://doi.org/10.1016/0001-8686(94)80008-1.
[24] J. Feder, J. Theor. Biol. 87 (2) (1980) 237–254, https://doi.org/10.1016/0022-5193(80)90358-6.
[25] P. Kubala, P. Batys, J. Barbasz, P. Weroński, M. Cieśla, Adv. Colloid Interface Sci. 306 (2022) 102692, https://doi.org/10.1016/j.cis.2022.102692.
[26] P.R. Van Tassel, P. Viot, G. Tarjus, J. Chem. Phys. 106 (2) (1997) 761–770, https://doi.org/10.1063/1.473164.
[27] M. Morga, A. Michna, Z. Adamczyk, Colloid Surf. A 529 (2017) 302–310, https://doi.org/10.1016/j.colsurfa.2017.05.033.
[28] R. Pericet-Camara, G. Papastavrou, M. Borkovec, Langmuir 20 (8) (2004) 3264–3270, https://doi.org/10.1021/la035955k.
[29] J.W. Evans, RevModPhys. 65 (4) (1993) 1281, https://doi.org/10.1103/RevModPhys.65.1281.
[30] J. Talbot, G. Tarjus, P.R. Van Tassel, P. Viot, Colloid Surf. A 165 (1–3) (2000) 287–324, https://doi.org/10.1016/S0927-7757(99)00409-4.
[31] Z. Adamczyk, P. Warszyński, Adv. Colloid Interface Sci. 63 (1996) 41–149, https://doi.org/10.1016/0001-8686(95)00281-2.
[32] R. Pericet-Camara, B.P. Cahill, G. Papastavrou, M. Borkovec, Chem. Commun. 3 (2007) 266–268, https://doi.org/10.1039/b612249c.
[33] B.P. Cahill, G. Papastavrou, G.J. Koper, M. Borkovec, Langmuir 24 (2) (2008) 465–473, https://doi.org/10.1021/la7021352.
[34] A.V. Delgado, F. González-Caballero, R.J. Hunter, L.K. Koopal, J. Lyklema, J. Colloid Interface Sci. 309 (2) (2007) 194–224, https://doi.org/10.1016/j.jcis.2006.12.075.
[35] R.J. Hunter, Zeta potential in colloid science, Elsevier, 1981.
[36] R.W. O'Brien, L.R. White, J. Chem. Soc., Faraday Trans. 2 (74) (1978) 1607–1626, https://doi.org/10.1039/F29787401607.
[37] H. Ohshima, J. Colloid Interface Sci. 163 (2) (1994) 474–483, https://doi.org/10.1006/jcis.1994.1126.
[38] A. Michna, Z. Adamczyk, K. Sofińska, K. Matusik, J. Colloid Interface Sci. 485 (2017) 232–241, https://doi.org/10.1016/j.jcis.2016.09.007.
[39] R. Zimmermann, W. Norde, M.A. Cohen Stuart, C. Werner, Langmuir 21 (11) (2005) 5108–5114, https://doi.org/10.1021/la050191p.
[40] Z. Adamczyk, K. Sadlej, E. Wajnryb, M. Nattich, M.L. Ekiel-Jeżewska, J. Bławzdziewicz, Adv. Colloid Interface Sci. 153 (1–2) (2010) 1–29, https://doi.org/10.1016/j.cis.2009.09.004.
[41] Z. Adamczyk, M. Zaucha, M. Zembala, Langmuir 26 (12) (2010) 9368–9377, https://doi.org/10.1021/la1003534.
[42] C. V. Ruiz M, M. Terlinden, M. Engelhardt, G. Magnabosco, G. Papastavrou, N. Vogel, M. Thommes and J. Bachmann, Adv. Mater. Interfaces, 10(33), 2023, 2300436. https://doi.org/10.1002/admi.202300436.
[43] A. Hofer, N. Taccardi, M. Moritz, C. Wichmann, S. Hübner, D. Drobek, M. Engelhardt, G. Papastavrou, E. Spiecker, C. Papp, RSC Adv. 13 (6) (2023) 4011–4018, https://doi.org/10.1039/D2RA07585G.
[44] A. Michna, Z. Adamczyk, K. Kubiak, K. Jamroży, J. Colloid Interface Sci. 428 (2014) 170–177, https://doi.org/10.1016/j.jcis.2014.04.013.
[45] M. Morga, Z. Adamczyk, J. Colloid Interface Sci. 407 (2013) 196–204, https://doi.org/10.1016/j.jcis.2013.05.069.
[46] M. Morga, Z. Adamczyk, S. Gödrich, M. Oćwieja, G. Papastavrou, J. Colloid Interface Sci. 456 (2015) 116–124, https://doi.org/10.1016/j.jcis.2015.05.044.
[47] B. Jachimska, K. Tokarczyk, J. Phys. Chem. C 120 (35) (2016) 19678–19685, https://doi.org/10.1021/acs.jpcc.6b05020.
[48] A. Michna, A. Pomorska, M. Nattich-Rak, M. Wasilewska, Z. Adamczyk, J. Phys. Chem. C 124 (32) (2020) 17684–17695, https://doi.org/10.1021/acs.jpcc.0c04638.
[49] L. Muresan, P. Maroni, I. Popa, M. Porus, R. Longtin, G. Papastavrou, M. Borkovec, Macromolecules 44 (13) (2011) 5069–5071, https://doi.org/10.1021/ma201103n.
[50] M. Porus, F. Clerc, P. Maroni, M. Borkovec, Macromolecules 45 (9) (2012) 3919–3927, https://doi.org/10.1021/ma3004295.
[51] M. Gosika, P.K. Maiti, Soft Matter 14 (10) (2018) 1925–1938, https://doi.org/10.1039/C8SM00179K.
[52] P. Wolski, T. Panczyk, J. Phys. Chem. C 123 (36) (2019) 22603–22613, https://doi.org/10.1021/acs.jpcc.9b05752.
[53] M. Gosika, T. Mandal, P.K. Maiti, Langmuir 36 (20) (2020) 5492–5501, https://doi.org/10.1021/acs.langmuir.0c00208.
[54] L. Bocquet, E. Trizac, M. Aubouy, J. Chem. Phys. 117 (17) (2002) 8138–8152, https://doi.org/10.1063/1.1511507.
[55] R. Pericet-Camara, G. Papastavrou, M. Borkovec, Macromolecules 42 (5) (2009) 1749–1758, https://doi.org/10.1021/ma802374z.
[56] W. de Poel, S. Pintea, J. Drnec, F. Carla, R. Felici, P. Mulder, J.A.A.W. Elemans, W. J.P. van Enckevort, A.E. Rowan, E. Vlieg, Surf. Sci. 619 (2014) 19–24, https://doi.org/10.1016/j.susc.2013.10.008.
[57] W. Kern and D. A. Puotinen, RCA Review, 31(2), 1970, 187-206, A1970H070100002.
[58] S.L. Walker, S. Bhattacharjee, E.M.V. Hoek, M. Elimelech, Langmuir 18 (6) (2002) 2193–2198, https://doi.org/10.1021/la011284j.
[59] J. Schindelin, I. Arganda-Carreras, E. Frise, V. Kaynig, M. Longair, T. Pietzsch, S. Preibisch, C. Rueden, S. Saalfeld, B. Schmid, J.Y. Tinevez, D.J. White, V. Hartenstein, K. Eliceiri, P. Tomancak, A. Cardona, Nat. Methods 9 (7) (2012) 676–682, https://doi.org/10.1038/nmeth.2019.
[60] R.A. Van Wagenen, J. Colloid Interface Sci. 76 (2) (1980) 305–314, https://doi.org/10.1016/0021-9797(80)90374-4.
[61] C. Werner, H. Körber, R. Zimmermann, S. Dukhin, H.J. Jacobasch, J. Colloid Interface Sci. 208 (1) (1998) 329–346, https://doi.org/10.1006/jcis.1998.5787.
[62] M. Zembala, Z. Adamczyk, P. Warszyński, Colloid Surf. A 222 (1–3) (2003) 329–339, https://doi.org/10.1016/s0927-7757(03)00253-x.
[63] M. Zembala, Adv. Colloid Interface Sci. 112 (1–3) (2004) 59–92, https://doi.org/10.1016/j.cis.2004.08.001.
[64] K.S. Spiegler, Desalination 15 (1) (1974) 135–140, https://doi.org/10.1016/S0011-9164(00)82067-6.
[65] M.C. Wilbert, S. Delagah, J. Pellegrino, J. Membr. Sci. 161 (1–2) (1999) 247–261, https://doi.org/10.1016/S0376-7388(99)00117-9.
[66] H. Ohshima, Theory of colloid and interfacial electric phenomena, Academic Press, 2006.
[67] P.J. Scales, F. Grieser, T.W. Healy, Langmuir 6 (3) (1990) 582–589, https://doi.org/10.1021/la00093a012.
[68] K. Fa, V.K. Paruchuri, S.C. Brown, B.M. Moudgil, J.D. Miller, Phys. Chem. Chem. Phys. 7 (2005) 678–684, https://doi.org/10.1039/b417902a.
[69] M. Herzberg, S. Dobberschütz, D. Okhrimenko, N.E. Bovet, M.P. Andersson, S.L. S. Stipp, T. Hassenkam, EPL 130 (3) (2020) 36001, https://doi.org/10.1209/0295-5075/130/36001.
[70] C.E. Marshall, L.L. McDowell, Soil Sci. 99 (2) (1965) 115–131, https://doi.org/10.1097/00010694-196502000-00009.
[71] U. Raviv, P. Laurat, J. Klein, J. Chem. Phys. 116 (12) (2002) 5167–5172, https://doi.org/10.1063/1.1447911.
[72] P.J. Sides, D. Faruqui, A.J. Gellman, Langmuir 25 (3) (2009) 1475–1481, https://doi.org/10.1021/la802752g.
[73] M. Kobayashi, M. Skarba, P. Galletto, D. Cakara, M. Borkovec, J. Colloid Interface Sci. 292 (1) (2005) 139–147, https://doi.org/10.1016/j.jcis.2005.05.093.
[74] J.S. Lyons, D.N. Furlong, T.W. Healy, Aust. J. Chem. 34 (6) (1981) 1177–1187, https://doi.org/10.1071/ch9811177.
[75] P.J. Scales, F. Grieser, T.W. Healy, L.R. White, D.Y.C. Chan, Langmuir 8 (3) (1992) 965–974, https://doi.org/10.1021/la00039a037.

[76] T. Hiemstra, W.H. Van Riemsdijk, G.H. Bolt, J. Colloid Interface Sci. 133 (1) (1989) 91–104, https://doi.org/10.1016/0021-9797(89)90284-1.
[77] T. Hiemstra, J.C.M. De Wit, W.H. Van Riemsdijk, J. Colloid Interface Sci. 133 (1) (1989) 105–117, https://doi.org/10.1016/0021-9797(89)90285-3.
[78] S.H. Behrens, D.I. Christl, R. Emmerzael, P. Schurtenberger, M. Borkovec, Langmuir 16 (6) (2000) 2566–2575, https://doi.org/10.1021/la991154z.
[79] M. Kobayashi, F. Juillerat, P. Galletto, P. Bowen, M. Borkovec, Langmuir 21 (13) (2005) 5761–5769, https://doi.org/10.1021/la046829z.
[80] D. Kosior, M. Morga, P. Maroni, M. Cieśla, Z. Adamczyk, J. Phys. Chem. C 124 (8) (2020) 4571–4581, https://doi.org/10.1021/acs.jpcc.9b10870.
[81] A.R. Crothers, C. Li, C.J. Radke, Adv. Colloid Interface Sci. 288 (2021) 102335, https://doi.org/10.1016/j.cis.2020.102335.
[82] M. Zembala, Z. Adamczyk, Langmuir 16 (4) (2000) 1593–1601, https://doi.org/10.1021/la9905970.
[83] J. N. Israelachvili, G. E. Adams, J. Chem. Soc., Faraday Trans. 1 (74) (975-1001) 1978. https://doi.org/10.1039/f19787400975.
[84] D.A. Tomalia, Mater. Today 8 (3) (2005) 34–46, https://doi.org/10.1016/S1369-7021(05)00746-7.
[85] T.A. Betley, M.M. Banaszak Holl, B.G. Orr, D.R. Swanson, D.A. Tomalia, J.R. Baker, Langmuir 17 (9) (2001) 2768–2773, https://doi.org/10.1021/la001297h.
[86] V.N. Bliznyuk, F. Rinderspacher, V.V. Tsukruk, Polymer 39 (21) (1998) 5249–5252, https://doi.org/10.1016/S0032-3861(98)00069-X.
[87] A. Hierlemann, J.K. Campbell, L.A. Baker, R.M. Crooks, A.J. Ricco, J. Am. Chem. Soc. 120 (21) (1998) 5323–5324, https://doi.org/10.1021/ja974283f.
[88] J. Li, L.T. Piehler, D. Qin, J.R. Baker, D.A. Tomalia, D.J. Meier, Langmuir 16 (13) (2000) 5613–5616, https://doi.org/10.1021/la000035c.
[89] D. Cakara, J. Kleimann, M. Borkovec, Macromolecules 36 (11) (2003) 4201–4207, https://doi.org/10.1021/ma0300241.
[90] R. Longtin, P. Maroni, M. Borkovec, Langmuir 25 (5) (2009) 2928–2934, https://doi.org/10.1021/la8038818.
[91] S.J. Miklavic, J. Colloid Interface Sci. 171 (2) (1995) 446–455, https://doi.org/10.1006/jcis.1995.1201.
[92] M. Dabkowska, Z. Adamczyk, J. Colloid Interface Sci. 366 (1) (2012) 105–113, https://doi.org/10.1016/j.jcis.2011.09.030.
[93] R.H. Ottewill, J.N. Shaw, Kolloid z. z. Polym. 218 (1) (1967) 34–40, https://doi.org/10.1007/bf01517273.
[94] A.E. Childress, M. Elimelech, J. Membr. Sci. 119 (2) (1996) 253–268, https://doi.org/10.1016/0376-7388(96)00127-5.
[95] S.L. Carnie, D.Y.C. Chan, J. Colloid Interface Sci. 161 (1) (1993) 260–264, https://doi.org/10.1006/jcis.1993.1464.
[96] G. Trefalt, S.H. Behrens, M. Borkovec, Langmuir 32 (2) (2016) 380–400, https://doi.org/10.1021/acs.langmuir.5b03611.

Supporting Information

Effective charge of high-generation PAMAM dendrimers in the adsorbed state

*Matthias B. Engelhardt, Paul Markus, Nicolas Helfricht, and Georg Papastavrou**

Physical Chemistry II, University of Bayreuth, Bayreuth, Germany

Asymmetric streaming potential cell

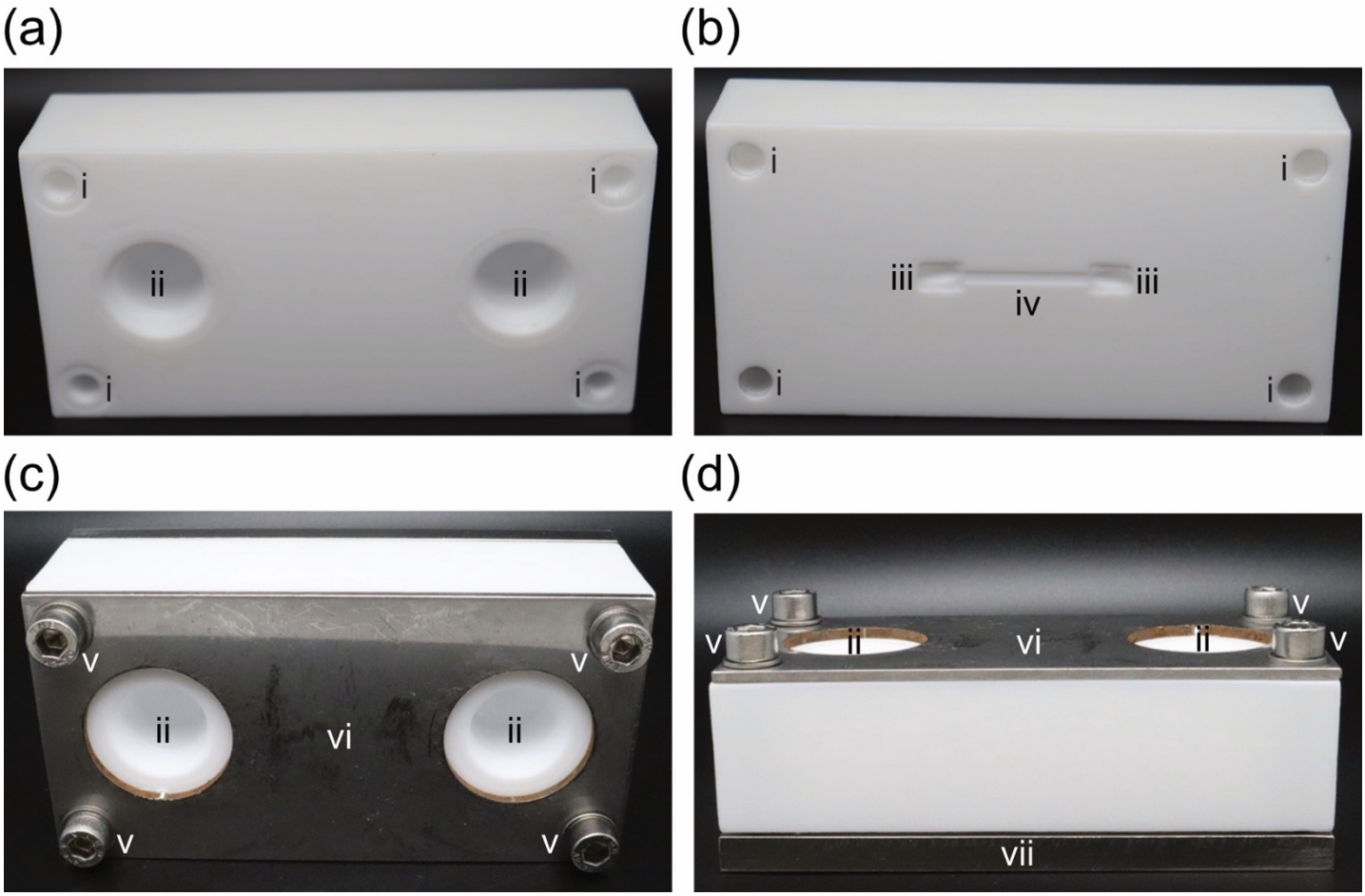

Figure S1: Photos of the (a) top and (b) bottom of the base unit of the asymmetric streaming potential cell. (c) and (d) show the top and side views, including the bracket and base plate.

Table TS1: Components of the asymmetric streaming potential cell shown in Figure S1.

i	Thread to mount the base unit in between the bracket and carrier plate.
ii	Thread connecting the cell to the electrolyte reservoirs, Ag/AgCl electrodes, and the differential pressure sensor.
iii	Channel connecting (i) with the streaming potential channel (iv).
iv	Streaming potential channel. Nominal geometry: L = 2 cm, b = 1.5 mm, h = 300 μm
v	Screws mounting the PTFE cell body between the top bracket (vi) and the carrier plate (viii).
vi	Top bracket
vii	Carrier plate

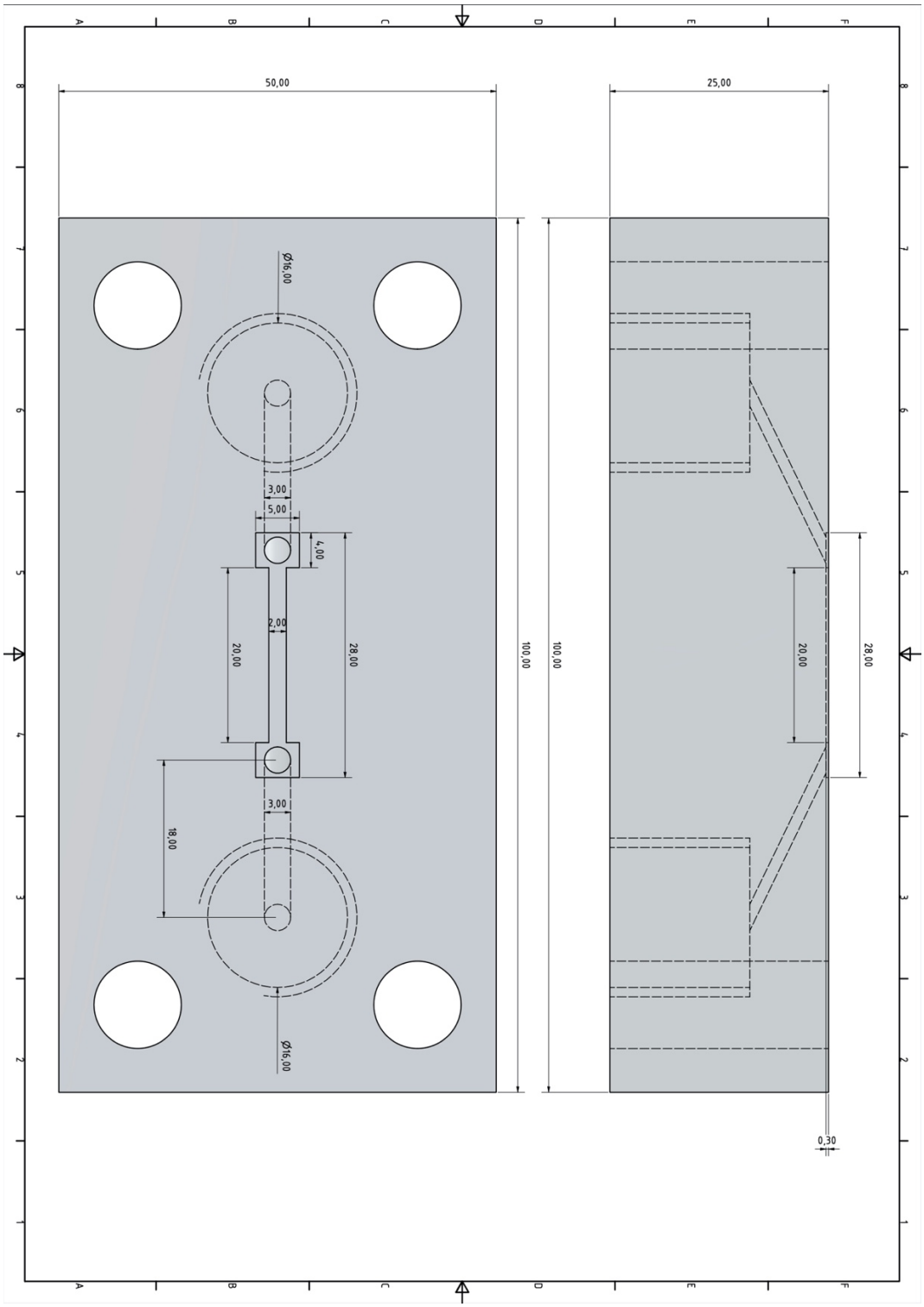

Figure S2: Technical drawing of the asymmetric cell shown in Figure S1.

Symmetric streaming potential cell

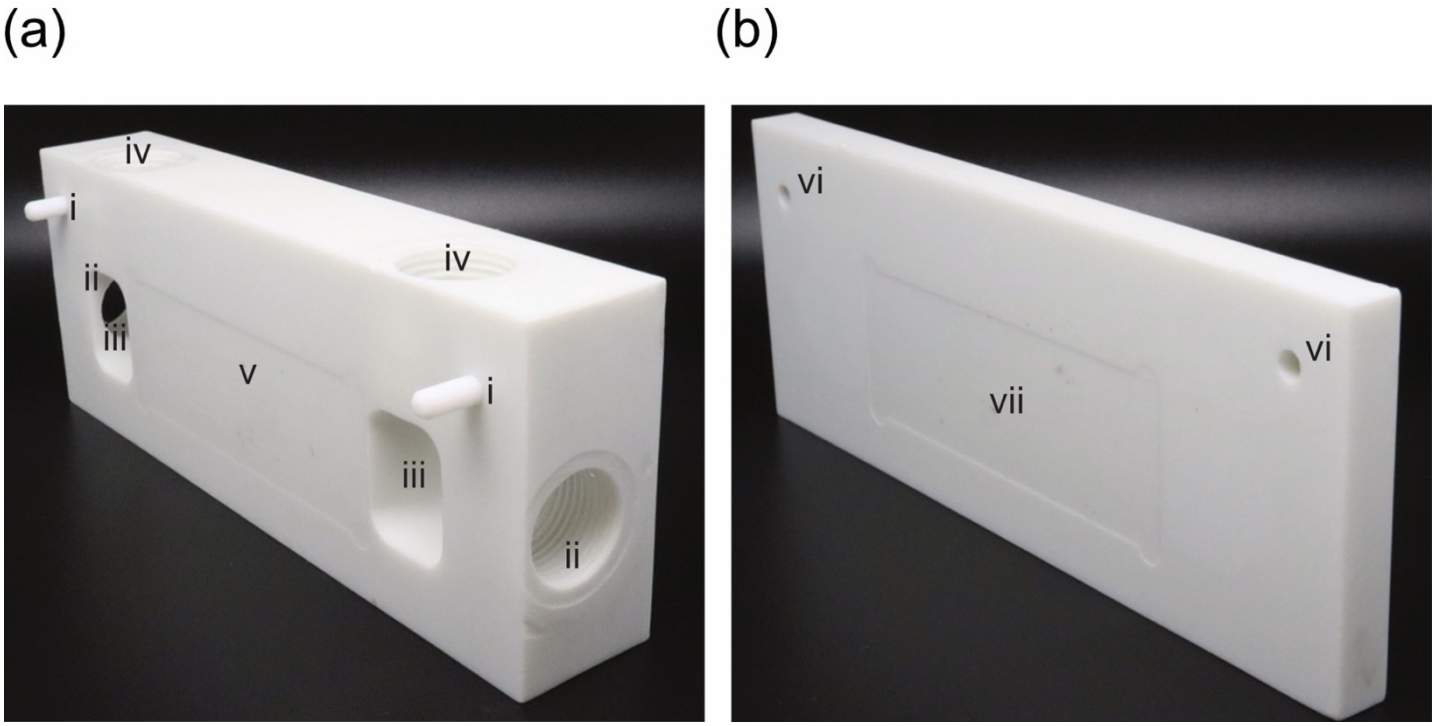

Figure S3: Photos of the (a) base and (b) lid of the symmetric streaming potential cell for (7.5 x 2.5) cm^2 muscovite mica substrates.

Table TS2: Components of the symmetric streaming potential cell shown in Figure S3.

i	Alignment joint to combine the base unit and the lid of the cell.
ii	Thread connecting the cell to the electrolyte reservoirs and Ag/AgCl electrodes.
iii	Intermediate electrolyte volume connecting the reservoirs, differential pressure sensor, and the streaming channel.
iv	Thread connecting both sides of the substrate to the differential pressure sensor.
v	Sample holder in the base unit of the cell.
vi	Alignment joint recess to combine the base unit and the lid of the cell.
vii	Sample holder in the lid of the cell.

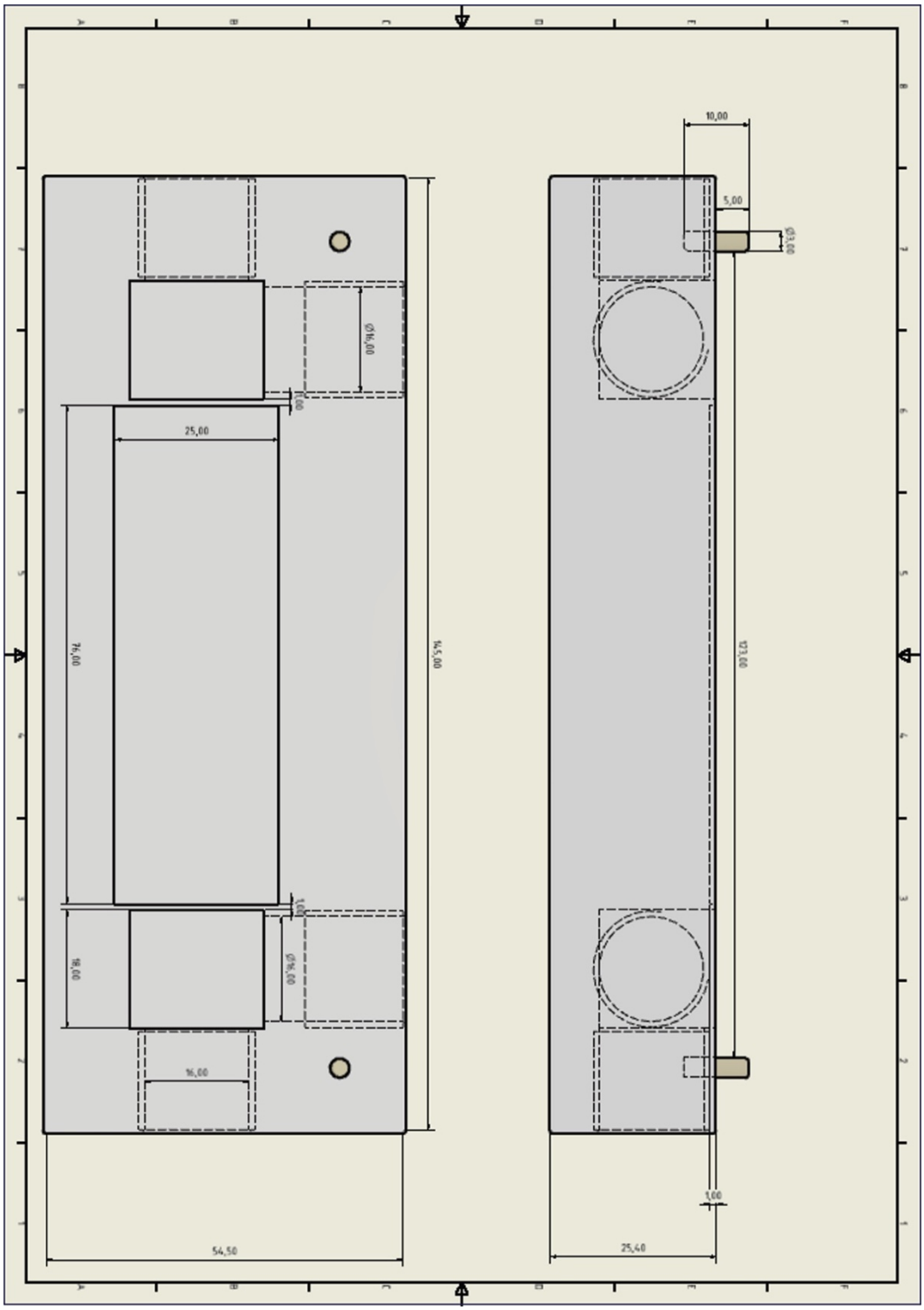

Figure S4: Technical drawing of the base unit of the symmetric cell shown in Figure S3a.

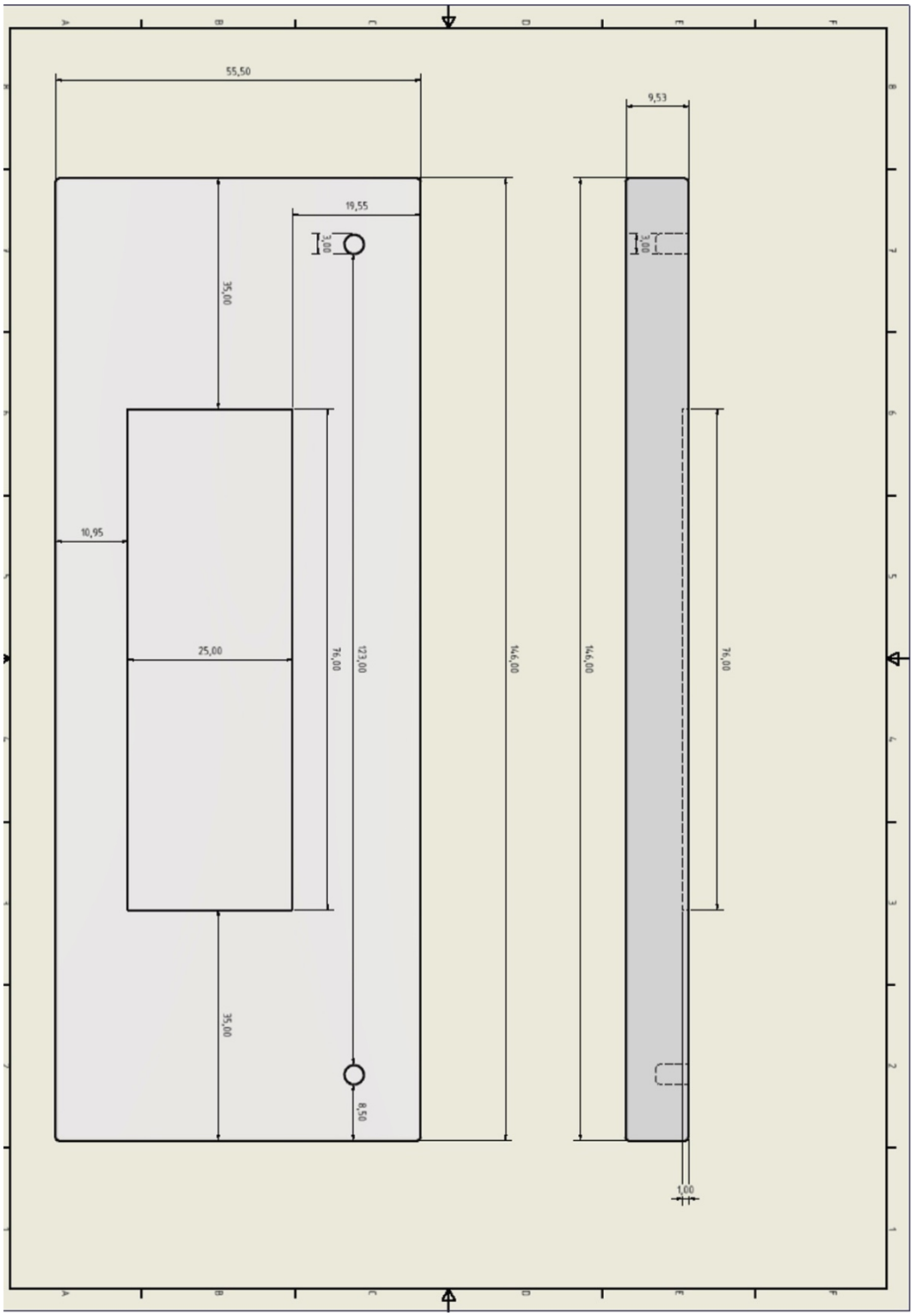

Figure S5: Technical drawing of the lid of the symmetric cell shown in Figure S3b.

Electrokinetic properties of PTFE

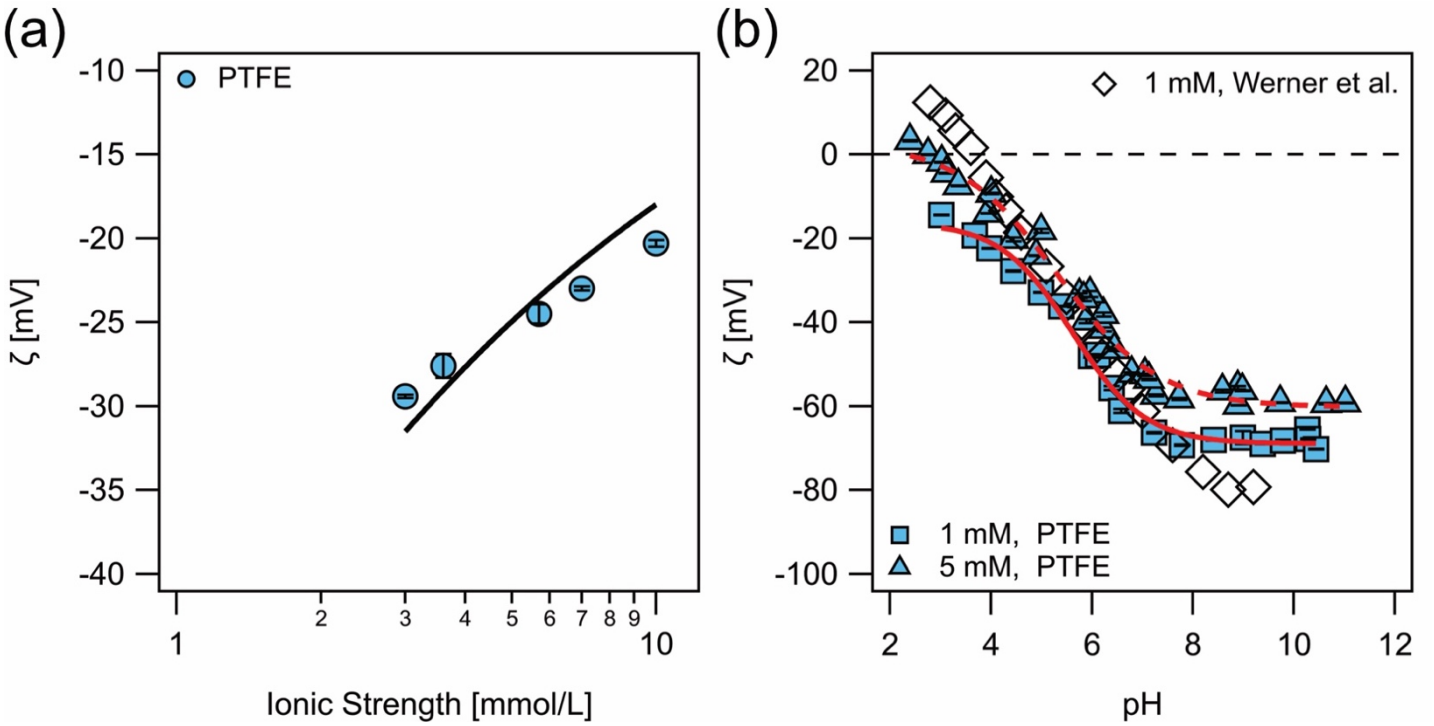

Figure S6: (a) Zeta-potential ζ of PTFE as a function of the total ionic strength I at pH 5. The solid line represents the fit to the modified Grahame equation. (b) Zeta-potential ζ of PTFE as a function of the pH for overall ionic strengths of 1 mM and 5 mM, respectively. Dashed and colored solid lines represent sigmoidal fits for ionic strengths of 1 mM and 5 mM, respectively. Open symbols show the results obtained from plasma-deposited fluoropolymers from Werner and coworkers[1].

Calibration of surface coverage by PAMAM dendrimers

Table TS3: Comparison of the number of dendrimers in 1 μm^2 by manual counting and the counting algorithm used.

Substrate	**Figure**	**Ads. Time [min]**	**dendrimers/μm^2 [Manual, "Cell Counter" Plugin]**	**dendrimers/μm^2 [ImageJ Automatic]**	**% of dendrimers/μm^2 relative to counting**
Mica asym. cell	5a	0.5	119	120	100.8
Mica asym. cell	5a	80	536	494	92.2
Silica asym. cell	5b	0.75	122	125	102.5
Silica asym. cell	5b	81	369	365	98.9
Mica sym. cell	S11	0.5	124	123	99.2
Mica sym. cell	S11	81	536	521	97.2

We evaluated the images listed in Table TS3 with the "Cell Counter"-plugin of the ImageJ software[2] to verify the counting algorithm. Images of the manually counted PAMAM dendrimers on mica and fused silica are shown in Figure S7.

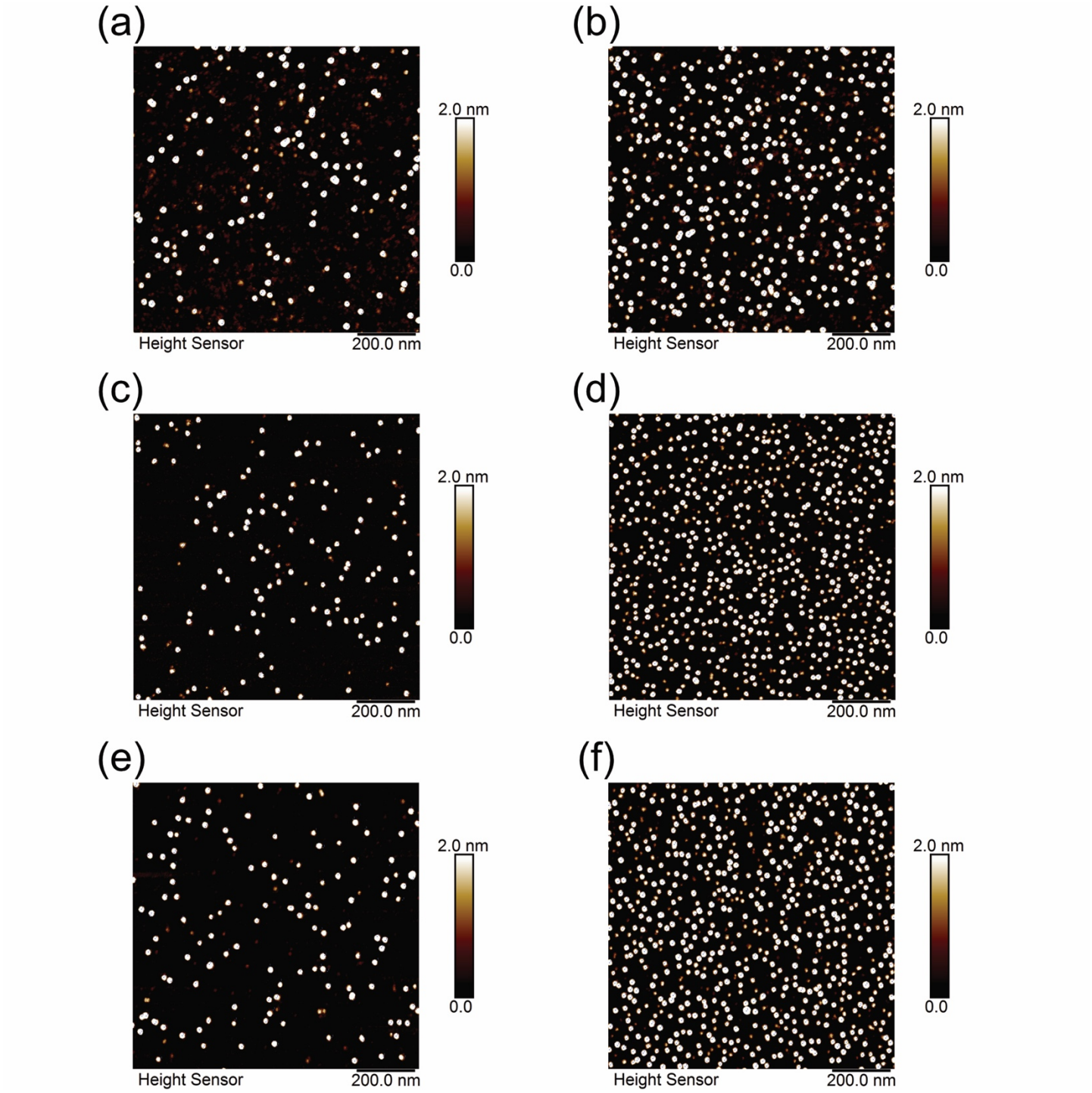

Figure S7: AFM images for PAMAM G10-covered interfaces on silica (a, b) and mica (c-f). All images have a scan-size of 1 x 1 μm^2. Blue dots show the objects considered as dendrimers by manual evaluation. (a, b) correspond to Fig. 5b (45 s and 81 min, respectively), (c, d) correspond to Fig. 5a (30 s and 80 min, respectively), and (e, f) correspond to Fig. S11 (30 s and 81 min, respectively).

Table TS4: Comparison of surface coverages θ of PAMAM G10 dendrimers on fused silica interfaces with varying counting parameters with the software Fiji and its "Analyze Particles" function. Only objects with radii between 6.7 nm and 18.3 nm have been counted as dendrimers.

Radius [nm]	**Coverage θ [%]**
6.7 – 18.3	θ = 9.3
4.0 – 18.3	θ = 10.9
0 – Infinity	θ = 11.8 (counting everything)
Manual counting	θ = 9.7

Electrokinetic properties of mica via the symmetric streaming potential cell

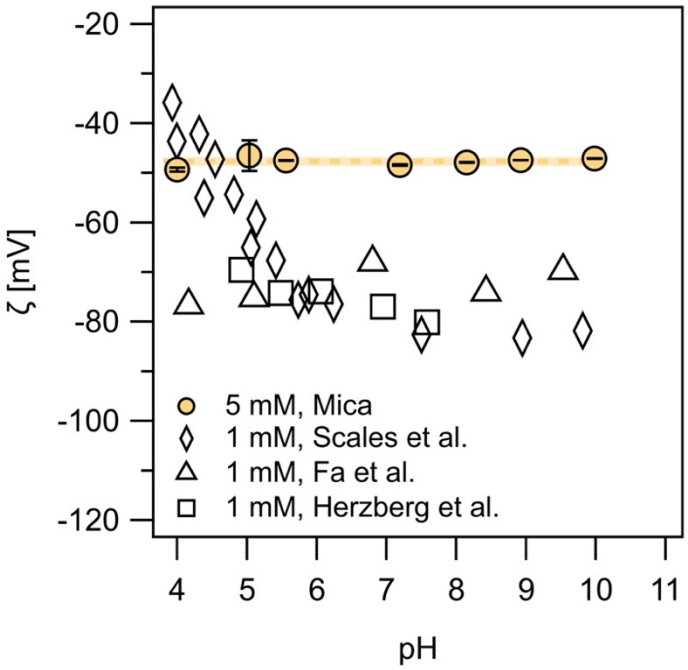

Figure S8: Zeta-potential ζ of muscovite mica as a function of the pH at a constant ionic strength of 5 mM. Literature data for mica at an ionic strength of 1 mM were from Scales et al.[3], Fa et al.[4], and Herzberg et al.[5]. The experimental data for mica (filled symbols) were acquired with the symmetric streaming potential cell. The dashed line is the mean constant zeta- potential ζ with the corresponding standard deviation.

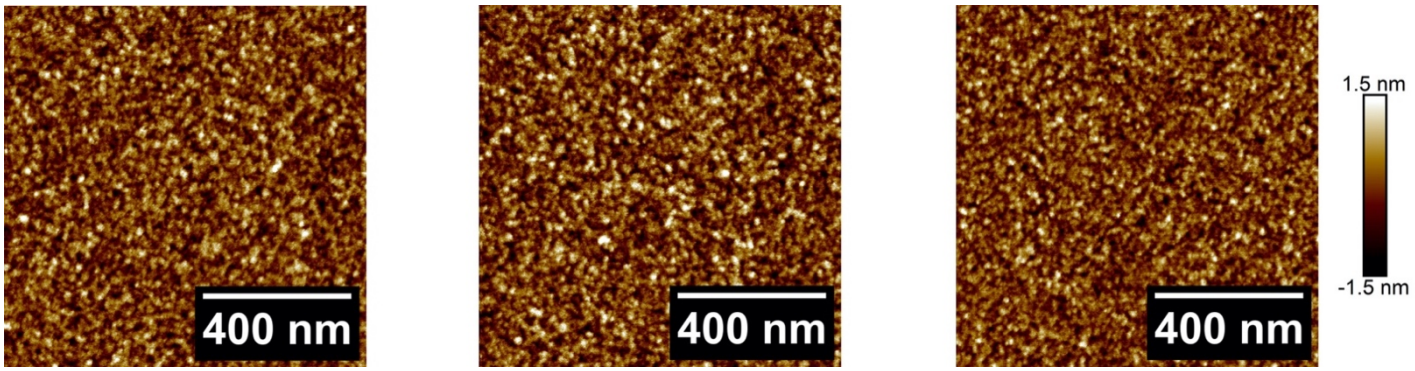

Figure S9: AFM images of fused silica surfaces after the cleaning process. The scan size was 1 µm x 1 µm for all images. The AFM-images have been acquired by PeakForce Tapping® mode in air.

The root-mean-square roughness of the AFM topography images in Figure S9 is R_q = 0.451 ± 0.033 nm while the arithmetic roughness average is R_a = 0.359 ± 0.026 nm. The roughness was evaluated using the in-built function in the NanoScope Analysis software.

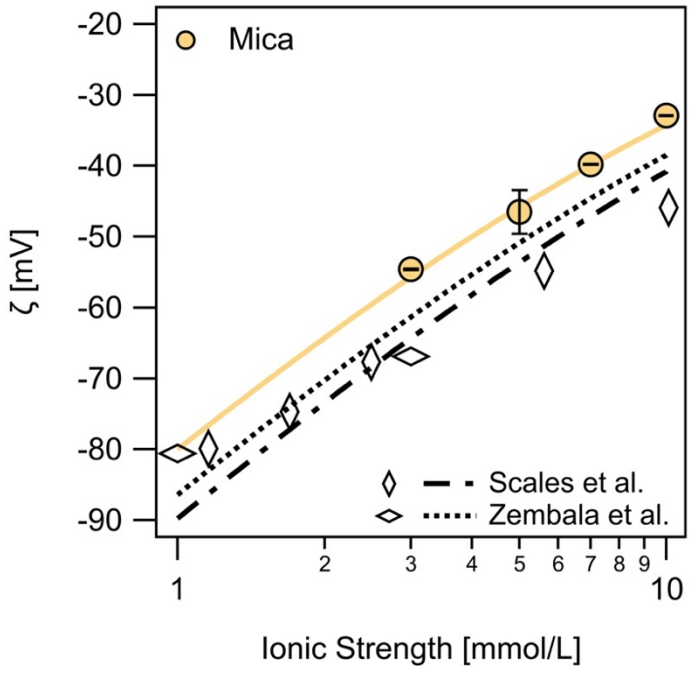

Figure S10: Zeta-potential ζ of muscovite mica as a function of the overall ionic strength in the presence of KCl at pH = 5.0. The data from the literature were measured at pH 5.8 and are indicated by open symbols. Fits to the modified Grahame equation are shown as solid lines for experimental data, broken lines from data of Scales et al.[3], and dotted lines for Zembala and Adamczyk[6].

PAMAM dendrimers adsorbed onto mica and studied in the symmetric streaming potential cell

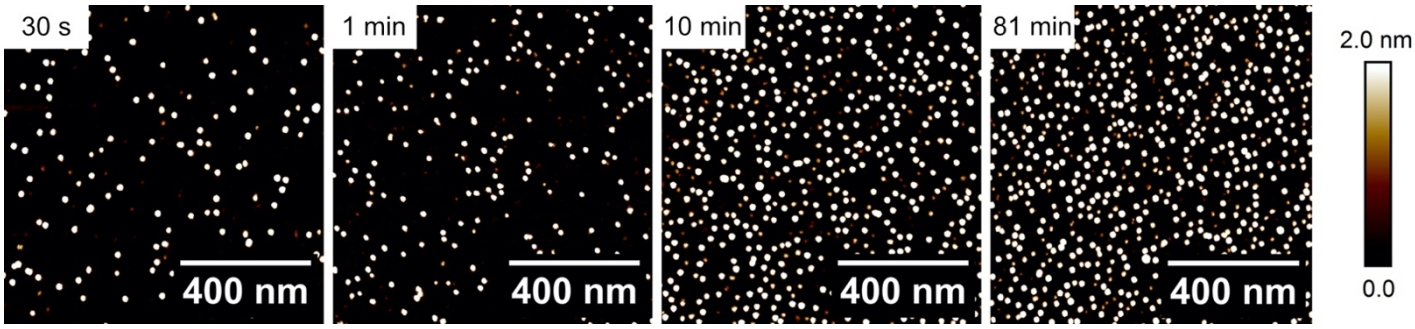

Figure S11: AFM images of adsorbed PAMAM G10 dendrimers for different adsorption times on mica. The scan size was 1 µm x 1 µm for all images. The AFM-images have been acquired by PeakForce Tapping® mode in air. Slight variations in the dimensions of the dendrimers resulted from the different AFM tips used.

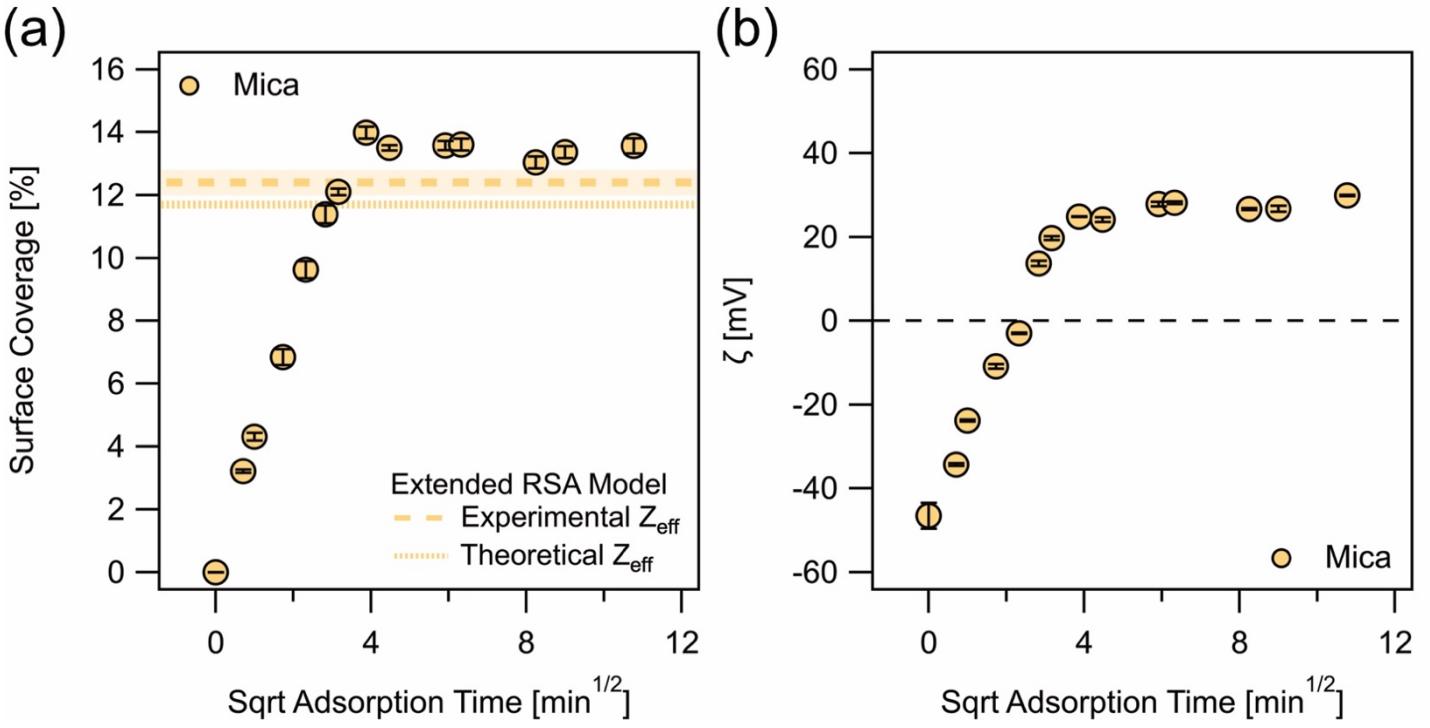

Figure S12: (a) Fractional surface coverage and (b) zeta-potential ζ of adsorbed PAMAM G10 dendrimers as a function of adsorption time ($t^{1/2}$) on mica. The pH = 5.0 and ionic strength I = 5 mM by addition of KCl. The black dashed line represents the isoelectric point. The dashed colored line shows the calculated fractional surface coverage in the jamming limit from the experimentally derived Z_{eff} (cf. Fig. S13b), including the corresponding error as a colored rectangle. The dotted line represents theoretical θ calculated following the extended RSA model[7].

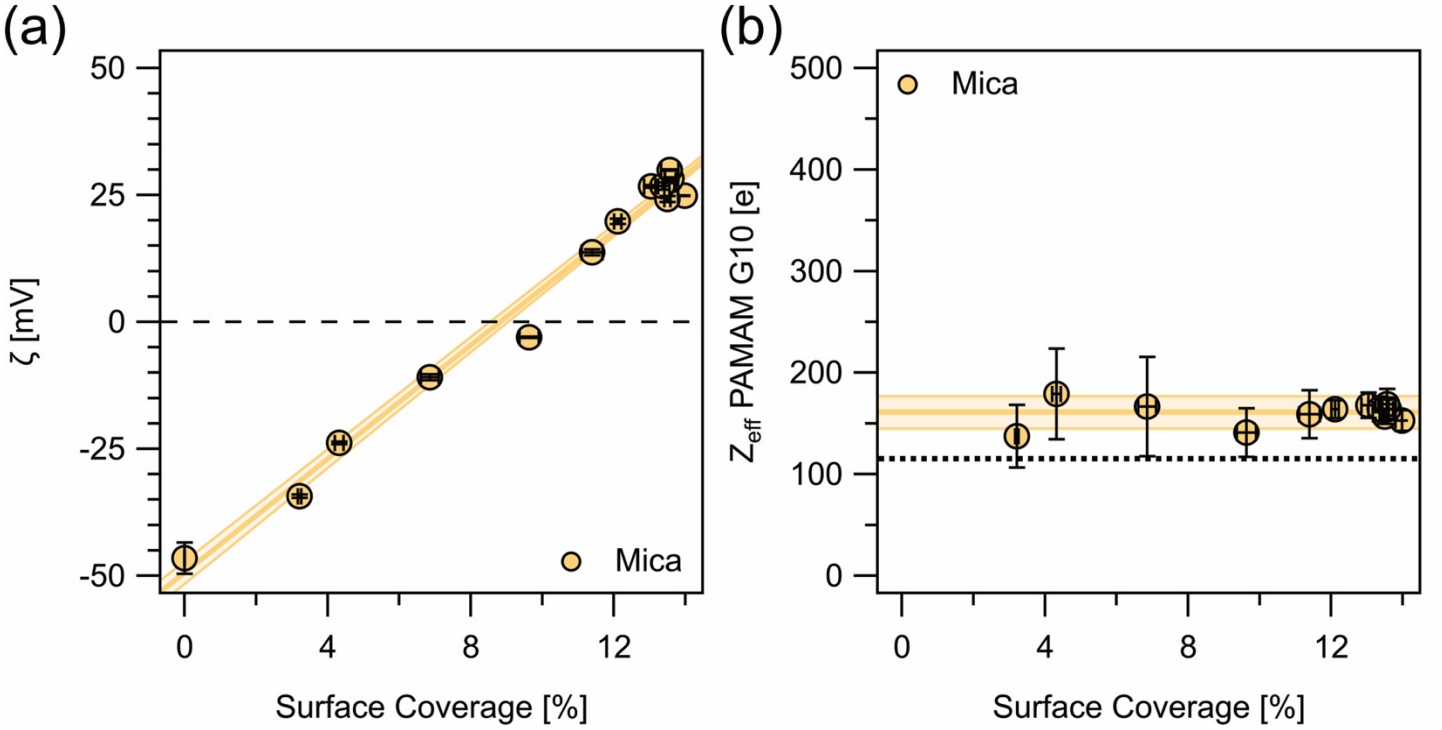

Figure S13 (a) Zeta-potential ζ as a function of the surface coverage for mica. The solid line is a fit assuming a linear dependence of ζ on the fractional surface coverage, including the fit errors as a colored region around the fit line. (b) Effective charge in units of the elementary charge as a function of the surface coverage. The solid line represents the mean effective charge including the corresponding RMS-error as colored rectangle. The dotted line represents the mean field approximation for Z_{eff} of PAMAM G10 dendrimers in solution with I = 5 mM.

pKs of adsorbed PAMAM G10 dendrimers

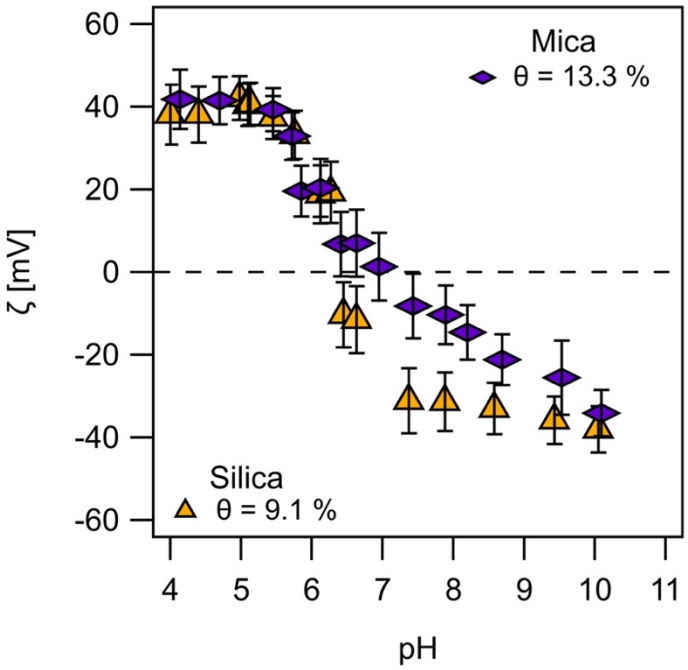

Figure S14: Zeta-potential ζ of PAMAM G10 on mica and fused silica, respectively. The surface coverages on both substrates corresponded to the jamming limits. The ionic strength was I = 5 mM by addition of KCl.

Table TS5: Comparison of determined pKs of the respective maximum surface coverages of PAMAM G10 on mica and silica, respectively.

Substrate	**pK, Ottewill and Shaw[8]**	**pK, Inflection point**	**Coverage [%]**
Mica	6.2 ± 0.2	6.5 ± 0.1	13.3
Silica	6.5 ± 0.2	6.4 ± 0.1	9.1

Effective charge as function of pH

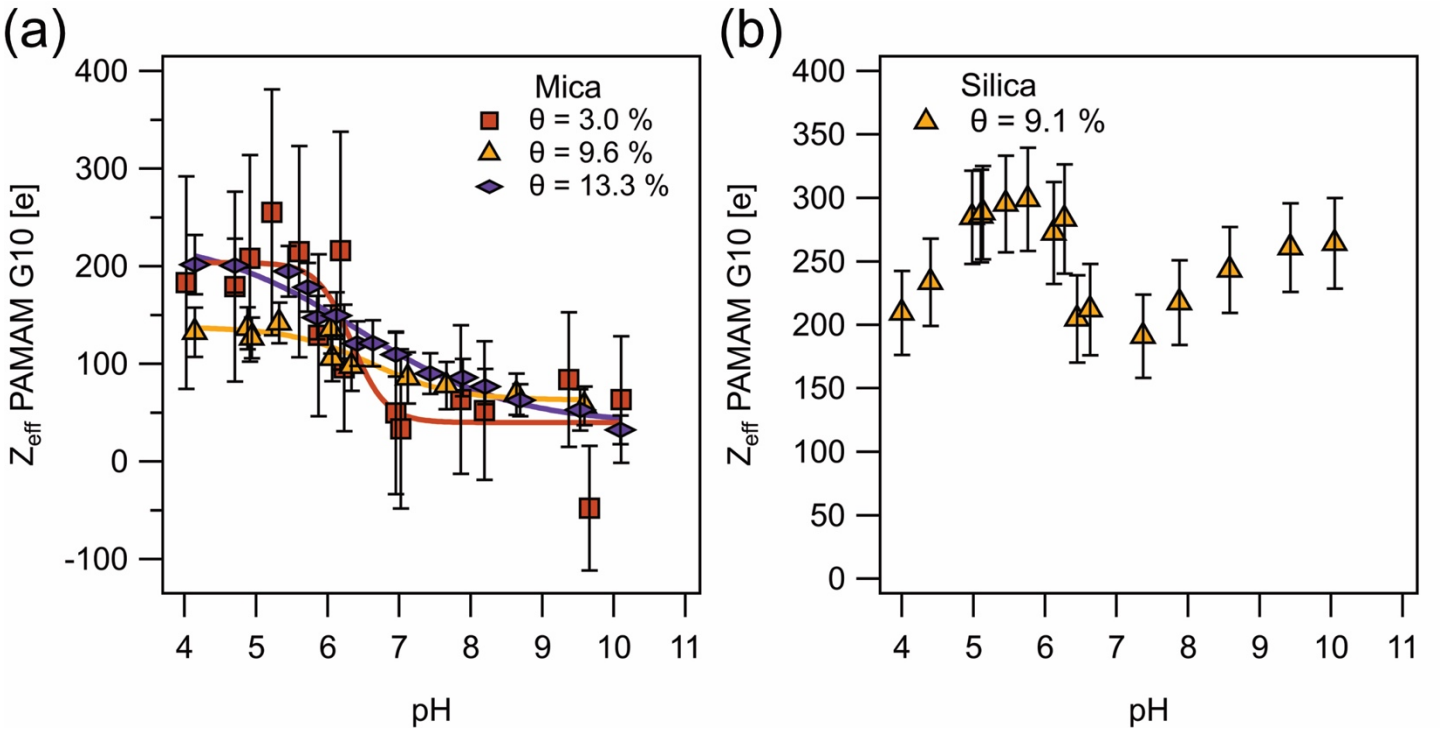

Figure S15: The effective dendrimer charge Z_{eff} for (a) mica and (b) fused silica as function of pH in correspondence to Fig. 8. In the case of silica, the resulting errors are too large for the lower coverages and are not shown. Z_{eff} has been determined by Eq. (3), Eq. (7), and Eq. (8). Measurements were conducted at an overall ionic strength of I = 5 mM. Solid lines show sigmoidal fits.

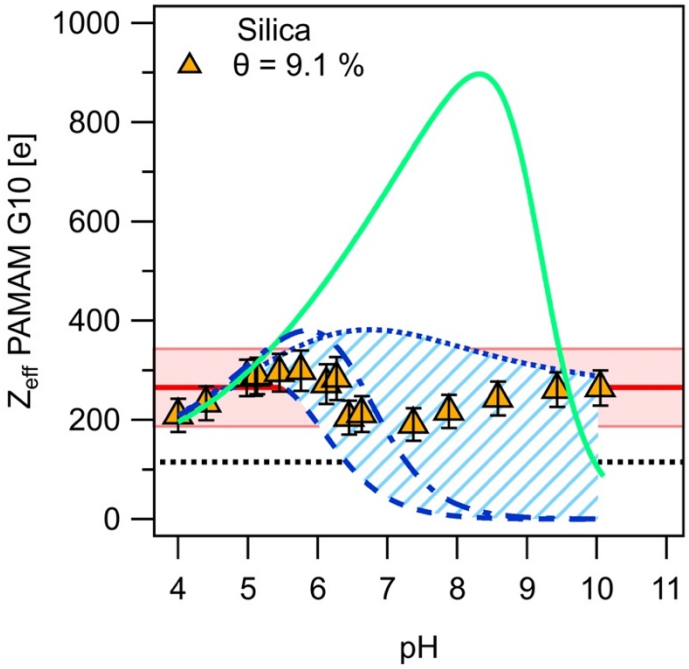

Figure S16: The effective dendrimer charge Z_{eff} for single PAMAM G10 on silica as a function of pH as shown in Fig. 8d. The additional green solid line represents Z_{eff} calculated from Eq. 6, Eq. 9, and Eq. 10 with data from Michna et al. for the titration of PAMAM in solution[9].

References

[1] C. Werner, H. Körber, R. Zimmermann, S. Dukhin and H. J. Jacobasch, J. Colloid Interface Sci., 208(1), 1998, 329-346, 10.1006/jcis.1998.5787

[2] J. Schindelin, I. Arganda-Carreras, E. Frise, V. Kaynig, M. Longair, T. Pietzsch, S. Preibisch, C. Rueden, S. Saalfeld, B. Schmid, J. Y. Tinevez, D. J. White, V. Hartenstein, K. Eliceiri, P. Tomancak and A. Cardona, Nat. Methods, 9(7), 2012, 676-682, 10.1038/nmeth.2019

[3] P. J. Scales, F. Grieser and T. W. Healy, Langmuir, 6(3), 1990, 582-589, 10.1021/la00093a012

[4] K. Fa, V. K. Paruchuri, S. C. Brown, B. M. Moudgil and J. D. Miller, Phys. Chem. Chem. Phys., 7, 2005, 678-684, 10.1039/b417902a

[5] M. Herzberg, S. Dobberschütz, D. Okhrimenko, N. E. Bovet, M. P. Andersson, S. L. S. Stipp and T. Hassenkam, EPL, 130(3), 2020, 36001, 10.1209/0295-5075/130/36001

[6] M. Zembala and Z. Adamczyk, Langmuir, 16(4), 2000, 1593-1601, 10.1021/la9905970

[7] R. Pericet-Camara, G. Papastavrou and M. Borkovec, Langmuir, 20(8), 2004, 3264-3270, 10.1021/la035955k

[8] R. H. Ottewill and J. N. Shaw, Kolloid Z. Z. Polym., 218(1), 1967, 34-40, 10.1007/bf01517273

[9] A. Michna, Z. Adamczyk, K. Sofińska and K. Matusik, J. Colloid Interface Sci., 485, 2017, 232-241, 10.1016/j.jcis.2016.09.007

5. Preparation of geometrically highly controlled Ga particle arrays on quasi-planar nanostructured surfaces as a SCALMS model system

Andre Hofer, Nicola Taccardi, Michael Moritz, Christoph Wichmann, Sabine Hübner, Dominik Drobek, Matthias Engelhardt, Georg Papastavrou, Erdmann Spiecker, Christian Papp, Peter Wasserscheid, and Julien Bachmann*

"Preparation of geometrically highly controlled Ga particle arrays on quasi-planar nanostructured surfaces as a SCALMS model system"

RSC Advances, **2023**, *13, 4011-4018*.

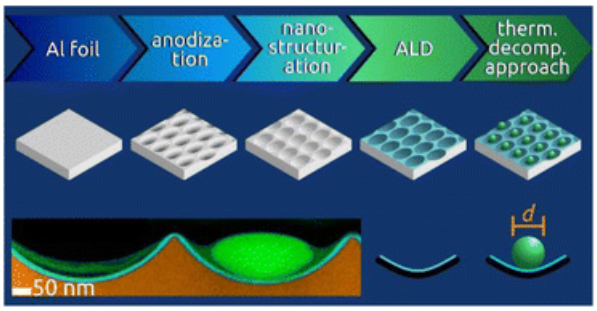

Reprinted with permission from:

"Preparation of geometrically highly controlled Ga particle arrays on quasi-planar nanostructured surfaces as a SCALMS model system", A. Hofer, N. Taccardi, M. Moritz, C. Wichmann, S. Hübner, D. Drobek, M. Engelhardt, G. Papastavrou, E. Spiecker, C. Papp, P. Wasserscheid, J. Bachmann, *RSC Advances,* **2023**, *13, 4011-4018*.

DOI: 10.1039/D2RA07585G

Under terms of the CC BY 3.0 license

RSC Advances

PAPER

Cite this: *RSC Adv.*, 2023, **13**, 4011

Preparation of geometrically highly controlled Ga particle arrays on quasi-planar nanostructured surfaces as a SCALMS model system†

André Hofer,[a] Nicola Taccardi,[b] Michael Moritz,[c] Christoph Wichmann,[c] Sabine Hübner,[d] Dominik Drobek,[d] Matthias Engelhardt,[e] Georg Papastavrou,[e] Erdmann Spiecker,[d] Christian Papp,[cf] Peter Wasserscheid[bg] and Julien Bachmann*[a]

This study establishes a preparative route towards a model system for supported catalytically active liquid metal solutions (SCALMS) on nanostructured substrates. This model is characterized by a uniquely precise geometrical control of the gallium particle size distribution. In a SCALMS system, the Ga serves as a matrix material which can be decorated with a catalytically active material subsequently. The corresponding Ga containing precursor is spin-coated on aluminum based substrates, previously nanostructured by electrochemical anodization. The highly ordered substrates are functionalized with distinct oxide coatings by atomic layer deposition (ALD) independently from the morphology. After preparation of the metal particles on the oxide interface, the characterization of our model system in terms of its geometry parameters (droplet diameter, size distribution and population density) points to SiO_2 as the best suited surface for a highly controlled geometry. This flexible model system can be functionalized with a dissolved noble metal catalyst for the application chosen.

Received 29th November 2022
Accepted 23rd January 2023

DOI: 10.1039/d2ra07585g

rsc.li/rsc-advances

Introduction

Liquid metals (LM) have recently emerged in catalysis due to their unique properties: existing in the liquid phase at a wide range of process temperature, low toxicity, negligible vapor pressure, high electric and thermal conductivity (improving heat transfer), low viscosity compared to heavy oils, and, perhaps most importantly, elimination of deactivation by coking and high ability of alloying.[1] Here, the liquid material itself acts as the catalyst for the chemical transformation. This principle can be extended to systems that increase the practical applicability in two ways. If firstly, the catalytically active element is dissolved in the liquid metal to reduce its total amount and secondly the liquid alloy is placed on a porous solid substrate for ease of handling, one obtains a so-called SCALMS, a supported catalytically active liquid metal solution. In such systems, the dynamics of the catalyst element in a dynamic liquid matrix protects it from undesired deactivation and opens the possibility of simple catalyst modifications (dissolution of distinct catalysts or mixtures). However, the experimental determination of fundamental kinetic parameters such as turnover frequencies (per noble metal center) has not been possible so far. This limitation is due to the physical state of dispersion, in which an extremely broad distribution of metal particle sizes exists with a porous glass support of complex geometry. In this work, we present a preparative approach to resolve this issue experimentally. We establish a system of SCALMS particles with a narrow size distribution placed on a quasi-planar structure. We also pay attention to preventing the massive oxidation of the air-sensitive metallic phase. Furthermore, we prove the generality of the method by applying it to four different types of metal oxide substrates, and demonstrate a marked influence of the support chemistry on the particles.

[a]*Friedrich-Alexander-Universität Erlangen-Nürnberg (FAU), Department of Chemistry and Pharmacy, Chemistry of Thin Film Materials, IZNF, Cauerstr. 3, 91058 Erlangen, Germany. E-mail: julien.bachmann@fau.de*

[b]*Friedrich-Alexander-Universität Erlangen-Nürnberg (FAU), Department Chemical and Biological Engineering, Institute of Chemical Reaction Engineering (CRT), Egerlandstr. 3, 91058 Erlangen, Germany*

[c]*Friedrich-Alexander-Universität Erlangen-Nürnberg (FAU), Department of Chemistry and Pharmacy, Chair of Physical Chemistry II, Egerlandstr. 3, 91058 Erlangen, Germany*

[d]*Friedrich-Alexander-Universität Erlangen-Nürnberg (FAU), Institute of Micro- and Nanostructure Research (IMN) & Center for Nanoanalysis and Electron Microscopy (CENEM), IZNF, Cauerstr. 3, 91058 Erlangen, Germany*

[e]*Universität Bayreuth, Chair of Physical Chemistry II, Universitätsstr. 30, 95447 Bayreuth, Germany*

[f]*Angewandte Physikalische Chemie, FU Berlin, Arnimalle 22, 14195 Berlin, Germany*

[g]*Forschungszentrum Jülich GmbH, Helmholtz Institute Erlangen-Nürnberg for Renewable Energy (IEK-11), Cauerstr. 1, 91058 Erlangen, Germany*

† Electronic supplementary information (ESI) available. See DOI: https://doi.org/10.1039/d2ra07585g

© 2023 The Author(s). Published by the Royal Society of Chemistry

Experimental

Materials

Standard chemicals (phosphoric acid, hydrochloric acid, perchloric acid, chromium trioxide, ethanol, toluene) were purchased from Carl Roth and used without further purification. Ethanol was distilled in a rotary evaporator and aluminum plates (99.99%) were purchased from SmartMembranes.

Substrate preparation

The nanostructured substrates with a defined indentations diameter were prepared by a one-step anodization procedure.[2–4] For this process, ultrapure aluminum plates (area approx. 5 cm^2) were placed in purpose-built two-electrode cells based on a PVC beaker serving as container of the electrolyte with four circular openings, closed with a lid equipped with a silver wire mesh acting as counter-electrode and a mechanical stirrer. The Al sheets were held between an O-ring and a thick copper plate serving as the second electrical contact. Prior to anodization, the Al plates were electropolished in an ice-cooled solution of perchloric acid and ethanol ($HClO_4$: EtOH, 1 : 3 v/v) under stirring under a potential of +20 V applied for 7 min (DC Power Supply, PS-1302 D by Voltcraft). The beakers were subsequently rinsed, cooled, filled with 100 mL of electrolyte (aqueous 0.5 wt% H_3PO_4), thermally isolated and anodized under stirring at an applied potential of +195 V for 1 h at 0 °C (power supply, EA-PS-8360-10 DT or EA-PS-8360-10 T by EA-Elektro Automatik). Adjacent, the H_3PO_4 concentration was increased to 1.0 wt% and the anodization continued for another 23 h. The sacrificial disordered oxide layer obtained due to anodization was removed by a bath in chromic acid (0.18 M CrO_3 in 6 wt% H_3PO_4) at 45 °C for 24 h (VENTI-Line oven by VWR) yielding well-ordered indentations in the Al plates.

Atomic layer deposition (ALD)

In order to adjust the surface chemistry independently from the geometry of the substrate, various metal oxide thin films were deposited on the nanostructured substrate using ALD in a commercial Gemstar-XT-6 ALD reactor from Arradiance. In all cases, the nominal thickness of the metal oxide film was determined on native SiO_2 wafers by spectroscopic ellipsometry with a SENPro from SENTECH. SiO_2: 3-aminopropyltriethoxysilane (APTES) heated to 70 °C, water and ozone, generated by an ozone generator model BMT 803N, were used as precursors, whereas the reaction chamber was maintained at 170 °C.[5] MgO: di(cyclopentadienyl)magnesium heated to 57 °C and water were used as precursors, whereas the reaction chamber was maintained at 150 °C.[6] TiO_2: titanium(IV) isopropoxide heated to 70 °C and water were used as precursors, whereas the reaction chamber was maintained at 150 °C.[7] Al_2O_3: trimethylaluminium and water (both unheated) were used as precursors, whereas the reaction chamber was maintained at 120 °C.[8]

Gallium particle generation

H_3Ga(quinuclidine) was synthesized as described by Atwood *et al.*[9] All following steps were performed under inert atmosphere in order to prevent contact with moisture or oxygen and undesired oxidation of the highly sensitive Ga particles. A solution of trihydridogallium(quinuclidine) (1.0 M, 50 μL) in dry toluene was dropped on the nanostructured substrates (coated with metal oxide) and spin-coated for 30 s at 3000 rpm. The remaining solvent was evaporated and the Ga complex thermally decomposed on a hot plate at 300 °C within 60 s forming metallic Ga particles and volatile by-products.

Catalyst deposition by galvanic replacement

The Ga particles were decorated with noble metals, which are the catalytically active material in this SCALMS model system, by galvanic replacement reactions in an aqueous/IPA solution in air. Aqueous solutions of ammonium tetrachloropalladate(II) $(NH_4)_2[PdCl_4]$ with a Pd content of 1 mg mL^{-1} and chloroplatinic acid H_2PtCl_6 with a Pt content of 4.4 mg mL^{-1} were used as precursor and diluted with isopropanol to the noble metal to gallium ratio stated in the text. After the exchange was completed (pale yellow Pt solution turned colorless), the sample was rinsed with solvent and dried in a N_2 stream.

Analyses

The geometry, morphology and EDX mapping of the SCALMS model systems were investigated using a JSM-F100 field-emission scanning electron microscope by JEOL, the composition by a scanning electron microscope JEOL JSM 6400 equipped with a LaB_6 cathode combined with an energy-dispersive X-ray (EDX) detector from SAMx. The crystal structure was analyzed by X-ray diffraction (GI-XRD) in grazing-incidence geometry using a Bruker D8 Advance equipped with a Cu Kα source and LynxEye XE detector.

STEM imaging, more specifically with high-angle annular dark-field (HAADF), and STEM EDX analysis were performed in a double-aberration corrected FEI Titan Themis^3 300 transmission electron microscope with an accelerating voltage of 300 kV. For this purpose, a focused ion beam was used in an FEI Helios NanoLab 660 SEM/FIB dual beam system to prepare a thin cross-sectional lamella through a selected region containing several Ga particles. To this end, the area was covered with a protective carbon layer using the gas injection system (GIS), cut free from bulk material using the FIB, and transferred to a lift-out TEM grid (PELCO Indicator) using the so-called lift-out technique. Subsequently, the lamella was thinned down by FIB milling from both sides to a thickness of less than 100 nm to allow local and precise STEM-EDX analyses. The EDX measurements were performed at a convergence angle of 15.7°, a dwell time of 50 μs and a current of about 400 pA.

XPS measurements were carried out with a custom-built NAP-XPS instrument from the Institute of Physical Chemistry II in Erlangen. The measurement chamber is equipped with a Specs NAP XR50 X-ray tube with a dual Al/Mg anode. The hemispherical photoelectron analyzer is a modified Omicron EA 125 U7, which is separated from the measurement chamber by multiple pumping stages. More information about the XPS instrument can be found in Pantförder *et al.*[10] Sample transfer was performed using an airtight and mobile stainless steel UHV

© 2023 The Author(s). Published by the Royal Society of Chemistry

system equipped with a transfer arm, a Pirani gauge for pressure measurement, and a fine dosing valve for vacuum pumping. The compact system is closed with a gate valve and holds the required pressures for days without additional pumping. The system was inserted into the glovebox where the prepared sample was mounted on the transfer arm, sealed, taken out of the glovebox, and then connected to the XPS instrument. After pumping the mobile system to 5×10^{-6} mbar, the sample was transferred on a sample holder and then introduced into the XPS instrument (10^{-9} mbar) *via* a load lock. The data was analyzed by CasaXPS Version 2.3.18PR1.0. Peaks were fitted using LF lineshapes, as implemented in CasaXPS.[11] For quantification the respective intensities of the Ga 3d and transition metal regions were adjusted by custom sensitivity factors. These sensitivity factors are the product of the specific inelastic mean free paths (TPP-2M equation[12]), the photoionization cross-section,[13] and a instrument-specific factor. The atomic percentage at% was calculated by dividing these corrected intensities with the sum of all corrected intensities.

The streaming potential measurements have been performed on an improved setup as the one described by Morga *et al.*[14] Calibration of the streaming potential data has been obtained on muscovite mica (V1 grade, Plano GmbH) in 1 mM KCl solution (BioUltra, Merck) with a titration from pH 3 to pH 10 (HCl/KOH, Titrisol®, Merck). A very good agreement to the data reported by Scales *et al.*[15] has been found. For the cell a PTFE-spacer with a nominal channel height of 0.3 mm has been used to exclude effects due to surface conductivity. The reported ζ-potentials have been calculated by means of the Helmholtz–Smoluchowski approximation. The determination of the isoelectric point (IEP) for the different coatings (SiO_2, TiO_2, Al_2O_3) has been conducted on mica sheets on which the oxides have been deposited by ALD as described previously. The corresponding measurements have been performed at a constant overall ionic strength of 10 mM (KCl) and titrations from pH 2 to pH 11.

The surface topography of the oxide films on mica has been determined by atomic force microscopy. The AFM measurements have been performed in PeakForce Tapping® mode under ambient conditions (Bruker ICON, Nanoscope V controller). The cantilevers used (ScanAsyst Air, Bruker) have a nominal resonance frequency of 70 kHz and a tip radius <2 nm. The average roughness values reported have been calculated on a scan size of 1×1 μm^2 after plane fit of 1st order.

Results and discussion

Three main methods for the generation of liquid metal particles have recently been established:

(i) Wet chemical route with thermolysis: the support is impregnated with an organic solution of freshly synthesized (non-purified) gallane–ammine complex (*e.g.* Et_3NGaH_3), dried and subsequently submitted to thermal decomposition of the gallane to elementary gallium and gaseous by-products.[16] However, the utilization of a precursor (Et_3NGaH_3) which is not only highly air-sensitive but also unstable at room temperature[17] hampers a quantitative control of the liquid particles' loading and diameter (distribution).

(ii) Another route is provided by the ultrasonication method. Here, a bulk amount of metallic gallium is dispersed in an organic solvent by ultrasonication. The particle size distribution can be optimized by physical separation techniques (*e.g.* centrifugation). Subsequently, the support is added to this suspension, and the solvent evaporated.[17]

(iii) A broadly applicable route for the synthesis of monodisperse nanocrystals, which is also relevant for the liquid metal particles is the hot injection method. In short, a cold (room-temperature) organometallic precursor solution is injected into a hot (*e.g.* 300 °C) high-boiling apolar coordinating solvent. Upon decomposition of the precursor, the rapid injection results in immediate nucleation of metal particles. The prompt decrease in temperature and concentration then prevents further nucleation and lead to a narrow size distribution *via* exclusive growth. The suspension is finally impregnated into or onto the support.[18,19]

In practice, each approach has its own limitations. Approach (i) can be performed under controlled atmosphere to prevent surface oxidation, but it not designed to allow for quantitative control of the particles size and loading. Approach (iii) delivers the best size distribution control but involves two separate steps, between which a transfer mostly interrupts a perfect inert atmosphere. Approach (ii) relies on a centrifugation step in order to narrow down the size distribution, which prevents an inert-atmosphere handling. In this work, we improve the thermolysis approach and propose a method to generate metallic gallium particles featuring simultaneously an accurate particle size control and minimized oxide layer. For this, we utilize a nanostructured and highly ordered substrate to influence the dewetting that occurs upon decomposition of the originally continuous precursor layer.

In concrete terms, a model substrate of overall planar shape but featuring a controlled surface roughness is generated by an one-step electrochemical anodization of aluminium. The anodization process yields indentations in the Al metal foil, forming a hexagonal arrangement with an diameter of approx. 300 nm (Fig. 1). This highly ordered surface nanostructuration serves as a template to tune (i) the spatial separation of the droplets formed and (ii) their size affected by the indentations diameter. Before treatment with a liquid metal precursor, this substrate is coated with the desired oxide surface by atomic layer deposition (ALD), a method allowing for a highly conformal coating of the three-dimensional geometry.[20,21] With this, the chemical identity of the surface can be adjusted independently of the geometry. For now, let us focus on SiO_2, as it has been the standard SCALMS substrate so far.[16] After a toluene solution of quinuclidine–gallane complex has been spin-coated and dried then the resulting layer finally thermally decomposed to volatile by-products and the desired elemental gallium, individual spherical particles nested in the indentations are obtained, as shown in Fig. 1. The high-magnification micrograph, Fig. 1(a), emphasizes how dewetting collects material in each individual indentation, resulting in spheres (droplets above the melting point) that remain separated from

© 2023 The Author(s). Published by the Royal Society of Chemistry

one another instead of coalescing. The lower magnifications in Fig. 1(b) and (c) allow one to evaluate how homogeneously the droplets are distributed over a large area. The backscattered electron detector (BED) is used for these micrographs due to its contrast based on materials (elements with higher atomic number, here Ga, appear brighter than Al or Si) instead of the mostly topographic information delivered by a secondary electron detector (SED). We will turn to a quantitative analysis of the Ga particle size distribution and coverage in a later section of this paper. Let us focus on the qualitative materials characterization first.

The elemental composition of the structures is determined by energy-dispersive X-ray microanalysis (EDX, Fig. 2). The chemical composition of the area shown in Fig. 2(a) is mapped in Fig. 2(b–d): on overlay of Al (orange) and Ga (green) signals on the SEM micrograph (b) is complemented with maps of the individual elements. The data prove the successful preparation of well-defined Ga spheres of homogeneous diameter spread and well separated from each other on an ordered, nanostructured SiO_2/aluminium substrate—an ideal model matrix for SCALMS systems (for which a noble metal still is be added).

The cross-section of a sample after lamella preparation with focused ion beam (FIB) is characterized by scanning transmission electron microscopy (STEM, Fig. 3 and S3 in ESI†). The micrographs and EDX mapping confirm our description above. Firstly, the indentations in Al (orange) have the shape of spherical caps and the SiO_2 layer has a perfectly constant thickness (cyan Si signal). The Ga particle (green) is in fact imperfectly spherical: it has an ellipsoidal shape instead. Fig. S3 (in ESI)† exhibits small amounts of what seems to be gallium oxide remnants (O signal: red) to the left and right of the metal particle. Fig. 3 confirms that some remnants of gallium oxide are left over from the quinuclidine gallane precursor film in the indentations unoccupied by Ga metal. In other words, imperfectly anaerobic conditions cause some of the material to be oxidized and some of the Ga contents are lost inasmuch as they do not contribute to the metal particles. The high reactivity of Ga to oxidation also causes the formation of a thin gallium oxide layer upon sample transfer. Its thickness is approximately 5 to 6 nm. This is in stark contrast to the significant oxidation

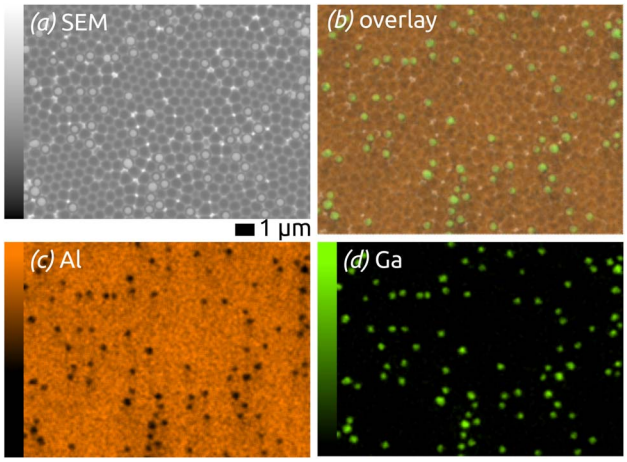

Fig. 2 EDX maps of the model SCALMS matrix system: (a) SEM micrograph of the area analyzed; (b) overlay of the Ga and Al signals (in green and orange, respectively) with the SEM micrograph; (c) and (d) individual element maps for Al and Ga.

observed usually, with tens if not hundreds of nm of oxide. In application, this oxide is reduced in conditions of catalysis (elevated temperature and hydrogen pressure), but it influences the size and shape of the SCALMS particles, as well as their mobility and agglomeration, in an uncontrolled manner. The near-pristine state obtained here will minimize this source of uncertainty.

The generation and existence of a (liquid) elementary Ga core in the particles on the nanostructured surface is further confirmed by X-ray photoelectron spectroscopy (XPS, Fig. 4). Although the extreme surface sensitivity of the method yields a predominant signal of Ga_2O_3 (Ga 3d doublet at approx. 20.3 eV and 20.8 eV with $\Delta = 0.42$ eV, O 2s at approx. 24.5 eV), a Ga 3d doublet at 18.2 eV and 18.6 eV with $\Delta = 0.42$ eV is visible and assigned to metallic Ga buried below the thin passivation layer formed on the surface.[22] In the experimental conditions of our XPS measurements, the probe depth is approximately 9 nm, indicating that the oxide layer thickness is slightly below this value. This is in perfect agreement with the value of 5–6 nm determined by STEM above.

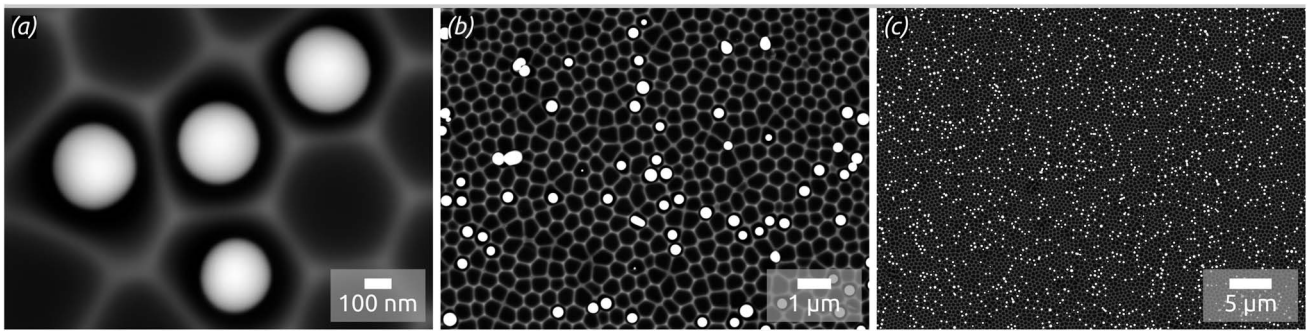

Fig. 1 SEM micrographs with distinct magnification levels decreasing from (a–c), taken using a backscattered electron detector (BED, enhancing material contrast): Ga spheres (brighter) formed with the thermal decomposition method using H_3Ga(quinuclidine) on highly ordered nanostructured substrates consisting of hexagons with a center-to-center distance of approx. 450 nm and indentations depth of approx. 130 nm previously coated with a thin (approx. 10 nm) silica film by atomic layer deposition (ALD).

© 2023 The Author(s). Published by the Royal Society of Chemistry

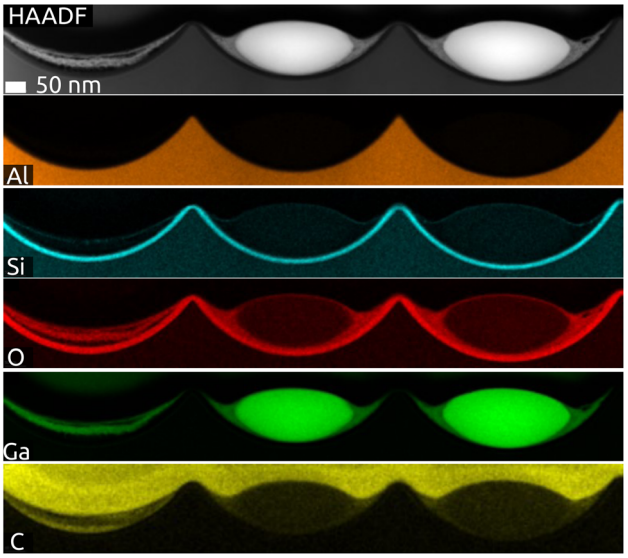

Fig. 3 STEM-EDX net intensity mapping of the model SCALMS matrix system in a FIB cross-section with Al (orange), Si (cyan), O (red), Ga (green) and C (yellow) signals: three indentations hosting two Ga particles (HAADF).

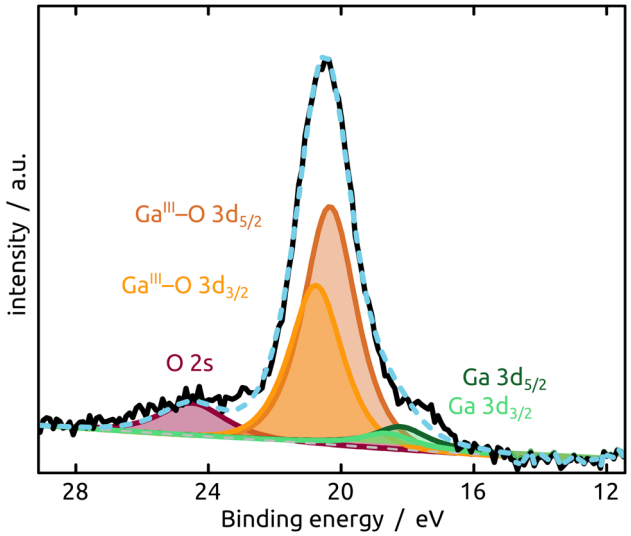

Fig. 4 XPS analysis of the model SCALMS matrix system indicating a passivating gallium oxide layer at the surface of the metallic Ga particle.

X-ray diffraction measured in grazing incidence geometry (GI-XRD, Fig. S1 and S2 in ESI†) does not provide any direct evidence for the presence of crystalline Ga or Ga_2O_3. The diffractograms most prominently display the signals of the Al substrate at 2θ values 38°, 45°, 65° and 78°, with additional small peaks for the ALD-deposited oxide, if that is crystalline (as in the case of TiO_2).

The final preparation step towards a functional SCALMS catalyst is the incorporation of the active noble metal in a small concentration in the Ga matrix. Fig. 5 demonstrates that our model system successfully incorporates either Pt or Pd as

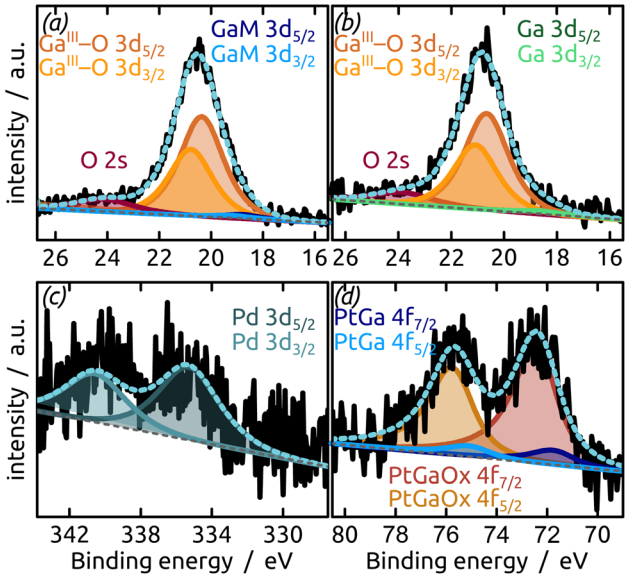

Fig. 5 XPS analysis ((a and b) Ga region; (c and d) noble metal region) of the model SCALMS system after partial transmetallation with a noble metal ((a and c) Pd; (b and d) Pt) from solution under air. The data indicate incorporation of the noble metals in the Ga-based particle (oxidized at its surface).

desired upon partial transmetallation with mixed (water/isopropanol) solutions of the corresponding Pt(IV) or Pd(II) precursors. The partial galvanic exchange of Ga particles with Pd leads to a system in which the binding energy of the palladium indicates a Pd^0 (Pd 3d doublet at 340.6 eV and 335.3 eV with spin–orbit separation of $\Delta = 5.26$ eV). However, a mixture of a GaPd alloy and Pd^0 seems likely due to the broad signal.[23] The exchange of Ga with Pt leads to the formation of a GaPt intermetallic compound (IMC, PtGa 4f doublet at 74.3 eV and 71.0 eV with $\Delta = 3.33$ eV),[24] as expected from the phase diagram of GaPt.[25] The main signal in the Pt 4f region results from Pt incorporated into gallium oxide, where Pt is positively charged.[26,27] A similar positive charge on Pt has been observed for PtGa systems in the past, as well as during the oxidation of GaRh SCALMS. In the latter case, DFT simulations and

Table 1 Summary of quantitative geometric Ga particle parameters obtained for oxides with various isoelectric points (IEP). We provide IEP values related to the bulk solids from the literature[31] and experimental ones obtained by streaming potential measurements (apart from MgO, which was insufficiently stable for reliable measurements). Particle diameter ∅ and *N* quantifies the sample size (total number of particles counted). *SE of mean: standard error of mean; **range: defined as the interquartile range (Q3–Q1)

Oxide	IEP bulk mat.	IEP thin film	∅ ± SE of mean*/nm	Range** nm	*N*
TiO_2	4–7 (ref. 32–35)	3–4	235 ± 6	154	414
SiO_2	<3 (ref. 36–39)	5–6	284 ± 1	38	6229
Al_2O_3	8 (ref. 40 and 41)	6–7	335 ± 31	332	55
MgO	11	n/a	440 ± 10	202	232

© 2023 The Author(s). Published by the Royal Society of Chemistry

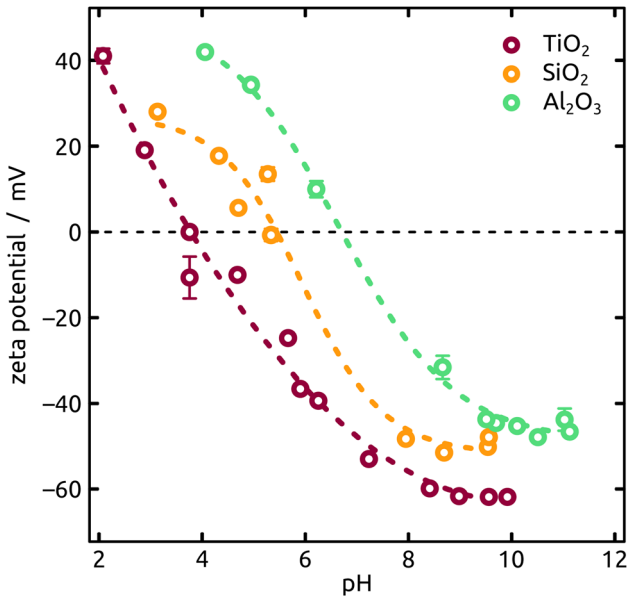

Fig. 6 Characterization of the IEP (ionic strength of 10 mM KCl and titrations from pH 2 to pH 11) of distinct metal oxides deposited on mica sheets by ALD (thicknesses in the range of approx. 10 nm to 15 nm).

calculations show Bader charges of approx. +1.25*e* for Rh in Ga_2O_3 (ref. 28) (PtGa oxide 4f doublet at 75.7 eV and 72.4 eV with $\Delta = 3.32$ eV).[26,27]

The XPS signals of Pt or Pd appear in low concentration as desired (1.5 at% transition metal), but incorporated in GaO_x due to the aerobic treatment. Thus, the data demonstrate that our geometrically near-perfect model system is adequate for studies of SCALMS catalysis. Let us now turn to the effect of the underlying surface chemistry.

An increasing body of catalysis literature shows that even in redox catalysis, not only the redox-active noble metal but also the acid–base interaction with the underlying oxide substrate is of relevance.[29,30] Let us investigate, accordingly, how the oxide layer present on the Al indentations affects the distribution of Ga particles, going from acidic oxides (TiO_2, SiO_2) to amphoteric (Al_2O_3) and basic (MgO) ones. The surface chemistry can affect both the distribution of gallane precursor film upon spin coating and the subsequent dewetting of the Ga layer generated by thermal decomposition. The quantitative parameters which we will consider here are the particle diameter (and the diameter distribution) and the number of particles per unit area (particle density). We will correlate them with the isoelectric point (IEP), as defined by the pH value at which a certain oxide in contact with an aqueous solution has equal density of positive (protonated) and negative (deprotonated) surface sites (Table 1). The IEP determined by streaming potential measurements for the amorphous, partially hydrated ALD thin films (Fig. 6) exhibit slight deviations from the values commonly accepted for the corresponding bulk materials. The data presented in the table are obtained by automatic image analysis of BED-SEM micrographs, which provides a number of bright particles and total surface of bright pixels as the raw data. The data are then converted to particle density and diameter distribution based on the following assumptions and procedures: (i) spherical shape assumption to calculate diameter from area, (ii) known micrograph area to calculate the particle density as number of particles per unit area (1 μm^2), and (iii) the coverage factor as ratio between bright pixels and total pixel number. These numbers also allow us to calculate an equivalent Ga layer thickness, corresponding to the thickness of a hypothetical Ga film homogeneously covering the substrate with the same total amount of Ga as actually present in the particles.

The Ga particles on substrates coated with more acidic oxides (TiO_2: Fig. 7(a); SiO_2: Fig. 1 and 7(b)) yield the smallest average diameters, followed by the amphoteric (Al_2O_3) and basic (Mg) ones, Fig. 7. In fact, we observe an approximately linear increase of particle diameter with IEP, Fig. S5 (in ESI,† using the literature value for IEP of MgO). This trend (increase by a factor

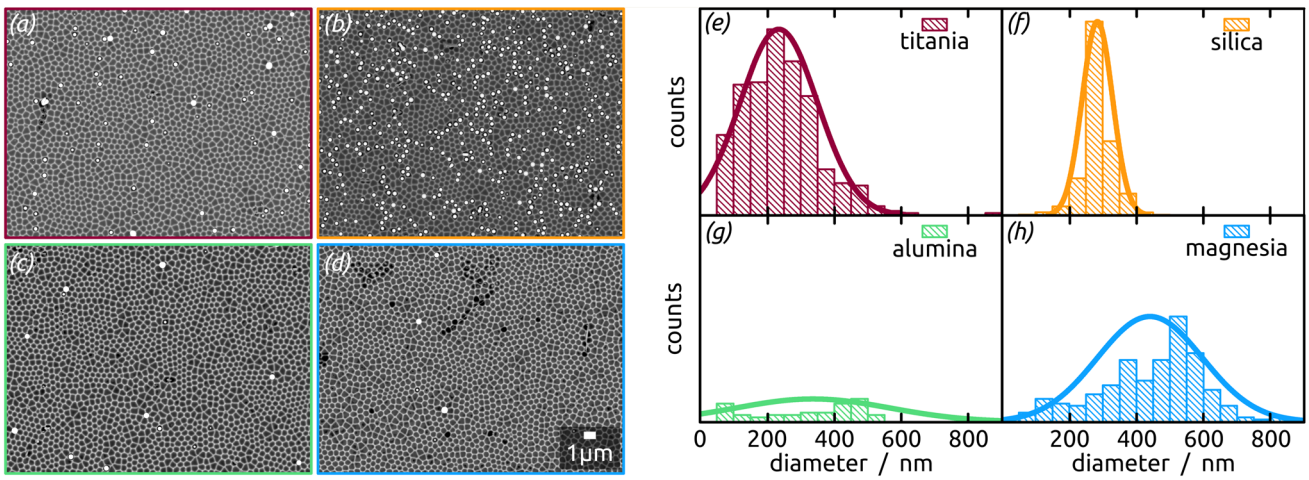

Fig. 7 (a–d) SEM micrographs (BED) of Ga particles (brighter due to higher atomic number) formed with the thermal decomposition method using H_3Ga(quinuclidine) on highly ordered nanostructured substrates previously coated with distinct metal oxide thin films by ALD, and (e–h) corresponding histogram of diameter distributions with the normal distribution fits: (a) and (e) TiO_2, (b) and (f) SiO_2, (c) and (g) Al_2O_3 and (d) and (h) MgO.

© 2023 The Author(s). Published by the Royal Society of Chemistry

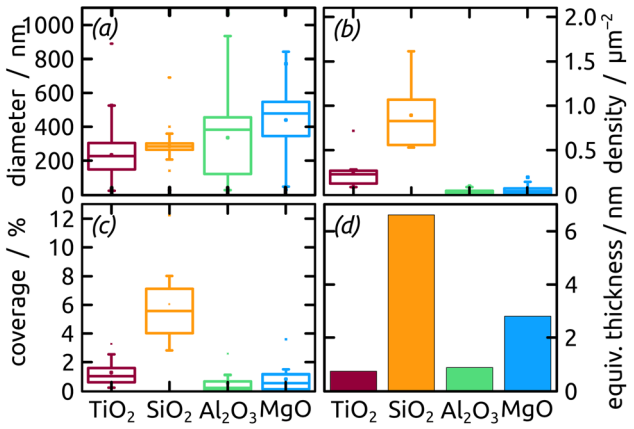

Fig. 8 Box–whisker-plot of particle (a) diameter, (b) density, (c) coverage distribution and (d) equivalent thickness of Ga on distinct metal oxides with different surface chemistry.

2 approximately) is roughly accompanied by an even steeper, albeit less monotonous, broadening of the size distribution (by a factor 50 approximately), whereby the narrowest distribution is obtained not for TiO_2 but for SiO_2 instead.

The micrographs evidence in obvious manner that samples featuring larger particles also exhibit a lower particle density, which is intuitive. Are the two parameters inversely proportional to each other to conserve mass? To address this question, we summarize all three quantitative parameters in the box–whisker-plot, Fig. 8, together with a quantification of the total Ga amount present on each sample, namely the equivalent Ga thickness. This way of presenting the results emphasizes that the various oxides not only influence the particle size distribution (by affecting the dewetting) but also the absolute amount of material present (that is, they already influence film formation during spin coating of the precursor solution). The surfaces best able to fix quinuclidine–gallane are the most extreme ones on the IEP range, perhaps because their Lewis acid-based reactivity complements that of the Lewis acid–base complex ideally. The surface best able to prevent large motions of metallic Ga and coalescence to large particles are the acidic ones, probably due to a lower interfacial energy.

In summary, the highest degree of control in terms of diameter distribution (smallest average Ga particle diameter and narrowest size distribution both in absolute and relative terms), the highest density (highest number of Ga particles per unit area) and thus the highest areal and mass coverage are all achieved with SiO_2 as the substrate.

Conclusions

The results presented here establish the viability of a quasi-planar SCALMS model system offering a high degree of geometric control over the metal particles. The manufacturing procedure combines anodization as a nanostructuration method to generate highly controlled surfaces with ALD to adjust the substrates' surface chemistry independently of their geometry. The generation of elementary gallium droplets with well-defined diameter and size distribution by spin coating and subsequent thermal decomposition approach under inert atmosphere offers the possibility to prepare Ga as the liquid matrix material without the generation of a fully oxidized material as an intermediate or 'pre-catalyst'. Using indentations with a center-to-center distance of approx. 450 nm and indentations depth of approx. 130 nm coated with silicon dioxide yields a SCALMS model featuring Ga ellipsoids of *ca.* 280(±40) nm. These are still rather large particles in the catalysis field overall, but much smaller than the extremely wide size distributions available currently, which reach the >µm range. Furthermore, the preparative methods used offer a variety of experimental parameters that can be varied in order to optimize the system to any given application.

In the coming months, we will exploit this system to perform detailed kinetic investigations of SCALMS catalysis, hopefully enabling us to determine for the first time values such as the turnover frequencies. In parallel, we will study experimentally and theoretically interfacial energies in the metal oxide/Ga metal system in order to shed light onto the dewetting phenomena at work in SCALMS catalysis. Mastering them will be of utmost importance for the efficient use of every noble metal atom.

Author contributions

André Hofer: conceptualization, methodology, investigation, visualization, writing – original draft. Nicola Taccardi: investigation. Michael Moritz: investigation. Christoph Wichmann: investigation. Sabine Hübner: investigation. Dominik Drobek: investigation. Matthias Engelhardt: investigation. Georg Papastavrou: validation, resources. Erdmann Spiecker: validation, resources, funding acquisition. Christian Papp: validation, resources, funding acquisition. Peter Wasserscheid: conceptualization, validation, resources, project administration, funding acquisition. Julien Bachmann: conceptualization, resources, supervision, writing – review & editing, validation, funding acquisition.

Conflicts of interest

There are no conflicts to declare.

Acknowledgements

This research was funded by the German Ministry of Education and Research (BMBF) in the project 'Tubulyze' (project number 03SF0564A), by Deutsche Forschungsgemeinschaft (DFG, German Research Foundation) in the Collaborative Research Center (CRC)/Sonderforschungsbereich (SFB) 1452: 'Catalysis at Liquid Interfaces (CLINT)' and SFB 1411 "Design of Particulate Products" (Project-ID 416229255).

References

1 K. Zuraiqi, A. Zavabeti, F.-M. Allioux, J. Tang, C. K. Nguyen, P. Tafazolymotie, M. Mayyas, A. V. Ramarao, M. Spencer,

© 2023 The Author(s). Published by the Royal Society of Chemistry

K. Shah, C. F. McConville, K. Kalantar-Zadeh, K. Chiang and T. Daeneke, *Joule*, 2020, **4**, 2290–2321.
2 S. Schlicht, S. Haschke, V. Mikhailovskii, A. Manshina and J. Bachmann, *ChemElectroChem*, 2018, **5**, 1259–1264.
3 T. Grünzel, Y. J. Lee, K. Kuepper and J. Bachmann, *Beilstein J. Nanotechnol.*, 2013, **4**, 655–664.
4 K. Nielsch, J. Choi, K. Schwirn, R. B. Wehrspohn and U. Gösele, *Nano Lett.*, 2002, **2**, 677–680.
5 J. Bachmann, R. Zierold, Y. Chong, R. Hauert, C. Sturm, R. Schmidt-Grund, B. Rheinländer, M. Grundmann, U. Gösele and K. Nielsch, *Angew. Chem., Int. Ed.*, 2008, **47**, 6177–6179.
6 T. Törndahl, C. Platzer-Björkman, J. Kessler and M. Edoff, *Prog. Photovoltaics*, 2007, **15**, 225–235.
7 M. Ritala, M. Leskelä, L. Niinistö and P. Haussalo, *Chem. Mater.*, 1993, **5**, 1174–1181.
8 R. L. Puurunen, *J. Appl. Phys.*, 2005, **97**, 121301.
9 J. L. Atwood, S. G. Bott, F. M. Elms, C. Jones and C. L. Raston, *Inorg. Chem.*, 1991, **30**, 3792–3793.
10 J. Pantförder, S. Pöllmann, J. F. Zhu, D. Borgmann, R. Denecke and H.-P. Steinrück, *Rev. Sci. Instrum.*, 2005, **76**, 014102.
11 T. R. Gengenbach, G. H. Major, M. R. Linford and C. D. Easton, *J. Vac. Sci. Technol., A*, 2021, **39**, 013204.
12 H. Shinotsuka, S. Tanuma, C. J. Powell and D. R. Penn, *Surf. Interface Anal.*, 2015, **47**, 871–888.
13 J. Yeh and I. Lindau, *At. Data Nucl. Data Tables*, 1985, **32**, 1–155.
14 M. Morga, Z. Adamczyk, S. Gödrich, M. Oćwieja and G. Papastavrou, *J. Colloid Interface Sci.*, 2015, **456**, 116–124.
15 P. J. Scales, F. Grieser and T. W. Healy, *Langmuir*, 1990, **6**, 582–589.
16 N. Taccardi, M. Grabau, J. Debuschewitz, M. Distaso, M. Brandl, R. Hock, F. Maier, C. Papp, J. Erhard, C. Neiss, W. Peukert, A. Görling, H. P. Steinrück and P. Wasserscheid, *Nat. Chem.*, 2017, **9**, 862.
17 N. Raman, M. Wolf, M. Heller, N. Heene-Würl, N. Taccardi, M. Haumann, P. Felfer and P. Wasserscheid, *ACS Catal.*, 2021, **11**, 13423–13433.
18 C. de Mello Donegá, P. Liljeroth and D. Vanmaekelbergh, *Small*, 2005, **1**, 1152–1162.
19 S. G. Kwon and T. Hyeon, *Small*, 2011, **7**, 2685–2702.
20 M. Knez, K. Nielsch and L. Niinistö, *Adv. Mater.*, 2007, **19**, 3425–3438.
21 N. Biyikli and A. Haider, *Semicond. Sci. Technol.*, 2017, **32**, 093002.
22 R. Carli and C. Bianchi, *Appl. Surf. Sci.*, 1994, **74**, 99–102.
23 H. Wittkämper, S. Maisel, M. Moritz, M. Grabau, A. Görling, H.-P. Steinrück and C. Papp, *Phys. Chem. Chem. Phys.*, 2021, **23**, 16324–16333.
24 Y. Nakaya, J. Hirayama, S. Yamazoe, K.-i. Shimizu and S. Furukawa, *Nat. Commun.*, 2020, **11**, 2838.
25 H. Okamoto, *J. Phase Equilib. Diffus.*, 2007, **28**, 494.
26 V. B. Kumar, J. Sanetuntikul, P. Ganesan, Z. Porat, S. Shanmugam and A. Gedanken, *Electrochim. Acta*, 2016, **190**, 659–667.
27 M. Grabau, S. Krick Calderón, F. Rietzler, I. Niedermaier, N. Taccardi, P. Wasserscheid, F. Maier, H.-P. Steinrück and C. Papp, *Surf. Sci.*, 2016, **651**, 16–21.
28 H. Wittkämper, S. Maisel, M. Wu, J. Frisch, R. G. Wilks, M. Grabau, E. Spiecker, M. Bär, A. Görling, H.-P. Steinrück and C. Papp, *J. Chem. Phys.*, 2020, **153**, 104702.
29 Q. Fu and T. Wagner, *Surf. Sci. Rep.*, 2007, **62**, 431–498.
30 V. Lyaskovskyy and B. De Bruin, *ACS Catal.*, 2012, **2**, 270–279.
31 M. Kosmulski, *J. Colloid Interface Sci.*, 2002, **253**, 77–87.
32 M. Chadwick, J. Goodwin, E. Lawson, P. Mills and B. Vincent, *Colloids Surf., A*, 2002, **203**, 229–236.
33 J. Ryu and W. Choi, *Environ. Sci. Technol.*, 2008, **42**, 294–300.
34 J. Moser, S. Punchihewa, P. P. Infelta and M. Graetzel, *Langmuir*, 1991, **7**, 3012–3018.
35 G. Girod, J. Lamarche and A. Foissy, *J. Colloid Interface Sci.*, 1988, **121**, 265–272.
36 M. L. Fisher, M. Colic, M. P. Rao and F. F. Lange, *J. Am. Ceram. Soc.*, 2001, **84**, 713–718.
37 G. V. Franks, Z. Zhou, N. J. Duin and D. V. Boger, *J. Rheol.*, 2000, **44**, 759–779.
38 J. Han and E. Kumacheva, *Langmuir*, 2001, **17**, 7912–7917.
39 J. Sonnefeld, M. Löbbus and W. Vogelsberger, *Colloids Surf., A*, 2001, **195**, 215–225.
40 T.-y. Chen and P. Somasundaran, *J. Am. Ceram. Soc.*, 1998, **81**, 140–144.
41 T. Waite, J. Cleaver and J. Beattie, *J. Colloid Interface Sci.*, 2001, **241**, 333–339.

© 2023 The Author(s). Published by the Royal Society of Chemistry

Preparation of geometrically highly controlled Ga particle arrays on quasi-planar nanostructured surfaces as a SCALMS model system

André Hofer,[a] Nicola Taccardi,[b] Michael Moritz,[c] Christoph Wichmann,[c] Sabine Hübner, [d] Dominik Drobek,[d] Matthias Engelhardt,[e] Georg Papastavrou,[e] Erdmann Spiecker,[d] Christian Papp,[c,f] Peter Wasserscheid,[b,g] and Julien Bachmann[a]*

Contents

1 Grazing incidence x-ray crystallography **2**

2 Scanning transmission electron microscopy **3**

3 Atomic force microscopy **3**

4 Characterization of the isoelectric point **4**

5 Automated SEM micrograph analysis **4**

[a] *Friedrich-Alexander-Universität Erlangen-Nürnberg (FAU), Department of Chemistry and Pharmacy, Chemistry of Thin Film Materials, IZNF, Cauerstr. 3, 91058 Erlangen, Germany; *E-mail: julien.bachmann@fau.de*

[b] *Friedrich-Alexander-Universität Erlangen-Nürnberg (FAU), Department Chemical and Biological Engineering, Institute of Chemical Reaction Engineering (CRT), Egerlandstr. 3, 91058 Erlangen, Germany*

[c] *Friedrich-Alexander-Universität Erlangen-Nürnberg (FAU), Department of Chemistry and Pharmacy, Chair of Physical Chemistry II, Egerlandstr. 3, 91058 Erlangen, Germany*

[d] *Friedrich-Alexander-Universität Erlangen-Nürnberg (FAU), Institute of Micro- and Nanostructure Research (IMN) & Center for Nanoanalysis and Electron Microscopy (CENEM), IZNF, Cauerstr. 3, 91058 Erlangen, Germany*

[e] *Universität Bayreuth, Chair of Physical Chemistry II, Universitätsstr. 30, 95447 Bayreuth, Germany*

[f] *Angewandte Physikalische Chemie, FU Berlin, Arnimalle 22, 14195 Berlin*

[g] *Forschungszentrum Jülich GmbH, Helmholtz Institute Erlangen-Nürnberg for Renewable Energy (IEK-11), Cauerstr. 1, 91058 Erlangen, Germany*

1 Grazing incidence x-ray crystallography

The crystal structure of the Ga matrix for a SCALMS model system was analysed by GI-XRD. The pattern of the particles on nanostructured substrates previously coated with either silica (Fig. S1) or titania (Fig. S2) by ALD indicates predominantly the Al (2θ: 38 °, 45 °, 65 ° and 78 °) signal of the support.

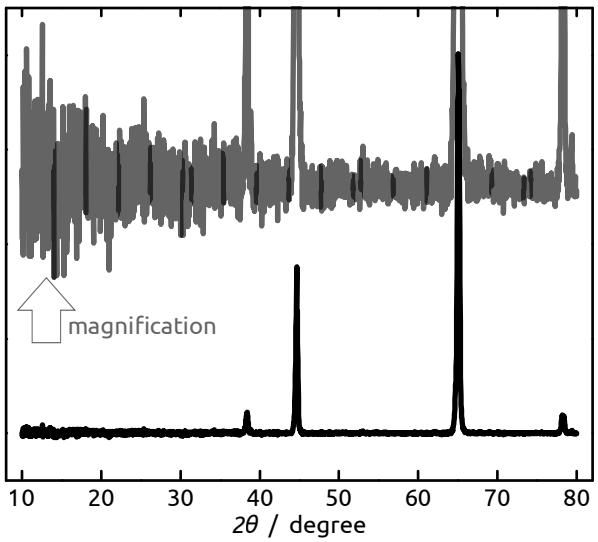

Fig. S1 GI-XRD pattern of of SCALMS matrix model system: Ga particles on silica coated nanostructured indentations indicating predominantly Al (2θ: 38 °, 45 °, 65 ° and 78 °) signal of the substrate material.

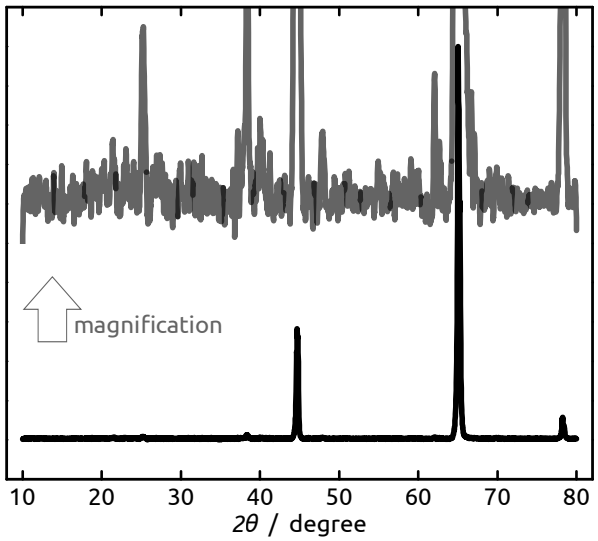

Fig. S2 GI-XRD pattern of of SCALMS matrix model system: Ga particles on titania coated nanostructured indentations indicating TiO_2 in anatase structure, and a predominantly Al (2θ: 38 °, 45 °, 65 ° and 78 °) signal of the substrate material.

2 Scanning transmission electron microscopy

The cross-section of a sample after lamella preparation with focused ion beam (FIB) is characterized by scanning transmission electron microscopy (STEM, Figure S3). The indentations in Al (orange) have the shape of spherical caps and the SiO_2 layer has a perfectly constant thickness (cyan Si signal). The Ga particle (green) is in fact imperfectly spherical: it has an ellipsoidal shape instead. Fig. S3 exhibits small amounts of what seems to be gallium oxide remnants (O signal: red) to the left and right of the metal particle.

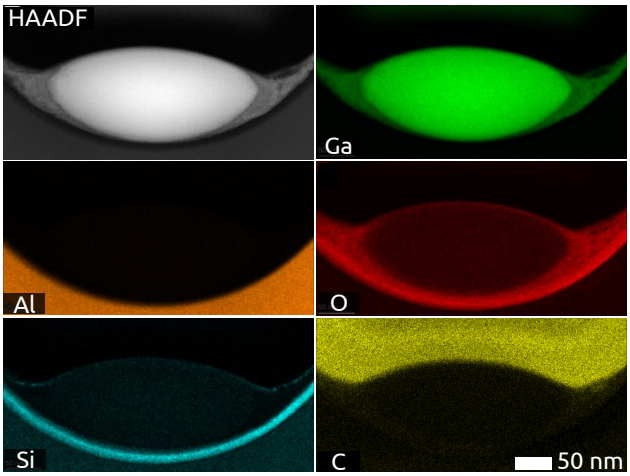

Fig. S3 STEM-EDX net intensity mapping of the model SCALMS matrix system in a FIB cross-section with Ga (green), Al (orange), O (red), Si (cyan) and C (yellow) signals: single indentation with Ga particle (HAADF).

3 Atomic force microscopy

Atomic force microscopy (AFM) characterizations were performed previously the streaming potential measurements to determine the roughness R_a of distinct metal oxide coated mica sheets. The oxides were deposited by atomic layer deposition (ALD). Figure S4 presents the topography of an approx. $1\,\mu$m x $1\,\mu$m area: *(a)* TiO_2 with a $R_a = 0.2$ nm (at flat spots), *(b)* SiO_2 with a $R_a = 0.2$ nm and *(c)* Al_2O_3 with a $R_a = 0.2$ nm. The pristine mica sheets exhibits a $R_a = 0.1$ nm after the streaming potential experiment (not shown).

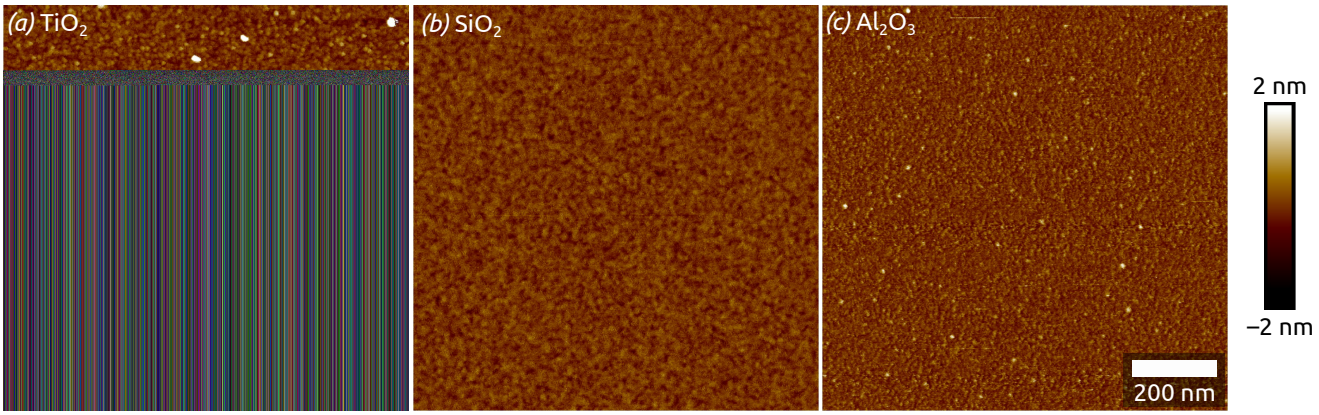

Fig. S4 Atomic force microscopy (AFM) roughness R_a characterization of distinct metal oxide coated mica sheets presenting the topography of an approx. $1\,\mu$m x $1\,\mu$m area: *(a)* TiO_2, *(b)* SiO_2 and *(c)* Al_2O_3.

4 Characterization of the isoelectric point

The IEP determined by streaming potential measurements for the amorphous, partially hydrated ALD thin films. The isoelectric point (IEP) is defined by the pH value at which a certain oxide in contact with an aqueous solution has equal density of positive (protonated) and negative (deprotonated) surface sites. An approximately linear increase of particle size diameter related to experimentally determined IEP values of the various metal oxide films (exception: literature value[1] used for MgO) can be observed.

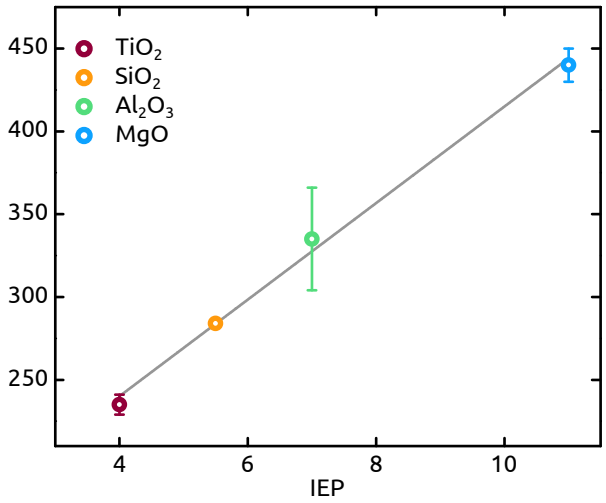

Fig. S5 Particle size diameter related to experimentally determined IEP values of the various metal oxide films (exception: literature value[1] used for MgO).

5 Automated SEM micrograph analysis

The Ga particle size is analysed by automated image-analysis (software: ImageJ, v1.53k). SEM-micrographs obtained using a SE-detector Fig. S6 *(a)* are detrimental due to morphology enhanced contrast. Contrast and brightness adjusted micrographs utilizing the BE-detector (enhancing material contract, Fig. S6 *(b)*) are used instead for further analysis. The Ga particles appear in brighter pixels due to their higher atomic number than the substrate elements. Subsequent threshold adjustment (Fig. S6 *(c)*) yields to the format from which the particle size can be recognized and analyzed automatically (Fig. S6 *(d)*).

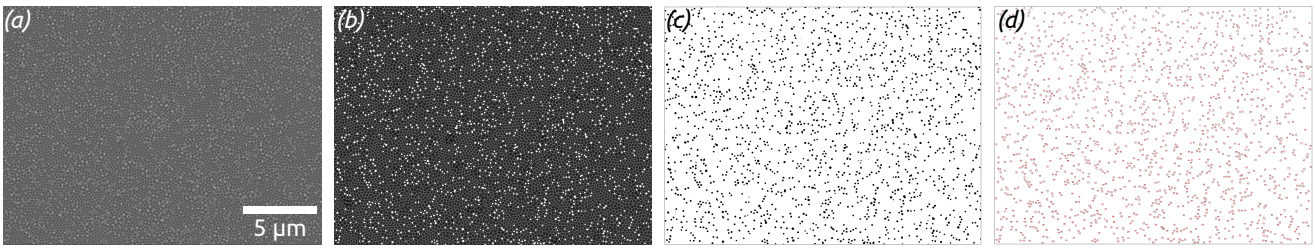

Fig. S6 Automated SEM-mirograph analysis using ImageJ, v1.53k.

References

1 M. Kosmulski, *J. Colloid Interface Sci.*, 2002, **253**, 77–87.

6. Preparation and Surface Functionalization of a Tunable Porous System Featuring Stacked Spheres in Cylindrical Pores

Christhy V. Ruiz M, Markus Terlinden, Matthias Engelhardt, Giulia Magnabosco, Georg Papastavrou, Nicolas Vogel, Matthias Thommes, and Julien Bachmann*

"Preparation and Surface Functionalization of a Tunable Porous System Featuring Stacked Spheres in Cylindrical Pores"

Advanced Materials Interfaces, **2023**, *10(33), 2300436*.

Reprinted with permission from:

"Preparation and Surface Functionalization of a Tunable Porous System Featuring Stacked Spheres in Cylindrical Pores", C. V. Ruiz M, M. Terlinden, M. Engelhardt, G. Magnabosco, G. Papastavrou, N. Vogel, M. Thommes, J. Bachmann, *Advanced Materials Interfaces,* **2023**, *10(33), 2300436*.

DOI: 10.1002/admi.202300436

Under terms of the CC BY license

RESEARCH ARTICLE

ADVANCED MATERIALS INTERFACES Open Access

www.advmatinterfaces.de

Preparation and Surface Functionalization of a Tunable Porous System Featuring Stacked Spheres in Cylindrical Pores

*Christhy V. Ruiz M, Markus Terlinden, Matthias Engelhardt, Giulia Magnabosco, Georg Papastavrou, Nicolas Vogel, Matthias Thommes, and Julien Bachmann**

A geometrically tunable nanoporous system featuring enhanced active surface area by stacking of spheres in cylindrical pores is fabricated. Highly ordered arrays of straight, constricted pores are obtained by anodization of metallic aluminum. Polystyrene (PS) spheres are assembled inside the pores by flowing their suspension through the porous membrane, whereas the construction serves as a filter. After surface functionalization with a noble metal catalyst, these model electrocatalysis systems exhibit functional properties (capacitance in electrochemical impedance spectroscopy) that mirror their geometric parameters. A systematic investigation of the system's geometry as it depends on the surface chemistry of the pores, on the one hand, and the physical parameters of the infiltration procedure, on the other hand, shows that mechanical stacking prevails over surface chemical interactions to determine the stacking density. The highest values of surface area are obtained when PS spheres are put in contact with HfO_2 followed by ZnO according to adsorption measurements. Surface derivatization with organic layers does not improve stacking any further. However, choosing the proper concentration of PS spheres and flow rate are crucial for obtaining densely packed sphere assemblies without clogging of the pore entrance.

1. Introduction

The control of geometry and morphology of nanostructured surfaces is of pivotal importance in catalysis, drug delivery, and environmental applications.[1,2] The structural engineering and control of geometrical parameters in porous structures featuring well-controlled sizes and shapes enable for adjusting properties and optimizing performance in applications.[3,4,5] The geometric aspect is of particular relevance in catalysis and electrocatalysis. First, chemical reactions occur at the surface, so its geometric area determines chemical (or electrochemical) turnover. Second, the transport mechanisms, and therefore kinetics, of the reagents and products (and charge carriers) within the fluid phase and potentially within the solid may place an upper boundary for their delivery to the surface. Therefore, the geometric nanostructuring of catalyst beds and electrodes as a strategy to improve the performance of chemical and energy conversion systems must compromise between two contradicting requirements.[2,6] On the one hand, maximizing the surface area of the solid phase is achieved by generating pores which increase the volumetric density of reactive sites at the phase boundary. On the other hand, the minimization of transport distances between the bulk of the fluid phase and each site of the interface favors low porosity.[7,8] These two conditions can be balanced by generating and studying

C. V. Ruiz M, J. Bachmann
Friedrich-Alexander-Universität Erlangen-Nürnberg, Chemistry of Thin Film Materials
IZNF
Cauerstr. 3, D-91077 Erlangen, Germany
E-mail: julien.bachmann@fau.de

The ORCID identification number(s) for the author(s) of this article can be found under https://doi.org/10.1002/admi.202300436

© 2023 The Authors. Advanced Materials Interfaces published by Wiley-VCH GmbH. This is an open access article under the terms of the Creative Commons Attribution License, which permits use, distribution and reproduction in any medium, provided the original work is properly cited.

DOI: 10.1002/admi.202300436

M. Terlinden, M. Thommes
Friedrich-Alexander-Universität Erlangen-Nürnberg
Institute of Separation Science and Technology
Egerlandstr. 3, D-91077 Erlangen, Germany

M. Engelhardt, G. Papastavrou
Universität Bayreuth
Physical Chemistry II
Universitätsstraße 30, D-95447 Bayreuth, Germany

G. Magnabosco, N. Vogel
Friedrich-Alexander-Universität Erlangen-Nürnberg
Institute of Particle Technology
Cauerstr. 4, D-91077 Erlangen, Germany

ADVANCED SCIENCE NEWS
www.advancedsciencenews.com

ADVANCED MATERIALS INTERFACES
Open Access
www.advmatinterfaces.de

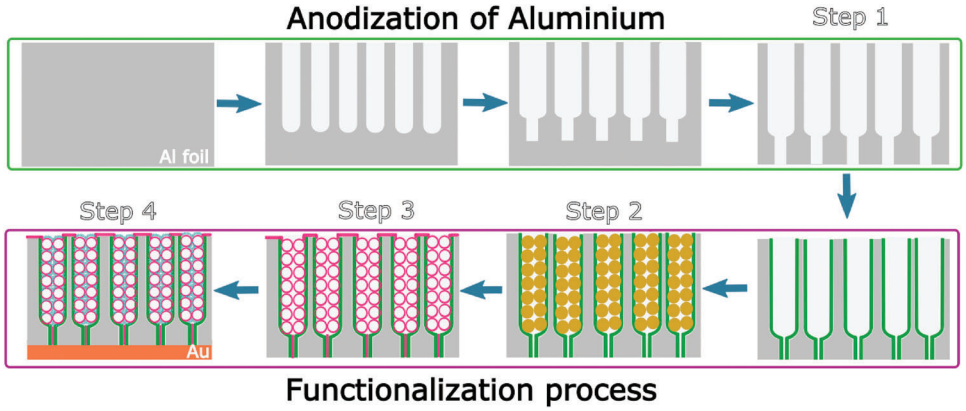

Figure 1. Schematic representation for nanostructuration of the samples for this study. Green lines: pore wall functionalization (metal oxide or molecular self-assembled layer); orange disks: sacrificial polystyrene spheres; pink lines: electrically conducting ZnO layer; cyan: Pt electrocatalyst.

systems in which pore structures are highly homogeneous and systematically variable.

One porous system that features outstanding versatility is anodic aluminum oxide (AAO) membranes. Not only does anodized aluminum offer engineering functionalities such as excellent hardness, corrosion, and abrasion resistance,[9,10] ordered porous systems based on AAO provide cylindrical, straight nanopores made with low-cost techniques for fundamental research.[11] The possibility to tune the pore diameter, pore length, and density of pores in wide ranges and in self-ordered conditions by proper choice of the anodization parameters (electrolyte bath, applied voltage, anodization duration) has been exploited for the preparation of diverse nanostructured materials as model systems for a variety of chemical and physical applications affected by geometry.[12] The outstanding structural characteristics of AAO make it a suitable template system that can confer its geometry to further materials (metals, carbon, polymers, biological materials) via infiltration of surface functionalization and thereby produce novel and enhanced nanostructured systems.[13–16]

In line with these considerations, a number of reports on catalyst surfaces and electrodes based on functionalized AAO have documented how the performance parameters of catalytic and electrocatalytic turnover depend on the pore geometry (diameter and depth) as well as on the surface functionalization itself. Not only steady-state performance but also impedance spectroscopy data have been shown to mirror the quite ideal geometry of electrodes and their increased surface area but also transport distances when pores are elongated.[17–21] However, the smooth pore walls of anodized alumina may not be the best model for real catalyst supports, which often exhibit significant roughness on the sub-100 nm length scale. Hence, we present here the preparation of a novel, geometrically tunable 3D substrate system featuring inner roughness within the cylindrical pores. A well-defined change in pore diameter obtained upon anodization serves to assemble polystyrene spheres in a filtration procedure. The assembly depends on both the chemical identity of the pore walls (after corresponding functionalization with either metal oxides or organic monolayers) and the physical parameters for their assembly (concentration of the suspension and flow rate). The electrochemical activity quantifiers of an electrode obtained after noble metal deposition into this model substrate exhibit effects that follow its geometric surface area.

2. Results and Discussion

2.1. Preparation of the Modulated Porous System

In the first preparative step (Step 1 in **Figure 1**), we use anodization of aluminum to generate a filter system that exhibits long, straight pores with a large diameter in their first segment complemented with a narrower second segment. Scanning electron microscopy (SEM) images of the array in cross-sectional, top, and bottom views, **Figure 2**, demonstrate the high degree of order, the straight geometry of the cylindrical pores, and the low polydispersity of their diameters. The porous anodic structure has a homogeneous net length of around 25 µm following the procedures described in the experimental section (Figure 2a). The pores clearly exhibit an abrupt change of diameter (Figure 2b) between the first segment with a diameter $D_1 \approx 320$ nm and length $L_1 \approx 17.5$ µm and the second one with $D_2 \approx 260$ nm and $L_2 \approx 8$ µm (Figure 2c,d). Each of these values is tunable experimentally upon adjustments of the anodization parameters: the length depends on the anodization duration linearly (with an approximate growth rate of 2.1 µm h^{-1}), whereas the diameter is set by the duration of the thermal pore widening treatments which in our conditions (10% H_3PO_4, 45 °C) achieve isotropic etching of the amorphous alumina at a rate of ≈0.67 nm min^{-1}.

2.2. Assembly of the PS Spheres Inside the Ordered Porous Systems

The subsequent processing step (Step 2 in Figure 1) shall result in a dense packing of spheres inside the wide pore section, so that the spacings between spheres later serve to separate metal particles from one another. The constriction created by the narrow segment in our anodic aluminum oxide (AAO) template enables us to trap polystyrene spheres via a procedure akin to filtration. To this goal, a suspension of polystyrene (PS) spheres with diameter $D_s = 130$ nm is pumped through the porous AAO template,

© 2023 The Authors. Advanced Materials Interfaces published by Wiley-VCH GmbH

ADVANCED SCIENCE NEWS
www.advancedsciencenews.com

ADVANCED MATERIALS INTERFACES
Open Access
www.advmatinterfaces.de

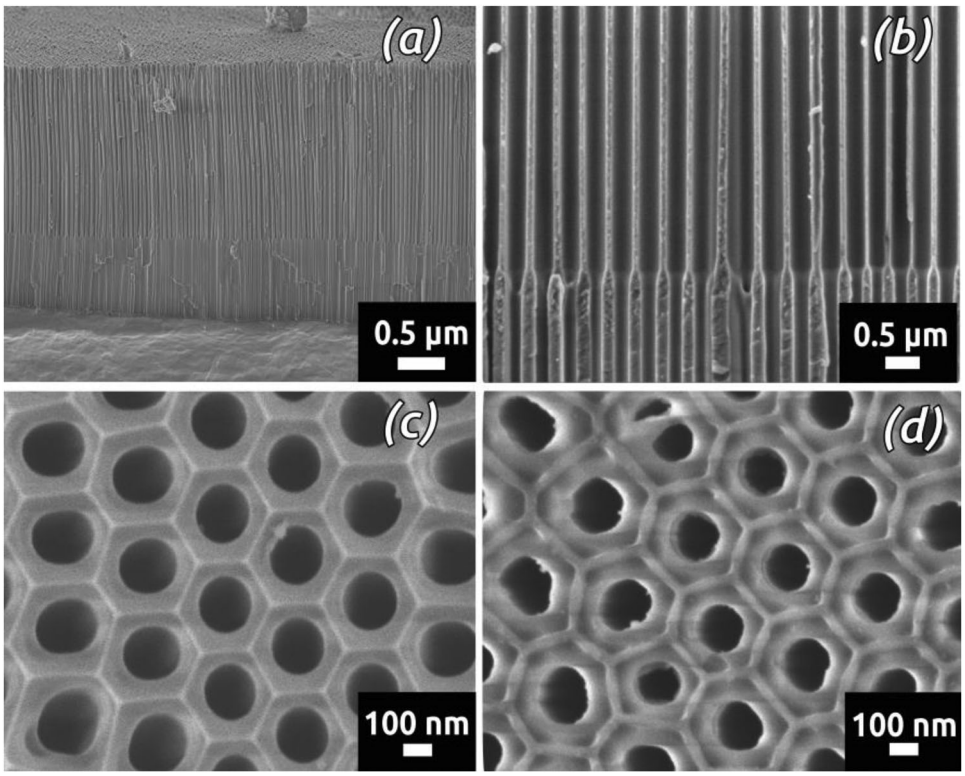

Figure 2. SEM images of the tuneable system of segmented pores after the first steps of preparation. The sample is shown in cross-section a,b) exhibiting an abrupt diameter modulation, whereas the face view of its upper surface c) and of the pore openings obtained at the end of anodization d) show distinct diameters.

whereby the dilution, flow rate, and total flow duration represent adjustable parameters. To perform this optimization in a quantitative manner, **Figure 3**a,b, we add a layer of ZnO by atomic layer deposition (ALD) in order to retain the arrangement of the particles within the pores and reduce charging in cross-section SEM analysis, then use energy-dispersive X-ray microanalysis (EDX) to quantify the carbon mass percentage within a rectangular area of the cross-section encompassing the full wide pore segment. The conditions that optimize the sphere stacking (i.e., that maximize the C content) are a dilution of 500 µL PS suspension (reference see the Experimental Section) in 10 mL ethanol and 60 s of flow deposition with a flow rate of 2.50 mL min^{-1}. The SEM images, Figure 3c,d, demonstrate the dense and homogeneous filling of pores obtained in these optimized conditions. Interestingly, the highest flow rates but not the highest suspension concentrations yield the best degree of order. The reason for this effect lies with a quite sensitive balance between an insufficient agglomeration tendency (which lets individual spheres traverse both pore segments without clogging at the constriction) and a too high agglomeration tendency (which lets spheres agglomerate on the top face of the template already, Figure S1, Supporting Information).

2.3. Effect of the Pore Wall Chemistry on the Sphere Assembly

Beyond the processing parameters during the filtering assembly, the stacking of spheres could also be affected by their interaction with the pore walls. To investigate this, we compare the behavior of porous templates submitted to various surface functionalization preliminarily, **Figure 4**a. Treatment of the alumina pores with the methylation agent HMDS (hexamethyldisilazane), which is a classic method for rendering oxides hydrophobic, clearly results in a much lower density of PS spheres in all processing conditions explored. We interpret this observation as a demonstration that the assembly is not mainly driven by the chemical interactions between the hydrophobic PS spheres and pore walls. Instead, spheres stack simply based on mechanical effects (clogging), in agreement with the strong dependence on flow and concentration parameters demonstrated in the previous section.

Do electrostatic effects influence the assembly of spheres in the porous system? Let us address this question by comparing alumina with HfO_2 and ZnO surfaces. A reliable determination of their ζ-potentials is enabled by streaming current experiments conducted on silicon wafers coated with a 10 nm thick layer of HfO_2 or ZnO, respectively, **Figure 5**.

Based on these streaming current measurements, the isoelectric points (IEPs) of HfO_2 and ZnO thin films are located at pH 4–5 and pH 8–10, respectively. Both IEPs are in excellent agreement with the data reported by Kosmulski et al.[22] HfO_2 exhibits a ζ-potential of $-37(\pm6)$ mV at neutral pH, whereas the ZnO thin film degrades at pH <9 in an aqueous solution. However, a positive ζ-potential at neutral pH can be expected for ZnO.[23,24] Given the negative ζ-potential of our PS spheres in ethanol, $-31(\pm1)$ mV, electrostatics may contribute to the significant differences in particle loading shown in Figure 4a

© 2023 The Authors. Advanced Materials Interfaces published by Wiley-VCH GmbH

ADVANCED SCIENCE NEWS
www.advancedsciencenews.com

ADVANCED MATERIALS INTERFACES Open Access
www.advmatinterfaces.de

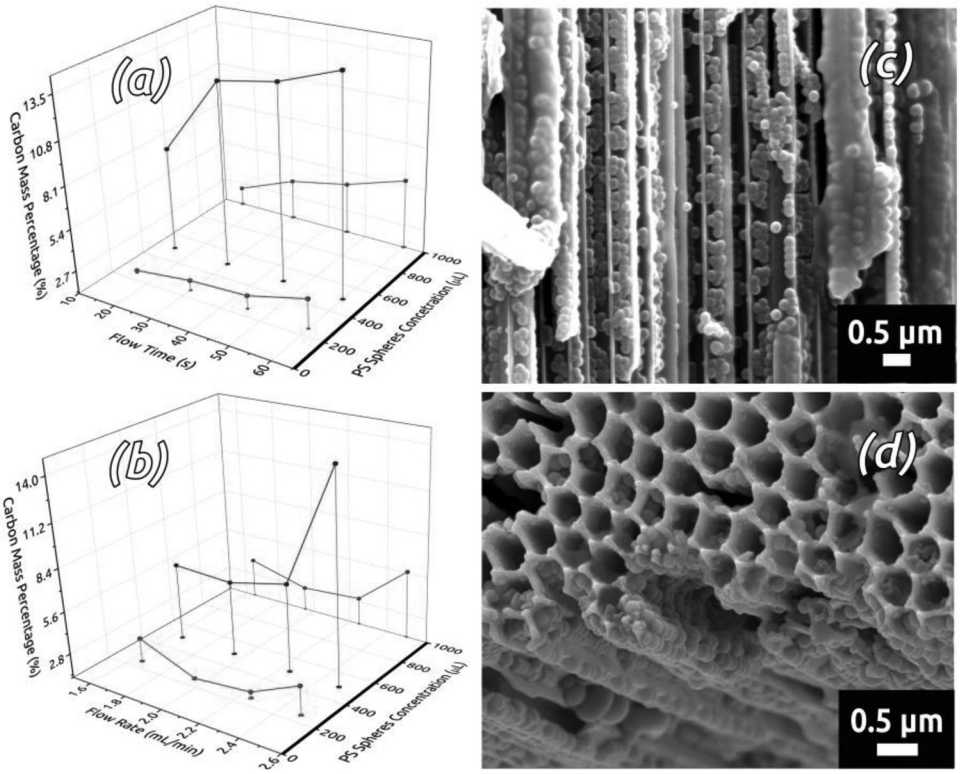

Figure 3. Assembly of polystyrene particles of D_s = 130 nm inside the ordered segmented porous system. Systematic study of the stacking density as a function of: a) flow rate, b) flow duration, and a,b) suspension dilution. SEM images of assembled PS sphere systems of the highest density in c) cross-sectional view and d) top view, showing the arrangement of spheres along the pores.

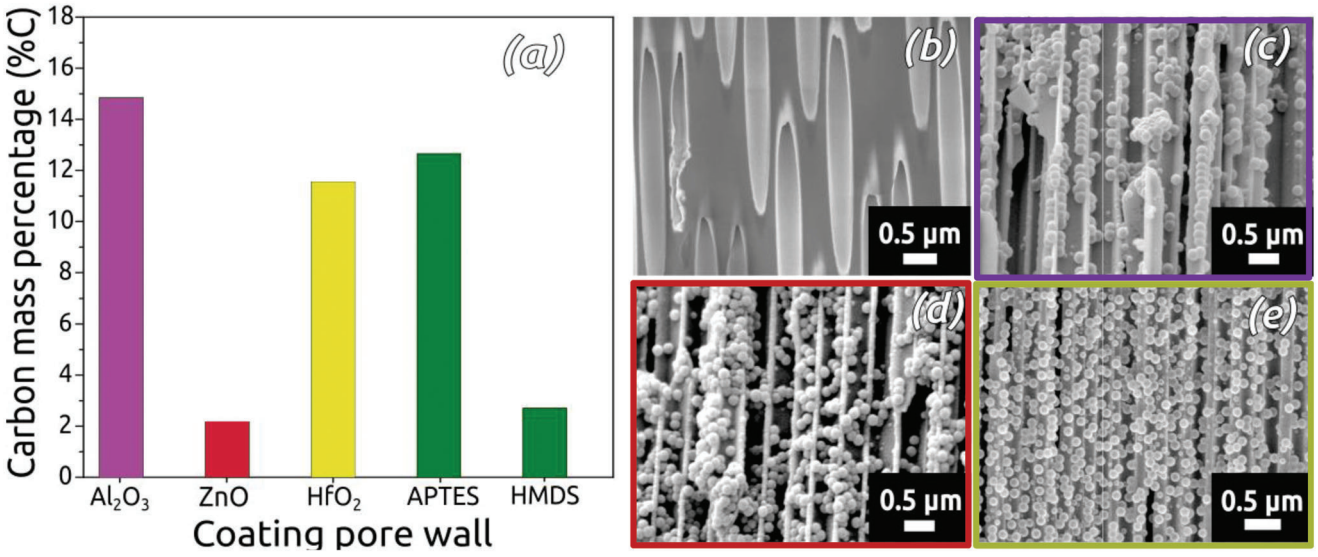

Figure 4. a) Quantification of the carbon mass percentage (%C) by EDX for various surface-functionalized porous systems. SEM images of the surface functionalization of the ordered porous system, b) coated pores with a layer of metal oxide (HfO_2). Arrangement of the polystyrene spheres template coated with ZnO layer by ALD, after thermal treatment at 450 °C: c) as arranged in anodic aluminum oxide (Al_2O_3) pores directly and in pores coated with d) ZnO and e) HfO_2.

© 2023 The Authors. Advanced Materials Interfaces published by Wiley-VCH GmbH

ADVANCED SCIENCE NEWS
www.advancedsciencenews.com

ADVANCED MATERIALS INTERFACES Open Access
www.advmatinterfaces.de

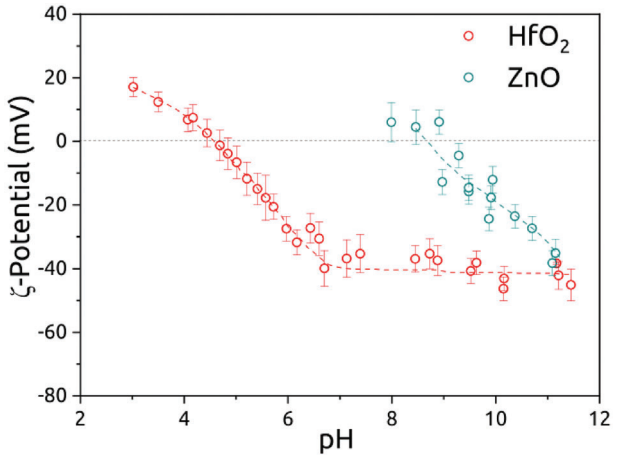

Figure 5. ζ-potential of HfO_2 and ZnO coated on silicon wafers as a function of the pH at an overall ionic strength of 10 mM in KCl.

between HfO_2 and ZnO. The oppositely charged ZnO and PS interfaces lead to electrostatic attraction, which increases the chance of disordered pore clogging instead of a dense, mechanically driven, stacking of spheres (**cf.** Figure 4d). In contrast to this, the negative surface charge of HfO_2 tends to maintain the spheres suspended throughout their travel through the pores until they encounter the stack. This mechanism favors high particle loadings in the pores (**cf.** Figure 4e). In other words, the data are consistent with our model of mainly mechanically driven stacking. Adhesion of spheres to the walls, be it caused by electrostatics or a hydrophobic effect, is not conducive to a high-density assembly. **Table 1** summarizes the experimental IEPs.

2.4. Characterization of Functional Samples

In the closing steps of our preparative procedure (Steps 3–5 in Figure 1), the PS spheres are coated with ZnO as an electrically conductive layer by ALD, the only method able to coat such highly porous systems with complex geometries in a conformal and homogeneous manner. The spheres can be removed via thermal oxidation, upon which a purely inorganic sample is obtained. Figure 4c,d,e demonstrates that PS is removed without damage to the ZnO overcoating. Finally, the electrocatalyst Pt is added by ALD (nominal thickness 6 nm). The final samples obtained after the full procedure established in this study exhibit the same morphology as in the previous steps (SEM in **Figure 6**a,c,e but with all materials desired in their crystalline form, as shown by X-ray diffraction (XRD, Figure 6b,d,f). All XRD patterns after the thermal step evidence the peaks for the hexagonal (hcp) phase of ZnO (zincite, COD 9004180). The samples featuring ZnO on ZnO exhibit a crystalline layer even as deposited. However, samples with only one ZnO layer on another metal oxide are originally amorphous, and ZnO crystallizes upon annealing. These observations are in line with the ALD literature, where ZnO transitioning to a crystalline form upon reaching a critical film thickness during growth is documented. In case it is crystalline before thermal treatment, annealing generates a preferential orientation along the (100) direction (peak at 31.5°). Furthermore, the final samples also reveal the peaks associated with the cubic (ccp) structure of Pt (COD 9013417), deposited in crystalline form after the thermal step. HfO_2 is deposited in amorphous form and crystallizes upon thermal treatment (monoclinic, COD 1528988). Note that anodic alumina is amorphous throughout and gives rise to both broad signals below 30°. For the reference sample with a ZnO layer but without PS spheres within the pores, weak peaks associated with the ZnO layer are observed, whereas in contrast with those, pronounced peaks appear for Pt. The XRD patterns of all nanostructured samples are consistent with the crystalline phases expected on them.

Table 1. IEP values were determined experimentally by streaming current measurements for the ALD-coated samples used in this work, compared with bulk materials from the literature.

Oxide	IEP (bulk mat.)	IEP thin film
ZnO	8.8–10.0[22]	8–10
HfO_2	5.0[22]	4–5

The chemical composition of all samples (**Figure 7**) follows expectations with the presence of the elements Al, Zn, Pt, O, and optionally Hf. EDX line profiles recorded for Al, Zn, and Hf along the cross-section exhibit the sharp step functions expected due to the presence of the pore diameter constriction. Along each pore segment, the signals are constant, evidencing that the deposition of the spheres within the pores and of the metal oxides on the surfaces are homogeneous. The Pt profiles also feature a quite sharp step on three of the four samples. The HfO_2 sample, however, is less perfect in that the Pt signal trails and reaches close to zero at about half of the spheres-infiltrated segment. This aspect is probably associated with the slow diffusion of ALD precursors through the meanders of the complex pore geometry generated by the densely packed spheres, and it will be important for the functional performance presented below.

2.5. Quantification of Specific Surface Area Via Sorption Experiments

A total of six samples are chosen for sorption analysis. One set of samples exhibits the unmodified Al_2O_3 surface while the other two variants are coated with ZnO and HfO_2. Of each variant, we also compare one fully prepared to the stage of Step 3 in Figure 1 (including ZnO-coated spheres) and one in the state prior to the addition of the spheres (no spheres, smooth cylindrical pores). Krypton (77 K) adsorption expressed as a function of relative pressure is shown for HfO_2 and ZnO in **Figure 8**a,b. The adsorbed amount is stated per unit of macroscopic sample area for a more straightforward comparison. Clearly, the amount adsorbed on the spheres-containing samples is significantly higher than with empty, smooth pores. This reflects an increase in effective surface area, assuming a similar state of the krypton adsorbate. This increase is quantified using the BET method for all three systems (Al_2O_3, HfO_2, ZnO) in **Table 2.** It is most appreciable in the HfO_2-based system, in line with the observations presented above by SEM and EDX.

© 2023 The Authors. Advanced Materials Interfaces published by Wiley-VCH GmbH

ADVANCED SCIENCE NEWS
www.advancedsciencenews.com

ADVANCED MATERIALS INTERFACES
Open Access
www.advmatinterfaces.de

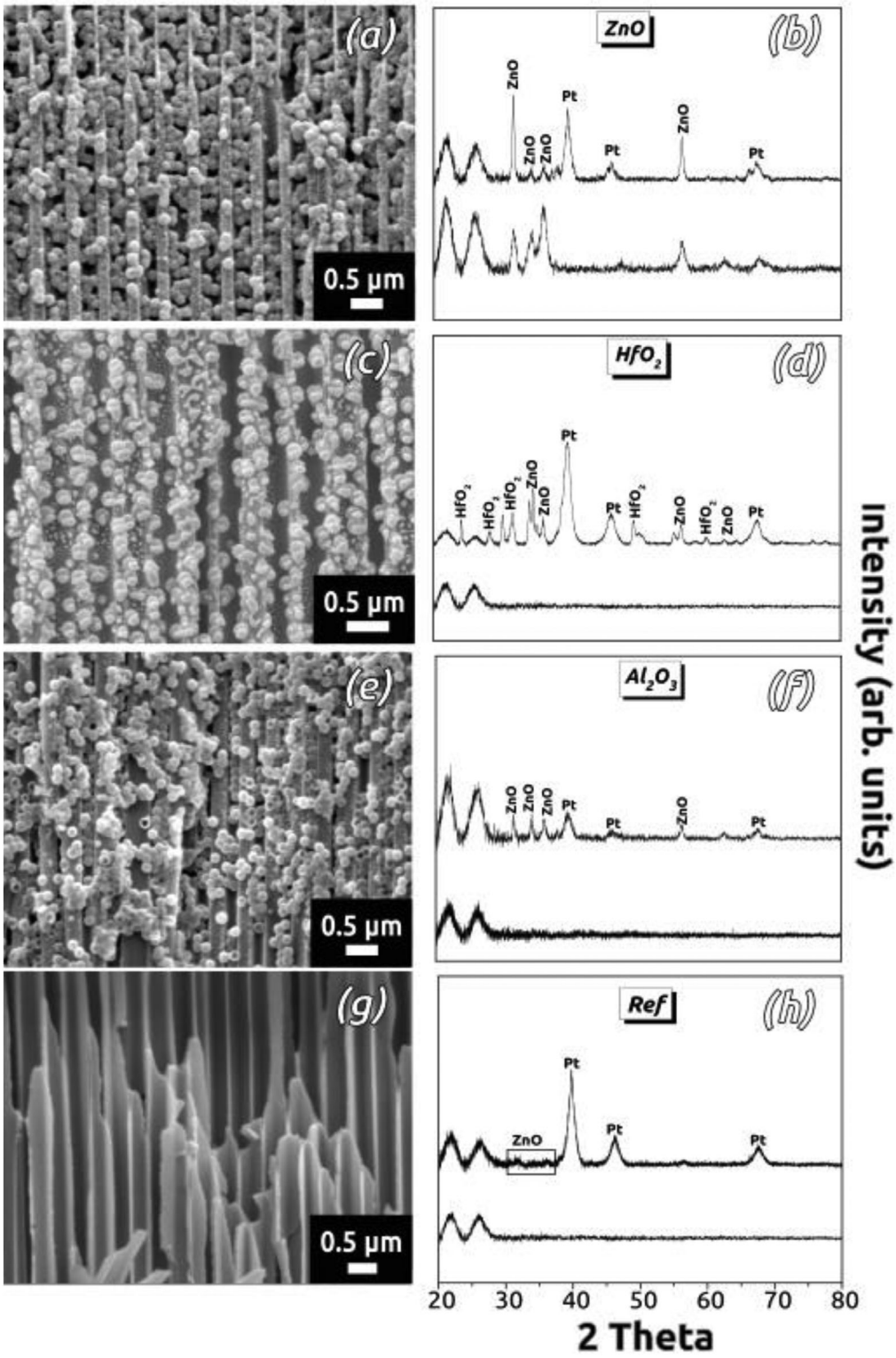

Figure 6. Cross-section SEM images and X-ray diffraction (XRD) patterns of the final electrodes of the three main types described, that is: a,b) AAO template ALD-coated with ZnO layer before PS spheres infiltration, c,d) AAO template ALD-coated with HfO_2, e,f) AAO template without ALD-coated, g,h)AAO template ALD-coated with ZnO without PS spheres. XRD patterns are always compared to the corresponding datasets (presented in the lower part of the graph) recorded after Step 4 of the preparative procedure (Figure 1).

© 2023 The Authors. Advanced Materials Interfaces published by Wiley-VCH GmbH

ADVANCED SCIENCE NEWS
www.advancedsciencenews.com

ADVANCED MATERIALS INTERFACES Open Access
www.advmatinterfaces.de

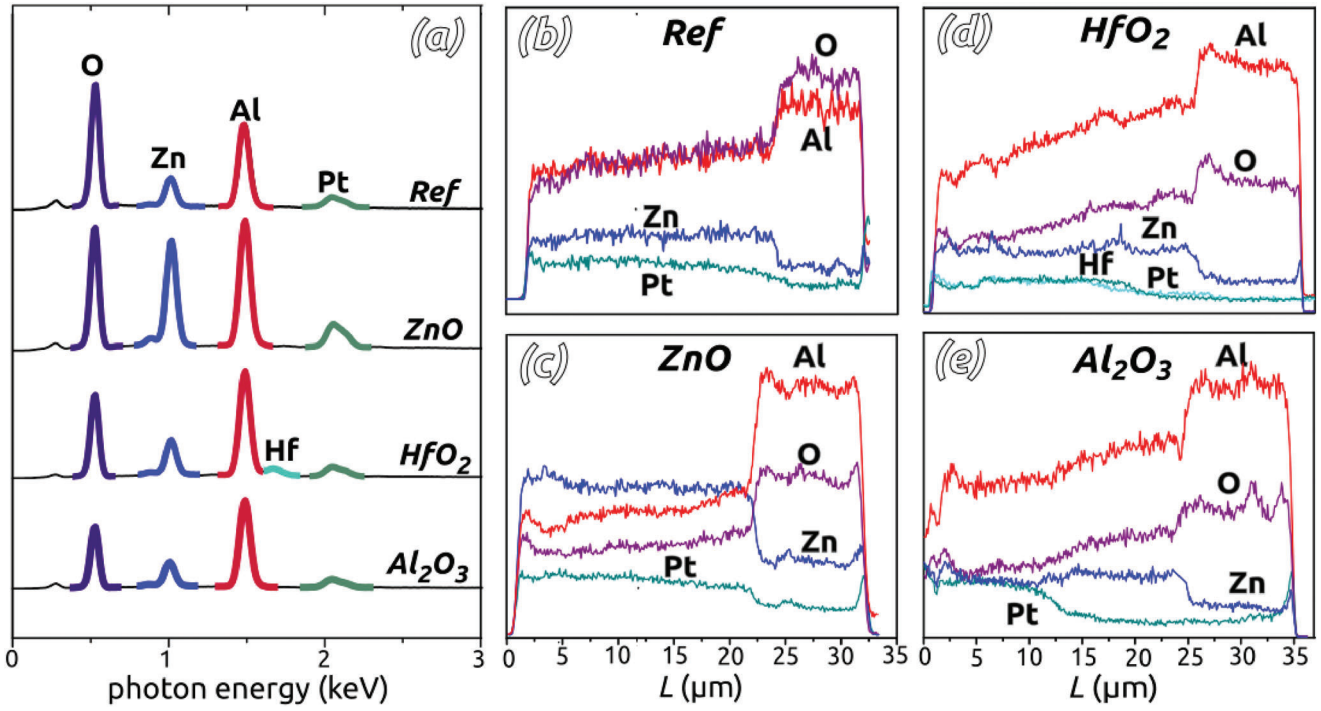

Figure 7. a) EDX spectra recorded from the cross-section of the samples prepared. EDX profiles along the cross-section for the various porous systems: b) ALD-coated with ZnO without PS. With spheres: c) AAO template ALD-coated with ZnO, d) AAO template ALD-coated with HfO_2, and e) AAO template.

2.6. Electrochemical Characterization

The final aspect of our study is dedicated to functionality. Taking the electrocatalytic hydrogen evolution as an example, we want to demonstrate catalytic activity and the effect of the increased specific surface area. This is achieved by quantifying the capacitive and resistive components of the samples' electrical response in electrochemical impedance spectroscopy, which can be correlated with the effective surface areas determined by sorption experiments. The data are collected in two quite different conditions in order to prove the validity of our conclusions: 1) at buffered pH 7 (phosphate buffer) under a constant applied voltage of −0.4 V with respect to the Ag/AgCl reference electrode, corresponding to a potential approximately 0.22 V less negative than the equilibrium potential at this pH under 1 bar H_2, and (2) at pH 3 under −0.8 V (to Ag/AgCl), corresponding to a potential approximately 0.41 V more negative than the equilibrium under 1 bar H_2. The Nyquist plots obtained for those systems are shown in **Figure 9**a,b. The impedance spectra for the nanostructured samples include a depressed semicircle in the high-frequency region representing the electron-transfer-limited process, and a straight line at the lower-frequency region corresponding to

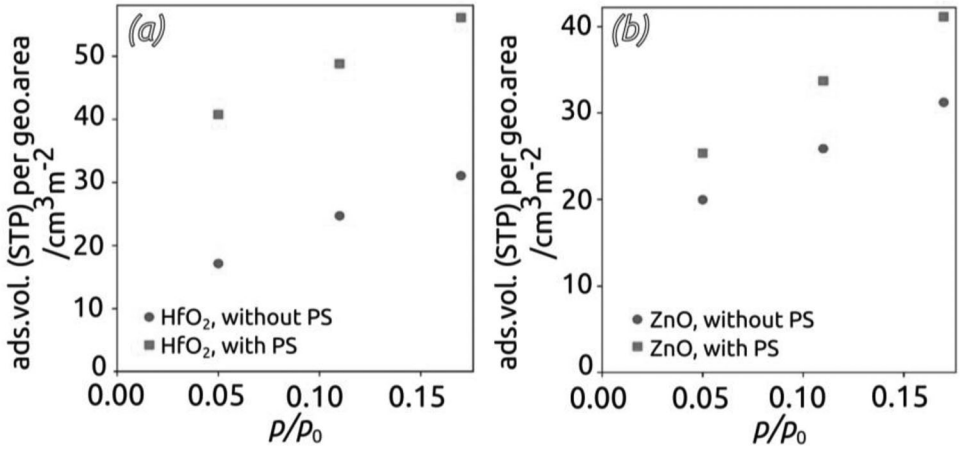

Figure 8. Krypton (77 K) adsorption isotherms for samples coated with a) HfO_2 and b) ZnO, with and without infiltrated spheres.

© 2023 The Authors. Advanced Materials Interfaces published by Wiley-VCH GmbH

ADVANCED SCIENCE NEWS
www.advancedsciencenews.com

ADVANCED MATERIALS INTERFACES Open Access
www.advmatinterfaces.de

Table 2. Kr BET surface areas per unit of macroscopic sample area, in $m^2\ m^{-2}$.

	Smooth pores without spheres	With ZnO-coated spheres
Al_2O_3	138 (±6)	139 (±6)
HfO_2	124 (±3)	204 (±1)
ZnO	116 (±2)	155 (±1)

diffusion-limited conditions. The electrodes based on Al_2O_3 and HfO_2 surfaces (prior to PS infiltration) yield a truncated semicircle at pH 7, indicating fast surface turnover. This is consistent with the high quality of nanostructuring through PS spheres assembly within the porous system (quantified by high EDX carbon content). The comparison between the sample with spheres assembled on ZnO surface and the reference without spheres shows that surface area increase by spheres is associated with a semicircle of smaller diameter, consistent with the higher surface area.

A quantitative treatment of the EIS data is afforded by fitting the datasets to a classic equivalent circuit model shown in Figure 9c [25–27] The physical-chemical interpretation of the electrical element centers around the crucial double layer capacity C_{dl} in parallel to the charge transfer resistance R_{ct} to Faradaic electron transfer across the interface. A Warburg element W is placed in series with it to model mass and charge transport along the pore. Additionally, the Ohmic resistance to electron transport along the ZnO layer places a resistance element R_{ohm} in series. This whole set of elements is placed in parallel with a capacitor C_{por} representing the entire oxide matrix behaving as a dielectric.

The values determined from the fits are presented in **Table 3** for three samples prepared as presented above with HfO_2, ZnO, and Al_2O_3 (from the AAO walls) as surfaces before PS spheres infiltration, with a sample featuring smooth pores (ZnO-coated pore wall), unfunctionalized with spheres, as a reference (labeled "ref" on the graphs). Standard deviations determined from the fit quality are very small and therefore not included in the table. Both datasets yield similar trends despite the slightly distinct values obtained as a result of the widely different experimental conditions. As expected, C_{por} remains on the same order of magnitude for all samples, as well as W and R_{ohm}, for both pH values evaluated. The most significant differences appear in the crucial C_{dl} values. The largest double-layer capacitance is obtained for the sample preliminarily functionalized with HfO_2. This is in line with our observations reported above concerning the quality of spheres ordering inside the pores (quantified above as EDX carbon content and specific surface area via Kr sorption). Accordingly, the sample preliminarily treated with HfO_2 and the untreated one (bare alumina) have both a higher density of spheres and a higher roughness (indicated by higher C_{dl}) than the sample treated with ZnO before infiltration. The reference sample which has the same chemical identity as all others but without the added roughness inside the pores caused by the spheres has the lowest C_{dl} of all. This trend is observed for both pH values evaluated for the electrodes in this study.

Overall, high C_{dl} correlates with low R_{ct} as expected based on surface area. One notable deviation from this trend is observed with the HfO_2-coated sample. Here, R_{ct} is high despite the large surface area. The most likely reason for this behavior is the imperfect coating with Pt demonstrated by EDX line profiles (Figure 7). In summary, one example of functional performance provided by electrocatalytic proficiency for hydrogen evolution on Pt demonstrates that all geometric and chemical features of the samples are mirrored in the functional performance quantifiers. Most importantly, the surface area increase achieved with stacked PS spheres translates into electrocatalytic performance as expected. This model system can now be applied to a variety of case studies in catalysis and electrocatalysis.

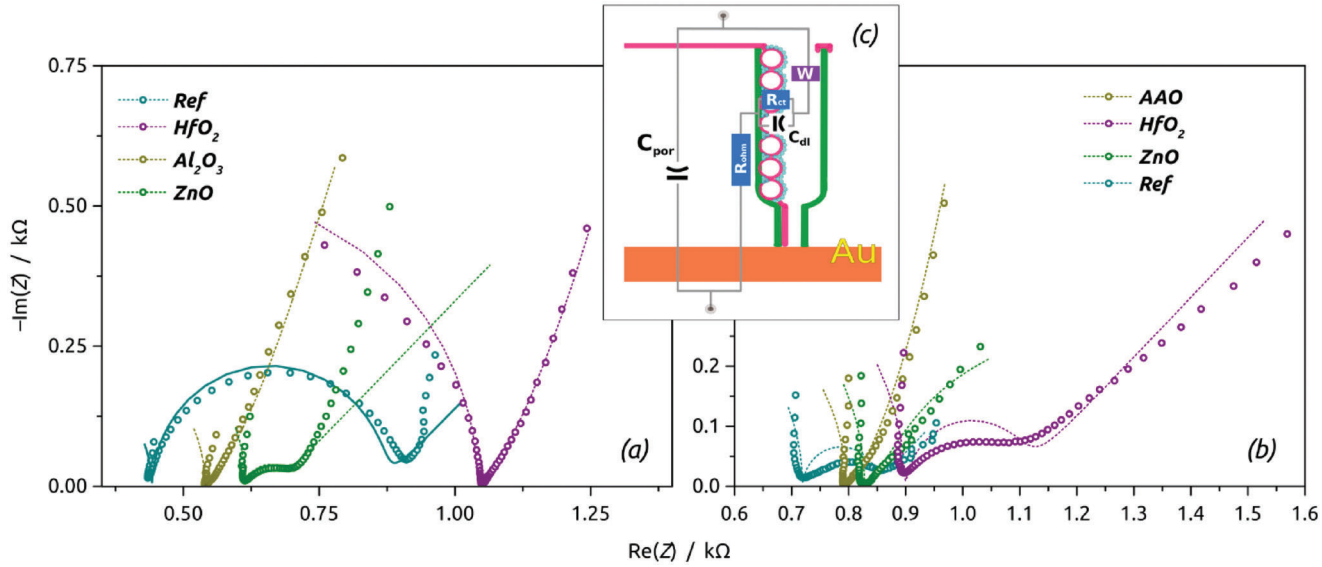

Figure 9. EIS datasets recorded in a phosphate electrolyte prepared from 0.1 M NaH_2PO_4 electrolyte adjusted to a) pH 7 and b) pH 3 for nanostructured porous electrodes coated with various metal oxides [fitted data: black solid line; measured data: line + symbol]. c) The equivalent circuit model for the nanostructured porous electrodes.

© 2023 The Authors. Advanced Materials Interfaces published by Wiley-VCH GmbH

ADVANCED SCIENCE NEWS
www.advancedsciencenews.com

ADVANCED MATERIALS INTERFACES Open Access
www.advmatinterfaces.de

Table 3. Values of the elements of the equivalent circuit from the fitted model to impedance spectroscopy data at pH 7.0 and pH 3.0.

	pH 7.0				pH 3.0			
Elements	HfO_2	Al_2O_3	ZnO	ref.	HfO_2	Al_2O_3	ZnO	ref.
R_{ohm}/kΩ	1.0	0.5	0.6	0.4	1.5	0.8	0.8	0.9
R_{ct}/Ω	9000	6000	60	400	2000	13 000	200	250
C_{dl}/μF	2000	1000	5	1	3000	100	25	15
C_{por}/pF	100	60	50	60	70	60	50	30
W/mS $s^{1/2}$	2.3	2.0	1.1	3.0	2.2	0.2	1.1	0.2

3. Conclusions

This work establishes a preparative method for generating a tunable porous system based on anodized alumina acting as a template for a polystyrene spheres assembly achieved with high degree of control in a simple flow procedure. Our systematic exploration of the relevant experimental parameters during assembly toward achieving a high-density packing of the PS spheres inside the pores reveals that the functionalization of the pore wall surface influences the packing quality, with uncharged oxide surfaces delivering the best results. Engineering the surface chemistry so as to enhance its affinity for the polystyrene of the spheres does not provide the desired effect. Both electrostatic attraction and hydrophobic interactions cause a less ordered, less dense packing. However, the physical parameters of suspension and flow provide a much more convenient set of tools to adjust and optimize the structure of the confined spheres stack.

The geometric quality of the stack can be assessed and quantified in several distinct ways. The absolute amount of organic material can be determined by EDX. Highly sensitive Kr 77 K adsorption allows one to assess the corresponding enhancement in specific surface area and we find excellent agreement with the semi-quantitative trends observed by EDX. Furthermore, when functionalized with Pt particles as an example of application, this model system yields physical-chemical performance parameters that also reflect its geometric properties. In electrochemical impedance spectroscopy, the nanostructured Pt electrode exhibits higher capacitance values when the electroactive surface area is enhanced by densely packed spheres. All three probes of the surface and its geometry, namely EDX, adsorption, and impedance spectroscopy, point to a HfO_2 coating of the smooth, cylindrical pores as the best suited to enable a dense sphere packing and maximal surface area enhancement under high flow and moderate concentration conditions.

This model system can now be applied to a broad variety of electrocatalysis and catalysis topics. Enhancing a catalyst support's geometric surface area is always advantageous to increase catalytic throughput. However, transport along long pathways in highly porous systems can become slower than turnover at the interface, in a manner which has mostly been difficult to pinpoint experimentally in an accurate and definitive manner. With the system presented here, the length and diameter of pores but also their internal roughness can all be adjusted independently and varied systematically to create samples featuring tailored residence times of the reactive mixture, tailored numbers of surface reactive sites, and tailored diffusion distances. This represents a novel experimental platform for testing and quantifying theoretical simulations, their hypotheses, and their predictions.

4. Experimental Section

Materials: Reagents for the preparation of the samples were purchased from Sigma–Aldrich, Alfa Aesar, Strem, or VWR and used as received. Millipore Direct-Q system was employed for the purification of water before use. Aluminum plates (99.99%) for the anodization process and Si (100) wafers for the atomic layer deposition (ALD) were supplied by Smart Membranes and Silicon Materials Inc, respectively. The sacrificial polystyrene (PS) spheres used in this study were prepared following the protocol reported in the literature.[28,29]

Anodization of aluminum into ordered pores: The generation of the tunable ordered porous system follows the standard two-step anodization procedure described in the literature.[30] A homemade setup was used to anodize four circular aluminum plates of 2.2 cm diameter, held by O-rings underneath a polyvinyl chloride beaker. A Cu plate was placed under them and acted as an electrical contact. The assembled beakers were cooled to 0 °C overnight. Subsequently, electropolishing was performed in a solution of 1:3 v/v $HClO_4$/EtOH for 7 min by applying +20V. The samples were rinsed and cooled down again in the anodization beakers for 2 h before the first anodization at 195 V (max. 0.20 A) for 24 h in 1 wt.% H_3PO_4. After this first anodization, ordered Al_2O_3 hemispherical indentations were achieved by submitting the samples to a treatment with chromic acid overnight at 45 °C. With a second anodization, a first segment was grown for 8 h in 1 wt.% H_3PO_4 under the same experimental conditions as previously. This step yielded a system with well-ordered Al_2O_3 pores. Subsequently, the pores were widened in 10% phosphoric acid solution for 45 min at 45 °C. Afterward, a short cooling was performed again, and a third anodization was carried out to grow up a second segment for 4 h. Finally, both segments were submitted to a final pore widening during 45 min at 45 °C in 10% phosphoric acid solution. The next step was to remove the metallic Al substrate on the backside of the Al_2O_3 porous membrane in a $CuCl_2$ solution (0.7 M $CuCl_2$ in 10% HCl). Finally, the resulting samples were treated with 10% phosphoric acid for 60 min at 45°C for opening the Al_2O_3 barrier layer and closing the pores.

Surface Functionalization of Ordered Porous System: Subsequently, the system of segmented pores with two distinct diameters was coated with ≈12 nm of either ZnO or HfO_2 by atomic layer deposition (ALD) to provide various surface properties (from acidic to basic) by using an ALD set-up with N_2 as carrier gas. The deposition of ZnO was carried out at 90°C with diethylzinc (DEZ) and H_2O both kept in stainless steel bottles maintained at room temperature. The pulse, exposure, and purge durations of the precursors, DEZ and H_2O, were 0.15, 40, and 70, and 0.3, 40, and 70 s, respectively. 55 ALD cycles gave rise to ≈12 nm of ZnO. For the deposition of HfO_2 tetrakis(ethylmethylamido)hafnium and H_2O maintained were used in steel bottles at 65 °C and room temperature, respectively, with pulses, exposures, and purges of 0.55, 40, and 70 s for both precursors. Two consecutive subcycles were pulsed for the TDMA-Hf precursor. Native silicon wafers were added to the reaction chamber for the determination of the

© 2023 The Authors. Advanced Materials Interfaces published by Wiley-VCH GmbH

ADVANCED SCIENCE NEWS
www.advancedsciencenews.com

ADVANCED MATERIALS INTERFACES Open Access
www.advmatinterfaces.de

layer thicknesses by spectroscopic ellipsometry. Molecular surface functionalization of the AAO walls by APTES, (3-aminopropyl)triethoxysilane, was performed by immersion in a 5% solution in toluene for 24 h under continuous stirring at room temperature.[31] For the functionalization with HMDS, hexamethyldisilazane, 100 µL of liquid HMDS was added to a closed, evacuated Schlenk flask containing the AAO sample at room temperature for 24 h. The APTES- and HMDS-modified AAO porous systems were dried before further use.

Assembly of Polystyrene (PS) Spheres: Polystyrene (PS) spheres with a diameter of 130 nm were synthesized as aqueous suspensions by a published procedure.[31] After dilution in EtOH in ratios of 250, 500, and 1 mL to 10 mL of EtOH, they were assembled in porous systems with and without surface functionalization by flowing in a microfluidic system. A peristaltic pump (Model 400 A) was used to generate a flow rate set to values from 1.65 mL min^{-1} to 2.5 mL min^{-1} for a duration from 15 to 60 s. After the stacking of PS spheres was achieved within the porous system, a new layer of ZnO (≈12 nm) was deposited by ALD following the conditions described previously. Subsequently to the quantification of carbon content on the samples by EDX, the removal of the PS spheres was performed via thermal decomposition at 450 °C in the air for 5 h in an oven. Finally, electrical contact was defined on one face of the samples by sputter-coating 10 nm of gold in a Torr CRD 622 operating in DC mode.

Isoelectric Point Determination: The electrokinetic measurements were performed by the streaming current method in a setup similar to the ones described previously.[32,33] An asymmetric cell for this setup was manufactured out of PTFE (Auer Kunststofftechnik GmbH) with a nominal channel height of 0.3 mm. The measurement cell was symmetrically calibrated with a PTFE piece, and the asymmetrically measured data were evaluated according to the procedure reported by Walker et al.[34] All streaming current measurements were performed at constant ionic strength (10 mM, KCl, BioUltra, Merck) between pH 3 and pH 11 (HCl/KOH, Titrisol, Merck). Calibration of the streaming current data was obtained on thermally oxidized silicon wafers (CrysTec GmbH). A good agreement with the data reported by Scales et al. was found.[35] The reported ζ-potentials were calculated by the Helmholtz–Smoluchowski approximation. The isoelectric point (IEP) determination for the different coatings (HfO_2 and ZnO) was performed on silicon wafers onto which the oxides were preliminarily deposited by ALD as described above.

Catalyst Deposition: The samples dedicated to electrochemical analysis were then provided with a catalyst layer by ALD. Trimethyl(methylcyclopentadienyl)platinum (MeCp)$PtMe_3$ and ozone were used as precursors for the deposition of platinum (Pt). A generator model BMT 803N produced the ozone from O_2. The deposition of Pt was carried out at 220 °C while (MeCp)$PtMe_3$ was kept in a steel bottle at 50 °C and delivered with pulse, exposure, and purge durations of 0.5, 30, and 90 s. Two consecutive subcycles with pulse and exposures of 0.5 and 30 s, respectively were performed before the purge with N_2 for 90 s for the metal precursor, and four microcycles were used with ozone in ALD. Approximately 6 nm were deposited with 100 cycles.

Electrochemical Studies: The final nanostructured samples were laser-cut (GCC Laser Pro Spirit LS Laser) into small disks of 3.5 mm in diameter and glued on square double-sided conductive copper foils in contact with the gold current collector. An electrically insulating polyimide (Kapton) adhesive tape provided a circular window of 2 mm as the area in contact with the electrolyte for the electrochemical analysis. A three-electrode electrochemical cell was built with Pt mesh as the counter-electrode and Ag/AgCl as the reference electrode. The electrochemical measurements of EIS were done at room temperature with a Gamry Interface 1000 potentiostat in a phosphate electrolyte based on 0.1 M NaH_2PO_4 adjusted to pH 7 or pH 3. The Gamry Echem Analyst software was used to generate the fits to Nyquist plots obtained on all samples.

Material Characterization: The morphology and geometry of the nanostructured samples were characterized by scanning electron microscopy (SEM) and the quantification of the elements by energy-dispersive X-ray microanalysis (EDX) using a JEOL 3010 microscope. The crystalline structure was determined by powder X-ray diffraction measurements using a Bruker D8 Advance diffractometer with Cu K_α radiation (λ = 1.5405 Å). The determinations of the layer thicknesses were performed on Si (100) wafers with a Sentech spectroscopic ellipsometer SENpro equipped with a tungsten halogen lamp. Atomic force microscopy (AFM) was utilized to determine the surface topography of planar ALD-deposited oxide films in PeakForce Tapping mode (Bruker ICON, Nanoscope V controller) with ScanAsyst Air cantilevers (Bruker) under ambient conditions. The cantilevers have a nominal resonance frequency of 70 kHz and a tip radius <5 nm. AFM images of 1×1 µm^2 were recorded to determine the average roughness after a plane fit of 1st order, Figure S2, Supporting Information.

Adsorption Experiments: Adsorption isotherms were measured using an Autosorb iQ automatic volumetric adsorption analyzer (Anton Parr QuantaTec, formerly Quantachrome instruments, Boynton Beach, FL). In order to assess the very small surface area of the macroporous alumina samples, krypton (purity 99.9999%, obtained from Air Liquide) was used as adsorptive. The sorption measurements were performed at liquid nitrogen temperature (77 K). Samples were outgassed at 120 °C for 12 h under turbomolecular pump vacuum.

Surface areas were calculated by applying the BET method to krypton 77 K adsorption data in the relative pressure range p/p_0 of 0.05 to 0.1, assuming the customary p_0 for supercooled krypton of 2.63 Torr (i.e. at 77 K krypton is ca 38 K below its triple point).[36] Due to this extremely low saturation pressure, the number of molecules in the free space of the sample cell is significantly reduced (to 1/300th as compared to nitrogen or argon at their respective boiling temperatures: this leads to the high sensitivity of krypton adsorption at 77 K (enabling the assessment of absolute surface areas as low 0.01 m^2), which is needed here. An effective Kr cross-sectional area of 0.16 nm^2, determined by utilizing nonporous alumina materials with known specific surface areas (i.e., benchmark data), was used for the surface area determination.[37] The Kr BET surface areas obtained in this way on the porous membrane samples were normalized to the respective macroscopic geometric sample areas.

Statistical Analysis: The determination of sphere loading density by EDX (Figure 3,4) was performed on cross-sections of porous samples, whereby the full sample depth was probed and averaged over time. The datapoints represent values obtained from the instrument's Jeol software by integration of the peaks without further processing. The uncertainty is on the order of 0.5%. Each data point of the zeta potentials vs. pH results from three measurements and is represented as a mean and corresponding standard deviation. Each zeta potential has been determined from the slope of current vs. pressure by a line fit. The fit is based on 10 different pressures, at each pressure value, the pressure and current, respectively, have been averaged from 10 measurements. No data points have been excluded as statistical outliers. However, for ZnO no data were acquired in the pH-range below pH 8 as under these conditions the film dissolved. The above data treatment is in line with the IUPAC report on electrokinetic measurements, by Delgado et al.[38] and specialized studies on the reproducibility of streaming potential measurements.[39,40] The specific surface area values determined by krypton adsorption result from up to three repeats and the uncertainties cited in Table 2 are associated with the maximum deviations from the corresponding mean BET areas. The quantities determined by electrochemical impedance spectroscopy (Table 3) are derived from the model described in Figure 9 via a fitting procedure performed by the Gamry Analyst software. The uncertainties resulting from the fits being very small, we chose to present in Table 3 values with as many significant digits as reasonable based on at least three repeats on nominally identical samples.

Supporting Information

Supporting Information is available from the Wiley Online Library or from the author.

Acknowledgements

The authors acknowledged the Deutsche Forschungsgemeinschaft (DFG, German Research Foundation) in the Collaborative Research

© 2023 The Authors. Advanced Materials Interfaces published by Wiley-VCH GmbH

Center (CRC)/Sonderforschungsbereich (SFB) 1452: Catalysis at Liquid Interfaces (CLINT) for financial support.

Open access funding enabled and organized by Projekt DEAL.

Conflict of Interest

The authors declare no conflict of interest.

Author Contributions

Conceptualization: J.B.; Methodology: C.V.R.M. and J.B.; sample preparation, data collection, and investigation: C.V.R.M., M.T., and M.E.; data interpretation: all authors; writing – original draft preparation: C.V.R.M.; editing: C.V.R.M.; writing – review: all authors; funding acquisition: J.B., M.T., and G.P. All authors have read and agreed to the published version of the manuscript.

Data Availability Statement

The data that support the findings of this study are available from the corresponding author upon reasonable request.

Keywords

anodic aluminum oxide, assembly, impedance spectroscopy, nanostructured electrodes, surface area

Received: May 24, 2023
Revised: July 14, 2023
Published online:

[1] Y. Xiao, Q. Lv, J. Zhu, S. Yao, C. Liu, W. Xing, *RSC Adv.* **2014**, *4*, 21176.
[2] H. Zhu, Y. V. Tolmachev, D. A. Scherson, *J. Phys. Chem.* **2010**, *114*, 13650.
[3] L. Liu, E. Pippel, R. Scholz, U. Gösele, *Nano Lett.* **2009**, *9*, 4352.
[4] K. Indira, U. K. Mudali, T. Nishimura, N. Rajendran, *J. Bio. Tribocorros.* **2015**, *1*, 28.
[5] R. Xu, L. Du, D. Adekoya, G. Zhang, S. Zhang, S. Sun, Y. Lei, *Adv. Energy Mater.* **2021**, *11*, 2001537.
[6] J. Shen, D. Lan, T. Yang, *Int. J. Electrochem. Sci.* **2018**, *13*, 9847.
[7] L. B. Sun, X.-Q. Liu, H.-C. Zhou, *Chem. Soc. Rev.* **2015**, *44*, 5092.
[8] M.-H. Sun, S.-Z. Huang, L.-H. Chen, Y. Li, X.-Y. Yang, Z.-Y. Yuan, B.-L. Su, *Chem. Soc. Rev.* **2016**, *45*, 3479.
[9] W. Lee, *JOM* **2010**, *62*, 57.
[10] W. Lee, S. J. Park, *Chem. Rev.* **2014**, *114*, 7487.
[11] Y. Piao, H. Kim, *J. Nanosci. Nanotechnol.* **2009**, *9*, 2215.
[12] Z. B. Yang, J. C. Hu, K. Q. Li, S. Y. Zhang, Q. H. Fan, S. A. Liu, *IOP Conf. Ser.: Mater. Sci. Eng.* **2018**, *283*, 012003.
[13] A. Sharma, D. G. Bracewell, *J. Memb. Sci.* **2019**, *580*, 77.
[14] M. Lu, Q. Zhang, Z. Zhang, X. Wang, B. Yan, Y. Wang, *J. Photochem. Photobiol. A Chem.* **2021**, *410*, 113167.
[15] N. Thormann, N. Teuscher, M. Pfannmöller, U. Rothe, A. Heilmann, *Small* **2007**, *3*, 1032.
[16] N. T. Phuong, A. Andisetiawan, D. V. Lam, J. H. Kim, D.-S. Choi, K.-H.- Whang, J. Nham, Y. J. Lee, Y.-E. Yoo, J. S. Yoon, *Sci. Rep.* **2016**, *6*, 37673.
[17] J. Gemmer, Y. Hinrichsen, A. Abel, J. Bachmann, *J. Catal.* **2012**, *290*, 220.
[18] S. Haschke, D. Pankin, Y. Petrov, S. Bochmann, A. Manshina, J. Bachmann, *ChemSusChem* **2017**, *10*, 3644.
[19] E. Wierzbicka, G. D. Sulka, *Sens. Actuators B Chem.* **2016**, *222*, 270.
[20] R. Xu, L. Xiao, L. Luo, H. Jia, C. Wang, F. Wang, *J. Electrochem. Soc.* **2017**,*164*, B382.
[21] Y. Shi, B. Zhou, P. Wu, K. Wang, C. Cai, *J. Electroanal. Chem.* **2007**, *611*, 1.
[22] M. Kosmulski, *Adv. Colloid Interface Sci.* **2020**, *275*, 102064.
[23] M. Bukáčková, R. Maršálek, *NANOCON* **2017**, proceedings, 473.
[24] Y. Furubayashi, T. Hayashi, S. Morito, Y. Hiragina, W. Yeh, Y. Kajikawa, H. Hashimoto, Y. Fujita, *Jpn. J. Appl. Phys.* **2014**, *53*, 05FF01.
[25] J. Z. Wang, C. H. Xu, W. Cao, Y. He, *Adv. Mater. Res.* **2014**, *953–954*, 1282.
[26] S. Yu, L. Wang, C. Wu, T. Feng, Y. Cheng, Z. Bu, S. Zhu, *J. Alloys Compos.* **2020**, *817*, 153251.
[27] W. Tao, D. Pan, Z. Gong, X. Peng, *Anal. Chim. Acta* **2018**, *1035*, 44.
[28] A. Manzke, A. Plettl, U. Wiedwald, L. Han, P. Ziemann, E. Schreiber, U. Ziener, N. Vogel, C. K. Weiss, K. Landfester, K. Fauth, J. Biskupek, U. Kaiser, *Chem. Mater.* **2012**, *24*, 1048.
[29] Y. Galvan, J. Bauernfeind, P. Wolf, R. Zarraga, M. Haumann, N. Vogel, *ACS Omega* **2021**, *6*, 20956.
[30] S. Bochmann, D. Döhler, B. Trapp, M. Staňo, O. Fruchart, J. Bachmann, *J. Appl. Phys.* **2018**, *124*, 163907.
[31] D. Dutta, J. Markhoff, N. Suter, K. Rezwan, D. Brüggemann, *ACS Appl. Bio. Mater.* **2021**, *4*, 1852.
[32] M. Morga, Z. Adamczyk, S. Gödrich, M. Oćwieja, G. Papastavrou, *J. Colloid Interface Sci.* **2015**, *456*, 116.
[33] A. Hofer, N. Taccardi, M. Moritz, C. Wichmann, S. Hübner, D. Drobek, M. Engelhardt, G. Papastavrou, E. Spiecker, C. Papp, P. Wasserscheid, J. Bachmann, *RSC Adv.* **2023**, *13*, 4011.
[34] S. L. Walker, S. Bhattacharjee, E. M. V. Hoek, M. Elimelech, *Langmuir* **2002**, *18*, 2193.
[35] P. Scales, F. Grieser, T. W. Healy, L. R. White, D. Y. C. Chan, *Langmuir* **1992**, *8*, 965.
[36] M. Thommes, K. Kaneko, A. V. Neimark, J. P. Oliver, F. Rodriguez-Reinoso, J. Rouquerol, K. S. W. Sing, *Pure Appl. Chem.* **2015**, *87*, 1051.
[37] C. Schlumberger, C. Scherdel, M. Kriesten, P. Leicht, A. Keilbach, H. Ehmann, P. Kotnik, G. Reichenauer, M. Thommes, *Microporous Mesoporous Mater.* **2022**, *329*, 111554.
[38] A. V. Delgado, F. González-Caballero, R. J. Hunter, L. K. Koopal, J. Lyklema, *Pure Appl. Chem.* **2005**, *77*, 1753.
[39] M. J. Ariza, J. Benavente, *J. Membr. Sci.* **2001**, *190*, 119.
[40] M. Chapman Wilbert, S. Delagah, J. Pellegrino, *J. Membr. Sci.* **1999**, *161*, 247.

 © 2023 The Authors. Advanced Materials Interfaces published by Wiley-VCH GmbH

ADVANCED MATERIALS INTERFACES
Open Access

Supporting Information

for *Adv. Mater. Interfaces*, DOI 10.1002/admi.202300436

Preparation and Surface Functionalization of a Tunable Porous System Featuring Stacked Spheres in Cylindrical Pores

*Christhy V. Ruiz M, Markus Terlinden, Matthias Engelhardt, Giulia Magnabosco, Georg Papastavrou, Nicolas Vogel, Matthias Thommes and Julien Bachmann**

Preparation and surface functionalization of a tuneable porous system featuring stacked spheres in cylindrical pores

Christhy V. Ruiz M.,[a] Markus Terlinden,[b] Matthias Engelhardt,[d] Giulia Magnabosco,[c] Georg Papastavrou,[d] Nicolas Vogel,[c] Matthias Thommes,[b] Julien Bachmann[a,*]

[a] *Friedrich-Alexander-Universität Erlangen-Nürnberg, Chemistry of Thin Film Materials, IZNF, Cauerstr. 3, D-91077 Erlangen, Germany*

[b] *Friedrich-Alexander-Universität Erlangen-Nürnberg, Institute of Separation Science and Technology, Egerlandstr. 3, D-91077 Erlangen, Germany*

[c] *Friedrich-Alexander-Universität Erlangen-Nürnberg, Institute of Particle Technology, Cauerstr. 4, D-91077 Erlangen, Germany*

[d] *Universität Bayreuth, Physical Chemistry II, Universitätsstraße 30, D-95447 Bayreuth, Germany*

corresponding author: *julien.bachmann@fau.de

Supporting Information

Figure S1

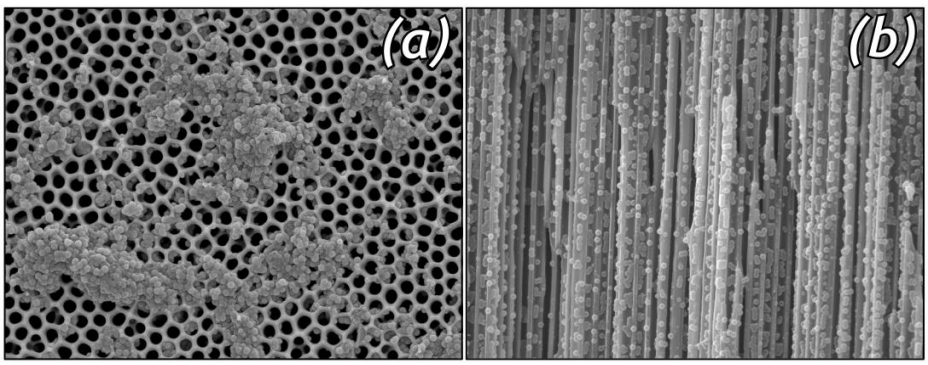

Assembly of PS spheres at higher concentration and flow rate within ordered porous system: (a) Top view: Agglomeration of PS spheres on surface of AAO reducing packing along the pores, (b) cross-section view.

Figure S2

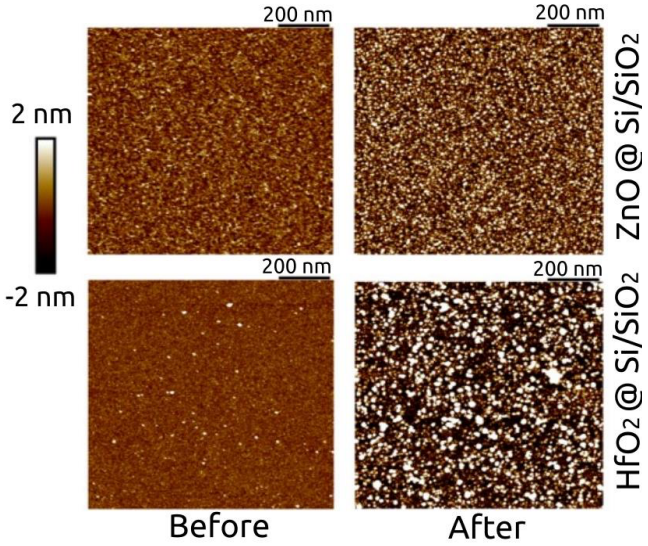

Oxide	*Ra [nm] before*	*Ra [nm] after*
ZnO	0.40	0.83
HfO_2	0.22	1.55

AFM images of the HfO_2 and ZnO on Si wafers before and after streaming current studies. Increase in roughness due to slight solubility in alkaline regimes.

7. Following Changes at the Solid/Liquid Interface for Large Microplastic Particles by Streaming Potential

Matthias B. Engelhardt, Daniel Wagner, Mohsen Zarebanadkouki, Nora Meides, Christian Schulbert, Martin G. J. Löder, Nicolas Helfricht, Seema Agarwal, Andrea Carminati, Peter Strohriegl, Jürgen Senker, Christian Laforsch, and Georg Papastavrou*

"Following Changes at the Solid/Liquid Interface for Large Microplastic Particles by Streaming Potential"

Chemistry-Methods, **2025**, *5(12), e202500102*.

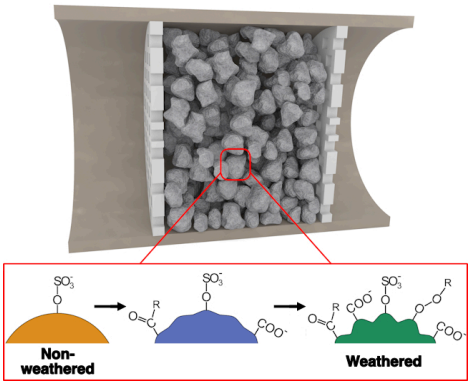

Reprinted with permission from:

"Following Changes at the Solid/Liquid Interface for Large Microplastic Particles by Streaming Potential", M. B. Engelhardt, D. Wagner, M. Zarebanadkouki, N. Meides, C. Schulbert, M. G. J. Löder, N. Helfricht, S. Agarwal, A. Carminati, P. Strohriegl, J. Senker, C. Laforsch, and G. Papastavrou, *Chemistry-Methods,* **2025**, *5(12), e202500102*.

DOI: 10.1002/cmtd.202500102

Under terms of the CC BY license

Chemistry—Methods

Research Article
doi.org/10.1002/cmtd.202500102

Chemistry Europe
European Chemical Societies Publishing

www.chemistrymethods.org

Following Changes at the Solid/Liquid Interface for Large Microplastic Particles by Streaming Potential

Matthias B. Engelhardt, Daniel Wagner, Mohsen Zarebanadkouki, Nora Meides, Christian Schulbert, Martin G. J. Löder, Nicolas Helfricht, Seema Agarwal, Andrea Carminati, Peter Strohriegl, Jürgen Senker, Christian Laforsch, and Georg Papastavrou*

The electrolyte/solid interface is ubiquitous in nature and for many applications. In particular, the double-layer properties are essential for predicting adsorption and transport behavior. While for small colloidal particles, electrophoretic mobility has developed into a routine technique, there is currently a lack of analogously established techniques for particles with diameters larger than 10 microns. Such particles are often encountered in natural soils, industrial formulations, and as contaminants in the form of microplastics. Herein, a systematic method development using the streaming potential technique of particle plugs composed of large particles is presented. This approach revives an analytical method that was first introduced nearly 75 years ago, which has rarely been used for particulate systems. Comparing the zeta-potential versus pH of polystyrene particles with varying surface functionalization demonstrated that streaming potential measurements can distinguish these surface groups. In agreement with theoretical predictions, no dependence on the particle dimensions and shape is observed. Moreover, the particle arrangement within the particle plugs has been characterized by X-ray microtomography. The viability of this technique is tested by monitoring the artificial weathering of artificially fragmented microplastic particles of nonspherical shape. This technique opens new possibilities for characterizing the interfacial properties of environmentally relevant microplastics.

1. Introduction

Microplastic particles (MPP) are among the most widespread environmental contaminants.[1–7] They can be found in aquatic and terrestrial environments, including rivers, soil, and the sea; MPPs are also present geographically everywhere on earth, even in remote locations such as Antarctica and the deep sea.[8,9] The composition and size range of microplastics sampled in the environment and the underlying transport mechanisms are important to model the fate of microplastics in the future and propose solutions for this urgent environmental problem. However, our understanding of microplastics is strongly constrained by the analytical methods currently available.[10–12] For the transport of MPPs in the environment, their colloidal and interfacial properties at the solid/liquid interface are highly important.[3,7,13–19] To date, nearly all studies on the solid/liquid interface of MPPs have relied on model systems composed of small micrometer-sized particles that were obtained by suspension polymerization and

M. B. Engelhardt, N. Helfricht, G. Papastavrou
Department of Physical Chemistry II
University of Bayreuth
95447 Bayreuth, Germany
E-mail: georg.papastavrou@uni-bayreuth.de

D. Wagner, S. Agarwal
Department of Macromolecular Chemistry II
University of Bayreuth
95447 Bayreuth, Germany

M. Zarebanadkouki
Department of Soil Biophysics and Environmental Systems
Technical University of Munich
85354 Freising, Germany

N. Meides, P. Strohriegl
Department of Macromolecular Chemistry I
University of Bayreuth
95447 Bayreuth, Germany

C. Schulbert
Geozentrum Nordbayern
Section Palaeontology
Friedrich-Alexander-University Erlangen-Nürnberg (FAU)
Loewenichstraße 28, 91054 Erlangen, Germany

M. G. J. Löder, C. Laforsch
Department of Animal Ecology I
University of Bayreuth
95447 Bayreuth, Germany

A. Carminati
Institute of Terrestrial Ecosystems
ETH Zürich
8092 Zürich, Switzerland

J. Senker
Department of Inorganic Chemistry III
University of Bayreuth
95447 Bayreuth, Germany

Supporting information for this article is available on the WWW under https://doi.org/10.1002/cmtd.202500102

© 2025 The Author(s). Chemistry - Methods published by Chemistry Europe and Wiley-VCH GmbH. This is an open access article under the terms of the Creative Commons Attribution License, which permits use, distribution and reproduction in any medium, provided the original work is properly cited.

© 2025 The Author(s). Chemistry - Methods published by Chemistry Europe and Wiley-VCH GmbH

Chemistry—Methods
Research Article
doi.org/10.1002/cmtd.202500102
Chemistry Europe
European Chemical Societies Publishing

have diameters smaller than 5 μm.[11,14,17,20–24] By contrast, the best-studied size range of environmental microplastics is around 50 μm to 1 mm.[10–12,25,26] Larger particles are not only easier to sample in the environment,[27–29] but they are also a natural part of the weathering and degradation sequence of plastics in the environment, which starts with macroscopic plastic foils, tires, or bottles.[30,31] Moreover, there are strong indications that the weathering of small MPPs obtained by suspension polymerization differs significantly from the artificially fragmented particles.[32] This size mismatch between model systems and environmentally dominant MPPs limits the transferability of existing interfacial data to real-world scenarios. Hence, there is currently a great demand to study the solid/liquid interface of large MPPs. Here, we present, to the best of our knowledge, the first approach to studying the aging of MPPs by streaming potential measurements.

Practically all inorganic and organic surfaces immersed in aqueous electrolyte solution carry charges, either by ionization of functional groups or by ion adsorption.[33] In consequence, the ion distribution at the interface is very different from that of the bulk solution; an effect that is long known in colloid and interface science as the electrical double layer.[33,34] One distinguishes between the so-called Stern-layer of strongly adsorbed, thus practically immobile ions, which extends only 1–2 nm from the interface, and the diffuse layer where the counterion concentration is enhanced and decays exponentially from the interface.[33,34] The measurement of diffuse layer properties is often essential, as they play an important role in the stability of colloidal suspensions in the framework of the so-called DLVO theory.[33,34] For MPPs, their diffuse layer properties determine not only their aggregation and adsorption behavior[14,20,24,35] but also their interaction with natural organic matter.[36–38]

Due to the importance of the diffuse layer properties in colloid science, the development of suitable analytical techniques for their characterization has been pursued for over a century. For small colloidal particles, the diffuse layer is commonly studied by the measurement of the electrophoretic mobility in an external electric field.[10,16,17,39–43] During the resulting particle movement in the viscous electrolyte solution, a significant part of the diffuse layer is sheared off and one measures the particle's velocity, which is directly connected with the so-called zeta-potential ζ, which is directly related to the diffuse layer potential and thus the surface charges.[44] However, in order to utilize electrophoretic mobility, the particle diameters must be well below 30 μm,[40] and even 10 μm.[45] Electrophoretic mobility measurement is widely used in MPP research.[18,19,46–48] For flat substrates, the so-called streaming potential measurements provide access to the zeta-potential. In this case, the flat substrate remains fixed, and the electrolyte solution is streamed over the substrate while the resulting potential due to the displacement of the ions is measured. The measurement of the streaming potential can be considered as "inverse" technique to electrophoretic mobility.[40,44] The basic principle of streaming potential measurements dates back more than 150 years.[49] Commonly, the streaming potential technique today is used with a channel made up of two macroscopic parallel plates.[50–61]

Considering the available techniques, it is no surprise that the diffuse layer of large MPPs liquid/solid interface remains largely a "blind spot" for analytics. By contrast, numerous analytical techniques are available to study the surface chemistry on the molecular level, also for large MPPs, such as Fourier transform infrared (FTIR) spectroscopy,[10,11,62,63] Raman spectroscopy,[10,11,24,64] scanning electron microscopy with energy-dispersive X-ray spectroscopy (SEM-EDX),[10,11,65–67] and nuclear magnetic resonance (NMR) spectroscopy.[63,66,68,69]

However, how can one determine the diffuse layer properties of particles that are too large to migrate in an external electric field, since sedimentation dominates, or that deviate from an ideal spherical shape, for example, of fibers or due to fragmentation processes? The primary answer was given already more than 60 years ago by introducing the so-called plug cells filled with beads or fibers in a defined confinement.[70,71] The streaming potential measured over such a particle or fiber plug allows the determination of its zeta-potential[70,71] also for large particles with irregular shapes.[72] Unfortunately, this technique has largely fallen out of focus in interface and colloid sciences. Notably, the use of streaming potential for characterizing large immobile particles was somehow not generally followed up in colloid science after some initial studies in the 1990s,[73–76] with some exceptions in recent years.[77,78] By contrast, the streaming potential technique has been widely used in soil science.[79–81]

This study demonstrates that streaming potential measurements are well-suited for characterizing large colloidal particles that would otherwise sediment and are therefore not accessible by electrophoretic mobility measurements. The specific application studied here is MPPs that have been prepared by mechanical fragmentation. Their change of surface chemistry during artificial weathering has been monitored by streaming potential measurements.[68,82–86] The knowledge about the solid/liquid interface of such MPPs is crucial for understanding their environmental fate and aging processes. The surface chemistry during environmental weathering is particularly important, as MPPs often originate from the breakdown of millimeter-sized plastic items.[30,31] Here, we demonstrate how streaming potential measurements can be used to determine the surface charge properties of large MPPs, which is impossible with "standard" techniques used for small particles as synthesized by suspension polymerization. For this study, we directly connected to a previous study based primarily on NMR measurements to characterize the surface of artificially weathered, fragmented MPPs.[66] While NMR and SEM-EDX are sensitive to the molecular composition, the here-presented technique probes the Stern and diffuse layer at the solid/liquid interface and thus reveals information about the ionization behavior at the surface. In order to provide a quantitative evaluation, we demonstrated that the streaming potential protocol used here was largely independent of the size fraction by studying artificially fragmented poly(styrene) particles ranging from 200 to 20 μm. The limits in terms of identifying functional groups by their titration behavior were verified by comparing the streaming potentials for commercial spherical particles with different surface functional groups.

© 2025 The Author(s). Chemistry - Methods published by Chemistry Europe and Wiley-VCH GmbH

Chemistry—Methods
Research Article
doi.org/10.1002/cmtd.202500102
Chemistry Europe
European Chemical Societies Publishing

2. Results and Discussion

In this study, we concentrated primarily on artificially fragmented MPPs. These particles were artificially weathered through simulated solar exposure combined with simultaneous mechanical stress by stirring.[66] Our source polystyrene (PS) material, the fragmentation, and the weathering process are fully analogous to the study performed by Meides et al. (2021) with a complementary set of analytical techniques that concentrated primarily on the molecular composition at the MPP surface.[66] The weathering process did lead to a significant reduction in particle size for artificial weathering times of up to 3200 h. Hence, we verified how far the particle size distribution affected the streaming potential by comparing different size fractions before artificial weathering. Moreover, commercial spherical particles bearing various functional groups at the surface have been studied to corroborate the technique's sensitivity to different functional groups.

2.1. Particle Size and Morphology

The following size fractions of fragmented MPPs from PS were studied: 1) 20–75 µm, 2) 75–125 µm, and 3) 125–200 µm. Fractionation was carried out by sieving after fragmentation.[66] The particle size distributions for three different size fractions of the fragmented PS particles were determined by laser diffraction (**Figure 1**a). All fractions showed rather broad size distributions, which were partially overlapping. The evaluated mean diameters from the Gaussian fits are listed in Table S1, Supporting Information. The size fractionation was corroborated by imaging with SEM, as shown in Figure 1b. These exemplary SEM images were acquired at the same magnification, illustrating the difference between the different size fractions. The smallest size fraction appears to have more elongated fragments than the larger fractions. More SEM images of the fragmented particles are shown in Figure S1–S3, Supporting Information. As expected, fragmentation induced considerable roughness on the nanoscale (Figure 1c). Further atomic force microscopy (AFM) images in Figure S4–S6, Supporting Information, highlight the observed variability of the topography on the nm-level. As the fragmented particles did show generally pronounced nonspherical shapes (Figure 1b), we additionally analyzed spherical particles. These were commercially available PS particles synthesized by suspension polymerization. The first batch of bare, spherical PS particles had a nominal diameter of 29.32 µm. Moreover, we studied spherical PS particles with diameters of ≈15 µm carrying three different chemical surface terminations (bare, amino-, and carboxy-modified). The corresponding SEM data can be found in the SI (Figure S7–S10 and Table S2, Supporting Information).

2.2. Particle Beds for Streaming Potential Measurements

Electrophoretic mobility measurements are commonly used to determine the zeta-potential of colloidal particles, relying on their movement under an external electric field. However, this technique becomes impractical for larger particles, such as microplastics, due to gravitational sedimentation and insufficient Brownian motion.[13,17,21,51] Large particles cannot migrate in a controlled manner in an external electric field as they sediment. Moreover, the light scattering for such large particles is not suitable anymore for the standard dynamic light scattering setups with an autocorrelator as commonly used in commercial instruments. For microplastics, particles with diameters larger than 5 µm fall in these regimes. Hence, a different approach to determine the zeta-potential of such particles has to be followed: streaming potential measurements. During those measurements, the large particles rest immobile while the electrolyte is streamed around them. To immobilize the particles during measurement, they are encapsulated in a so-called particle plug that is schematically shown in **Figure 2**a. The two electrodes measure the streaming potential and current, respectively, when the liquid passes through the particle plug. For particle plugs, the works of Lyklema and coworkers[87–89] and of Jacobasch and coworkers on textile fibers have to be mentioned.[90,91] In the following, we refer to the slightly compressed particle ensemble as the "particle bed". Such particle beds remained here largely intact after removal and allowed for further studies, e.g., by X-ray microtomography (µCT). Figure 2b shows a photograph of a typical particle plug removed from the cell after the measurement.

The particles must be homogeneously distributed within the particle bed for accurate streaming potential measurements. Inhomogeneous distributions or the presence of channels without particles could lead to significant deviations in the zeta-potentials.

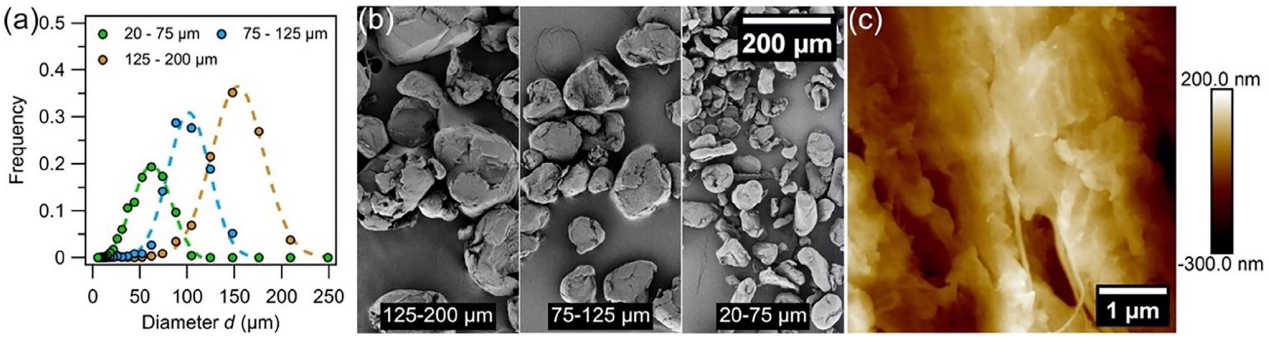

Figure 1. Size- and topography-related overview of fragmented polystyrene MPPs. a) Particle size distributions of different size fractions as determined by laser diffraction. b) Exemplary SEM micrographs of particles for the different size fractions. c) Exemplary (5 × 5) µm² AFM topography of a particle surface from the largest size fraction with 125–200 µm.

© 2025 The Author(s). Chemistry - Methods published by Chemistry Europe and Wiley-VCH GmbH

Chemistry—Methods
Research Article
doi.org/10.1002/cmtd.202500102
Chemistry Europe
European Chemical Societies Publishing

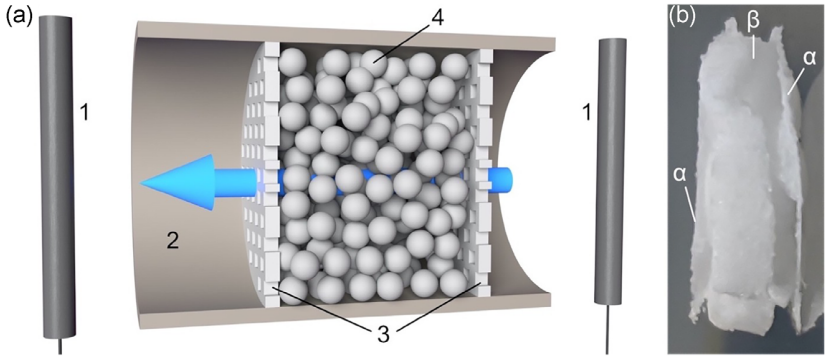

Figure 2. a) Schematic of a particle plug cell for the streaming potential measurements. The streaming potential was measured between the two Ag/AgCl electrodes (1). An outer cylindrical body machined from polyether ether ketone (PEEK) (2) and two PA-6,6 filter mats (3) encapsulate the particle bed (4), which is formed by randomly packed MPPs. The perforated bottom of the cylindrical body and the perforated stamp are not depicted for simplicity. The blue arrow indicates the liquid flow through the particle plug. b) Photograph of a particle plug after streaming potential measurements. (α) Represents the PA-6,6 filter mats around the plug and (β) shows the MPPs forming the particle bed. The particle plug had approximately a diameter of 10 mm and a thickness of 3 mm.

In particular, the formation of so-called seepage could lead to artifacts.[92] While Figure 2b demonstrates that the particle plugs had a dense appearance, their internal structure could not be resolved by optical methods. To evaluate the state of the particle beds after the measurements, we imaged some exemplary ones by µCT.[93,94] **Figure 3** shows the reconstructions of a particle bed from commercial spherical particles with a nominal approximate diameter of $d_{nom} = 30$ µm synthesized by suspension polymerization (Figure 3a) and an analogous reconstruction for fragmented PS particles originating from the 20–75 µm size fraction (Figure 3b). The 3D reconstructions were calculated from data acquired by a dedicated µCT scanner with a 180 kV nanotube without any filter applied. Scanning resolution was 1.5 µm at 50 kV and 200 µA current.

The µCT reconstruction of the particle bed with the spherical PS particles demonstrated not only their highly spherical shape and uniform size distributions but also corroborated that no deformations of MPPs due to compression in the particle plug (Figure S7, Supporting Information) took place. There were no indications for the formation of large seepages, and quantitative data evaluation yielded a solid volume fraction of 56.3% for the commercial spherical PS particles. This value was below the value for the densest possible hexagonal packing of equally sized spheres of 74% but indicated nevertheless dense particle packing. Further reconstructions for these particle beds by µCT are given in the SI (Figure S11, Supporting Information). By contrast, the reconstruction of the particle beds with fragmented MPPs of the size fraction 20–75 µm illustrated their irregular shape and the much broader size distribution (Figure 1b and S1, Supporting Infirmation). However, a dense packing was observed for these irregular particles. Moreover, additional µCT reconstructions are given in the SI (Figure S12, Supporting Information).

2.3. Electrokinetic Characterization of the Spherical Particles

The streaming potential originates from the dislocation of charges in the diffuse layer at the solid/electrolyte interfaces of the particles within the particle plug.[40,95] The extension of the diffuse layer is given by its exponential decay constant, the Debye length κ^{-1}.[33,44,95] The inverse Debye length κ is given by

$$\kappa = \sqrt{\frac{2e^2 N_A I}{\varepsilon_r \varepsilon_0 kT}} \tag{1}$$

where N_A is Avogadro's number, e the elementary charge, T the temperature, k the Boltzmann constant, I the ionic strength,

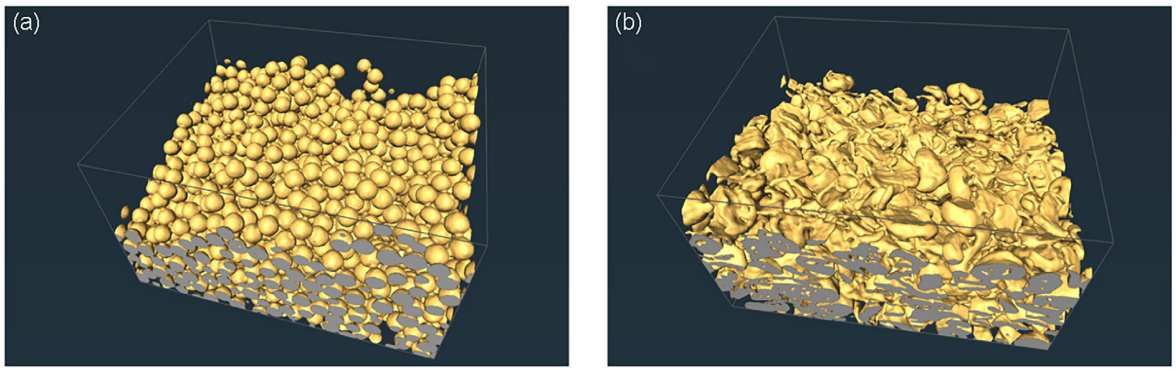

Figure 3. Reconstructed particle beds by X-ray µ-tomography. a) Reconstruction for commercial polystyrene particles with a nominal diameter of about 30 µm, which have been synthesized by suspension polymerization. b) Reconstruction for fragmented polystyrene particles with diameters in the range of 20–75 µm.

© 2025 The Author(s). Chemistry - Methods published by Chemistry Europe and Wiley-VCH GmbH

Chemistry—Methods | Research Article doi.org/10.1002/cmtd.202500102 | Chemistry Europe European Chemical Societies Publishing

ε_r the permittivity of the electrolyte, and ε_0 is the permittivity of free space.[33,95]

The flow due to the externally applied hydrostatic pressure difference Δp displaces the counterions in the diffuse layer, which results in an electric current, the so-called streaming current I_{str}. Under open-circuit conditions, the resulting charge transport leads to an accumulation of opposite charges at the two ends of the capillary, which corresponds to a potential difference ΔU_{str}, the so-called streaming potential.[44] For sufficiently large capillary radii h and high ionic strengths I with $\kappa h >> 10$, the zeta-potential ζ is given by:[40,44,95]

$$\zeta = \frac{\eta K_L}{\varepsilon_r \varepsilon_0} \frac{\Delta U_{str}}{\Delta p} \tag{2}$$

where η is the dynamic viscosity of the electrolyte and K_L is its bulk conductivity. Equation (2) is also valid for porous plugs as long as the double layer relaxation effects and surface conduction can be neglected,[40] which is commonly the case for $\kappa r_{eff} >> 100$ with r_{eff} as the effective pore radius.[75] The effective pore radius r_{eff} can be calculated by[76]

$$r_{eff} = \left(\frac{\phi}{(1-\phi)}\right) \frac{d_{sv}}{4.5} \tag{3}$$

where ϕ is the porosity of the plug and d_{sv} is the surface volume mean diameter of the particles. ϕ can be determined from µCT evaluations. In the case of Figure 3a, one obtains for $I = 10$ mM and a particle diameter $d = 29.32$ µm for the spherical particles packed with $\phi = 1–0.563 = 0.437$ (evaluation of Fig. S11, Supporting Information) the estimation $\kappa r_{eff} \cong 1661$. Additionally, the zeta-potential ζ becomes independent from the details of the plug geometry and the particle shape for $\kappa r >> 100$.[75,96] We assume that this condition (i.e., $\kappa r >> 100$) has been fulfilled for all particle beds studied here by streaming potential measurements (Figure 3). It should be noticed that for hydrophobic particles an additional factor, the so-called hydrodynamic slip effect in pressure driven flows, can contribute.[97,98] However, this effect has not been considered here.

2.4. Influence of Functional Groups on Streaming Potential of Small Spherical Particles

In the following, we verified that streaming potential measurements with particle beds are indeed sensitive to the surface chemistry of the particles. This initial evaluation of the particle beds was based on spherical PS-particles of the same diameter, namely ≈15 µm, which have been synthesized by suspension polymerization. While the particles all have the same diameter, they carry different groups at their surface, namely bare PS and particles modified with carboxylic groups (PS-COOH), and amino groups (PS-NH_2), respectively. Thereby, the zeta-potentials ζ (Equation (2)) as a function of pH could be acquired for functional groups whose ionization behavior should differ. The particle diameters have been verified by SEM-imaging (Figure S7–S10 and Table S2, Supporting Information).

Figure 4 compares the zeta-potentials ζ as a function of pH for the small spherical PS-particles with different surface functional groups. In the acidic regime, the bare and COOH-modified PS particles started both at streaming potentials near 0 mV. This corresponds to very low surface charge densities and, thus, ζ according to the modified Grahame equation, where the charge density at the plane of shear σ_{ek} is set in relation to ζ for the planar limiting case.[99]

$$\sigma_{ek} = \frac{2\varepsilon_r \varepsilon_0 kT\kappa}{e} \sinh\left(\frac{e\zeta}{2kT}\right) \tag{4}$$

Upon increase of pH, the bare PS particles and the ones with COOH-groups develop more negative zeta-potentials in the basic regime. For the carboxylic groups at the particle surface, such a behavior was expected due to the deprotonation of the functional groups with $pK_a = 4.9$.[100] For the bare PS particles, which also develop an increasingly negative surface charge density, two other mechanisms were responsible: ion adsorption and

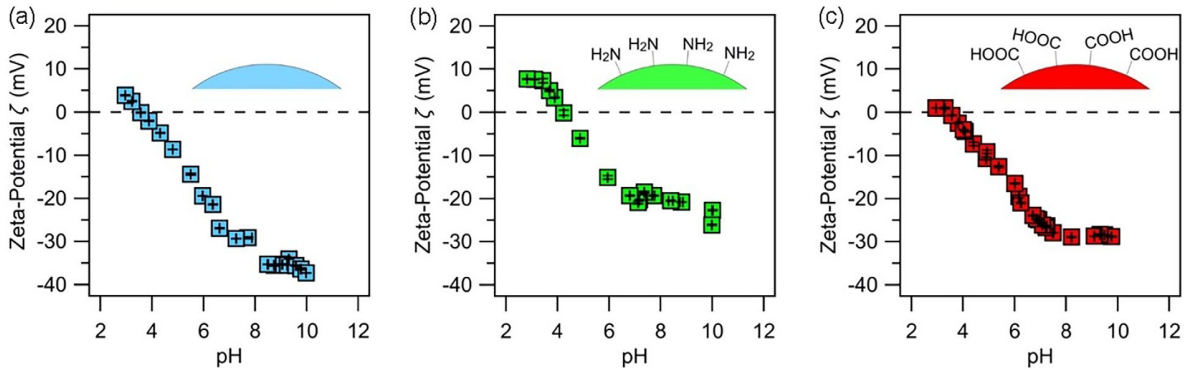

Figure 4. Zeta-potential ζ as a function of the pH for commercial a) PS, b) PS-NH_2, and c) PS-COOH particles synthesized by suspension polymerization as model systems for MPPs with different functional groups. The data were acquired by streaming potential measurements for particles with a diameter of ≈15 µm. The total ionic strength was 10 mM for all measurements.

© 2025 The Author(s). Chemistry - Methods published by Chemistry Europe and Wiley-VCH GmbH

Chemistry—Methods
Research Article
doi.org/10.1002/cmtd.202500102
Chemistry Europe
European Chemical Societies Publishing

ionization of the remaining initiator molecules. These mechanisms will be discussed in more detail below. By contrast, the amino-modified particles are positively charged under acidic conditions, as it would be expected from the protonation of the NH_2-groups, which are assumed to have a pK_a in the range of 8–11, depending on the electrical environment of the amino groups.[101,102] However, with increasing pH, negative surface charges also accumulate by the same mechanisms as for the bare PS particles. Thus, PS-NH_2 also showed negative zeta-potentials in the basic regime, but less than those for PS-COOH or bare PS.

It is important to highlight that negative charges accumulate on bare PS particles without any ionizable groups. The adsorption of hydroxyl-ions (OH^-) to hydrophobic surfaces is well known in the literature.[58,61,103,104] It has been observed for flat surfaces as well as for colloidal particles.[58,61,104] Furthermore, specific adsorption of predominantly anions to the apolar regions on PS particles is another factor leading to an overall more negative surface charge.[16,105] The presence of ionizable groups, here -COOH and -NH_2, reduces ion adsorption effects.[91,106] Additionally, the residues from the organo-sulfate initiators used in the polymerization can be often traced on the particles,[18,104,107–110] which are another source of negative charges and shift the isoelectric point (IEP) in the more acidic regime.[57,60,61,111,112]

PS-particles are often sterically stabilized by a layer of polyvinyl alcohol (PVA).[113] A soft polymeric layer shifts the shear plane further away from the interface, leading to zeta-potentials of smaller magnitude.[55,95,114,115] PVA around the particles also influences the specific ion adsorption of predominantly anions to the interface. PVA is more hydrophilic than PS, which leads to reduced specific anion adsorption in the basic regime.[91,106] AFM micrographs of the PVA-coated surface of nonmodified particles with diameters of 15 μm are shown in Figure S13, Supporting Information. The topographies reveal thick layers of PVA, creating a crater-like surface. In turn, a strong shift of the shear plane away from the interface must be assumed, leading to smaller zeta-potentials in magnitude. Another factor to consider is the PA-6,6 filter mats, which hold all the presented particle plugs in place. Hence, these filter mats (Figure S14b, Supporting Information), which were present in all measurements, have been characterized in a set of separate measurements. Figure S14a, Supporting Information shows the streaming potential measurements of a set of filter mats without particles. These measurements do not serve strictly as a baseline as a sufficient number of these mats had to be assembled. The streaming potential versus pH differs from those acquired for the PS particles and MPPs. Figure S14b, Supporting Information presents an exemplary SEM image of a cleaned filter mat.

2.5. Electrokinetic Characterization of Microplastics after Fragmentation

The fragmentation process produced MPPs with broad size distribution (Figure 1a) and irregular shapes (Figure 1b).[66,116] Due to their size, such particles cannot migrate in an electric field without sedimentation. Streaming potential measurements using packed particle plugs were the only feasible method to determine their diffuse layer properties, i.e., the zeta-potential ζ. As all size fractions studied here show lateral dimensions in all axes with $r > 7.5$ μm, hence, the condition $\kappa r >> 100$ is fulfilled at a total ionic strength $I = 10$ mM with $\kappa^{-1} \simeq 3$ nm, which was the ionic strength I at which the streaming potential measurements were carried out. To verify that the resulting streaming potential was independent of the particle size and geometry under these conditions, we studied the three different size fractions of the artificially fragmented PS. The particles were prepared from one fragmentation experiment and selected by size through sieving, so their surface chemistry was comparable. For further comparison, we also performed experiments with commercial spherical PS particles with diameters of ≈30 μm (Figure S7d–f, S10b, and Table S2, Supporting Information), which were produced by suspension polymerization. Their diameter falls nicely within the size range of the smallest fragment fraction, but the particles provided a highly defined, non-varying geometry, and a smoother surface. μCT images of the corresponding particle beds are shown for these particles in Figure 3a and for the fragmented particles in Figure 3b.

Figure 5a shows the zeta-potential as a function of pH for the spherical model PS particles (30 μm in diameter). For low pH, i.e., pH < 4, the zeta-potential was slightly positive with an IEP between pH 3 and 4. Upon increasing the pH, the zeta-potential becomes more negative without reaching a plateau value in the basic regime (pH ≲ 10) compared to the smaller particles (Figure 4a). The discrepancy in zeta-potentials between Figure 4a and 5a is likely attributed to the different amounts of PVA-coating of the particles. The particles with nominal diameters $d_{nom} = 15$ μm appear to be heavily coated with PVA, while the particles with $d_{nom} = 30$ μm are less coated (Fig. S15, Supporting Information). A thicker PVA coating shifts the shear plane further away from the PS interface compared to a thinner coating, thus leading to smaller zeta-potentials in comparison.

Figure 5b shows the zeta-potential as a function of the pH for the three size fractions of the fragmented MPPs. The overall shape of the curves was practically independent of the size fraction. This experimental finding also corroborates the theoretical postulate that for particle dimensions with $\kappa r >> 100$, the zeta-potential even becomes independent from the details of the plug geometry and the particle shape.[75,96] Moreover, we find a surprisingly good correspondence in the surface titration behavior between highly defined spherical bare PS particles with low amounts of PVA at the interface and the fragmented particles obtained from solid PS. The IEP was slightly more acidic, but the increase in the zeta-potential's magnitude with increasing pH followed the same trend observed for large colloidal particles. However, in the case of the fragmented particles, the zeta-potentials level off after pH 7–8 into a pronounced plateau.

2.6. Charging Mechanisms of the Polystyrene/Water Interface

The zeta-potential versus pH curves for spherical 30 μm sized PS particles and bare as well as aged MPP are surprising as polystyrene has in principle no ionizable groups. **Figure 6** illustrates schematically several different charging processes that can lead

© 2025 The Author(s). Chemistry - Methods published by Chemistry Europe and Wiley-VCH GmbH

Chemistry—Methods
Research Article
doi.org/10.1002/cmtd.202500102
Chemistry Europe
European Chemical Societies Publishing

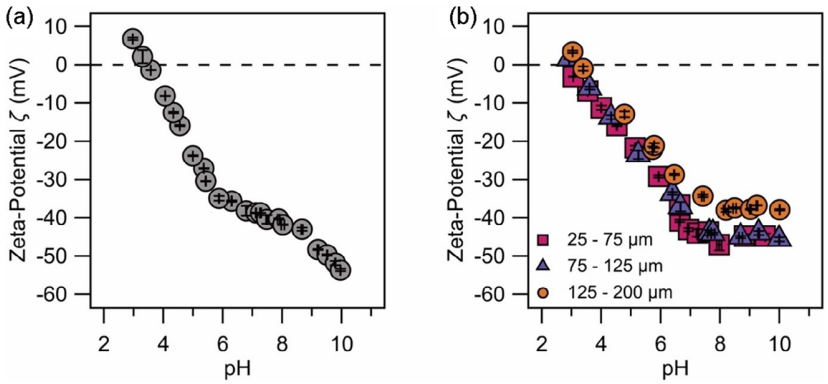

Figure 5. Zeta-potential as a function of the pH at a constant ionic strength of 10 mM in KCl for a) commercial polystyrene particles with $d \approx 30$ µm and b) fragmented microparticles of three different size fractions as determined by streaming potential measurements with a particle plug cell.

to the presence of charges at a PS-surface. The dominance of one mechanism or the presence of several mechanisms depends critically on several factors, particularly the origin of these PS particles. One process common to all types of PS solids is the presence of initiator molecules, which were necessary for polymerization and have not been fully consumed.[107] A schematic representation is shown in Figure 6a. For particles synthesized by emulsion polymerization, also surfactants, which were originally present in the solution to stabilize the emulsion droplets, can remain at the interface. Their hydrophilic groups are also charged and will accumulate at the particle's interface (schematic representation in Figure 6a). A different type of molecules are stabilizers, like polyvinyl alcohol, which were added to suspension polymerizations to increase the shelf life (Figure 6b). While the PVA-layer itself cannot directly accumulate charges, the shift of the shear plane and structural changes lead to the shift of the zeta-potential.[117] The stabilization of the suspension takes primarily place by steric interactions.[33] Nevertheless, negative charges can accumulate at PVA under alkaline conditions due to ion adsorption.

Surfaces from PS are generally hydrophobic.[118] For such surfaces, ion adsorption (Figure 6c) plays an important role, in particular by hydronium (H_3O^+) and hydroxyl ions (OH^-).[58,60,61,103,119] The corresponding charging processes on hydrophobic surfaces due to ion adsorption have been followed by streaming potential measurements as well as by direct force measurements by AFM in the past.[58,60,61,103,120] At low pH, i.e., under acidic conditions, the adsorption of hydronium ions is the dominating process.[52,60,61,103,119,120] However, the adsorption of hydroxyl ions is preferential at a hydrophobic surface already for pH $>$ 4 to 7.[52,60,61,120] Hence, the IEP for nonmodified PS particles often lies around pH 4.[40] By contrast, the specific adsorption of hydrated ions, such as K^+ and Cl^-, does practically not contribute to hydrophobic polymer interfaces[60] or molecularly defined hydrophobic self-assembled monolayers (SAMs).[120]

Additionally, the presence of organosulfates due to the remaining traces of the polymerization initiator can have a significant contribution to an overall negative surface charge due to the deprotonation of sulfate groups.[104,108–110] The mechanism is indicated in Figure 6a. Such sulfate groups are more present on the spherical particles synthesized by suspension polymerization than on the fragmented pristine PS. The thinner PVA-coating of the 30 µm sized particles compared to 15 µm sized particles, as deducted from the AFM imaging (Figure S15 and S13, Supporting Information, respectively), would be compatible with the zeta-potentials resembling that of the fragmented PS rather than the one observed for bare 15 µm sized particles. The observed differences can be attributed to the remaining initiator molecules on the surfaces of the 30 µm sized PS particles. By contrast for the MPP obtained by fragmentation, the presence of peroxides from initiator leftovers[121] and due to photo-oxidation/reduction can attribute to the surface charge (Figure 6d).[122] However, the peroxides generally contribute at much higher pH than the processes illustrated in Figure 6a-c.

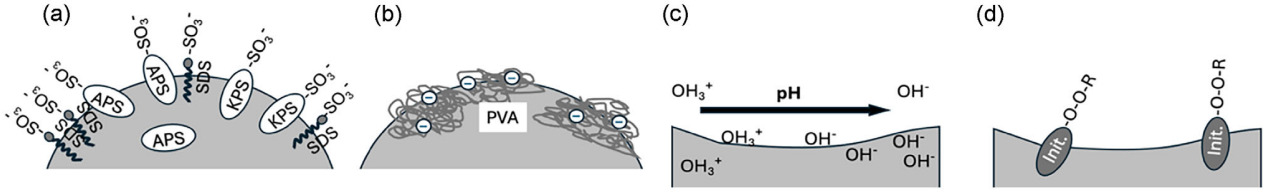

Figure 6. Schematic representation of the different charging processes for polystyrene surfaces. a) Charges due to the presence of remaining initiators such as (APS) and (KPS) as well as surfactants from emulsion polymerization. b) Polyvinyl alcohol as a steric stabilizer for particles synthesized by suspension polymerization. Under alkaline conditions, negative charges can be present on the PVA. c) Ion adsorption, especially of hydroxyl ions. This effect is more pronounced for a flat surface without any ionizable groups. d) For the bulk material PS, as used for the fragmentation procedure, some initiators bearing peroxides remain unreacted.

© 2025 The Author(s). Chemistry - Methods published by Chemistry Europe and Wiley-VCH GmbH

Chemistry—Methods
Research Article
doi.org/10.1002/cmtd.202500102
Chemistry Europe
European Chemical Societies Publishing

2.7. Artificial Weathering of the Microplastic Particles

Artificial weathering of fragmented PS (125–200 μm size fraction) was carried out by stirring and intense UV exposure of the aqueous suspension. Here, we used samples from the identical batches previously studied by Meides et al., which have been examined by SEM, laser scattering, and NMR spectroscopy.[66] We added streaming potential measurements to the original analytical selection to provide additional information on the level of the diffuse layer properties.

Figure 7a shows the size distribution of the fragmented PS for exposure times of 0, 600, 1200, and 3200 h to artificial weathering as reported previously.[66] Mean diameters after weathering exposure are shown in Table S3, Supporting Information. In this study, the identical batches studied by Meides et al. (open data points) have been used with the exception of the one for 0 h (closed data points). Nevertheless, the original size distribution for 0 h from Meides et al. has been added for comparison. The difference in the size distribution for these two batches at 0 h weathering time was found to be small. The artificial weathering process leads to a reduction in the particle size with time. For the longest exposure time, an average size reduction to 85% of the original was observed (Figure 7a). In consequence, the overall size distribution is comparable to the smallest size fraction of pristine, fragmented PS-particles of 20–75 μm (Figure 1a). This comparison will become important at a later point in order to exclude size effects on the here-determined streaming potential for weathered particles.

Figure 7b shows the zeta-potential ζ as a function of pH for the particle plugs prepared from the MPPs at different weathering times. For 0 h, the ζ versus pH data are identical to the ones shown in Figure 5b. For up to 1200 h of artificial weathering, ζ (pH) remained practically identical to the curve acquired for 0 h weathering, including the position of the IEP. However, for 3200 h of artificial weathering, a general shift to more negative zeta-potentials took place. The final size distribution of the MPPs at this weathering time was very similar to the size fraction 20–75 μm (Figure 1a), which did show no change of ζ (pH) in comparison to the larger size fractions (Figure 5b). Hence, we assume that the size of the MPPs after 3200 h had no or only a very minor effect on ζ (pH). However, with increasing weathering time, the surface of the MPPs became significantly rougher. The former process can be directly followed by microscopy, such as SEM and AFM. Some exemplary results for SEM are shown in **Figure 8** and in Figure S16–S19, Supporting Information.

On a more local scale, the effect of artificial weathering on the particle surfaces becomes even more evident. **Figure 9** shows the particle surface topographies for the same weathering times. However, this time the surface topography has been determined by TappingMode AFM in air. The images shown are based on the phase data, which have been acquired simultaneously with topographic data. The former provided a good image of the surface ultrastructure as its first derivative entered the phase image contrast and allowed access to the chemical homogeneity based on differences in adhesion or elasticity. The phase images show a chemically homogeneous surface but with an increasing roughness on the nm-level with weathering time. The corresponding topography images can be found in Figure S20, Supporting Information and roughness data in Table S4, Supporting Information.

Hence, we attributed the observed shift primarily to changes in the surface chemistry of the MPPs during weathering. Which new groups at the surface of the MPPs can be responsible for the increasingly negative charge on the MPPs as the weathering progressed? Meides and coworkers investigated the same batches of weathered particles via SEM-EDX and NMR spectroscopy.[66] Their experiments show increased oxygen species, especially peroxides, carboxylic groups, and ketones with artificial weathering time. For interfacial carboxylic groups, one commonly assumes $pK_a = 4.9$,[100] while peroxides and ketones typically have a pK_a of > 7 and $\simeq 19$, respectively.[123,124] Due to their much higher pK_a-values, these groups should contribute significantly less to the overall negative charge. However, the carboxylic groups have a pK that would be compatible with the observed pH behavior and explain the increasing negatively charged surfaces in the neutral and basic pH-regime with aging time. An increase of carboxylic groups with weathering times was also observed by NMR spectroscopy. Hence, a technique that is sensitive to the

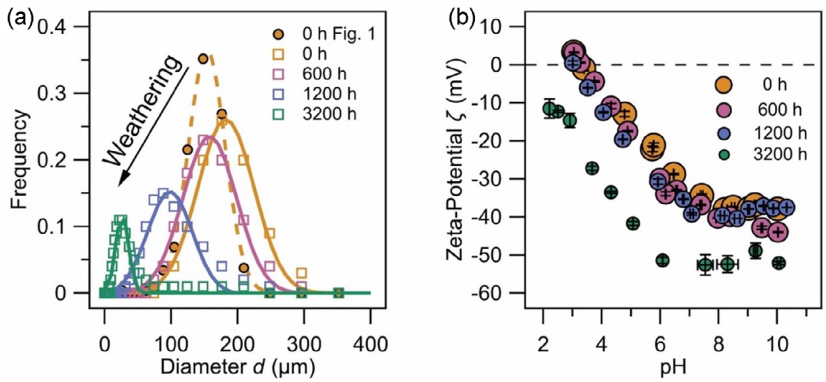

Figure 7. a) Size distribution of weathered microparticles (i.e., solid lines and open data points) as determined by laser diffraction from Meides et al.[66] and the non-weathered (i.e., 0 h) particles as shown in Figure 1 (dashed line, filled data points). b) Zeta-potential as a function of the pH at a constant ionic strength of 10 mM in KCl for weathered fragmented MPPs.

© 2025 The Author(s). Chemistry - Methods published by Chemistry Europe and Wiley-VCH GmbH

Chemistry—Methods
Research Article
doi.org/10.1002/cmtd.202500102
Chemistry Europe
European Chemical Societies Publishing

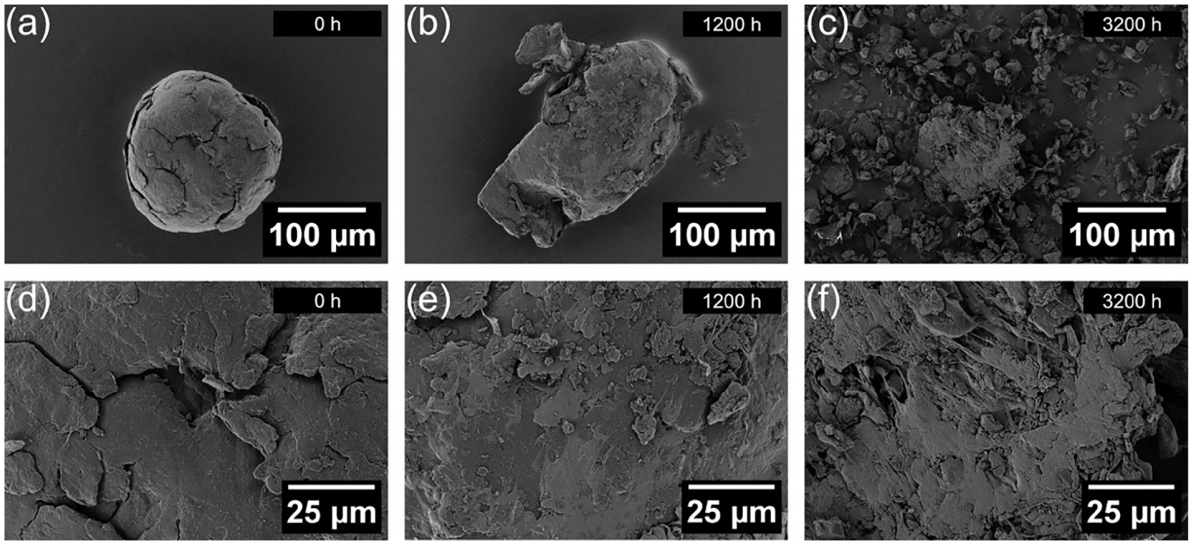

Figure 8. a,d) SEM images of fragmented, i.e., 0 h weathering and b,c,e,f) subsequently artificially weathered MPPs. The top row shows some exemplary particles for the different weathering times. The bottom row shows some ultrastructure on the particles shown in the top row.

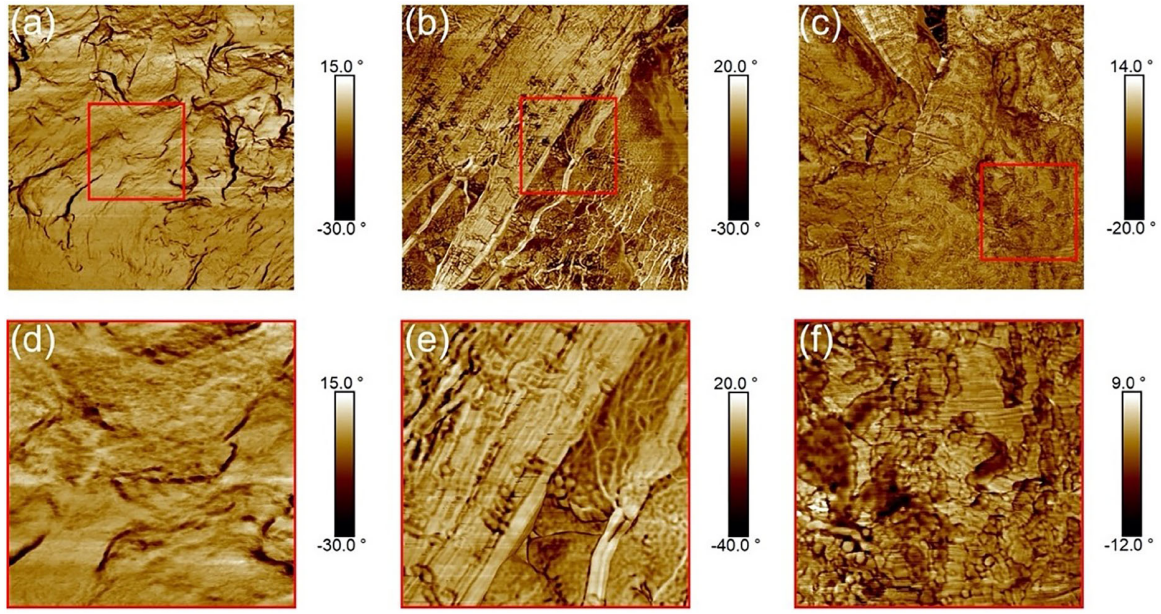

Figure 9. a,d) AFM images of fragmented, i.e., 0 h weathering and b,c,e,f) subsequently artificially weathered MPPs. The top row shows images with a scan area of (3 × 3) µm^2. The bottom row shows some ultrastructure on the particles as indicated by the red squares with scan areas of (1 × 1) µm^2. The AFM images have been acquired in TappingMode in air and only the phase image data are shown.

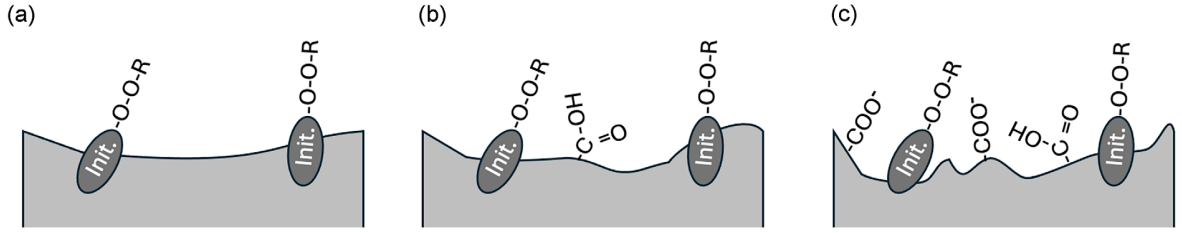

Figure 10. Schematic representation of the changes in the surface chemistry during the weathering of the polystyrene surfaces. a) Initial state of the surface. b) The artificial weathering did lead with increasing time to more charged groups, especially due to the formation of carboxyl groups. Moreover, not only was the size of the particles reduced, but their roughness was also increased. c) With increasing weathering, the number of carboxylic groups and the roughness increased.

© 2025 The Author(s). Chemistry - Methods published by Chemistry Europe and Wiley-VCH GmbH

Chemistry—Methods
Research Article
doi.org/10.1002/cmtd.202500102
Chemistry Europe
European Chemical Societies Publishing

molecular composition of the MPP's surface chemistry and a technique that probes the diffuse layer resulting from charges at the MPPs provide matching results.

Figure 10 summarizes the proposed changes at the MPP surface with aging. The density of the leftover initiator groups most likely did not change significantly, as these are present in the bulk for solid PS. Thus, degradation of the particles should lead to a more or less constant background of negative charges from the peroxides from the initiator groups. With increasing weathering time, the surface of the MPPs not only became rougher, but also the number of carboxylic groups increased, which is perfectly in line with the results previously reported by different techniques.[66]

3. Conclusions

Streaming potential measurements with particle plugs provide an analytical approach to determine the diffuse layer properties of large particles with irregular shapes. Such particles are not accessible by electrophoretic mobility measurements, which represent the standard technique to characterize colloidal particles with a diameter of less than 5 μm, since such particles rapidly sediment or float, making electrophoretic methods ineffective. Moreover, dynamic light scattering, which is often used for determining the electrophoretic mobility, would not provide reasonable results for large particle diameters. Streaming potential measurements are most often carried out for flat, cm-sized samples but can also be used for large particles or fibers. However, this analytical possibility has been largely ignored in the past decade in colloid and interface science. As we demonstrated here, particle plugs provide an important analytical method for a critical size regime in microplastic research. While many initial studies in this field have used small particles (<5 μm) synthesized by emulsion polymerization, these particles are not the dominant component of microplastics in the environment.[125] The here-studied weathering of larger plastic segments represents a much more relevant insight into the processes that determine the fate of microplastics in the natural environment and provides complementary information to techniques such as NMR spectroscopy for the molecular composition or microscopy for the particle dimensions and morphology.

Here, we demonstrated that the size of the MPPs does not play a role for the size range of 20–200 μm, which is in line with studies on smaller particles in particle plugs[73–76] and theoretical predictions.[75,96] Moreover, we showed that PS particles with defined functional groups (carboxylic, amino, and bare) but the same size do indeed lead to different zeta-potential versus pH curves as expected for these groups. However, for plastics, the presence of ion adsorption and the rest of the initiator and surfactant molecules lead to very similar charging curves in the neutral and acidic regimes. Due to the presence of steric stabilizers and more pronounced ion adsorption to bare PS particles obtained by suspension polymerization, these can accumulate more negative charges than those bearing carboxylic groups. This counterintuitive finding is also in line with studies on small colloidal particles by electrophoretic mobility measurements. It should be kept in mind that ion adsorption, especially of hydroxyl-ions, and remnants of initiators are omnipresent for plastic surfaces. Hence, the filter membranes that are used to constrain the particles in the filter plug also show a similar pH dependence as the plastic material under examination. Presently, we have no indication that the sensitivity of the streaming potential measurements would be affected thereby. Future studies should also address how far the reduction of hydrophobic slip might influence the streaming potentials of MPPs during aging.

Our findings for the aging of microplastics due to artificial weathering match the results from complementary techniques, such as NMR spectroscopy and SEM, for the same batches.[66] Streaming potential measurements allow direct determination of the zeta-potential, i.e., the most relevant property of the solid/liquid interface, of environmentally relevant microplastic surfaces. The zeta-potential has a large influence on the adsorption of natural organic matter as well as the adhesion of MPPs to sediments. Hence, we believe that this technique has a large application field in environmentally oriented research with artificial contaminants. Large MPPs are sampled routinely in environmental studies. Hence, it would be important to have analytical techniques that allow for the determination of their surface properties. In principle, the here-presented approach would also be suitable to study MPP samples from the environment. However, the presence of an ecocorona made up from natural organic matter and the requirement of having several mg of sample at disposition will severely restrict the application.

4. Experimental Section

Materials

Millipore-grade quality water (MilliQ IQ 7000, Merck KGaA, Darmstadt, Germany) was used for all cleaning processes and solution preparations. The total organic content of the water was always below 5 ppb with a specific resistivity of 18.2 MΩ cm. 1 M analytic grade hydrochloric acid and potassium hydroxide Titrisol ampoules (Merck KGaA, Darmstadt, Germany) and potassium chloride (BioUltra, Merck KGaA, Darmstadt, Germany) were used to prepare all aqueous electrolyte solutions. The pH value of these solutions ranged between pH 2 and pH 12 and was adjusted with KCl to an overall solution ionic strength of 10 mM.

Samples and Sample Preparation: Particles

Commercial spherical polystyrene particles with different surface modifications were obtained from microParticles GmbH (Berlin, Germany). These particles had either no surface functionalization (bare PS), amino groups (PS-NH_2), or carboxy groups (PS-COOH). The bare PS particles had nominal diameters of 15.10 μm, and 29.32 μm (Figure S7, Supporting Information). The modified polystyrene beads had nominal diameters of 15.47 μm (Figure S8 and S9, Supporting Information, respectively). The diameters were corroborated from the SEM images, and the results are summarized in Figure S10 and Table S2, Supporting Information. All commercial particles were received as aqueous suspensions.

Fragmented polystyrene particles were produced from commercially available Styrolution PS 158 N polystyrene pellets (INEOS Styrolution

© 2025 The Author(s). Chemistry - Methods published by Chemistry Europe and Wiley-VCH GmbH

Chemistry—Methods | Research Article
doi.org/10.1002/cmtd.202500102
Chemistry Europe
European Chemical Societies Publishing

Group, Frankfurt am Main, Germany) by a milling process. The pellets were precooled with liquid nitrogen, milled using an Ultra Centrifugal Mill ZM 200 (Retsch GmbH, Haan, Germany) with a 12-teeth rotor at 18,000 RPM, and subsequently sieved with an Alpine Air Jet Sieve E200 LS (Hosokawa Alpine AG, Augsburg, Germany).[66] The process was conducted in air and yielded particles with size ranges of 20–75, 75–125, and 125–200 μm, respectively. SEM images of these fractions are shown in Figure S1–S3, Supporting Information.

Samples and Sample Preparation: Artificial Particle Weathering

The 125–200 μm size fraction of the fragmented polystyrene particles was artificially weathered in water. Environmental weathering was simulated via sunlight irradiation and mechanical stress by stirring under ambient conditions for various exposure times. A detailed description of the preparation process of the fractionation as well as the weathering has been described previously.[66] Briefly, the weathering experiments were conducted in a Q-SUN XE-3 industrial test chamber (Q-LAB Corporation, Westlake, OH, USA). The irradiation source consisted of three xenon arc lamps, emitting radiation similar to natural sunlight, which was achieved using a Daylight-Q filter system (Q-LAB Corporation, Westlake, OH, USA), filtering out radiation with wavelengths below 295 nm. The irradiance was set to 60 W m^{-2} at wavelengths between 300 and 400 nm, corresponding to a total irradiance of 594 W m^{-2}.[66] The relative humidity was maintained at 50% and the chamber temperature was held at 38 °C. During irradiation, 20 g of the PS particle powder was constantly stirred in a quartz glass beaker containing 600 mL of deionized water. The water temperature was 55 °C, and the stirring was performed using a poly(tetrafluoroethylene) (PTFE)-coated magnetic stirrer at 150 rpm.[66] Particle samples were analyzed after 600, 1200, and 3200 h without further purification.

Methods: Scanning Electron Microscopy

In order to image the used PS MPP particles by SEM, commercial particle suspensions were spin-coated onto a clean silicon wafer piece at 2000 rpm for 60 s. The wafer piece was oxidatively cleaned as shown previously.[126] Afterward, the substrate was dried at 40 °C for 2 h in an oven. Fragmented particles were immobilized on conductive carbon adhesive pads (Plano GmbH, Wetzlar, Germany) and the pad was hardened for at least 12 h at ambient conditions. Before SEM imaging, a 1 to 2 nm thin layer of platinum was sputtered onto the sample using a sputter coater (Cressington 208HR, Cressington Scientific Instruments Ltd., Watford, UK). Imaging of the particles was performed using the secondary electron detector of a Zeiss LEO 1530 (Carl Zeiss Microscopy GmbH, Jena, Germany). The particle diameters of the spherical PS particles were quantitatively evaluated with the ImageJ software (Version 1.54f) and the built-in line tool.[127]

Methods: Laser Diffraction

In contrast, the particle diameters and size distributions of the fragmented and weathered PS particles were determined via laser diffraction with a Microtrac FlowSync particle size analyzer (Microtrac Retsch GmbH, Haan, Germany). This instrument uses laser diffraction (three lasers and two detectors) coupled with dynamic image analysis. Measurements were run as wet analysis using deionized water as the mobile phase. 2 to 5 mg of particles were added to 2 mL of 5 wt% $Na_4P_2O_7$ (Sigma Aldrich, St. Louis, USA) and a few droplets of Tween 20 detergent (Sigma Aldrich, St. Louis, USA) to avoid aggregation. This mixture was poured into the water-filled measuring cell and diluted with 200 mL of water. A 180 s ultrasound treatment (40 kHz) was further performed to ensure complete suspension of the particles. Mean values are generated from three measurements.

Methods: Atomic Force Microscopy

Samples for AFM measurements were prepared analog to SEM samples, except that no sputtering was performed. The topography of the fragmented PS particles was imaged by AFM using a Dimension Icon (Bruker Corp., Billerica, MA, USA) with a Nanoscope V controller in TappingMode under ambient conditions. OMCL AC160TS cantilevers (Olympus Corp., Tokyo, Japan) with a nominal resonance frequency of 300 kHz, a nominal tip radius of <10 nm, and a nominal spring constant of 26 N m^{-1} were used. AFM images were analyzed using the NanoScope Analysis software (Version 1.8, Bruker Corp., Billerica, MA, USA) with first-order plane fits applied.

Methods: Streaming Potential Measurements

Streaming potential experiments of the PS particles were conducted with a SurPASS 3 streaming potential analyzer and a cylindrical cell (Anton Paar GmbH, Graz, Austria). Streaming potential measurements involved the preparation of well-defined particle plugs of the polystyrene particles. Plugs were prepared with either spherical commercial, fragmented, or weathered particles. To immobilize the particle beds for streaming potential measurements, polyamide-6,6 (PA-6,6) filter mats with nominal pore diameters of 10 μm and an open surface area of 2% (Pieper Filter GmbH, Bad Zwischenahn, Germany) were used. Before usage, the filters were sonicated with a volumetric 3:1 solution of analysis grade isopropyl alcohol (VWR Chemical, Darmstadt, Germany) and water for 20 min at 40 °C. Afterward, the filters were sonicated in water for 20 min at 40 °C and dried under a nitrogen gas stream. An SEM image of the used PA-6,6 filter mats and a streaming potential reference experiment of a stack of six filters are given in the Supporting Information (Figure S14, Supporting Information).

Before the streaming potential measurements, the particle powder or suspension was filled in the cylindrical cell on top of a filter. The used particle mass was adjusted to a normalized surface area of $\approx$43 cm^2, given the assumption of spherical particles. Thus, the surface area of the particles was always comparable and it was ensured that the area was larger than the surface area of the PA-6,6 filters. The particle bed was first covered with a second filter mat, and the cell was sealed in the second step. The particle plugs were rinsed four times with 100 mL of the corresponding pH-adjusted solution before each measurement set. The electric conductivity of the solution and the temperature were recorded before each streaming potential experiment. The streaming potential measurements followed a pH titration protocol progressing from neutral to alkaline conditions and subsequently from neutral to acidic conditions. All streaming potential experiments were conducted at a constant total ionic strength of 10 mM in KCl across a pH range from 2 to 12. The experiments measured the streaming potential as a function of pressure, with the zeta-potential values calculated using the Helmholtz–Smoluchowski equation. The pressure range for the rinsing and streaming potential measurements was 600 to 400 mbar via a nitrogen gas stream. Four measurements were averaged per experiment after a stable zeta-potential was achieved. All streaming potential measurements were performed at a temperature of (295 $\pm$ 2) K.

Methods: X-Ray Microtomography

Samples were fixated on the top of a 2 mm thin glass rod and were immobilized using dental wax in order to be mounted in the beam

© 2025 The Author(s). Chemistry - Methods published by Chemistry Europe and Wiley-VCH GmbH

Chemistry—Methods | Research Article doi.org/10.1002/cmtd.202500102 | Chemistry Europe European Chemical Societies Publishing

path of the μCT scanner at a distance of 6.3 mm to the focal point of the X-ray tube (FOD). The distance from the focal point to the detector (FDD) was 808 mm. For the scanning with the 180NF nanotube and a high-energy tungsten target at 50 kV/200 μA, we did not use any filters applied in the beam path. During a full revolution of the sample, we took 1500 2D projection images (acquired with a Phoenix DXR 250RT detector at 200 μm pixel size and 1.000 × 1.000 pixels). The reconstruction of the μCT images was performed with the Avizo software (Thermo Fisher Scientific GmbH, Schwerte, Germany). To distinguish the plastic particles from background and voids in the reconstructed volumes, image segmentation was performed using gray-scale thresholding in Avizo. The threshold values were determined empirically based on histogram analysis and visual inspection of representative slices. Due to the low X-ray attenuation contrast between the plastic particles and surrounding air, particular attention was paid to minimizing partial volume effects at the particle edges. A combination of non-local means filtering and contrast enhancement was applied prior to segmentation to reduce noise and enhance edge definition. The resulting binary masks were then validated against orthogonal slice views to ensure that particle geometry and pore structure were faithfully preserved, enabling reliable assessment of packing homogeneity and porosity relevant for interpreting streaming potential measurements.

Acknowledgments

The authors acknowledge the Keylab for Optical and Electron Microscopy at the Bavarian Polymer Institute (BPI). The authors are grateful to Nina Volk, Carmen Kunert, and Tamino Rößler for their help with the SEM measurements and to Markus Hund for his help with the AFM measurements. The authors also thank the GeoZentrum Nordbayern for providing μCT measurement facilities and Hao Liu from the University of Bayreuth for rating the quality of the μCT measurements. M.B.E. appreciates the support from the Elite Network of Bavaria (ENB) via the "Macromolecular Science" study program and the University of Bayreuth Graduate School. The authors thank Anika Mauel and the C01 project of the CRC 1357 Microplastics for providing the weathered MPPs. Open Access funding enabled and organized by Projekt DEAL. This work was funded by the Deutsche Forschungsgemeinschaft (DFG, German Research Foundation)—project no. 391977956—SFB 1357 (projects B01, B06, Z01, C01, and A04).

Open Access funding enabled and organized by Projekt DEAL.

Conflict of Interest

The authors declare no conflict of interest.

Author Contributions

Matthias B. Engelhardt: formal analysis (equal); investigation (lead); methodology (supporting); visualization (equal); writing—original draft (equal); writing—review & editing (equal). **Daniel Wagner**: formal analysis (supporting); investigation (supporting); methodology (supporting); writing—review & editing (supporting). **Mohsen Zarebanadkouki**: formal analysis (supporting); investigation (supporting); writing—review & editing (supporting). **Nora Meides**: investigation (supporting); resources (supporting). **Christian Schulbert**: investigation (supporting); methodology (supporting); writing—review & editing (supporting). **Martin G. J. Löder**: conceptualization (supporting); data curation (supporting); investigation (supporting); writing—original draft (supporting); writing—review & editing (supporting). **Nicolas Helfricht**: conceptualization (supporting); data curation (supporting); investigation (supporting); writing—original draft (supporting); writing—review & editing (supporting). **Seema Agarwal**: funding acquisition (supporting); methodology (supporting); resources (supporting); supervision (supporting). **Andrea Carminati**: funding acquisition (supporting); methodology (supporting); supervision (supporting). **Peter Strohriegl**: methodology (supporting); resources (supporting). **Jürgen Senker**: conceptualization (supporting); resources (supporting); supervision (supporting); writing—review & editing (supporting). **Christian Laforsch**: funding acquisition (equal); methodology (supporting); resources (supporting); supervision (supporting); writing—review & editing (supporting). **Georg Papastavrou**: conceptualization (lead); formal analysis (equal); funding acquisition (lead); methodology (lead); resources (lead); visualization (equal); writing—original draft (equal); writing—review & editing (lead).

Data Availability Statement

The data that support the findings of this study are available in the supplementary material of this article.

[1] Y. Chae, Y. J. An, *Environ. Pollut.* **2018**, *240*, 387.
[2] A. A. de Souza Machado, W. Kloas, C. Zarfl, S. Hempel, M. C. Rillig, *Glob. Change Biol.* **2018**, *24*, 1405.
[3] T. S. Galloway, M. Cole, C. Lewis, *Nat. Ecol. Evol.* **2017**, *1*, 116.
[4] R. Geyer, J. R. Jambeck, K. L. Law, *Sci. Adv.* **2017**, *3*, e1700782.
[5] S. Lambert, M. Wagner, *Microplastics Are Contaminants of Emerging Concern in Freshwater Environments: An Overview*, Springer International Publishing, Cham **2018**, 25.
[6] A. F. R. M. Ramsperger, E. Bergamaschi, M. Panizzolo, I. Fenoglio, F. Barbero, R. Peters, A. Undas, S. Purker, B. Giese, C. R. Lalyer, A. Tamargo, M. V. Moreno-Arribas, H. P. Grossart, D. Kühnel, J. Dietrich, F. Paulsen, A. K. Afanou, S. Zienolddiny-Narui, S. E. Hammer, T. K. Ervik, P. Graff, B. C. Brinchmann, K. C. Nordby, H. Wallin, M. Nassi, F. Benetti, M. Zanella, J. Brehm, H. Kress, M. G. J. Löder, C. Laforsch, *NanoImpact* **2023**, *29*, 100441.
[7] Y. Wang, L. Xiang, W. Amelung, M. Elsner, J. Gan, S. Kueppers, L. Christian, X. Jiang, J. Adu-Gyamfi, L. Heng, Y. S. Ok, N. P. Ivleva, Y. Luo, D. Barceló, A. Schäffer, F. Wang, *Trends Anal. Chem.* **2023**, *169*, 117309.
[8] A. R. Aves, L. E. Revell, S. Gaw, H. Ruffell, A. Schuddeboom, N. E. Wotherspoon, M. LaRue, A. J. McDonald, *Cryosphere* **2022**, *16*, 2127.
[9] M. Bergmann, V. Wirzberger, T. Krumpen, C. Lorenz, S. Primpke, M. B. Tekman, G. Gerdts, *Environ. Sci. Technol.* **2017**, *51*, 11000.
[10] Z. Huang, B. Hu, H. Wang, *Environ. Chem. Lett.* **2023**, *21*, 383.
[11] M. G. J. Löder, G. Gerdts, *Methodology Used for the Detection and Identification of Microplastics—A Critical Appraisal*, Springer International Publishing, Cham **2015**, 201.
[12] J. N. Möller, M. G. J. Löder, C. Laforsch, *Environ. Sci. Technol.* **2020**, *54*, 2078.
[13] Y. Adachi, L. Feng, M. Kobayashi, *Colloids Surf. A.* **2015**, *471*, 38.
[14] A. A. Harraq, B. Bharti, *ACS Environ. Au* **2022**, *2*, 3.
[15] A. Cramer, J. Schmidtmann, P. Benard, A. Kaestner, M. Engelhardt, S. Peiffer, A. Carminati, *Environ. Sci.: Process. Impacts.* **2023**, *25*, 1094.
[16] M. Elimelech, C. R. O'Melia, *Colloids Surf.* **1990**, *44*, 165.
[17] M. Kobayashi, M. Ookawa, S. Yamada, *J. Jpn. Soc. Civ. Eng., Ser. A2* **2014**, *70*, 743.
[18] A. F. R. M. Ramsperger, J. Jasinski, M. Völkl, T. Witzmann, M. Meinhart, V. Jérôme, W. P. Kretschmer, R. Freitag, J. Senker, A. Fery, H. Kress, T. Scheibel, C. Laforsch, *J. Hazard. Mater.* **2022**, *425*, 127961.

© 2025 The Author(s). Chemistry - Methods published by Chemistry Europe and Wiley-VCH GmbH

Chemistry—Methods | Research Article doi.org/10.1002/cmtd.202500102 | Chemistry Europe European Chemical Societies Publishing

[19] S. Wieland, A. F. R. M. Ramsperger, W. Gross, M. Lehmann, T. Witzmann, A. Caspari, M. Obst, S. Gekle, G. K. Auernhammer, A. Fery, C. Laforsch, H. Kress, *Nat. Commun.* **2024**, *15*, 922.
[20] A. Amobonye, P. Bhagwat, S. Raveendran, S. Singh, S. Pillai, *Front. Microbiol.* **2021**, *12*, 768297.
[21] M. Kobayashi, *Colloid Polym. Sci.* **2008**, *286*, 935.
[22] B. Nguyen, D. Claveau-Mallet, L. M. Hernandez, E. G. Xu, J. M. Farner, N. Tufenkji, *Acc. Chem. Res.* **2019**, *52*, 858.
[23] W. J. Shim, S. H. Hong, S. E. Eo, *Anal. Methods* **2017**, *9*, 1384.
[24] Z. Sobhani, X. Zhang, C. Gibson, R. Naidu, M. Megharaj, C. Fang, *Water Res.* **2020**, *174*, 115658.
[25] J. L. Conkle, C. D. Báez D. Valle, J. W. Turner, *Environ. Manag.* **2018**, *61*, 1.
[26] A. Shamskhany, Z. Li, P. Patel, S. Karimpour, *Front. Mar. Sci.* **2021**, *8*, 760649.
[27] G. A. Covernton, C. M. Pearce, H. J. Gurney-Smith, S. G. Chastain, P. S. Ross, J. F. Dower, S. E. Dudas, *Sci. Total Environ.* **2019**, *667*, 124.
[28] C. Hung, N. Klasios, X. Zhu, M. Sedlak, R. Sutton, C. M. Rochman, *Integr. Environ. Assess. Manag.* **2021**, *17*, 282.
[29] F. Stock, C. Kochleus, B. Bänsch-Baltruschat, N. Brennholt, G. Reifferscheid, *Trends Anal. Chem.* **2019**, *113*, 84.
[30] D. K. A. Barnes, F. Galgani, R. C. Thompson, M. Barlaz, *Trans. R. Soc. B.* **2009**, *364*, 1985.
[31] P. Sethia, D. Nandhini, S. Amutha, *Mar. Ecol.* **2024**, *45*, 1.
[32] J. Schmidtmann, H.-K. Weishäupl, L. Hopp, N. Meides, S. Peiffer, *Environ. Sci.: Process. Impacts.* **2025**, *27*, 992.
[33] H. Butt, K. Graf, M. Kappl, *Physics and Chemistry of Interfaces*, Wiley-VCH, Weinheim **2003**.
[34] J. N. Israelachvili, *Intermolecular and Surface Forces*, Academic Press, Boston **1992**.
[35] A. Abdurahman, K. Cui, J. Wu, S. Li, R. Gao, J. Dai, W. Liang, F. Zeng, *Ecotoxicol. Environ. Saf.* **2020**, *198*, 110658.
[36] X. Wu, P. Liu, Z. Gong, H. Wang, H. Huang, Y. Shi, X. Zhao, S. Gao, *Environ. Sci. Technol.* **2021**, *55*, 15810.
[37] Y. Wang, P. Zhao, H. Yi, X. Tang, *Environ. Sci.: Process. Impacts.* **2025**, *27*, 849.
[38] Y. Chen, H. Tang, Y. Cheng, T. Huang, B. Xing, *J. Hazard. Mater.* **2023**, *455*, 131636.
[39] K. L. Chen, M. Elimelech, *Environ. Sci. Technol.* **2009**, *43*, 7270.
[40] A. V. Delgado, F. González-Caballero, R. J. Hunter, L. K. Koopal, J. Lyklema, *J. Colloid Interface Sci.* **2007**, *309*, 194.
[41] J. F. Duval, H. Ohshima, *Langmuir* **2006**, *22*, 3533.
[42] J. R. Martin, I. Bihannic, C. Santos, J. P. Farinha, B. Demé, F. A. Leermakers, J. P. Pinheiro, E. Rotureau, J. F. Duval, *Langmuir* **2015**, *31*, 4779.
[43] J. Stone-Masui, A. Watillon, *J. Colloid Interface Sci.* **1975**, *52*, 479.
[44] R. J. Hunter, *Zeta Potential in Colloid Science: Principles and Applications*, Academic Press, London **1981**.
[45] S. Antunez-Vela, V. H. Perez-Gonzalez, A. C. De Peña, C. J. Lentz, B. H. Lapizco-Encinas, *Anal. Chem.* **2020**, *92*, 14885.
[46] A. A. Harraq, P. J. Brahana, O. Arcemont, D. Zhang, K. T. Valsaraj, B. Bharti, *ACS Environ. Au* **2022**, *2*, 549.
[47] A. Hakim, M. Kobayashi, *J. Polym. Environ.* **2021**, *29*, 1921.
[48] D. Takács, T. Szabó, A. Jamnik, M. Tomšič, I. Szilágyi, *Langmuir* **2023**, *39*, 12835.
[49] G. V. Quincke, *Ann. Phys. (Berlin)* **1861**, *189*, 513.
[50] Z. Adamczyk, M. Zembala, A. Michna, *J. Colloid Interface Sci.* **2006**, *303*, 353.
[51] A. E. Childress, M. Elimelech, *Environ. Sci. Technol.* **2000**, *34*, 3710.
[52] C. Werner, R. Zimmermann, T. Kratzmüller, *Colloids Surf. A.* **2001**, *192*, 205.
[53] Z. Adamczyk, K. Sadlej, E. Wajnryb, M. Nattich, M. L. Ekiel-Jezewska, J. Bławzdziewicz, *Adv. Colloid Interface Sci.* **2010**, *153*, 1.
[54] Z. Adamczyk, M. Zaucha, M. Zembala, *Langmuir* **2010**, *26*, 9368.
[55] J. F. L. Duval, R. Zimmermann, A. L. Cordeiro, N. Rein, C. Werner, *Langmuir* **2009**, *25*, 10691.
[56] J. F. Duval, D. Küttner, C. Werner, R. Zimmermann, *Langmuir* **2011**, *27*, 10739.
[57] R. Schweiss, P. B. Welzel, C. Werner, W. Knoll, *Langmuir* **2001**, *17*, 4304.
[58] C. Werner, H. Körber, R. Zimmermann, S. Dukhin, H. J. Jacobasch, *J. Colloid Interface Sci.* **1998**, *208*, 329.
[59] M. Zembala, Z. Adamczyk, *Langmuir* **2000**, *16*, 1593.
[60] R. Zimmermann, S. Dukhin, C. Werner, *J. Phys. Chem. B.* **2001**, *105*, 8544.
[61] R. Zimmermann, U. Freudenberg, R. Schweiß, D. Küttner, C. Werner, *Curr. Opin. Colloid Interface Sci.* **2010**, *15*, 196.
[62] R. Akhbarizadeh, S. Dobaradaran, M. A. Torkmahalleh, R. Saeedi, R. Aibaghi, F. F. Ghasemi, *Environ. Res.* **2021**, *192*, 110339.
[63] J. Brehm, M. V. Wilde, L. Reiche, L. C. Leitner, B. Petran, M. Meinhart, S. Wieland, S. Ritschar, M. Schott, J. P. Boos, S. Frei, H. Kress, J. Senker, A. Greiner, T. Fröhlich, C. Laforsch, *J. Hazard. Mater.* **2022**, *437*, 129351.
[64] C. F. Araujo, M. M. Nolasco, A. M. P. Ribeiro, P. J. A. Ribeiro-Claro, *Water Res.* **2018**, *142*, 426.
[65] E. Fries, J. H. Dekiff, J. Willmeyer, M. T. Nuelle, M. Ebert, D. Remy, *Environ. Sci.: Process. Impacts.* **2013**, *15*, 1949.
[66] N. Meides, T. Menzel, B. Poetzschner, M. G. J. Löder, U. Mansfeld, P. Strohriegl, V. Altstaedt, J. Senker, *Environ. Sci. Technol.* **2021**, *55*, 7930.
[67] J. Wagner, Z.-M. Wang, S. Ghosal, C. Rochman, M. Gassel, S. Wall, *Anal. Methods* **2017**, *9*, 1479.
[68] A. Mauel, B. Pötzschner, N. Meides, R. Siegel, P. Strohriegl, J. Senker, *RSC Adv.* **2022**, *12*, 10875.
[69] J. Schmidt, M. Haave, J. Underhaug, W. Wang, *Microplast. Nanoplast.* **2024**, *4*, 1.
[70] D. W. Fuerstenau, *PhD Thesis*, Massachusetts Institute of Technology **1953**.
[71] V. Pravdic, *Croat. Chem. Acta* **1958**, *30*, 113.
[72] M. A. Hubbe, F. Wang, *Paper Technol.* **2004**, *45*, 27.
[73] O. El-Gholabzouri, M. A. Cabrerizo, R. Hidalgo-Álvarez, *J. Colloid Interface Sci.* **1998**, *199*, 38.
[74] O. El-Gholabzouri, M. A. Cabrerizo, R. Hidalgo-Álvarez, *Colloids Surf. A.* **1999**, *159*, 449.
[75] R. Hidalgo-Álvarez, F. J. D. L Nieves, G. Pardo, *J. Colloid Interface Sci.* **1985**, *107*, 295.
[76] E. Rodier, J. Dodds, *Part. Part. Syst. Charact.* **1995**, *12*, 198.
[77] A. Drechsler, A. Caspari, A. Synytska, *Surf. Interface Anal.* **2020**, *52*, 991.
[78] E. Walker, P. W. J. Glover, *Transp. Porous Media* **2018**, *121*, 183.
[79] D. Jougnot, N. Linde, A. Revil, C. Doussan, *Vadose Zone J.* **2012**, *11*, 1.
[80] Z. Li, Y. Liu, D. Wang, P. Wang, R. Xu, D. Xie, *Eur. J. Soil Sci.* **2019**, *70*, 1063.
[81] C. M. Mboh, J. A. Huisman, E. Zimmermann, H. Vereecken, *Vadose Zone J.* **2012**, *11*, 1.
[82] N. Meides, A. Mauel, T. Menzel, V. Altstädt, H. Ruckdäschel, J. Senker, P. Strohriegl, *Microplast Nanoplast.* **2022**, *2*, 1.
[83] J. N. Möller, I. Heisel, A. Satzger, E. C. Vizsolyi, S. D. J. Oster, S. Agarwal, C. Laforsch, M. G. J. Löder, *Environ. Toxicol. Chem.* **2022**, *41*, 844.
[84] A. F. R. M. Ramsperger, A. C. Stellwag, A. Caspari, A. Fery, T. Lueders, H. Kress, M. G. J. Löder, C. Laforsch, *Water (Basel).* **2020**, *12*, 3216.
[85] B. Trotter, M. V. Wilde, J. Brehm, E. Dafni, A. Aliu, G. J. Arnold, T. Fröhlich, C. Laforsch, *Sci. Total Environ.* **2021**, *795*, 148822.
[86] M. Völkl, V. Jérôme, A. Weig, J. Jasinski, N. Meides, P. Strohriegl, T. Scheibel, R. Freitag, *J. Hazard. Mater.* **2022**, *435*, 128955.
[87] M. Minor, A. J. van der Linde, J. Lyklema, *J. Colloid Interface Sci.* **1998**, *203*, 177.
[88] M. Minor, A. J. van der Linde, H. P. van Leeuwen, J. Lyklema, *Colloids Surf. A.* **1998**, *142*, 165.
[89] N. Spanos, A. Tsevis, P. G. Koutsoukos, M. Marcel, A. J. van der Linde, J. Lyklema, *Colloids Surf. A.* **1998**, *141*, 101.
[90] H. J. Jacobasch, G. Bauböck, J. Schurz, *Colloid Polym. Sci.* **1985**, *263*, 3.
[91] H.-J. Jacobasch, J. Schurz, *Prog. Colloid Polym. Sci.* **1988**, *77*, 40.
[92] S. Laha, M. Roy, S. Chakraborty, *Langmuir* **2024**, *40*, 12878.
[93] O. Duliu, *Earth-Sci. Rev.* **1999**, *48*, 265.
[94] J. K. Jasti, G. Jesion, L. Feldkamp, *SPE Form. Eval.* **1993**, *8*, 189.
[95] H. Ohshima, *Electrical Phenomena at Interfaces and Biointerfaces: Fundamentals and Applications in Nano-, Bio-, and Environmental Sciences*, Wiley, New York / Chichester, UK **2012**.
[96] H. C. Li, P. L. De Bruyn, *Surf. Sci.* **1966**, *5*, 203.
[97] S. Chakraborty, *Phys. Rev. Lett.* **2008**, *100*, 097801.
[98] C. Zhao, C. Yang, *Colloids Surf. A.* **2011**, *386*, 191.
[99] H. Ohshima, T. W. Healy, L. R. White, *J. Colloid Interface Sci.* **1982**, *90*, 17.
[100] S. H. Behrens, M. Borkovec, P. Schurtenberger, *Langmuir* **1998**, *14*, 1951.
[101] R. Ruiz, C. Ràfols, M. Rosés, E. Bosch, *J. Pharm. Sci.* **2003**, *92*, 1473.
[102] A. Homola, R. O. James, *J. Colloid Interface Sci.* **1977**, *59*, 123.
[103] K. G. Marinova, R. G. Alargova, N. D. Denkov, O. D. Velev, D. N. Petsev, I. B. Ivanov, R. P. Borwankar, *Langmuir* **1996**, *12*, 2045.
[104] V. Tandon, S. K. Bhagavatula, W. C. Nelson, B. J. Kirby, *Electrophoresis* **2008**, *29*, 1092.
[105] L. P. Voegtli, C. F. Zukoski, *J. Colloid Interface Sci.* **1991**, *141*, 92.
[106] M. Elimelech, W. H. Chen, J. J. Waypa, *Desalination* **1994**, *95*, 269.
[107] H. Müller, W. Leube, K. Tauer, S. Förster, M. Antonietti, *Macromolecules* **1997**, *30*, 2288.
[108] S. Lu, K. Zhu, W. Song, G. Song, D. Chen, T. Hayat, N. S. Alharbi, C. Chen, Y. Sun, *Sci. Total Environ.* **2018**, *630*, 951.
[109] Q. M.égier du Sorbier, A. Aimable, C. Pagnoux, *J. Colloid Interface Sci.* **2015**, *448*, 306.
[110] Y. Utashiro, M. Takiguchi, M. Satoh, *Colloid Polym. Sci.* **2017**, *295*, 45.
[111] Y.-H. M. Chan, R. Schweiss, C. Werner, M. Grunze, *Langmuir* **2003**, *19*, 7380.

© 2025 The Author(s). Chemistry - Methods published by Chemistry Europe and Wiley-VCH GmbH

Chemistry—Methods
Research Article
doi.org/10.1002/cmtd.202500102
Chemistry Europe
European Chemical Societies Publishing

[112] J. K. Beattie, *Lab. Chip* **2006**, *6*, 1409.
[113] A. M. Pineda-Reyes, M. Hernández Delgado, M. D. L. L. Zambrano-Zaragoza, G. Leyva-Gómez, N. Mendoza-Muñoz, D. Quintanar-Guerrero, *RSC Adv.* **2021**, *11*, 2226.
[114] J. F. Duval, *J. Phys. Chem. A.* **2009**, *113*, 2275.
[115] A. Michna, *Adv. Colloid Interface Sci.* **2017**, *250*, 95.
[116] C. J. McColley, J. A. Nason, B. J. Harper, S. L. Harper, *Microplast Nanoplast.* **2023**, *3*, 10.
[117] M. Wisniewska, I. Ostolska, K. Szewczuk-Karpisz, S. Chibowski, K. Terpiłowski, V. M. Gun'ko, V. I. Zarko, *J. Nanopart. Res.* **2015**, *17*, 12.
[118] J. Xu, M. Li, Y. Zhao, Q. Lu, *Colloids Surf. A.* **2007**, *302*, 136.
[119] P. Beneš, M. Paulenová, *Z. Polym.* **1973**, *251*, 766.
[120] V. Kuznetsov, G. Papastavrou, *J. Phys. Chem. C.* **2014**, *118*, 2673.
[121] C. C. Price, R. W. Kell, E. Krebs, *J. Am. Chem. Soc.* **1942**, *64*, 1103.
[122] J. A. Mielczarski, Y. L. Jeyachandran, E. Mielczarski, B. Rai, *J. Colloid Interface Sci.* **2011**, *362*, 532.
[123] A. J. Everett, G. J. Minkoff, *Trans. Faraday Soc.* **1953**, *49*, 410.
[124] J. P. Guthrie, J. Cossar, A. Klym, *J. Am. Chem. Soc.* **1982**, *104*, 895.
[125] W. Li, B. Zu, Q. Yang, J. Guo, J. Li, *RSC Adv.* **2023**, *13*, 15566.
[126] M. B. Engelhardt, P. Markus, N. Helfricht, G. Papastavrou, *J. Colloid Interface Sci.* **2025**, *686*, 852.
[127] J. Schindelin, I. Arganda-Carreras, E. Frise, V. Kaynig, M. Longair, T. Pietzsch, S. Preibisch, C. Rueden, S. Saalfeld, B. Schmid, J. Y. Tinevez, D. J. White, V. Hartenstein, K. Eliceiri, P. Tomancak, A. Cardona, *Nat. Methods* **2012**, *9*, 676.

Manuscript received: July 30, 2025
Revised manuscript received: August 23, 2025
Version of record online: September 22, 2025

© 2025 The Author(s). Chemistry - Methods published by Chemistry Europe and Wiley-VCH GmbH

Supporting Information

Following Changes at the Solid/Liquid Interface for Large Microplastic Particles by Streaming Potential

Matthias B. Engelhardt, Daniel Wagner, Mohsen Zarebanadkouki, Nora Meides, Christian Schulbert, Martin G. J. Löder, Nicolas Helfricht, Seema Agarwal, Andrea Carminati, Peter Strohriegl, Jürgen Senker, Christian Laforsch, and Georg Papastavrou*

Dimensions of Fragmented Microplastic Particles

Table S1: Diameter overview of the fragmented microplastic particles prepared for this study.

Sieving Mesh Size (µm)	Average Particle Diameter (µm)
20 - 75	62.7 ± 0.6[a]
75 - 125	101.8 ± 1.0[a]
125 - 200	153.6 ± 0.4[a]

[a] from Gaussian fit to results from laser diffraction (cf. Figure 1a).

Scanning Electron Microscopy Micrographs of Fragmented Microplastic Particles

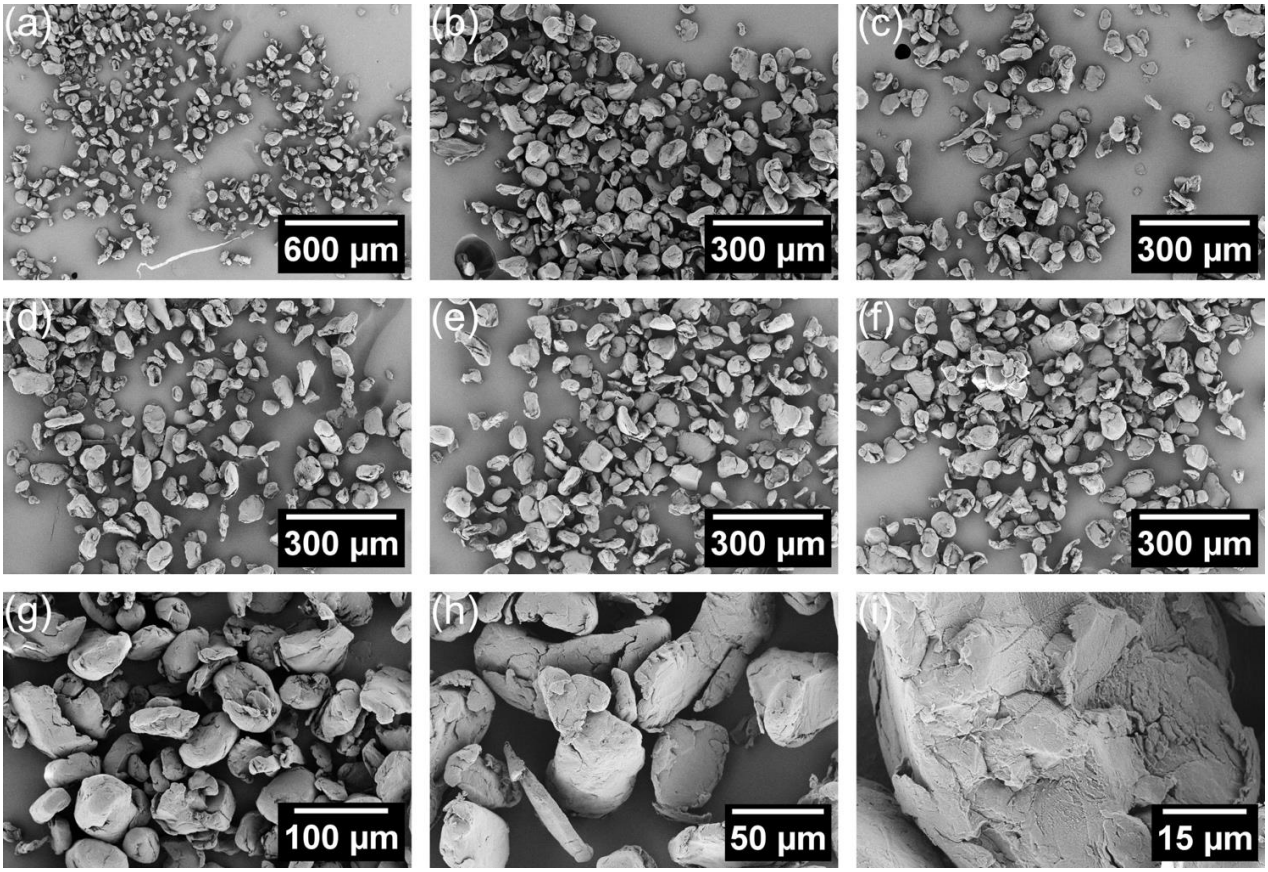

Figure S1: Representative SEM images of fragmented polystyrene microparticles of the small size fraction 20 – 75 µm.

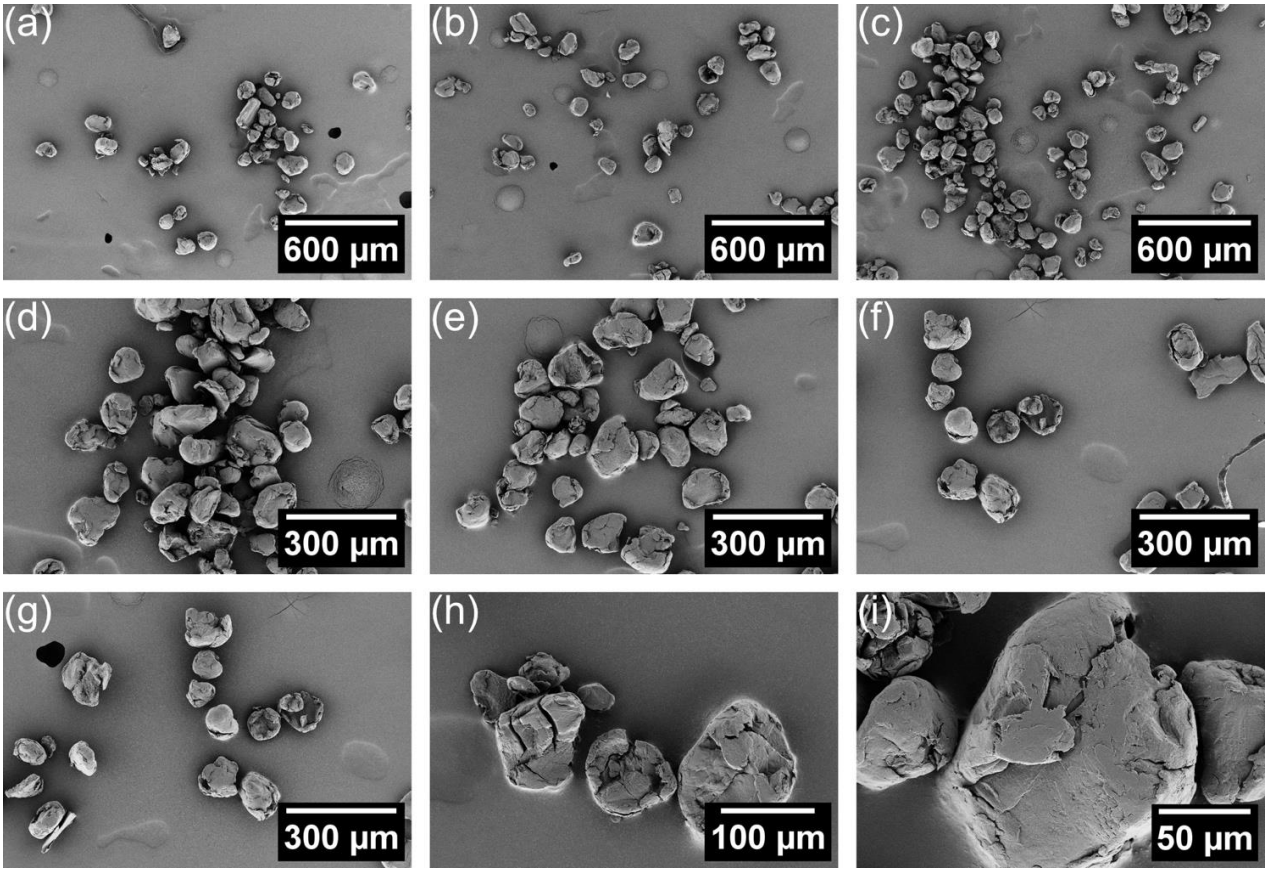

Figure S2: Representative SEM images of fragmented polystyrene microparticles of the size fraction 75 – 125 µm.

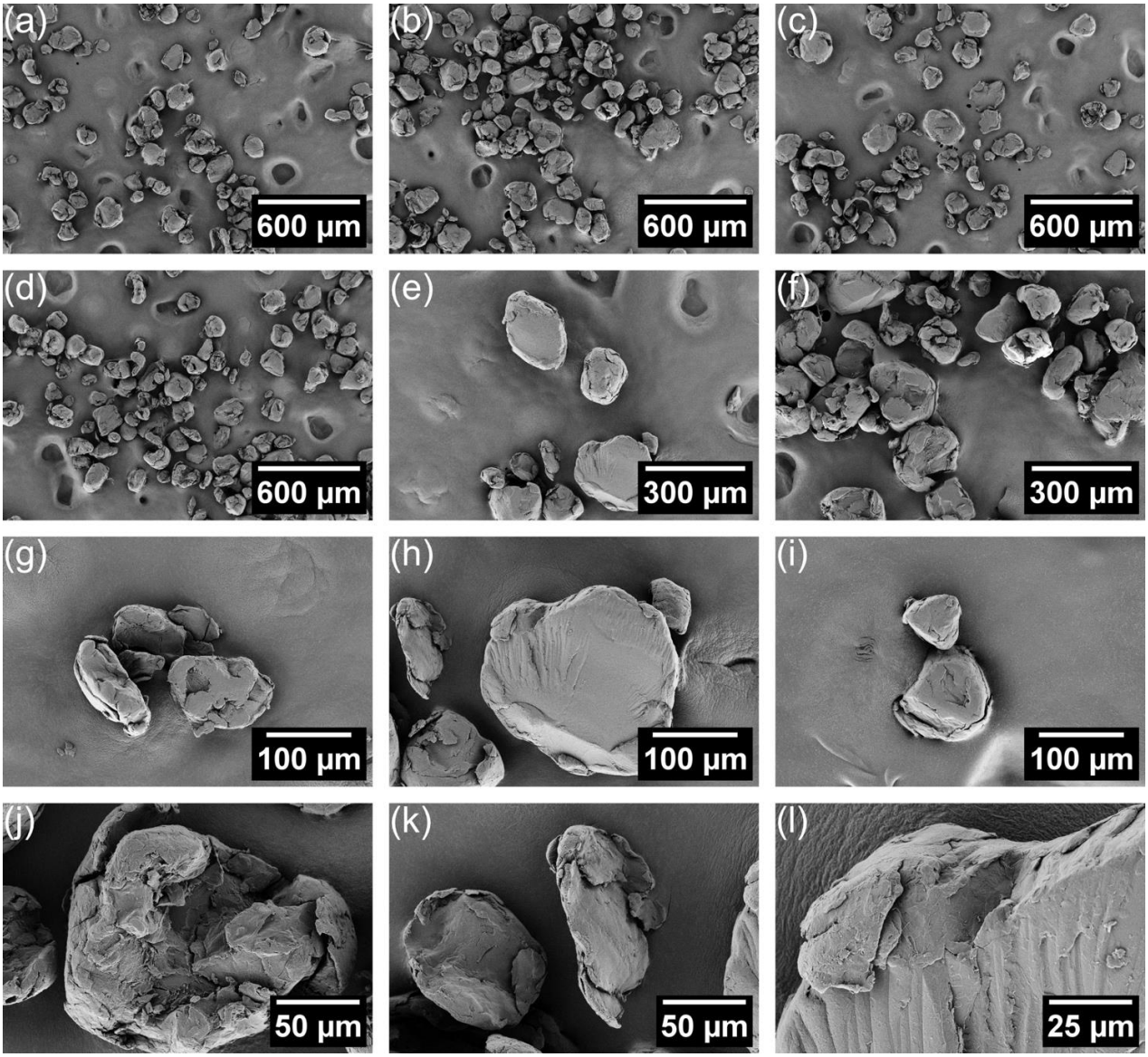

Figure S3: Representative SEM images of fragmented polystyrene microparticles of the size fraction 125 – 200 µm.

Surface Topography of Fragmented Microplastic Particles as Determined by Atomic Force Microscopy

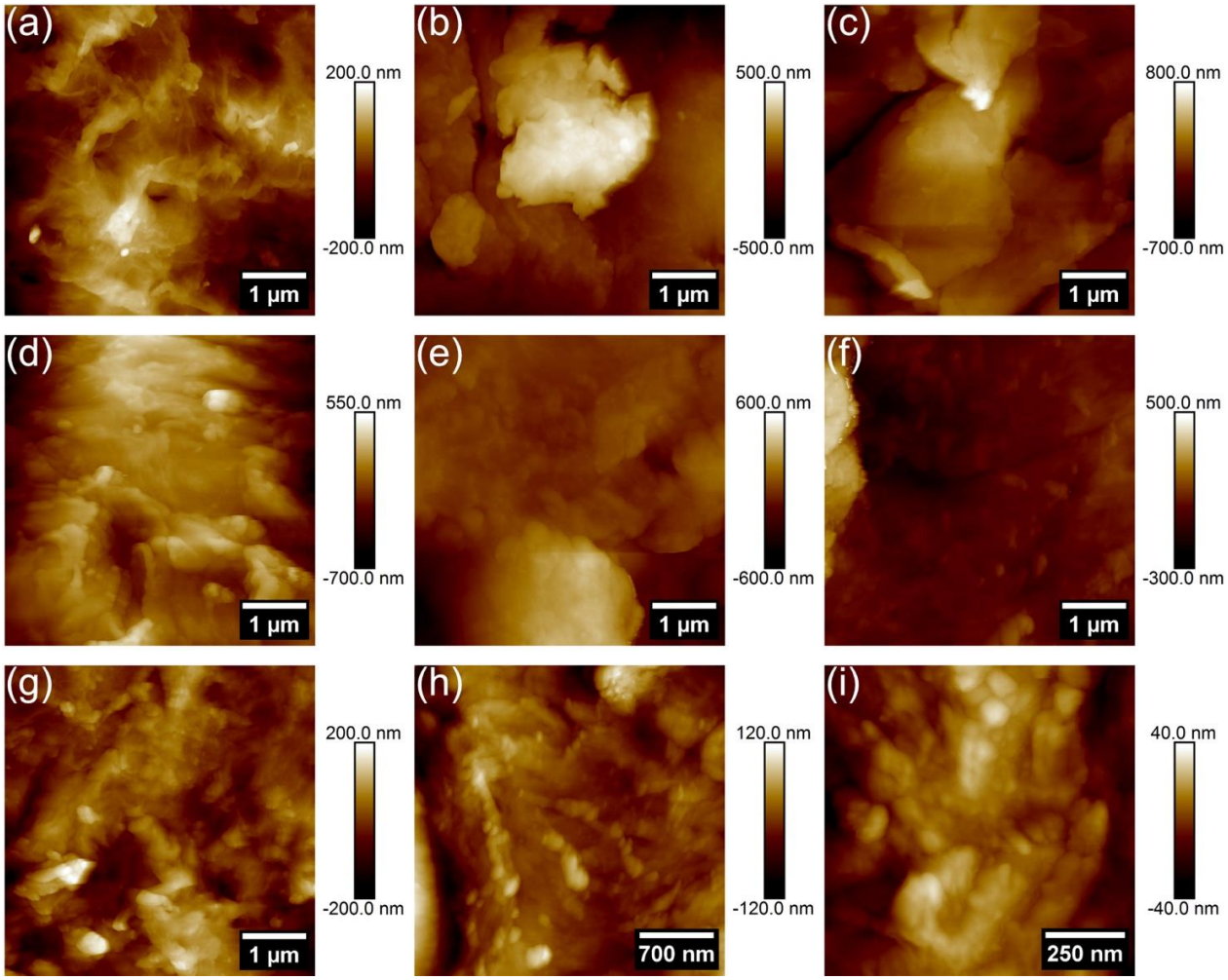

Figure S4: AFM topography images of fragmented polystyrene microparticles from diameter range 25 – 75 µm.

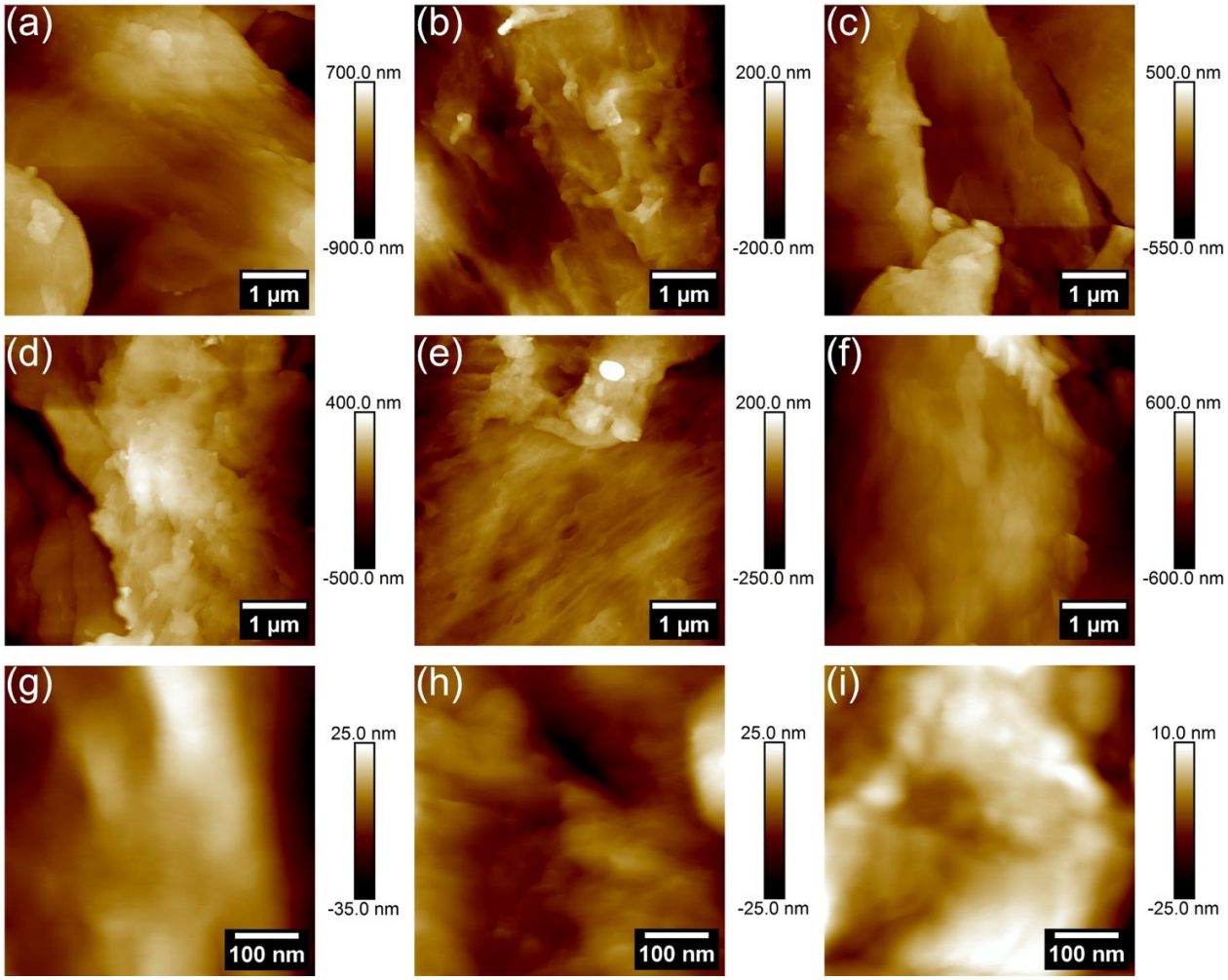

Figure S5: AFM topography images of fragmented polystyrene microparticles from diameter range 75 – 125 µm.

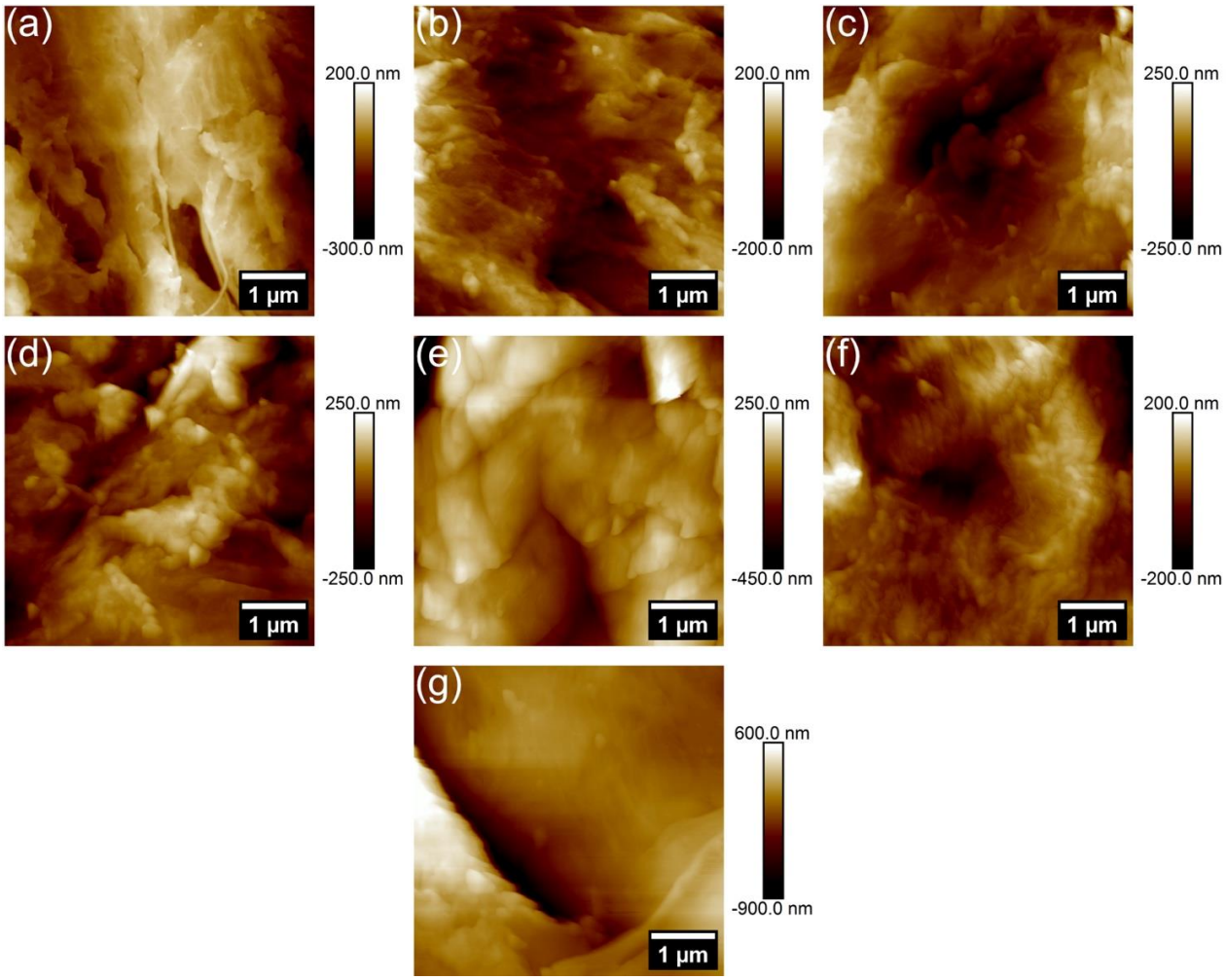

Figure S6: AFM topography images of fragmented polystyrene microparticles from diameter range 125 – 200 µm.

Scanning Electron Microscopy Images of Spherical Polystyrene Particles Obtained by Suspension Polymerization

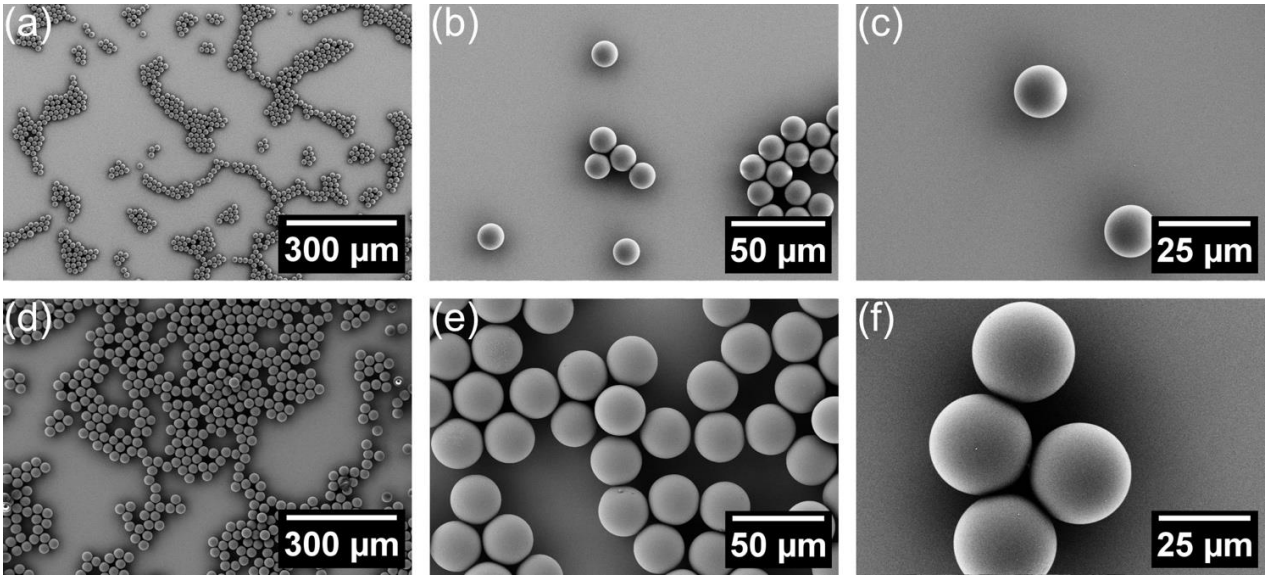

Figure S7: Exemplary SEM images of commercial non-modified polystyrene particles with nominal diameters of (a-c) (15.10 ± 0.26) µm and (d-f) (29.32 ± 0.25) µm, respectively.

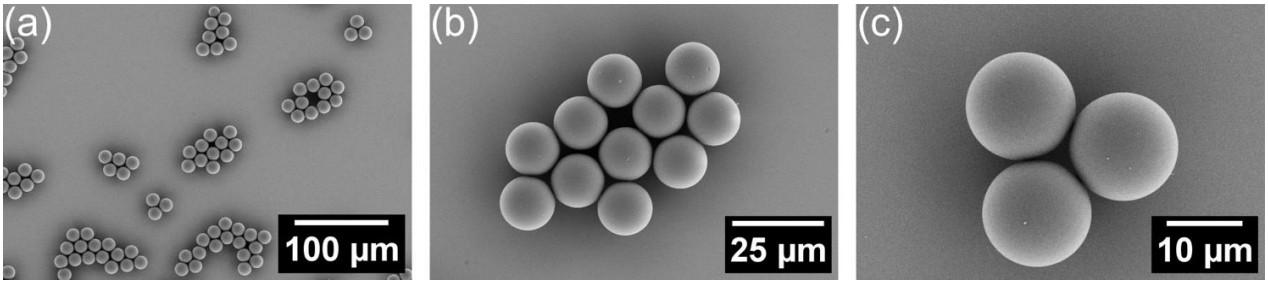

Figure S8: Exemplary SEM image of commercial NH_2-modified polystyrene particles with nominal diameters of (15.47 ± 0.26) µm.

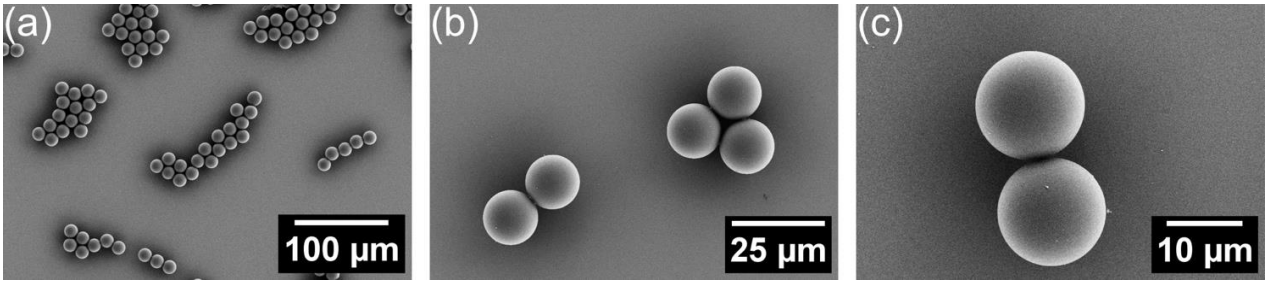

Figure S9: Exemplary SEM images of commercial COOH-modified polystyrene particles with nominal diameters of (a) (15.47 ± 0.19) µm.

Size Distributions for Spherical Polystyrene Particles Obtained by Suspension Polymerization

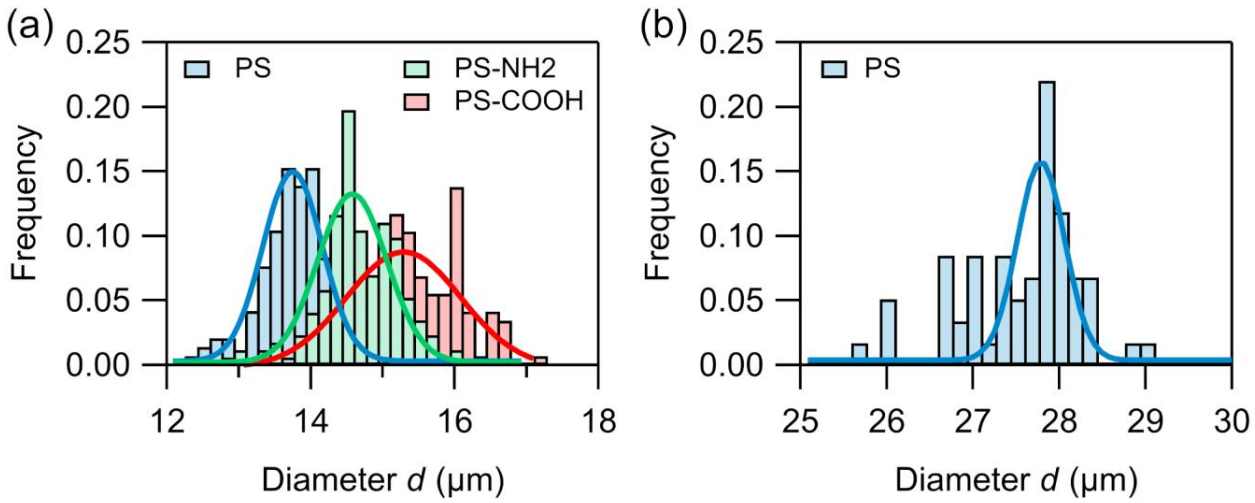

Figure S10: Size distributions as obtained from SEM images for the small commercial polystyrene particles with different surface functionalities and approximate diameters of (a) 15 µm and (b) 30 µm. Diameters were determined by ImageJ and the built-in line tool.

Table S2: Overview of the studied commercial polystyrene particles, the respective nominal and measured diameters from SEM experiments, and the number of evaluated particles according to Fig. S10.

Functionalization	Nominal diameter (µm)	Diameter by SEM (µm)	Number of evaluated particles
-bare (small)	15.10 ± 0.26	13.75 ± 0.51	144
-NH_2	15.47 ± 0.26	14.57 ± 0.56	172
-COOH	15.47 ± 0.19	15.26 ± 0.75	145
-bare (large)	29.32 ± 0.25	27.45 ± 0.69	59

X-Ray Microtomography (µCT) of Particle Beds

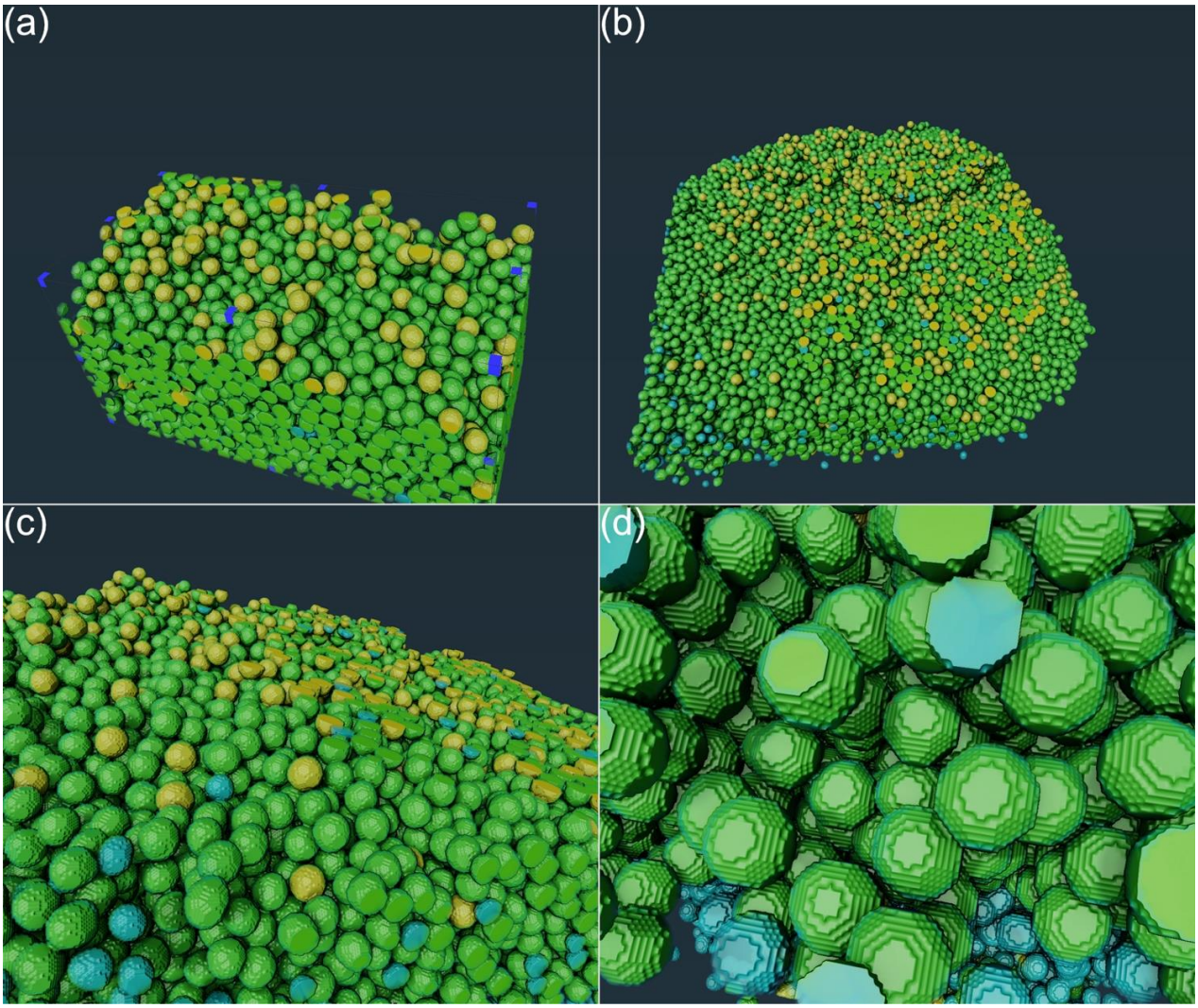

Figure S11: µCT reconstruction of a particle bed from spherical polystyrene microspheres formed in the particle plug. The particles had a nominal diameter of (29.32 ± 0.25) µm.

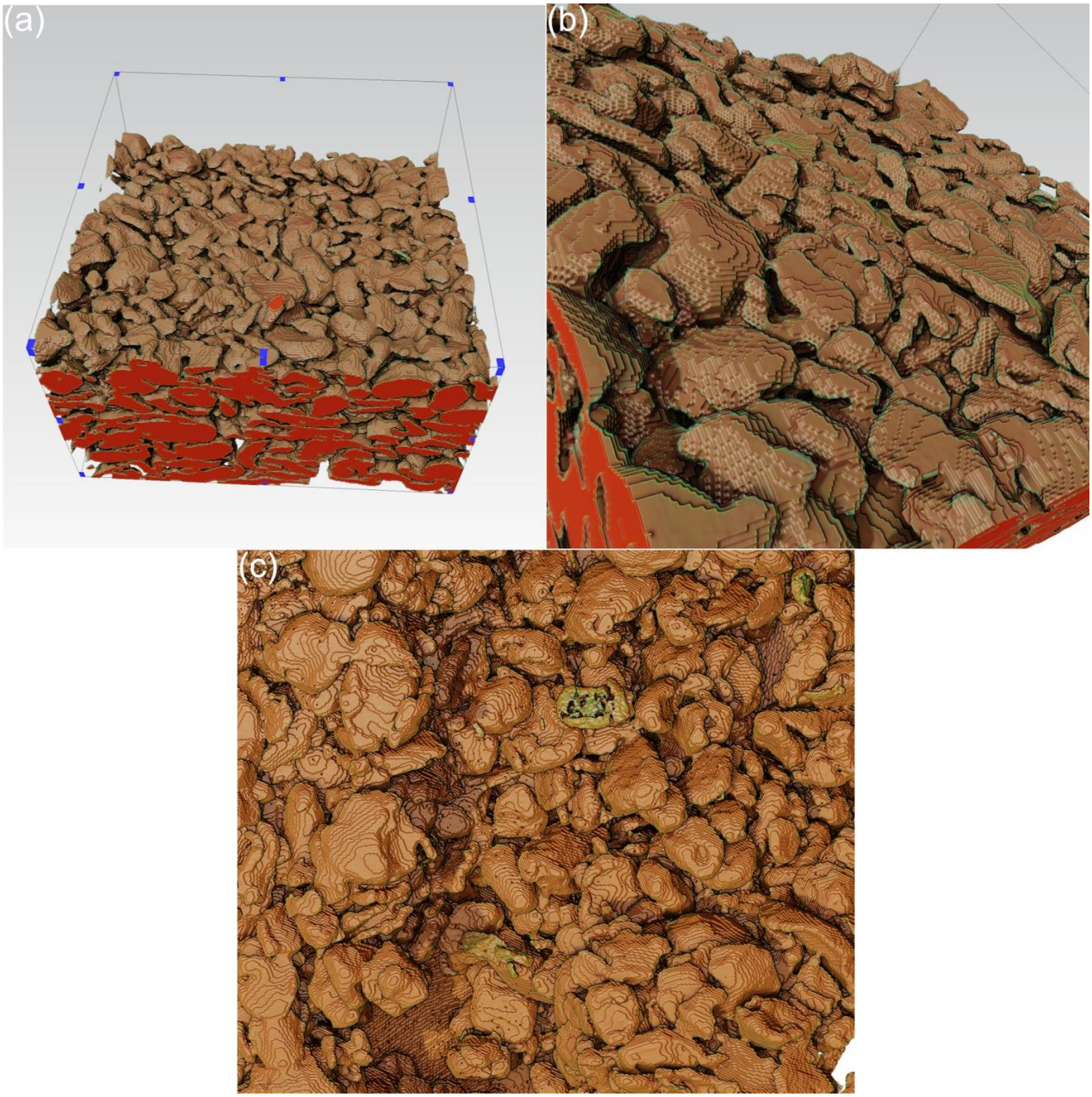

Figure S12: µCT reconstructions of a particle bed from fragmented microparticles of the size fraction 20 – 75 µm.

Ultrastructure on Bare Spherical Polystyrene Particles with a Nominal Diameter of 15 µm

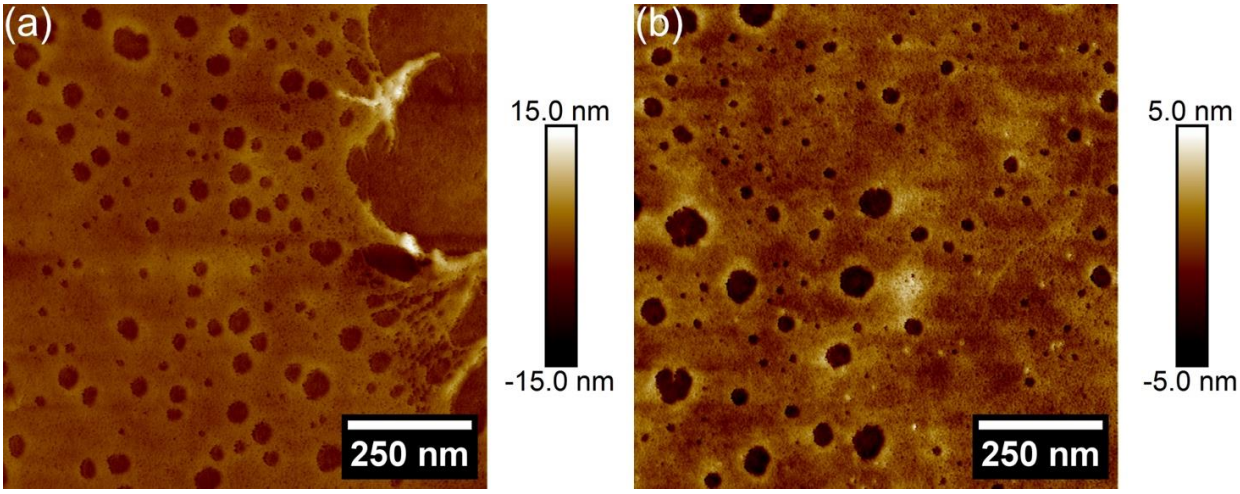

Figure S13: AFM images of commercial non-modified PS particles with a nominal diameter of (15.10 ± 0.26) µm. Images (a) and (b) show the interfaces of individual particles.

Streaming Potential and Scanning Electron Microscopy Characterization of the Polyamide-6,6 Filter Mats Used for the Particle Plugs

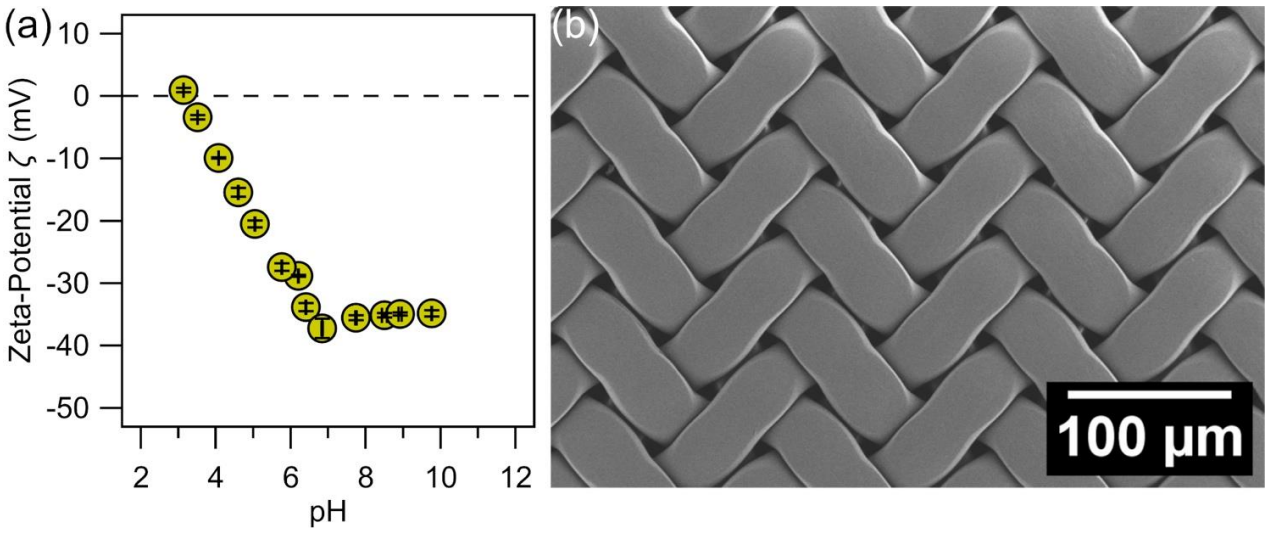

Figure S14: (a) Zeta-potential ζ of PA-6,6 filter mats with a nominal pore diameter of 10 µm as a function of the pH at a constant ionic strength of 10 mM in KCl. A filter stack of 6 filters was measured. (b) Scanning electron microscopy image of the corresponding filter mats.

Ultrastructure on Bare Spherical Polystyrene Particles with a Nominal Diameter of 30 µm

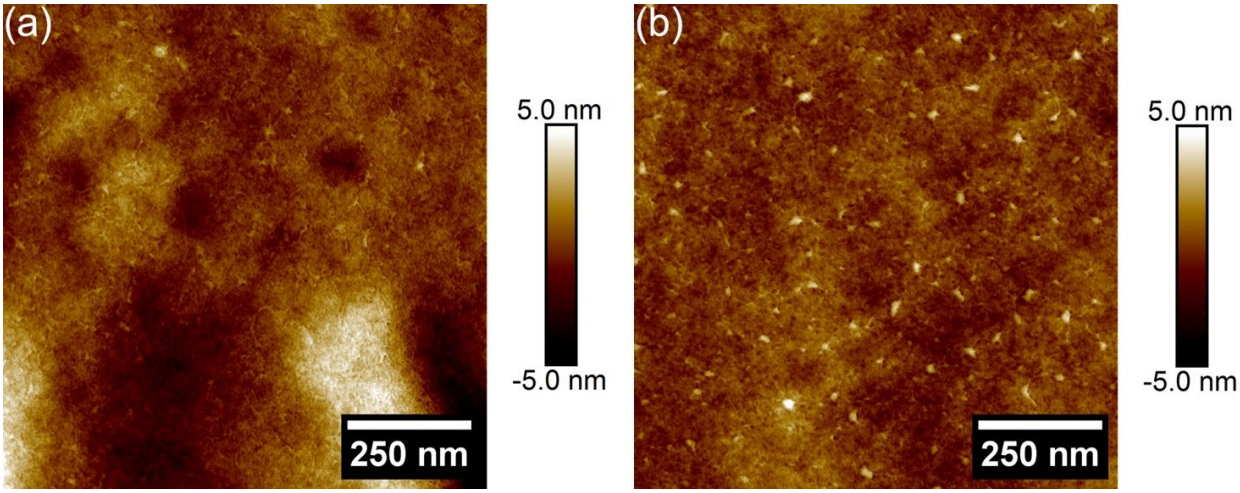

Figure S15: AFM images of commercial non-modified PS particles with a nominal diameter of (29.32 ± 0.25) µm. Images (a) and (b) show the interfaces of individual particles.

Average Diameter of Artificially Weathered Microplastic Particles Used in this Study

Table S3: Average diameters for the artificially weathered microplastic particles as reported by Meides et al.[73]

Weathering Exposure Time (h)	Average Diameter (µm)
600	138.6 ± 0.6 [b]
1200	90.0 ± 2.4 [b]
3200	22.3 ± 0.6 [b]

[b] from laser diffraction results reported by Meides et al.[73]

Scanning Electron Microscopy of the Surface Topography of Artificially Weathered Microplastic Particles

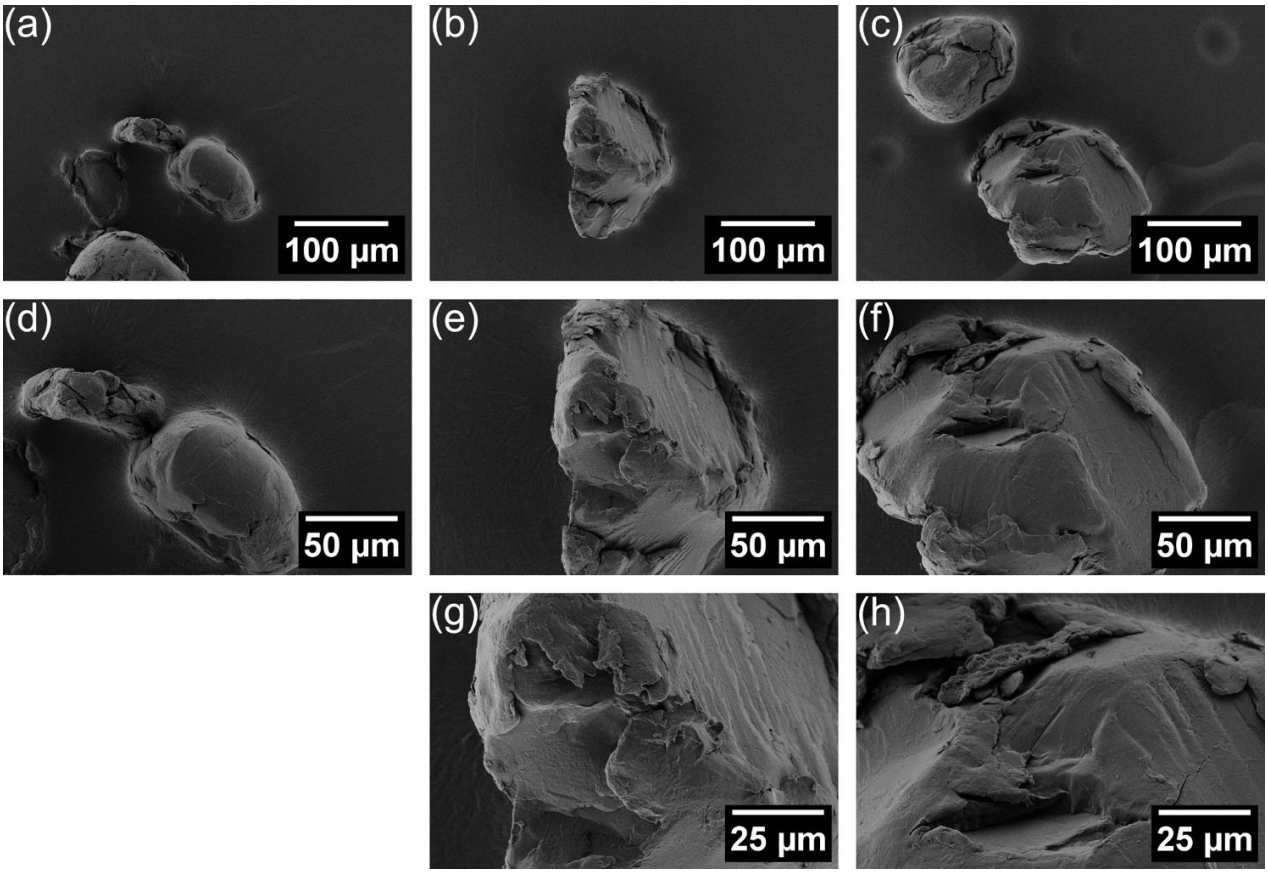

Figure S16: SEM images of fragmented microplastic particles from polystyrene before artificial weathering (i.e., 0 h). Here, images of the batch used for the weathering are shown. Each column corresponds to one particle.

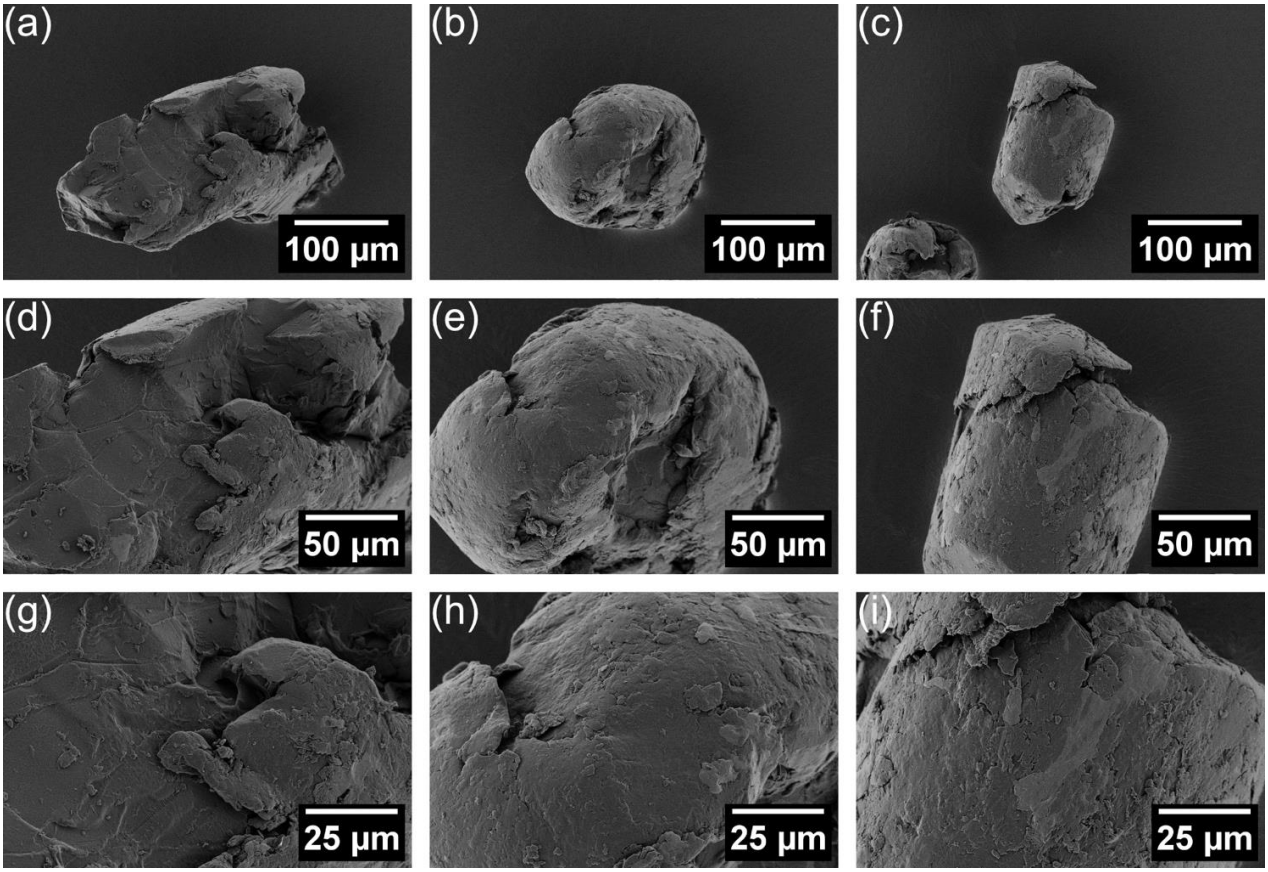

Figure S17: SEM images of microplastic particles after 600 h of artificial weathering. Each column corresponds to one particle at different magnifications.

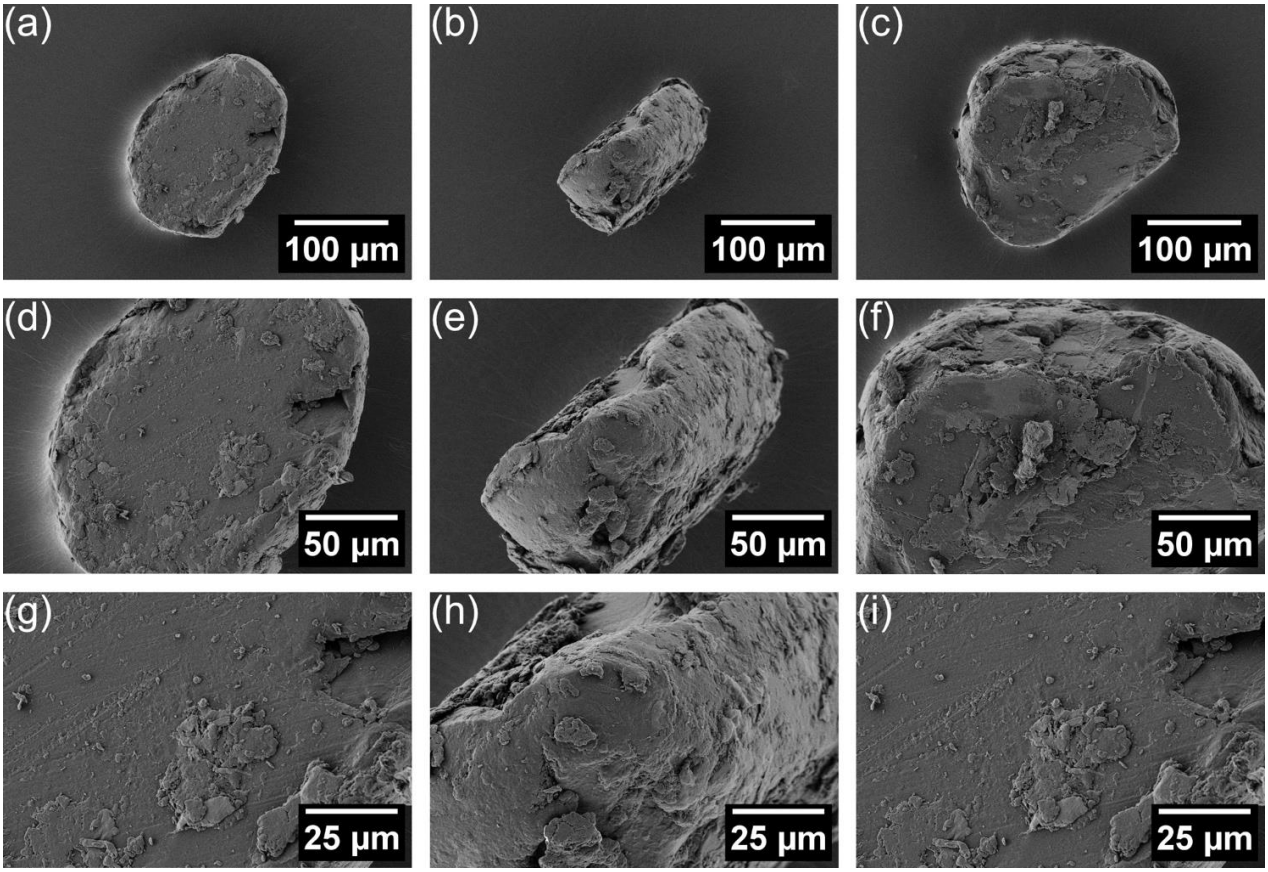

Figure S18: SEM images of microplastic particles after 1200 h of artificial weathering. Each column corresponds to one particle at different magnifications.

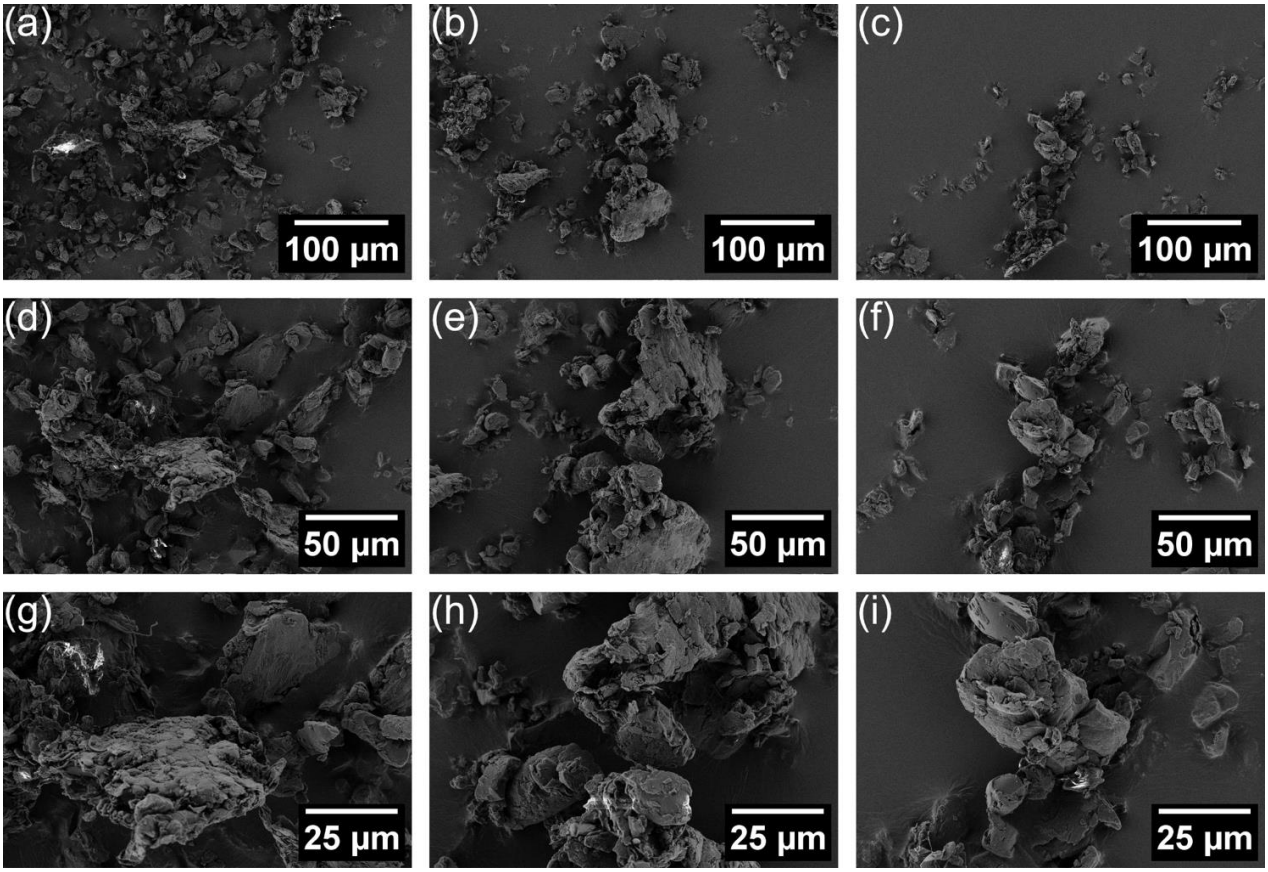

Figure S19: SEM images of microplastic particles after 3200 h of artificial weathering. Each column corresponds to one particle at different magnifications.

Surface Topography of Artificially Weathered Microplastic Particles as Determined by Tapping Mode Atomic Force Microscopy (AFM)

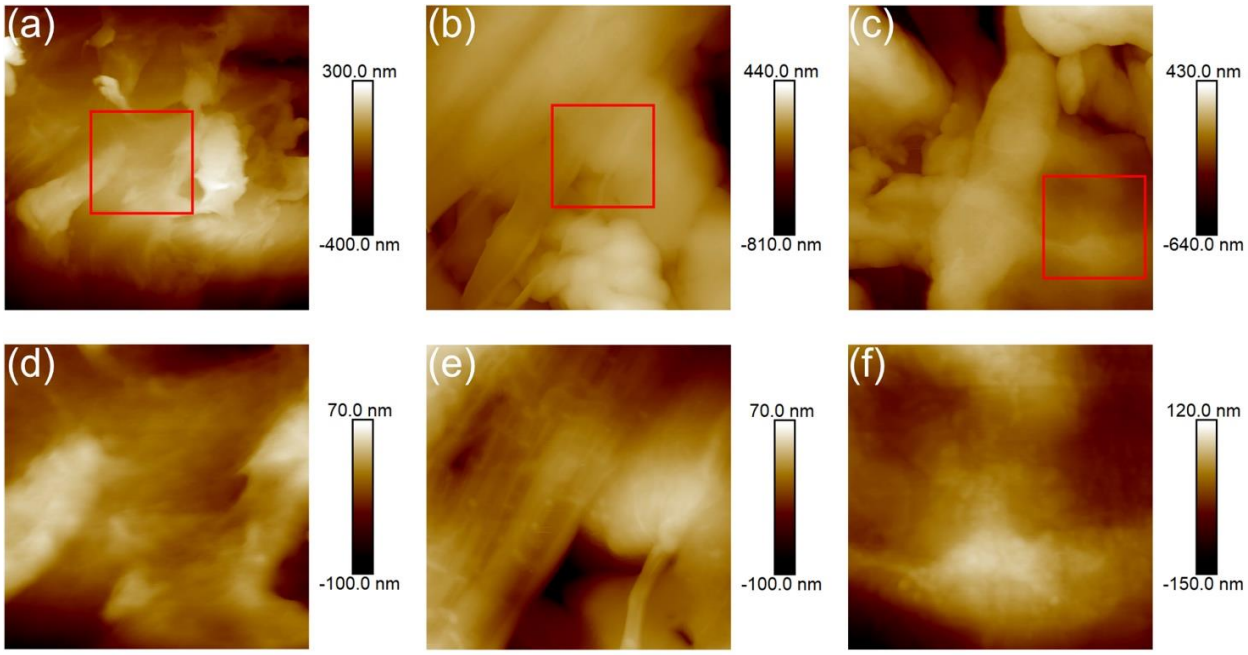

Figure S20. Images of the surface topography for microplastic particles (MPPs) with different magnifications as determined by AFM in Tapping Mode™. The corresponding phase images are shown in Figure 9. The first column has been acquired on a MPP after 0 h weathering, (a,d) , the second on a MPP after 1200 h (b,e), and on a MPP after 3600 h (c, f). The top row shows images with a scan area of 3x3 μm^2. The bottom row shows the ultrastructure of the particles as indicated by the red squares with scan areas of 1x1 μm^2.

The corresponding surface roughness values to Figure S20 a-c are given in Table S4 below.

Table S4: Roughness evaluation corresponding to Fig. S20 a, b, and c from 3 x 3 μm^2 AFM images. R_a is the arithmetic average of the absolute surface height deviations from the mean line and R_q is the root-mean-square average of the profile height deviations from the mean line.

Weathering Exposure Time (h)	R_a (nm)	R_q (nm)
0 h	22.8	117
1200 h	22.9	155
3200 h	35.9	148

8. Electrophoretic mobility of nanoparticle aggregates: Independence from aggregate size

Matthias B. Engelhardt, Takuya Sugimoto, Georg Papastavrou, and Motoyoshi Kobayashi*

"Electrophoretic mobility of nanoparticle aggregates: Independence from aggregate size"

Colloids and Surfaces A: Physicochemical and Engineering Aspects, **2024**, *703, Part 1, 135244.*

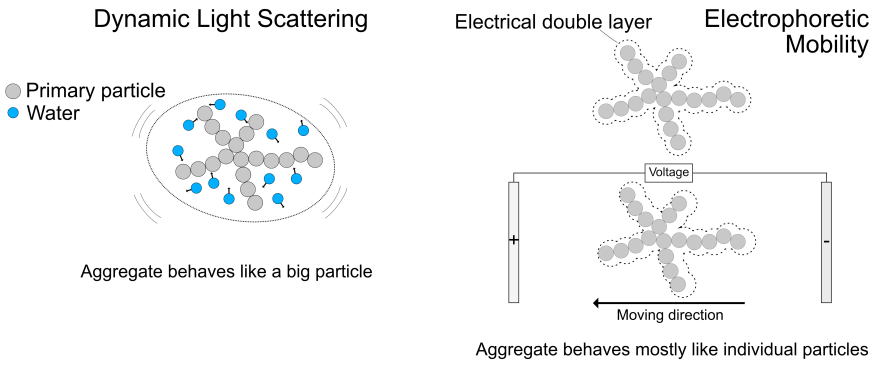

Reprinted with permission from:

"Electrophoretic mobility of nanoparticle aggregates: Independence from aggregate size", M. B. Engelhardt, T. Sugimoto, G. Papastavrou, M. Kobayashi, *Colloids and Surfaces A: Physicochemical and Engineering Aspects,* **2024**, *703, Part 1, 135244*.

DOI: 10.1016/j.colsurfa.2024.135244

Colloids and Surfaces A: Physicochemical and Engineering Aspects 703 (2024) 135244

Contents lists available at ScienceDirect

Colloids and Surfaces A: Physicochemical and Engineering Aspects

journal homepage: www.elsevier.com/locate/colsurfa

Electrophoretic mobility of nanoparticle aggregates: Independence from aggregate size

Matthias B. Engelhardt [a], Takuya Sugimoto [b], Georg Papastavrou [a], Motoyoshi Kobayashi [b,*]

[a] Physical Chemistry II, University of Bayreuth, Universitaetsstrasse 30, Bayreuth 95447, Germany
[b] Institute of Life and Environmental Sciences, University of Tsukuba, 1 Chome-1-1 Tennodai, Tsukuba, Ibaraki 305-8572, Japan

HIGHLIGHTS

- Primary particle diameter determines electrophoretic mobility of aggregates.
- Electrophoretic mobility is reliably used for zeta potentials of aggregates.
- Low double layer overlap between primary particles due to fractal-like structure.
- OBrien-White theory is suitable for fractal-like aggregates.
- Surfactant-free aggregation of fumed silicas.

GRAPHICAL ABSTRACT

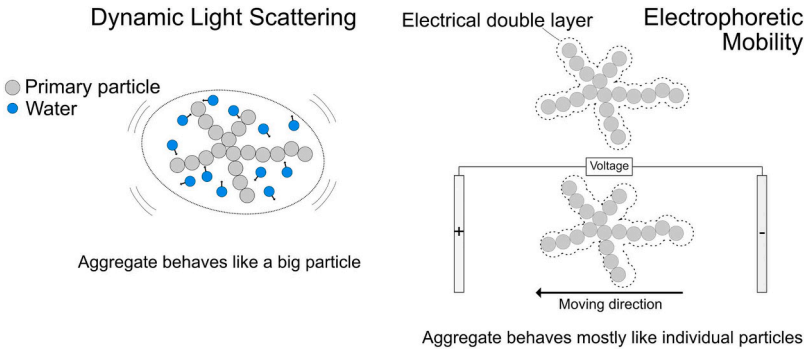

ARTICLE INFO

Keywords:
Zeta potential
Aggregation
Primary particle
Fractal

ABSTRACT

The zeta potential is a widely used parameter to categorize particle-particle interaction and aggregation. This parameter is often determined by the measurement of electrophoretic mobility. For single particles, various approximations allow a direct correlation between the mobility and the zeta potential. However, for aggregates, which are often found in the environment and in industrial applications, such approximations are less utilized. The relation between the size of aggregates and the resulting electrophoretic mobility has not yet been extensively explored and is often not considered. Here, we control the aggregate size additive-free of two fumed silica types with different primary particle diameters for comprehensive electrophoretic and dynamic light scattering measurements. We evaluate the influence of primary particle diameter and aggregate size on electrophoretic mobility. Our results reveal that the primary particle diameter is the defining factor for the electrophoretic mobility of the aggregates. This finding provides new insights into the electrokinetic behavior of aggregates and emphasizes the importance of primary particle properties in predicting colloidal interactions.

* Corresponding author.
E-mail addresses: matthias.engelhardt@uni-bayreuth.de (M.B. Engelhardt), sugimoto.takuya.gn@u.tsukuba.ac.jp (T. Sugimoto), georg.papastavrou@uni-bayreuth.de (G. Papastavrou), kobayashi.moto.fp@u.tsukuba.ac.jp (M. Kobayashi).

https://doi.org/10.1016/j.colsurfa.2024.135244

Available online 3 September 2024
0927-7757/© 2024 Elsevier B.V. All rights are reserved, including those for text and data mining, AI training, and similar technologies.

1. Introduction

Nano- and microparticles are ubiquitous in the environment [1–4], research [5–8], and in industrial applications [9–13]. The enhanced migration of insoluble chemicals adsorbed on the mobile colloidal particles such as clays [14,15], organic matter [16,17], and even air bubbles [18], known as colloid-facilitated transport, has been an issue in environmental science and technology. Nowadays, the fate and transport of engineered nanomaterials and micro-/nano-plastics are also concerned [1, 19–22]. For these matters, understanding aggregation and dispersion in colloidal suspension is a key problem.

The aggregation and dispersion of colloidal particles are strongly affected by the surface charge of particles. The addition of electrolytes induces aggregation due to the screening of surface charge [23]. The salt-induced aggregation is characterized by the existence of a critical coagulation concentration (CCC), which divides the fast aggregation regime and slow aggregation regime [24–26]. In the former regime, the electric double layer (EDL) repulsion is negligible, while in the latter regime, the EDL repulsion inhibits aggregation. The aggregation and dispersion of charge-stabilized colloidal particles are well-described by the Derjaguin-Landau-Verwey-Overbeek (DLVO) theory [27–29]. The relationship between critical coagulation ionic strength (CCIS) and the surface charge density predicted by the DLVO theory agrees well with the experimental data of CCIS and the electrokinetic surface charge density. The latter is evaluated from the zeta potential through the theory of EDL for solid polystyrene spheres as well as porous carbon nanohorns and allophane [24–32].

The zeta potential is usually obtained from the measured electrophoretic mobility (EPM) by one of the well-established electrokinetic theories [33–35]. So far, most of the widely used electrokinetic theories assume that a particle is a solid sphere or plate. Around CCC, however, the salt concentration is generally high, and the aggregation of colloidal particles can occur. Also, particles found in nature and industrial applications are often present in the form of colloidal aggregates [36,37]. Among these colloidal materials, fumed silica has gained significant attention due to its unique properties and versatility. Fumed silica aggregates are widely utilized because of their high surface area [38], thermal stability [39], and mechanical strength of composite materials [40].

It is reasonable to suppose that there are limitations to the deduction of the zeta potential due to the existence of aggregates, which are not considered in the prevalent electrokinetic theories. Sophisticated theories are now available and applied for rod-like particles [41,42], particles with hydrodynamic slip [43–45], and so-called soft particles with ions and fluid-penetrable regions [41,46,47]. Nevertheless, so far only theoretical studies have been reported for the EPM of aggregates or swarms of particles [48–50]. Miller et al. [48] and Levine and Neale [49] used the cell model, which, however, cannot take the structure of actual fractal-like aggregates into account. Coelho et al. [50] discussed the EPM of fractal objects with only the condition where the Debye length and the radius of the particle are the same. In this situation, we need to experimentally and systematically clarify if the aggregation would affect the EPM.

In order to unveil the effect of aggregation on EPM, we decided to measure the EPM of aggregates as a function of the size of aggregates. In this study, we focus on the controlled preparation of differently sized fumed silica aggregates to investigate the relationship between their structural characteristics and electrophoretic mobility. We employ two distinct types of fumed silica, each characterized by different primary particle diameters, to create a variety of aggregate sizes. This approach allows us to systemically investigate the impact of primary particle diameter and aggregate size on the electrophoretic mobility of aggregates. Our findings reveal a critical insight: the primary particle diameter, rather than the aggregate size, predominantly determines the electrophoretic mobility of fumed silica aggregates. These findings support that the EPM around CCC can be reliably applied, even if aggregates are present. This observation challenges the conventional emphasis on aggregate size as the primary determinant of colloidal behavior and highlights the importance of primary particle properties.

2. Material and methods

2.1. Materials

Pure water (Elix Advantage 5, MILLIPORE, Merck, Tokyo, Japan) was used for all solutions and suspensions. Analytic grade hydrochloric acid (JIS special grade, Fujifilm Wako Pure Chemical Corporation Ltd., Osaka, Japan), potassium hydroxide (JIS special grade, Fujifilm Wako Pure Chemical Corporation Ltd., Osaka, Japan), and potassium chloride (JIS special grade, Fujifilm Wako Pure Chemical Corporation Ltd., Osaka, Japan) were used for the preparation of measurement and aggregation solutions. Two different types of amorphous fumed silica powder were investigated: Aerosil 50 (NIPPON AEROSIL CO., LTD., Tokyo, Japan) and Aerosil 200 (NIPPON AEROSIL CO., LTD., Tokyo, Japan) which were kindly donated from the manufacturer.

Different sizes of Aerosil 50 and Aerosil 200 aggregates were manufactured with different parameter combinations of the pH, ionic strength, ultrasonication time and -temperature (ASU-10D, AS ONE Corporation, Osaka, Japan) as well as centrifugation time and -speed (3520, KUBOTA Corporation, Tokyo, Japan). Centrifugations were carried out at 293 K. A flow chart of the production process is shown in Fig. A1.

2.2. Methods

A Zetasizer Nano ZS (Malvern Panalytical Ltd., Malvern, UK) was utilized for measurements of the hydrodynamic diameter d_H via dynamic light scattering (DLS) and the EPM via electrophoretic light scattering (ELS). DLS was carried out with polystyrene cuvettes (AS One Corporation, Osaka, Japan) and the back scatter detector enabled. Folded capillary cells (Malvern Panalytical Ltd., Malvern, UK) were used for ELS. The EPM was investigated as a function of the pH in a range between pH 2 and pH 12. The KCl concentration was set in a range between 10^{-3} mol L^{-1} and 10^{-2} mol L^{-1}. The pH of the Aerosil suspensions was surveyed with a pH electrode (LAQUAtwin-pH-22, HORIBA Scientific, Kyoto, Japan). All the solutions and suspensions were degassed under reduced pressure before use. All measurements were carried out at 298 K.

Transmission Electron Microscopy (TEM) was performed with a JEM-2200FS (JEOL Ltd., Tokyo, Japan). A drop of 0.1 wt% Aerosil suspension was placed on a copper TEM grid with a mesh size of 200 (Plano GmbH, Wetzlar, Germany) and dried at 293 K. The prepared grid was coated with a thin carbon film before use.

3. Theory

3.1. Charging model

The 1-pK basic Stern model is utilized to evaluate the surface charge density σ and diffuse layer potential ψ_d as a function of pH and ionic strength [51,52]. The protonation/deprotonation equilibrium of surface SiOH groups determines the surface charge of silica as described by the following reaction:

$$\mathrm{SiOH} \leftrightarrows \mathrm{SiO^-} + \mathrm{H^+} \tag{1}$$

The mass action law governs the site densities of the surface groups Γ_{SiOH} and Γ_{SiO^-}:

$$\frac{\Gamma_{\mathrm{SiO^-}}\ a_{\mathrm{H}}}{\Gamma_{\mathrm{SiOH}}} = K\exp\left(\frac{e\psi_0}{kT}\right) \tag{2}$$

where a_H denotes the activity of protons (with pH = -$\log_{10}$ a_H), K is the

intrinsic equilibrium constant (with pK = -$\log_{10}$ K), e is the elementary charge, ψ_0 represents the surface potential, k is the Boltzmann constant, and T is the temperature. The total number density of these sites is given by:

$$\Gamma_0 = \Gamma_{SiOH} + \Gamma_{SiO^-} \tag{3}$$

Consequently, the surface charge density is defined as

$$\sigma = -e\Gamma_{SiO^-} \tag{4}$$

The surface charge density is associated with the potential drop across the Stern layer, expressed as

$$\sigma = C_s(\psi_0 - \psi_d) \tag{5}$$

where C_s denotes the capacitance of the Stern layer and ψ_d represents the potential at the origin of the diffuse layer. The diffuse layer potential ψ_d/ surface charge density σ relationship is obtained by solving the Poisson-Boltzmann (PB) equation for small particles with an arbitrary surface potential and a symmetric 1:1 electrolyte with $z = 1$ [53]:

$$\sigma = \frac{2\varepsilon_r\varepsilon_0\kappa kT}{e}\sinh\left(\frac{e\psi_d}{2kT}\right) \times\left[1+\frac{1}{\kappa a}\frac{2}{\cosh^2(e\psi_d/4kT)}+\frac{1}{(\kappa a)^2}\frac{8\ln[\cosh(e\psi_d/4kT)]}{\sinh^2(e\psi_d/2kT)}\right]^{1/2} \tag{6}$$

Here, ε_r is the relative permittivity of the medium, ε_0 is the permittivity of free space, and κ is the Debye-Hückel parameter for a 1:1 symmetrical electrolyte of ionic strength I:

$$\kappa = \left(\frac{2e^2N_AI}{\varepsilon_r\varepsilon_0kT}\right)^{1/2} \tag{7}$$

where N_A is Avogadrós constant. Eq. 6 is valid for $\kappa a \geq 1$ which is approximately true for most scenarios in this work. Solving the PB potential distribution around a small particle in 1:1 electrolyte solution, the potential distribution $\psi(r)$ is gained [54]:

$$\psi(r) = \frac{2kT}{e}\ln\left[\frac{(1+Bs)\left(1+\frac{Bs}{2\kappa a+1}\right)}{(1-Bs)\left(1-\frac{Bs}{2\kappa a+1}\right)}\right] \tag{8}$$

with r = distance from the center of a sphere, and

$$B = \frac{\left(\frac{2\kappa a+1}{\kappa a+1}\right)\tanh\left(\frac{e\psi_d}{4kT}\right)}{1+\left\{1-\frac{2\kappa a+1}{(\kappa a+1)^2}\tanh^2\left(\frac{e\psi_d}{4kT}\right)\right\}^{1/2}} \tag{9}$$

$$s = \frac{a}{r}\exp(-\kappa(r-a)) \tag{10}$$

The relative error of Eq. 8 is less than 1 % for $\kappa a \geq 1$ [54]. In this study, the term $(r-a)$ describes the distance between the particle surface and slipping plane x_s. The zeta potential ζ is defined as the electrical potential at the slipping plane, which is the boundary where the relative velocity of the solvent to the particle is zero. Consequently, ζ does not equal the diffuse layer potential ψ_d when the position of the slipping plane is displaced from the particle surface. In such cases, when $(r\text{-}a) = x_s$ in Eq. 10, Eq. 8 can be written as

$$\zeta = \frac{2kT}{ze}\ln\left[\frac{(1+Bs)\left(1+\frac{Bs}{2\kappa a+1}\right)}{(1-Bs)\left(1-\frac{Bs}{2\kappa a+1}\right)}\right] \tag{11}$$

3.2. Electrophoretic mobility

The electrophoretic mobility (EPM) is calculated from ζ. For large values of κa, say $\kappa a >> 1$, and moderate ζ, Smoluchowskíś formula can be used [35]:

$$\mu = \frac{\varepsilon_r\varepsilon_0\zeta}{\eta} \tag{12}$$

If $\kappa a < 1$, the Hückel equation is valid [55]:

$$\mu = \frac{2\varepsilon_r\varepsilon_0\zeta}{3\eta} \tag{13}$$

Very small or very large κa as well as low ζ allow to neglect relaxation effects of the double layer [56]. In contrast, if $|\zeta| < 40$ mV and for arbitrary κa, the Ohshima-Henry equation [34] can be used:

$$\mu = \frac{2\varepsilon_r\varepsilon_0\zeta}{3\eta}\left[1+\frac{1}{2(1+2.5/[\kappa a\{1+2\exp(-\kappa a)\}])^3}\right] \tag{14}$$

If ζ is high, say $|\zeta| > 75$ mV, numerical calculations based on the standard electrokinetic theory of OBrien and White [33] can be performed with a computer program from Bradshaw et al. [57]. In this study, the mean radius of primary particles is used as parameter a, which is needed for the computation with the equations above.

4. Results and discussion

Firstly, the microscopic structure of Aerosil 50 and Aerosil 200 is investigated with transmission electron microscopy (TEM). Fig. 1(a) and (b) show exemplary Aerosil 50 and Aerosil 200 aggregates, respectively.

The aggregates consist of individual small particles to which is referred as primary particles (PP). The structure of the aggregates is irregular and fractal-like [58]. The shape of the PP is mostly roughly circular. Some PPs do not show clear boundaries towards their neighbors. PP diameters of Aerosil 50 appear to be bigger than those of Aerosil 200. In contrast to the PP diameters d_{PP}, the hydrodynamic aggregate diameters d_H are determined by DLS. Table 1 compares d_H, d_{PP}, and the specific surface area (SSA) for both Aerosil types.

d_{PP} evaluation is performed with the software ImageJ [59] and the line-tool from TEM images. On the one hand, d_{PP} for Aerosil 50 is (24.9 ± 0.5) nm and in excellent agreement with diameters from TEM reported by Wiemann et al. [60]. On the other hand, d_{PP} of Aerosil 200 is determined as (10.8 ± 0.2) nm and in good agreement with the stated d_{PP} of 12 nm by the manufacturer Evonik. d_H is bigger for Aerosil 50 than for Aerosil 200, which is in line with the TEM micrographs (cf. Fig. 1, Fig. A2, and Fig. A3). While an aggregate concentration of 0.1 wt % is rather high, multiple scattering effects are negligible from Fig. A4 depicting similar intensity distributions and correlograms of Aerosil 50 and Aerosil 200 at 0.01 wt%, 0.1 wt%, and 0.2 wt%. The *SSA* of both Aerosil types is taken from the manufacturerś product specification sheets. All calculations of charging and electrokinetic models used in the following sections are based on d_{PP}.

The EPM was measured as a function of the KCl concentration to chart the electrokinetic properties of Aerosil 50 and Aerosil 200 in different salinities, as shown in Fig. 2(a) and (b), respectively.

Aerosil 50 and Aerosil 200 generally show similar trends. The magnitude of the EPM decreases with increasing ionic strength in an acidic environment (cf. Fig. 2(a) + (b)). However, Aerosil 50 (a) shows higher mobilities in magnitude compared to Aerosil 200 (b). The magnitude of the EPM of Aerosil 50 is also higher in the alkaline regime while the EPM is overall higher in alkaline environments than in acidic ones. We attribute the smaller EPM of Aerosil 200 to the smaller d_{PP} and, thus, stronger retardation effects of the EDL [33,61]. Fig. 2 depicts a trend towards higher magnitudes of the EPM in alkaline media with increasing ionic strength, whereas this trend is most pronounced with Aerosil 50. This trend can be also rationalized by the standard

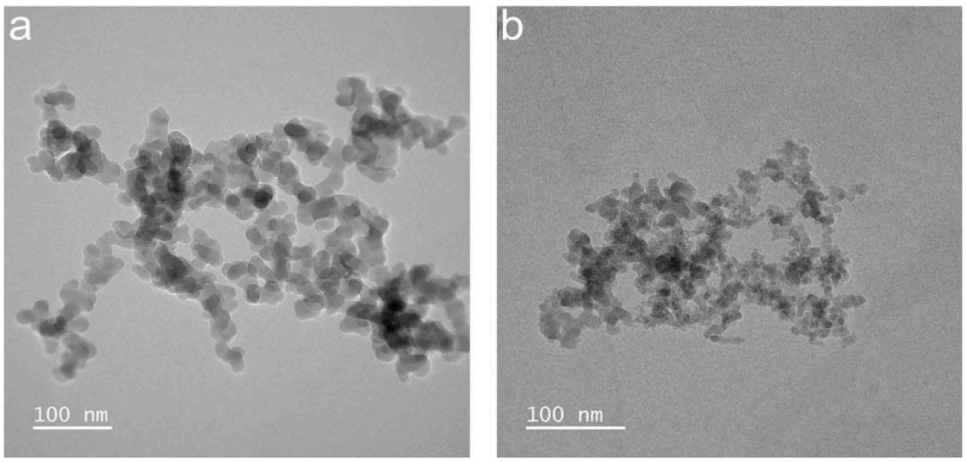

Fig. 1. : TEM images of Aerosil 50 (a) and Aerosil 200 (b). More images are shown in Fig. A2 and A3, respectively.

Table 1
Dry-state primary particle diameters d_{PP} from TEM, hydrodynamic diameters d_H of aggregates from DLS at a solid concentration of 0.1 wt%, corresponding numbers of measured primary particles N, and the respective specific surface areas (SSA) of Aerosil 50 and Aerosil 200 fumed silica. d_H is shown with standard deviations while d_{PP} is with standard errors of the mean. The diameter evaluation was performed based on the TEM micrographs shown in Fig. 1, Fig. A2, and Fig. A3.

	d_{PP} (nm)	d_H (nm)	N	SSA ($m^2\ g^{-1}$)
Aerosil 50	24.9 ± 0.5	328.2 ± 4.6	138	~50
Aerosil 200	10.8 ± 0.2	184.3 ± 1.0	133	~200

electrokinetic theory by OBrien and White [33]. Strongly charged particles show EPM maxima in magnitude as a function of the ionic strength as previously demonstrated by Antonietti and Vorweg [62] and Borkovec et al. [63].

Given these considerations, it is crucial to understand how variations in the pH influence the electrokinetic behavior under a fixed ionic strength. The EPM is investigated as a function of the pH in a range between pH 2 and pH 12 while the ionic strength is kept constant at $I = 10^{-2}$ mol L^{-1} as shown in Fig. 3.

Both Aerosil types show no EPM at pH < 5. In the neutral to alkaline regimes, the EPM is distinctly different. The magnitude of the EPM increases more for Aerosil 50 at any given pH increment than for Aerosil 200. This leads to an alkaline EPM plateau at pH > 8 of roughly −4 $m^2\ V^{-1}s^{-1}$ for Aerosil 50 whereas Aerosil 200 exhibits roughly −3 $m^2\ V^{-1}s^{-1}$.

The EPM as a function of the pH is modeled by Eqs. 12, 13, 14, and numerical calculations of the OBrien-White theory and 1-pK basic Stern model. The 1-pK basic Stern model with parameters from Kobayashi et al. [64] is used to calculate ζ as input variable for the EPM. The parameters are $\Gamma_{SiO^-} = 8 \times 10^{18}\ m^{-2}$, pK = 7.5, $x_s = 0.5$ nm for Aerosil 50 and $x_s = 1.0$ nm for Aerosil 200, $C_{St} = 2.9\ F\ m^{-2}$, $I = 10^{-2}$ mol L^{-1}, and $T = 298$ K. The OBrien-White theory reflects the overall trend for both Aerosil types reasonably well, which indicates that the EPM of fumed silica aggregates is determined by the EPM of the primary particle influenced by double layer polarization. The result partly agrees with the claim by Levine and Neale [49]. That is, they claim the EPM of a swarm of particles is the same as that of single particles at low volume fractions, where the overlapping of the diffuse double layers is weak, although they neglect the fractal-like structure and the double layer polarization. This agreement is probably because the overlap of diffuse double layers within the fractal-like fumed silica is not significant.

The distances x_s are within the reported values [45,63,64]. However, the $x_s = 1$ nm is rather large, compared to the size of water molecules. To rationalize this larger x_s, we assume a soft hairy or gel-like layer of poly (silicilic acid) chains at the surface of silica nanoparticles [64]. The influence of this hairy layer on the EPM is highest in the alkaline regime due to deprotonated silanol groups, which cause repulsive forces

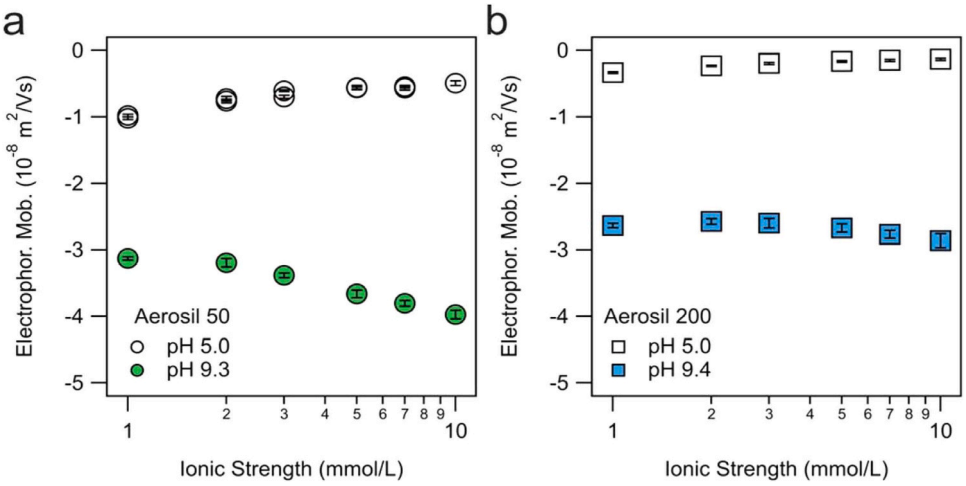

Fig. 2. : Electrophoretic mobilities of (a) Aerosil 50 and (b) Aerosil 200 aggregates in acidic and alkaline environments at ionic strengths between 10^{-3} mol L^{-1} and 10^{-2} mol L^{-1}. The solid concentration is 0.1 wt%.

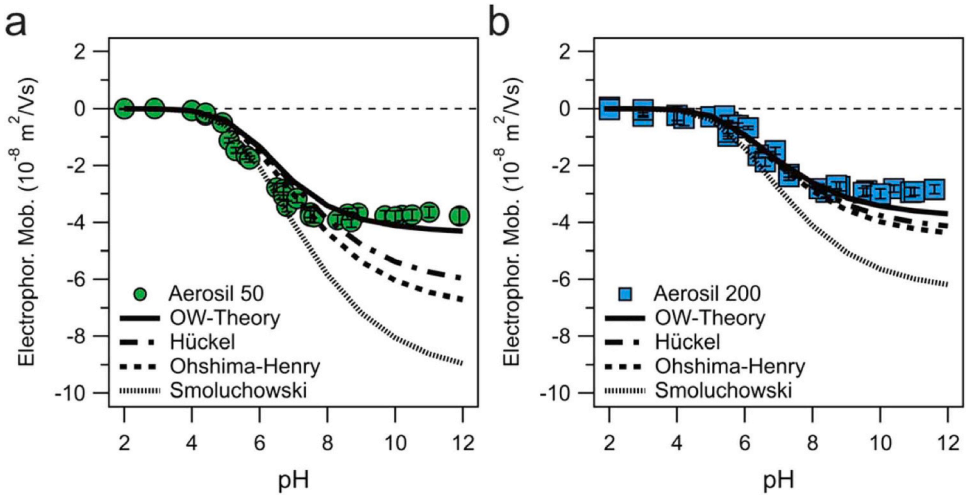

Fig. 3. : Electrophoretic mobilities of Aerosil 50 (a) and Aerosil 200 (b) aggregates from the respective stock suspensions at $I = 10^{-2}$ mol L^{-1} and an aggregate concentration of 0.1 wt% as a function of the pH. Solid lines are calculated following the OW(O'Brien-White)-Theory, dash-dot lines are calculated from the Hückel equation, dashed lines are based on the Ohshima-Henry equation, and broken lines are from the Smoluchowski equation.

between the poly(silicilic acid) chains [65]. The OBrien-White theory does not consider a soft permeable polymer-like interface, and thus, the model deviates from the experimental results. Moreover, d_{PP} of Aerosil cannot be considered ideally spherical, which is a prerequisite for this theory.

Considering these limitations, the OBrien-White theory fits the data well. The Hückel equation (Eq. 13) and the Ohshima-Henry equation (Eq. 14) fail to describe the trend of the EPM for Aerosil 50 (cf. Fig. 3a) at pH > 5 since ζ strongly exceeds moderate ζ. However, both models fit the trend of Aerosil 200 (cf. Fig. 3b) until pH 8 due to the significantly lower magnitude of ζ compared to Aerosil 50. As expected, the Smoluchowski equation (Eq. 12) fails to describe the observed trends for Aerosil aggregates at pH > 5. This model is only valid for $\kappa a >> 1$ (say, $\kappa a > 20$) and moderate ζ, which is not fulfilled. It should be noted that the theoretical calculation of ζ, which is used for the calculation of the EPM by the electrokinetic theories, can also be performed for non-spherical particles, as shown by Ohshima [54]. The results of the EPM of elongated colloids have been obtained [42,66,67]. According to the irrotational-flow model [68], the Smoluchowski equation is valid for arbitrarily shaped colloids in the thin-double-layer limit at low ζ. At moderate to high ζ and thick double layers, the EPM of non-spherical particles is anisotropic. Yariv and Schnitzer compiled various approaches for this case [69].

Because both Aerosil types exhibit a distinctly different EPM plateau in alkaline environments, we want to investigate the dependency of the EPM on the aggregate diameter. We prepared various sizes of aggregates from chemically identical Aerosil 50 and Aerosil 200 powders. Control over aggregate sizes was achieved without the use of surfactants or additives as described in the methods section. All produced aggregates have a polydispersity < 0.3 from DLS (cf. Fig. A5). Fig. 4 shows the EPM of Aerosil aggregates on the hydrodynamic diameter.

Aerosil 50 and Aerosil 200 exhibit distinctly different EPMs in accordance with the respective alkaline plateaus shown in Fig. 3. The EPM is independent of the hydrodynamic aggregate diameter. The mean mobilities are listed in Table 2.

We conclude that the only differentiating factors between the two Aerosils are d_{PP}, probably surface roughness, shape irregularity of primary particles (cf. Fig. 1), and a soft hairy layer of poly(silicilic acid) at the primary particle interfaces [64] and not the hydrodynamic diameter. However, the effect of the hairy layer hypothesis is linked to d_{PP}. Ohshima [41] and Gopmandal and Duval [70] showed that the ratio between d_{PP} and the soft polymeric coating is crucial. The thicker the hairy layer is relative to d_{PP}, the smaller the EPM becomes. This finding

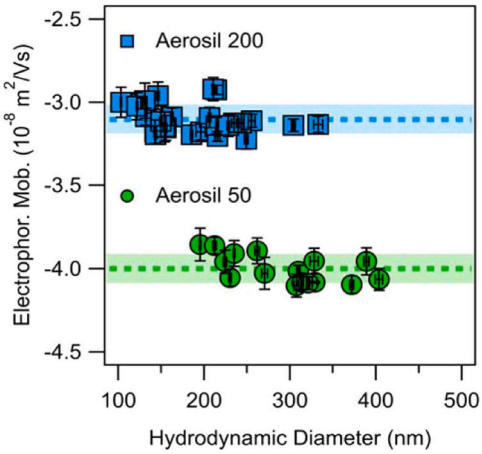

Fig. 4. : Electrophoretic mobilities of Aerosil 50 and Aerosil 200 aggregates of various hydrodynamic diameters in $I = 10^{-2}$ mol L^{-1} and in the alkaline mobility plateau. Dashed lines represent the mean values, and the solid area shows the respective standard deviations.

Table 2
EPM of Aerosil 50 and Aerosil 200 aggregates at various hydrodynamic diameters d_H including standard deviations.

	Aerosil 50	Aerosil 200
EPM (10^{-8} m^2 $V^{-1}s^{-1}$)	−4.00 ± 0.09	−3.10 ± 0.09

agrees with the smaller EPM of Aerosil 200 compared to Aerosil 50. The roughness of primary particles is closely linked to the synthesis parameters of fumed silica [71] and, in consequence, may be related to d_{PP} as well. These parameters can contribute to shifts of the shear plane away from the surface [56]. To account for the shear plane displacement, we use $x_s = 0.5$ nm for Aerosil 50 and $x_s = 1.0$ nm for Aerosil 200 in our models shown in Fig. 3.

It should be emphasized that the EPM of fumed silica aggregates is determined by the EPM of the primary particle and not by the hydrodynamic diameter of aggregates, probably due to the weak overlap of double layers in the fractal-like fumed silica. Colloidal aggregates are, in general, fractal-like [72]. Therefore, this result can be generalized to the EPM of aggregates of colloid/nanoparticles, and thus, the EPM around

CCC with co-existing aggregates is reasonably available. Future studies are expected for highly-packed aggregates with significant overlapping of double layers in the aggregates.

5. Conclusion

This study systematically investigated the relationship between the size of primary particles as well as aggregates and the electrophoretic mobility of fumed silica aggregates. We prepared differently sized aggregates of low polydispersity from two distinct types of fumed silica, each characterized by unique primary particle diameters. The aggregation was performed without the use of surfactants or additives to conserve the original surface chemistry. Our analysis revealed that the electrophoretic mobility of these aggregates is primarily determined by the primary particle diameter rather than the aggregate size. This finding is similar to the suggestion by Levine and Neale [49] that the EPM of a swarm of particles is the same as that of a single particle at low volume fractions. The standard electrokinetic theory by OBrien and White with the 1-pK basic Stern model using the size of primary particles successfully describes the electrophoretic mobility as a function of the pH for both particle types. These results suggest that the EPM for suspensions with possible aggregation at relatively high ionic strength can be used for the evaluation of the zeta potential.

Fumed silica aggregates are known to possess a fractal-like structure that exposes most of the primary particle surface to the surrounding liquid, and the overlap of double layers is weak. The results reported here are of importance to many environmental samples, also of organic origin such as for the degradation of microplastics [73]. Future research should explore whether the relationship between primary particle diameter and electrophoretic mobility extends to, for example, densely packed spherical aggregates with comparatively low effective surface area.

Funding sources

The authors are thankful for the support from the Kurita Water and Environment Foundation (24A024), the JSPS KAKENHI (24K01875, 24K17982), the Deutsche Forschungsgesellschaft (DFG) within the collaborative research center 1357: “Microplastics – Understanding the mechanisms and processes of biological effects, transport and formation: From model to complex systems as a basis for new solutions” (391977956; SFB 1357), and the Elite Network of Bavaria.

CRediT authorship contribution statement

Matthias B. Engelhardt: Writing – review & editing, Writing – original draft, Visualization, Methodology, Investigation, Formal analysis. **Takuya Sugimoto:** Writing – review & editing, Software, Methodology. **Georg Papastavrou:** Writing – review & editing, Funding acquisition. **Motoyoshi Kobayashi:** Writing – review & editing, Supervision, Resources, Conceptualization.

Declaration of Competing Interest

The authors declare that they have no known competing financial interests or personal relationships that could have appeared to influence the work reported in this paper.

Data Availability

Data will be available upon reasonable request.

Acknowledgments

The authors thank the Keylab for Optical and Electron Microscopy of the Bavarian Polymer Institute (BPI). They thank Nina Volk for the corresponding measurements. M.B.E. acknowledges the Elite Network of Bavaria (ENB) through the study program “Macromolecular Science” and the University of Bayreuth Graduate School for their ongoing support. The authors are thankful to Prof. Adachi at the University of Tsukuba for his support.

Appendix A. Supporting information

Supplementary data associated with this article can be found in the online version at doi:10.1016/j.colsurfa.2024.135244.

References

[1] J.N. Möller, M.G.J. Löder, C. Laforsch, Environ. Sci. Technol. 54 (4) (2020) 2078–2090, https://doi.org/10.1021/acs.est.9b04618.
[2] A. Cramer, J. Schmidtmann, P. Benard, A. Kaestner, M. Engelhardt, S. Peiffer, A. Carminati, Environ. Sci. Process Impacts 25 (6) (2023) 1094–1101, https://doi.org/10.1039/d3em00077j.
[3] A. Hakim, M. Kobayashi, J. Polym. Environ. 29 (6) (2021) 1921–1929, https://doi.org/10.1007/s10924-020-01985-4.
[4] S. Wieland, A.F.R.M. Ramsperger, W. Gross, M. Lehmann, T. Witzmann, A. Caspari, M. Obst, S. Gekle, G.K. Auernhammer, A. Fery, C. Laforsch, H. Kress, Nat. Commun. 15 (1) (2024) 922, https://doi.org/10.1038/s41467-024-45281-4.
[5] M. Hildebrandt, D. Pham Thuy, J. Kippenberger, T.L. Wigger, J.E. Houston, A. Scotti, M. Karg, Soft Matter 19 (37) (2023) 7122–7135, https://doi.org/10.1039/d3sm01062g.
[6] M. Karg, S. Wellert, S. Prevost, R. Schweins, C. Dewhurst, L.M. Liz-Marzán, T. Hellweg, Colloid Polym. Sci. 289 (5-6) (2011) 699–709, https://doi.org/10.1007/s00396-010-2327-2.
[7] A. Michna, Z. Adamczyk, M. Oćwieja, E. Bielańska, Colloid Surf. A 377 (1-3) (2011) 261–268, https://doi.org/10.1016/j.colsurfa.2011.01.021.
[8] A. Michna, M. Morga, Z. Adamczyk, K. Kubiak, Mater. Chem. Phys. 227 (2019) 224–235, https://doi.org/10.1016/j.matchemphys.2019.01.072.
[9] C. Götz, G.T. Lim, J.E. Puskas, V. Altstädt, J. Mech. Behav. Biomed. Mater. 39 (2014) 355–365, https://doi.org/10.1016/j.jmbbm.2014.08.008.
[10] W.J. Stark, P.R. Stoessel, W. Wohlleben, A. Hafner, Chem. Soc. Rev. 44 (16) (2015) 5793–5805, https://doi.org/10.1039/c4cs00362d.
[11] S. Dhawan, P. Sharma, S. Nanda, Nanocosmetics (2020) 141–169, https://doi.org/10.1016/b978-0-12-822286-7.00017-6.
[12] X. Hu, Q. Li, Z. Wu, S. Yang, Eng. Fract. Mech. 259 (2022) 108158, https://doi.org/10.1016/j.engfracmech.2021.108158.
[13] M. Moradi, R. Razavi, A.K. Omer, A. Farhangfar, D.J. McClements, Trends Food Sci. Technol. 120 (2022) 75–87, https://doi.org/10.1016/j.tifs.2022.01.012.
[14] D. Takács, T. Szabó, A. Jamnik, M. Tomšič, I. Szilágyi, Langmuir 39 (36) (2023) 12835–12844, https://doi.org/10.1021/acs.langmuir.3c01700.
[15] T. Lu, B.S. Gilfedder, H. Peng, G. Niu, S. Frei, Sci. Total Environ. 796 (2021) 148982, https://doi.org/10.1016/j.scitotenv.2021.148982.
[16] Q.V. Ly, T. Maqbool, Z. Zhang, Q. Van Le, X. An, Y. Hu, J. Cho, J. Li, J. Hur, Chemosphere 269 (2021) 128690, https://doi.org/10.1016/j.chemosphere.2020.128690.
[17] M. Kleber, I.C. Bourg, E.K. Coward, C.M. Hansel, S.C.B. Myneni, N. Nunan, Nat. Rev. Earth Environ. 2 (6) (2021) 402–421, https://doi.org/10.1038/s43017-021-00162-y.
[18] M. Lehmann, F.P. Häusl, S. Gekle, Micro Nanoplastics 3 (1) (2023) 6, https://doi.org/10.1186/s43591-023-00053-7.
[19] K. Bere, X. Xiong, S. Sáringer, G. Douglas, I. Szilagyi, J. Mol. Liq. 384 (2023) 122285, https://doi.org/10.1016/j.molliq.2023.122285.
[20] R. Dris, H. Imhof, W. Sanchez, J. Gasperi, F. Galgani, B. Tassin, C. Laforsch, Environ. Chem. 12 (5) (2015) 539, https://doi.org/10.1071/en14172.
[21] J. Zhang, S. Zhan, L.B. Zhong, X. Wang, Z. Qiu, Y.M. Zheng, J. Hazard. Mater. 443 (2023) 130130, https://doi.org/10.1016/j.jhazmat.2022.130130.
[22] M.R. Islam, B. Singh, F.A. Dijkstra, Biogeochemistry 160 (2) (2022) 145–158, https://doi.org/10.1007/s10533-022-00956-2.
[23] J.F.L. Duval, R.M. Town, H.P. van Leeuwen, J. Phys. Chem. C. 122 (30) (2018) 17328–17337, https://doi.org/10.1021/acs.jpcc.8b05168.
[24] G. Trefalt, I. Szilágyi, M. Borkovec, Colloid Polym. Sci. 298 (8) (2020) 961–967, https://doi.org/10.1007/s00396-020-04665-w.
[25] M. Galli, S. Sáringer, I. Szilágyi, G. Trefalt, Colloids Interfaces 4 (2) (2020) 20, https://doi.org/10.3390/colloids4020020.
[26] Y. Huang, A. Yamaguchi, T.D. Pham, M. Kobayashi, Colloid Polym. Sci. 296 (1) (2018) 145–155, https://doi.org/10.1007/s00396-017-4226-2.
[27] B. Derjaguin, Actra Physicochim. U. R. S. S. 10 (1939) 333–346, https://doi.org/10.1016/0079-6816(93)90010-s.
[28] B. Derjaguin, L. Landau, Actra Physicochim. U. R. S. S. 14 (1941) 633–662, https://doi.org/10.1016/0079-6816(93)90013-l.
[29] E.J. Verwey, J.T.G. Overbeek, J. Phys. Colloid Chem. 51 (3) (1947) 631–636, https://doi.org/10.1021/j150453a001.
[30] G. Trefalt, I. Szilagyi, G. Téllez, M. Borkovec, Langmuir 33 (7) (2017) 1695–1704, https://doi.org/10.1021/acs.langmuir.6b04464.
[31] K. Omija, A. Hakim, K. Masuda, A. Yamaguchi, M. Kobayashi, Colloid Surf. A 619 (2021) 126552, https://doi.org/10.1016/j.colsurfa.2021.126552.

[32] C. Takeshita, K. Masuda, M. Kobayashi, Colloid Surf. A 577 (2019) 103–109, https://doi.org/10.1016/j.colsurfa.2019.05.054.
[33] R.W. O'Brien, L.R. White, J. Chem. Soc., Faraday Trans. 2 74 (1978) 1607, https://doi.org/10.1039/f29787401607.
[34] H. Ohshima, J. Colloid Interface Sci. 168 (1) (1994) 269–271, https://doi.org/10.1006/jcis.1994.1419.
[35] M. von Smoluchowski, Handbuch der Elektrizität und des Magnetismus, J.A. Barth, Leipzig, 1921.
[36] Y. Fan, G.D. Fowler, M. Zhao, J. Clean. Prod. 247 (2020) 119115, https://doi.org/10.1016/j.jclepro.2019.119115.
[37] J. Buffle, K.J. Wilkinson, S. Stoll, M. Filella, J. Zhang, Environ. Sci. Technol. 32 (19) (1998) 2887–2899, https://doi.org/10.1021/es980217h.
[38] V.M. Gun'ko, I.F. Mironyuk, V.I. Zarko, E.F. Voronin, V.V. Turov, E.M. Pakhlov, E. V. Goncharuk, Y.M. Nychiporuk, N.N. Vlasova, P.P. Gorbik, O.A. Mishchuk, A. A. Chuiko, T.V. Kulik, B.B. Palyanytsya, S.V. Pakhovchishin, J. Skubiszewska-Zieba, W. Janusz, A.V. Turov, R. Leboda, J. Colloid Interface Sci. 289 (2) (2005) 427–445, https://doi.org/10.1016/j.jcis.2005.05.051.
[39] J. Tarrío-Saavedra, J. López-Beceiro, S. Naya, R. Artiaga, Polym. Degrad. Stab. 93 (12) (2008) 2133–2137, https://doi.org/10.1016/j.polymdegradstab.2008.08.006.
[40] A. Dorigato, M. D'Amato, A. Pegoretti, J. Polym. Res. 19 (6) (2012), https://doi.org/10.1007/s10965-012-9889-2.
[41] H. Ohshima, Electrical Phenomena at Interfaces and Biointerfaces. Fundamentals and Applications in Nano-, Bio-, and Environmental Sciences, 1, Wiley, Hoboken, 2012.
[42] Y. Sato, Y. Kusaka, M. Kobayashi, Langmuir 33 (44) (2017) 12660–12669, https://doi.org/10.1021/acs.langmuir.7b02742.
[43] P.P. Gopmandal, S. Bhattacharyya, H. Ohshima, Colloid Polym. Sci. 295 (10) (2017) 2077–2082, https://doi.org/10.1007/s00396-017-4181-y.
[44] H. Ohshima, Adv. Colloid Interface Sci. 272 (2019) 101996, https://doi.org/10.1016/j.cis.2019.101996.
[45] M. Kobayashi, Colloid Polym. Sci. 298 (10) (2020) 1313–1318, https://doi.org/10.1007/s00396-020-04716-2.
[46] N. Helfricht, E. Doblhofer, J.F.L. Duval, T. Scheibel, G. Papastavrou, J. Phys. Chem. C. 120 (32) (2016) 18015–18027, https://doi.org/10.1021/acs.jpcc.6b03957.
[47] S.K. Maurya, P.P. Gopmandal, H. Ohshima, J.F.L. Duval, J. Colloid Interface Sci. 558 (2020) 280–290, https://doi.org/10.1016/j.jcis.2019.09.118.
[48] N.P. Miller, J.C. Berg, and R. W. O'Brien, J. Colloid Interface Sci. 153 (1) (1992) 237–243, https://doi.org/10.1016/0021-9797(92)90315-d.
[49] S. Levine, G.H. Neale, J. Colloid Interface Sci. 47 (2) (1974) 520–529, https://doi.org/10.1016/0021-9797(74)90284-7.
[50] D. Coelho, J.-F. Thovert, R. Thouy, P.M. Adler, Fractals 05 (03) (1997) 507–522, https://doi.org/10.1142/s0218348x97000401.
[51] T. Hiemstra, W.H. Van Riemsdijk, G.H. Bolt, J. Colloid Interface Sci. 133 (1) (1989) 91–104, https://doi.org/10.1016/0021-9797(89)90284-1.
[52] T. Hiemstra, J.C.M. De Wit, W.H. Van Riemsdijk, J. Colloid Interface Sci. 133 (1) (1989) 105–117, https://doi.org/10.1016/0021-9797(89)90285-3.
[53] K. Makino, H. Ohshima, Langmuir 26 (23) (2010) 18016–18019, https://doi.org/10.1021/la1035745.
[54] H. Ohshima, T.W. Healy, L.R. White, J. Colloid Interface Sci. 90 (1) (1982) 17–26, https://doi.org/10.1016/0021-9797(82)90393-9.
[55] E. Hückel, Phys. Z. 25 (1924) 204–210.
[56] A. Michna, Adv. Colloid Interface Sci. 250 (2017) 95–131, https://doi.org/10.1016/j.cis.2017.09.004.
[57] B.H. Bradshaw-Hajek, S.J. Miklavcic, L.R. White, Langmuir 24 (9) (2008) 4512–4522, https://doi.org/10.1021/la703777g.
[58] F. Babick, K. Schießl, M. Stintz, Part. Syst. Charact. 29 (2) (2012) 104–115, https://doi.org/10.1002/ppsc.201000024.
[59] J. Schindelin, I. Arganda-Carreras, E. Frise, V. Kaynig, M. Longair, T. Pietzsch, S. Preibisch, C. Rueden, S. Saalfeld, B. Schmid, J.Y. Tinevez, D.J. White, V. Hartenstein, K. Eliceiri, P. Tomancak, A. Cardona, Nat. Methods 9 (7) (2012) 676–682, https://doi.org/10.1038/nmeth.2019.
[60] M. Wiemann, A. Vennemann, T.B. Schuster, J. Nolde, N. Krueger, Front. Public Health 10 (2022) 902799, https://doi.org/10.3389/fpubh.2022.902799.
[61] Y. Adachi, COCIS 24 (2016) 72–78, https://doi.org/10.1016/j.cocis.2016.06.003.
[62] M. Antonietti, L. Vorwerg, Colloid Polym. Sci. 275 (9) (1997) 883–887, https://doi.org/10.1007/s003960050161.
[63] M. Borkovec, S.H. Behrens, M. Semmler, Langmuir 16 (11) (2000) 5209–5212, https://doi.org/10.1021/la9916373.
[64] M. Kobayashi, F. Juillerat, P. Galletto, P. Bowen, M. Borkovec, Langmuir 21 (13) (2005) 5761–5769, https://doi.org/10.1021/la046829z.
[65] P.G. de Gennes, Macromolecules 13 (5) (1980) 1069–1075, https://doi.org/10.1021/ma60077a009.
[66] B. Katana, D. Takács, A. Szerlauth, S. Sáringer, G. Varga, A. Jamnik, F.D. Bobbink, P.J. Dyson, I. Szilagyi, Langmuir 37 (40) (2021) 11869–11879, https://doi.org/10.1021/acs.langmuir.1c01949.
[67] B. Katana, J. Baptista, R. Schneider, R.J. de Oliveira, I. Szilágyi, J. Phys. Chem. B 128 (28) (2024) 6957–6965, https://doi.org/10.1021/acs.jpcb.4c03193.
[68] F.A. Morrison, J. Colloid Interface Sci. 34 (2) (1970) 210–214, https://doi.org/10.1016/0021-9797(70)90171-2.
[69] E. Yariv, O. Schnitzer, J. Fluid Mech. 719 (2013) 7, https://doi.org/10.1017/jfm.2013.43.
[70] P.P. Gopmandal, J.F.L. Duval, COCIS 60 (2022) 101605, https://doi.org/10.1016/j.cocis.2022.101605.
[71] D.W. Schaefer, A.J. Hurd, Aerosol Sci. Tech. 12 (4) (1990) 876–890, https://doi.org/10.1080/02786829008959400.
[72] M.Y. Lin, H.M. Lindsay, D.A. Weitz, R.C. Ball, R. Klein, P. Meakin, Nature 339 (6223) (1989) 360–362, https://doi.org/10.1038/339360a0.
[73] N. Meides, T. Menzel, B. Poetzschner, M.G.J. Löder, U. Mansfeld, P. Strohriegl, V. Altstaedt, J. Senker, Environ. Sci. Technol. 55 (12) (2021) 7930–7938, https://doi.org/10.1021/acs.est.0c07718.

Supporting Information

Aggregate synthesis procedure

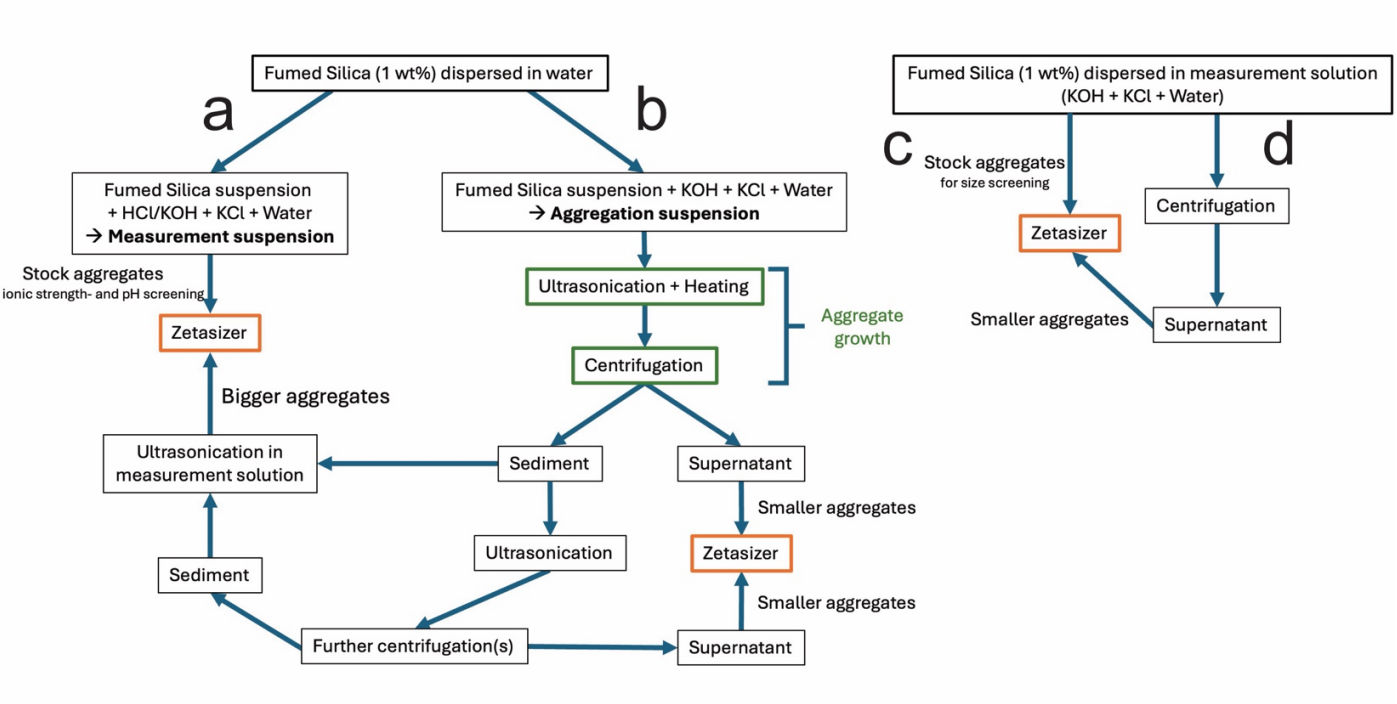

Fig. A1: Flow chart for the manufacturing of differently sized Aerosil aggregates. (a) shows the preparation of measurement suspensions and (b) aggregation suspensions from 1 wt% fumed silica in water. (c) depicts the production of stock aggregates for size screenings and (d) of smaller aggregates from fumed silica powder and electrolytes.

The flow chart outlines the process of synthesizing fumed silica aggregates, involving various steps of dispersion, aggregation and separation. Stock suspensions for pH- and ionic strength screenings are produced by diluting the stock suspension of 1 wt% Aerosil in water with the respective electrolytes for direct measurements (a). Path (b) shows the production route for bigger and smaller aggregates by sedimentation and taking the supernatant, respectively. Here, big and small aggregates can be produced from the same starting suspension at very high ionic strength for fast aggregation. Adjusting the ionic strength and pH is necessary after synthesis. Stock aggregates for size screenings are produced from fumed silica powder suspended in measurement solutions (c). A less laborious way to produce smaller aggregates is shown in (d) where the starting suspension is tailored to produce small aggregates in supernatants with the electrolyte environment suitable for measurements without the need to adjust the measurement solution afterward.

TEM micrographs of Aerosil 50 and Aerosil 200

Together with Fig. 1 (a), a total of 5 TEM micrographs of Aerosil 50 have been recorded and evaluated to calculate the corresponding mean diameter. The additional TEM micrographs are shown in Fig. A2:

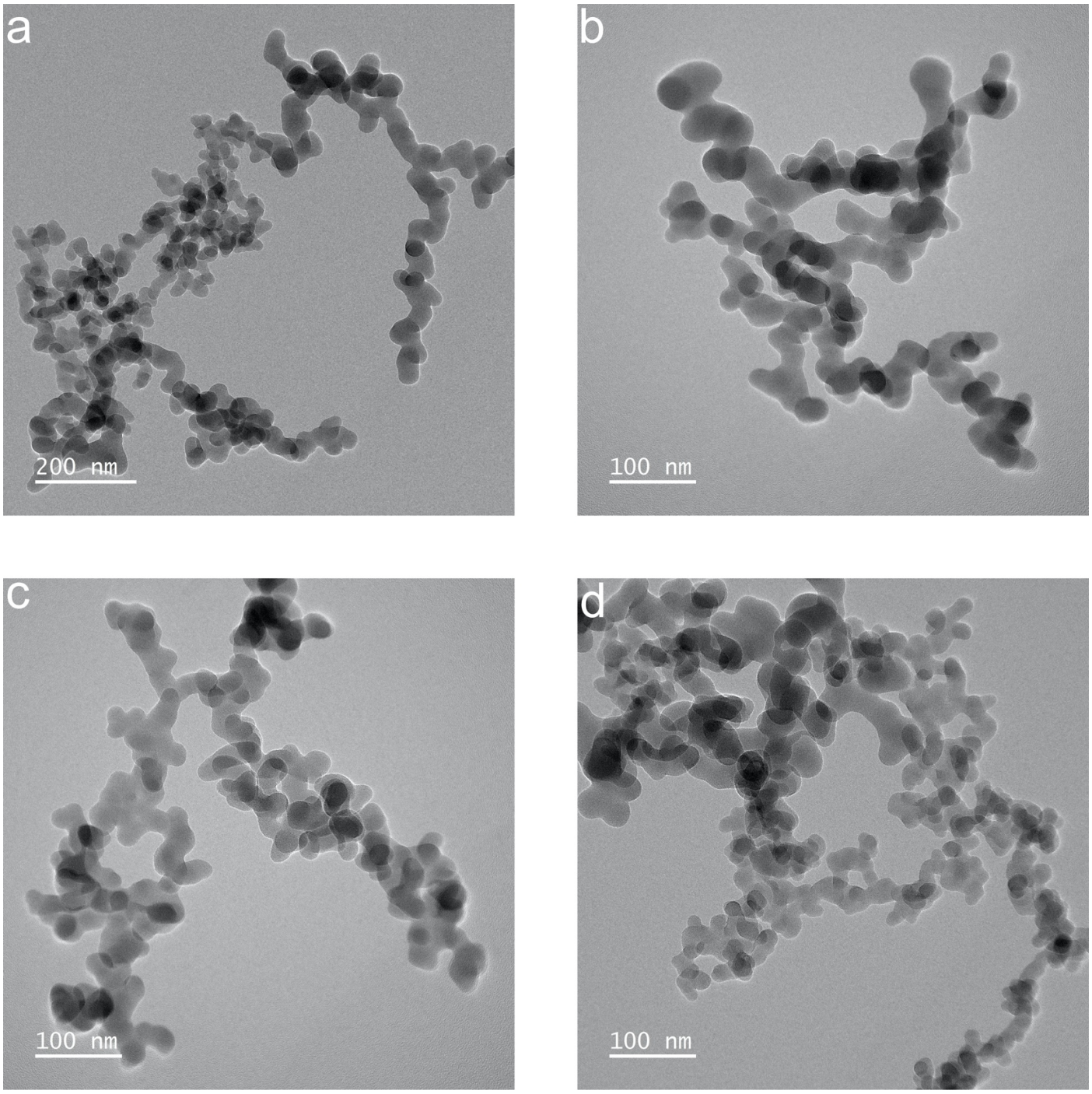

Fig. A2: TEM micrographs of Aerosil 50 aggregates.

Furthermore, a total of 11 additional TEM micrographs of Aerosil 200 in addition to Fig. 1 (b) have been recorded and evaluated. These TEM micrographs are shown in Fig. A3:

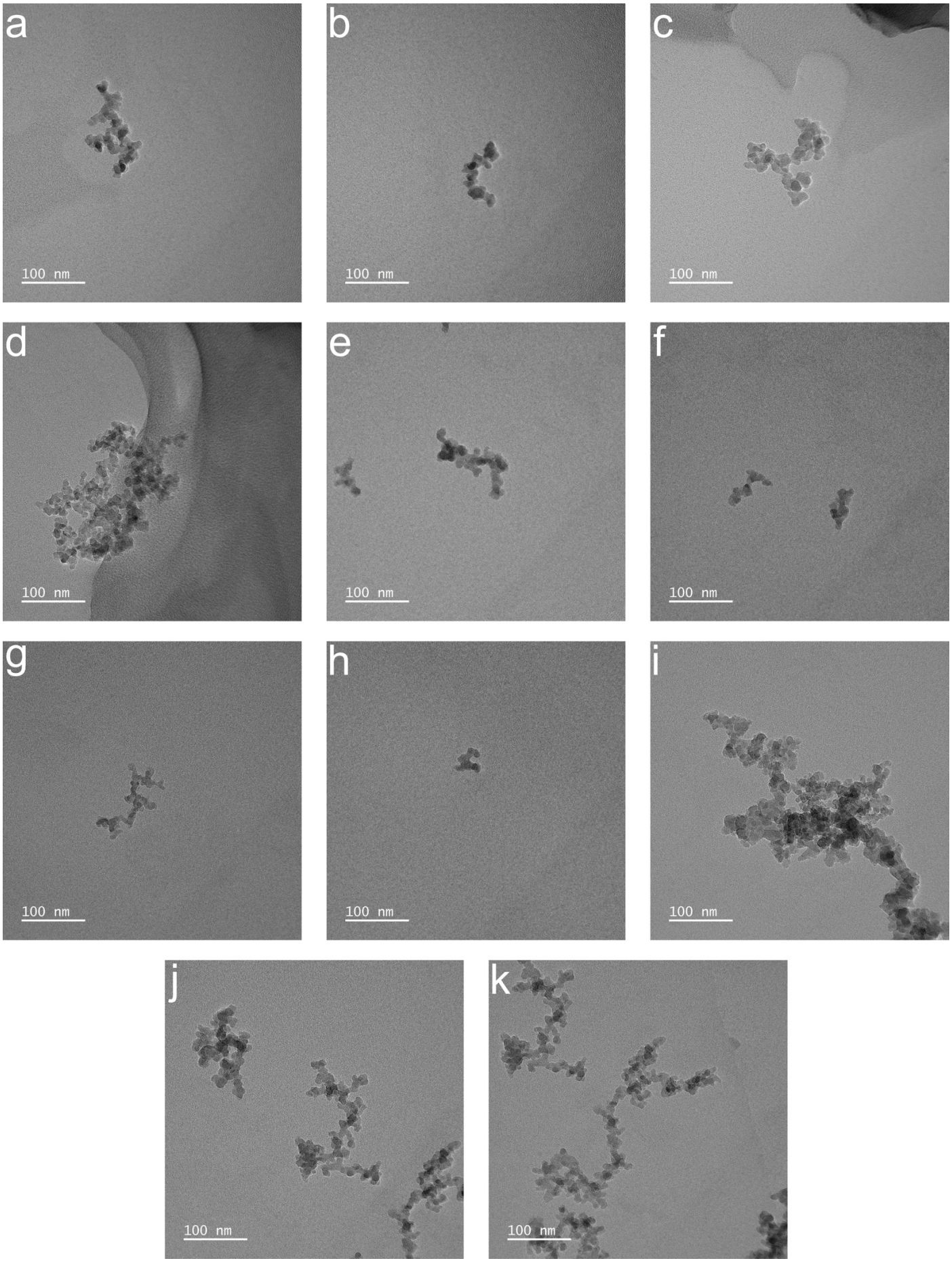

Fig. A3: TEM micrographs of Aerosil 200 aggregates.

DLS experiments to validate the chosen aggregate concentration

While the chosen aggregate concentration of 0.1 wt% in this work can be considered high for DLS and EPM measurements, Fig. A4 shows similar intensity distributions and correlograms for Aerosil 50 and Aerosil 200 at different aggregation concentrations below and above 0.1 wt%.

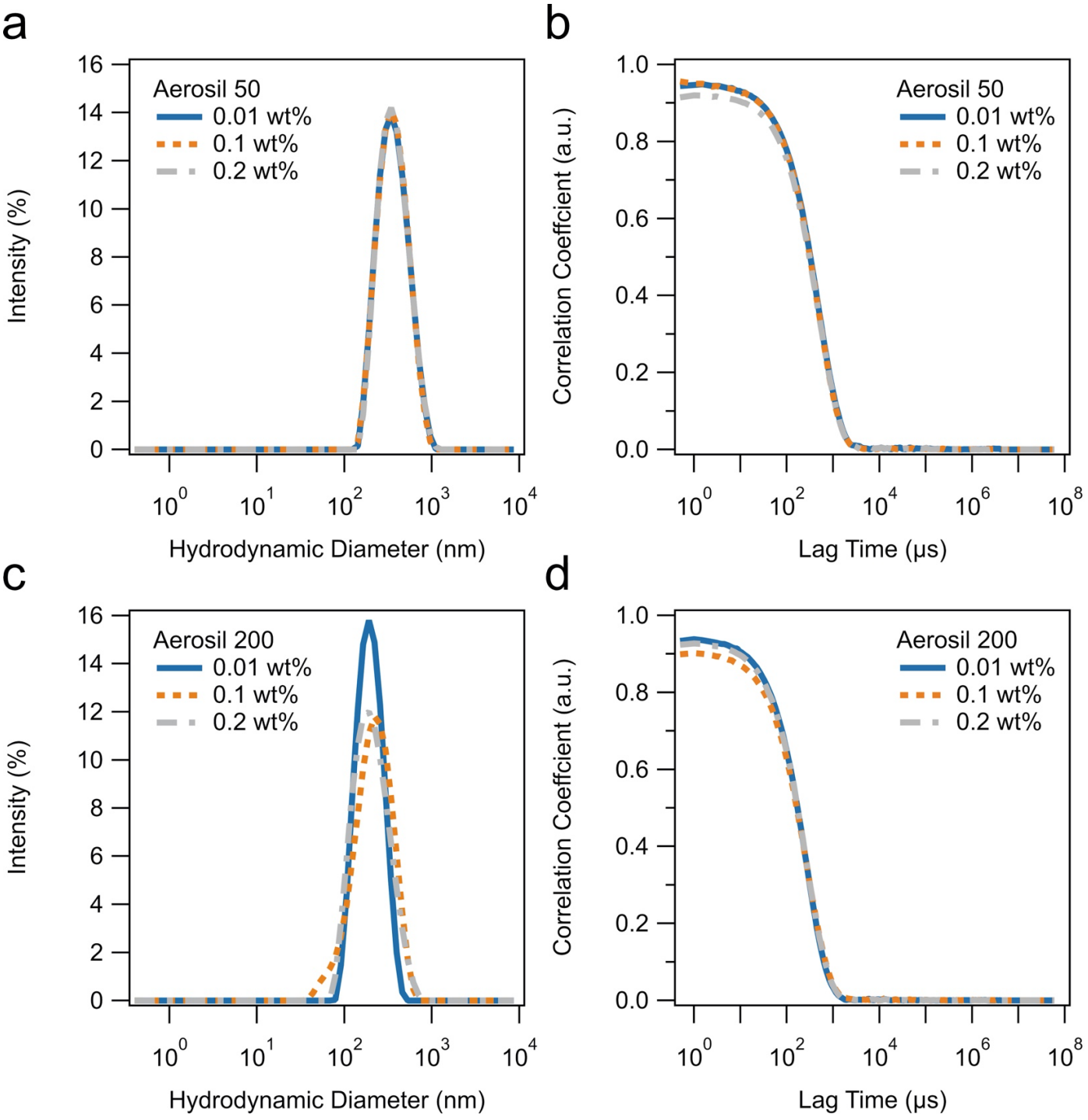

Fig. A4: Exemplary intensity distribution as a function of the hydrodynamic diameter for Aerosil 50 (a) and Aerosil 200 (c) at different aggregate concentrations and correlograms of different aggregate concentrations for Aerosil 50 (b) and Aerosil 200 (d).

Fig. A4 (a) and (b) show almost identical intensity distributions and correlograms, respectively, for Aerosil 50 at any given concentration. In the case of Aerosil 200, the concentrations of 0.1 wt% and 0.2 wt% show a slightly broader intensity distribution (cf. Fig. A4 c) compared to 0.01 wt%. However, this discrepancy is considered insignificant. Furthermore, the correlograms in Fig. A4 (d) of all investigated concentrations are very similar. These results show no indications of multiple scattering effects and validate the choice of the concentration of 0.1 wt% for the experiments presented in this study.

Polydispersities of produces Aerosil aggregates

The outlined aggregate production of Fig. A1 yields polydispersities < 0.3 shown in Fig. A5:

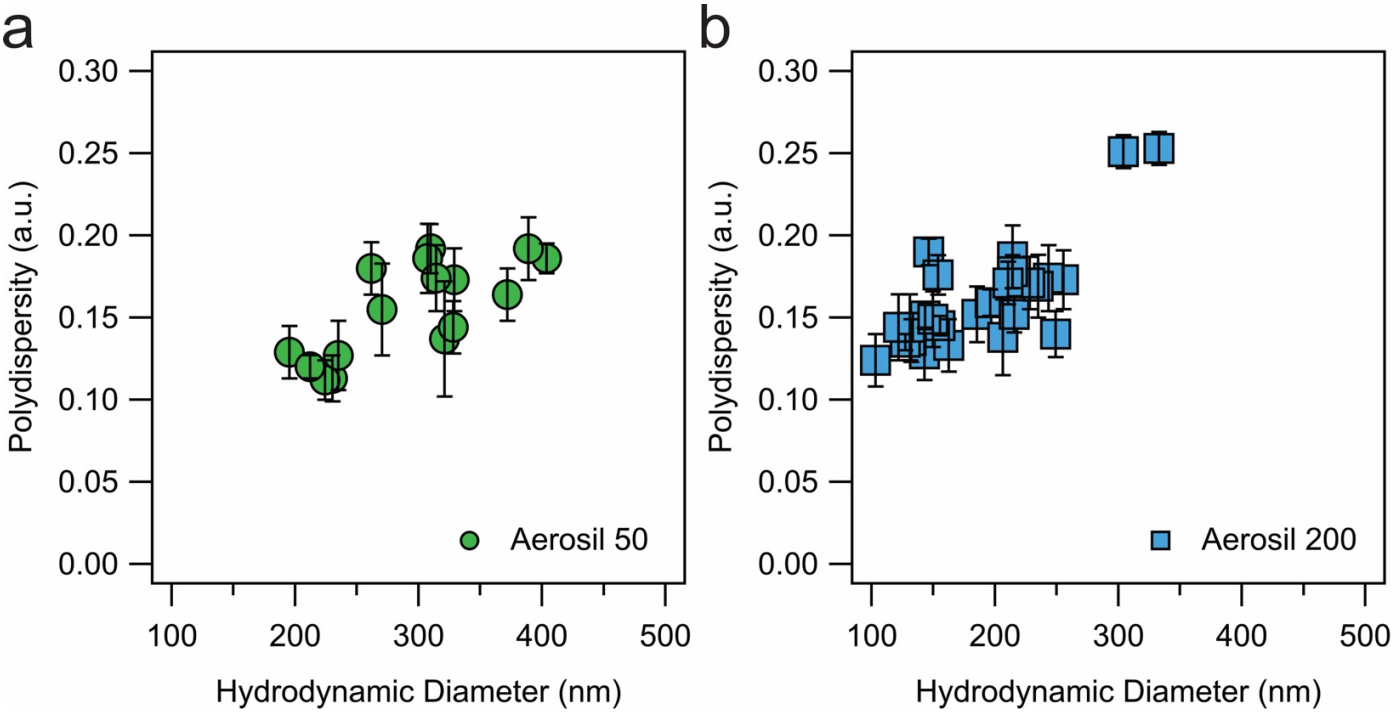

Fig. A5: Polydispersity from DLS experiments as a function of the hydrodynamic aggregate diameter.

The polydispersity increases with growing hydrodynamic aggregate diameters. Thus, the smallest aggregates, produced by centrifugation and measuring the supernatant, show the smallest polydispersity. In contrast, big aggregates from redispersing the sediment from centrifugation yield the broadest particle diameter distribution.

List of Publications

This thesis is presented as a cumulative dissertation and is based on the following peer-reviewed publications:

[1] Matthias B. Engelhardt, Paul Markus, Nicolas Helfricht, and Georg Papastavrou, "Effective charge of high-generation PAMAM dendrimers in the adsorbed state", *Journal of Colloid and Interface Science*, **2025**, *686, 852-863*. DOI: 10.1016/j.jcis.2025.02.008

[2] André Hofer, Nicola Taccardi, Michael Moritz, Christoph Wichmann, Sabine Hübner, Dominik Drobek, Matthias Engelhardt, Georg Papastavrou, Erdmann Spiecker, Christian Papp, Peter Wasserscheid, and Julien Bachmann, "Preparation of geometrically highly controlled Ga particle arrays on quasi-planar nanostructured surfaces as a SCALMS model system", *RSC Advances*, **2023**, *13, 4011-4018*. DOI: 10.1039/D2RA07585G

[3] Christhy V. Ruiz M, Markus Terlinden, Matthias Engelhardt, Giulia Magnabosco, Georg Papastavrou, Nicolas Vogel, Matthias Thommes, and Julien Bachmann, "Preparation and Surface Functionalization of a Tunable Porous System Featuring Stacked Spheres in Cylindrical Pores", *Advanced Materials Interfaces*, **2023**, *10(33), 2300436*. DOI: 10.1002/admi.202300436

[4] Matthias B. Engelhardt, Daniel Wagner, Mohsen Zarebanadkouki, Nora Meides, Christian Schulbert, Martin G. J. Löder, Nicolas Helfricht, Seema Agarwal, Andrea Carminati, Peter Strohriegl, Jürgen Senker, Christian Laforsch, and Georg Papastavrou, "Following Changes at the Solid/Liquid Interface for Large Microplastic Particles by Streaming Potential", *Chemistry-Methods*, **2025**, *5(12)*, *e202500102*. DOI: 10.1002/cmtd.202500102

[5] Matthias B. Engelhardt, Takuya Sugimoto, Georg Papastavrou, and Motoyoshi Kobayashi, "Electrophoretic Mobility of Nanoparticle Aggregates: Independence from Aggregate Size", *Colloids and Surfaces A: Physicochemical and Engineering Aspects*, **2024**, *703, Part 1, 135244*. DOI: 10.1016/j.colsurfa.2024.135244

This thesis does not include results from the following peer-reviewed publications and manuscripts:

[6] Andreas Cramer,* Johanna Schmidtmann,* Pascal Benard, Andreas Kaestner, Matthias Engelhardt, Stefan Peiffer, and Andrea Carminati, "Ferrihydrite coating reduces microplastic induced soil water repellency", *Environmental Science: Processes & Impacts*, **2023**, *25, 1094-1101*. DOI: 10.1039/d3em00077j **These authors contributed equally to the work.*

[7] Tamino Rößler, Matthias B. Engelhardt, Nicolas Helfricht, and Georg Papastavrou, "Actuation and Charging Mechanisms of Thin PEDOT:PSS Films Probed by Electrochemcial AFM and Impedance Spectroscopy", *Journal of Polymer Science,* **2025**, *63, 4661-4672*. DOI: 10.1002/pol.20250064

[8] Jonas Schwan, Matthias B. Engelhardt, Jürgen Senker, Georg Papastavrou, and Anna Schenk, "Polymer-Mediated Electrocrystallization of Nanostructured Co_3O_4 Thin Films and their Functional Properties in Electrocatalytic Water Splitting", Manuscript in preparation for submission in *Advanced Energy Materials,* **2025**.

[9] Sebastian Sittl,* Alexander Berger,* Parisa Atashkadi, Leonie Kanzler, Matthias B. Engelhardt, Lukas Baindl, Nicolas Helfricht, and Georg Papastavrou, "Humic Acid Adsorption and the Colloidal Properties of Microplastic Particles", Manuscript in preparation for submission in *Colloids and Surfaces A: Physicochemical and Engineering Aspects,* **2025**. **These authors contributed equally to the work.*

[10] Anika Mauel, Hülya Markl-Hahn, Nora Meides, Matthias B. Engelhardt, Georg Papastavrou, Peter Strohriegl, Holger Ruckdäschel, and Jürgen Senker, "Adverse effects of Irgafos 168 on polymer stability beyond the polymer's service life", Manuscript in preparation for submission in *Microplastics and Nanoplastics,* **2025**.

Danksagung

An dieser Stelle spreche ich meinen Dank all jenen aus, die diese Arbeit ermöglicht und zu ihrem Erfolg beigetragen haben.

Mein herzlicher Dank gilt zuerst meinem Betreuer Prof. Dr. Georg Papastavrou für die Möglichkeit, meine Doktorarbeit an seinem Lehrstuhl anzufertigen. Insbesondere bedanke ich mich für das entgegengebrachte Vertrauen, die wissenschaftliche Freiheit und die ermöglichten Kooperationen in Japan und in Deutschland.

Ich möchte mich auch bei meinen Kooperationspartnern für die äußerst erfolgreiche Zusammenarbeit bedanken. Großer Dank gebührt Prof. Dr. Motoyoshi Kobayashi für die Möglichkeit, drei Monate meiner Promotion in Japan leben und seiner Gruppe beitreten zu dürfen. An dieser Stelle möchte ich mich auch bei Prof. Dr. Yasuhisa Adachi, Prof. Dr. Takuya Sugimoto und Prof. Dr. Yuji Yamashita bedanken, die mich herzlich in ihre Arbeitsgruppen integriert und mir viel gelehrt haben. Auch möchte ich mich bei Prof. Dr. Jürgen Senker, Prof. Dr. Julien Bachmann, Prof. Dr. Anna Schenk, Prof. Dr. Stefan Peiffer, Prof. Dr. Andrea Carminati und Prof. Dr. Anke Nölscher für die erfolgreichen Kooperationen und die gute Zusammenarbeit bedanken. Nicht zuletzt habe ich die Zusammenarbeit mit anderen Doktoranden für gemeinsame Publikationen sehr genossen. Aus diesem Grund möchte ich mich bei Dr. André Hofer, Dr. Christhy V. Ruiz Madroñero, Dr. Andreas Cramer und Dr. Johanna Schmidtmann, Dr. Sebastian Sittl und Alexander Berger, Dr. Jonas Schwan, Tamino Rößler, Anika Mauel und Myriam Younes für die reibungslose Zusammenarbeit bei vielfältigen Publikationen bedanken.

Einen besonderen Platz nimmt Dr. Nicolas Helfricht ein. Er leistete einen erheblichen Beitrag zu meinem wissenschaftlichen Erfolg. Seit Anbeginn meiner Zeit am Lehrstuhl PC2 stand er mir betreuend zur Seite, lehrte mich wissenschaftliches Arbeiten und die Kunst der interuniversitären Kommunikation. Außerdem bin ich ihm für die persönlichen Ratschläge und sein Engagement für uns Doktoranden sehr dankbar.

Ganz große Anerkennung gebührt Paul Markus. Er war es, der mich im März 2018 frisch in der PC2 unter seine Fittiche nahm. Nicht nur sorgte Paul dafür, dass ich der Elektrokinetik und dem *Impedancen* bis zum Ende meiner Promotion treu blieb, sondern hat mir erst den Weg dazu geebnet.

Unseren „Lehrstuhlmamas“ Sybille Zimmermann und Sieglinde Hörath gebührt ebenso ein herzlicher Dank. Sie haben uns im Dokumentenurwald den Rücken freigehalten und sich immer herzlich um ihre „Kinder“ gekümmert. Große Stützen waren auch Carmen Kunert, Nina Volk, Markus Hund, Petra Zippelius und Dr. Wolfgang Häfner. Ihr trugt und tragt einen großen Teil dazu bei, den Lehrstuhl am Laufen zu halten!

„Trink mer ans?“ haben meine Kollegen und vor allem Freunde in der PC2, PC1 und MC2 nicht nur einmal gehört. Eine Promotion ohne treue Weggefährten ist für mich unvorstellbar. Zum Glück hätte ich mir kein tolleres Umfeld wünschen können. Angefangen bei Tamino Dion Linos Walter Rößler, der mit mir im März 2018 in der PC2 als Hiwi angeheuert hat, dicht gefolgt von Philipp *Ambientebeleuchtung* Dennstedt, der im Juli nachzog. Wir drei gingen nun sieben Jahren durch dick und dünn und ich bin euch für euren Rückhalt herzlichst dankbar. Gleichermaßen möchte ich Agnes Specht meinen großen Dank aussprechen. Du wurdest mir im Handumdrehen eine enge Freundin und botest mir stets die nötige private und universitäre Unterstützung.

Gerade, wenn man so lange an einem Lehrstuhl ist, gab es viele Altvordere, von denen ich lernen durfte. Daher möchte ich mich bei Sebastian Gödrich, Dr. Andreas Mark, Dr. Andreas Karg, Katharina Ottermann, Paul Markus, Dr. Nadine Raßmann, Dr. Sebastian Sittl und Steffen Trippmacher für all eure Unterstützung, Ratschläge, den wissenschaftlichen Diskurs und die Zusammenarbeit auf Augenhöhe bedanken. Auch meiner jüngeren Kollegin Leonie Kanzler, der neuen Generation an Hiwis aus Inka Krammel, Roman Glaß, Jessica Häfele, Samuel Hasenauer und Florian Thiem möchte ich für die schönen Pausen, die vielfältige Freizeitgestaltung und die sportliche Ertüchtigung an der Bodyweight Station danken. Lukas Baindl habe ich ebenso schöne Jahre am Lehrstuhl zu verdanken.

Meinen Forschungsalltag versüßten auch meine Freunde Dr. Ina Klein, Stefan Rettinger, Alexander Berger, Max Theis, Dr. Tobias Lauster und Sudeshna Sahoo aus der PC1 sowie Dr. Sophie Fritze und Roman Schaller aus der MC2 und Dr. Timon Schönauer aus der AC2. *Freitags um drei* war eine meiner liebsten Zeiten, nach der immer Spaß und Action auf uns warteten. Natürlich gelingen all diese Interaktionen am besten bei einem oberfränkischen Traditionsgetränk.

Weiterer Dank geht an meine Freunde an der Universität Tsukuba in Japan. Meine Bürokollegen Zihang Wang, Marita Wulandari und Dr. Medina Uli Alba Somala haben mich herzlich willkommen geheißen und mich mit Rat und Tat bei der Anpassung an das Leben in Japan unterstützt. Mein wissenschaftlicher Erfolg in Tsukuba ist nicht zuletzt Shunsuke Sato zu verdanken, der mich schnell in die neue Laborumgebung eingeführt hat.

Ich möchte auch meinen Freunden danken, die mich seit vielen Jahren begleiten und stets für mich da waren. Danke Thomas B., Patrick L., Stephan F. und Hanna S.

Abschließend gilt mein größter Dank meiner Familie – meiner Partnerin Vanessa, unserem Sohn Leo, meinen Eltern Tanja und Klaus sowie meinen Geschwistern Annika und Michael. Eure stetige und unablässige Unterstützung über all die Jahre hat diesen Weg erst möglich gemacht.

Herzlicher Dank!

(Eidesstattliche) Versicherung und Erklärung

(§ 8 Satz 2 Nr. 3 PromO Fakultät)

Hiermit versichere ich eidesstattlich, dass ich die Arbeit selbstständig verfasst und keine anderen als die von mir angegebenen Quellen und Hilfsmittel benutzt habe (vgl. Art. 97 Abs. 1 Satz 8 *BayHIG*).

(§ 8 Satz 2 Nr. 3 PromO Fakultät)

Hiermit erkläre ich, dass ich die Dissertation nicht bereits zur Erlangung eines akademischen Grades eingereicht habe und dass ich nicht bereits diese oder eine gleichartige Doktorprüfung endgültig nicht bestanden habe.

(§ 8 Satz 2 Nr. 4 PromO Fakultät)

Hiermit erkläre ich, dass ich Hilfe von gewerblichen Promotionsberatern bzw. -vermittlern oder ähnlichen Dienstleistern weder bisher in Anspruch genommen habe noch künftig in Anspruch nehmen werde.

(§ 8 Satz 2 Nr. 7 PromO Fakultät)

Hiermit erkläre ich mein Einverständnis, dass die elektronische Fassung meiner Dissertation unter Wahrung meiner Urheberrechte und des Datenschutzes einer gesonderten Überprüfung unterzogen werden kann.

(§ 8 Satz 2 Nr. 8 PromO Fakultät)

Hiermit erkläre ich mein Einverständnis, dass bei Verdacht wissenschaftlichen Fehlverhaltens Ermittlungen durch universitätsinterne Organe der wissenschaftlichen Selbstkontrolle stattfinden können.

_____

Ort, Datum, Unterschrift

Matthias Bruno Engelhardt

Surface Characterization by Electrokinetics:

Interfaces, Adsorption, and Microplastics

Dissertation, 2025

University of Bayreuth

Physical Chemistry 2

Faculty of Biology, Chemistry & Earth Sciences

Universitätsstraße 30

95447 Bayreuth